TRIBOLOGY OF ADVANCED MATERIALS FOR EXTREME CONDITIONS

INCLUDING SPACE APPLICATIONS

A Dissertation

by

VASILIS TSIGKI

Submitted to the Graduate and Professional School of
Texas A&M University
in partial fulfillment of the requirements for the degree of

DOCTOR OF PHILOSOPHY

Chair of Committee,	Andreas A. Polycarpou
Committee Members,	Ali Erdemir
	Matt Pharr
	Miladin Radovic
	Spyros Tseregounis
Head of Department,	Guillermo Aguilar

August 2023

Major Subject: Mechanical Engineering

ABSTRACT

Extreme conditions dictate the utilization of advanced materials and the development of state-of-the-art processes to accommodate the strong needs of low friction and wear in several bearing applications. Such extreme conditions can be found in the Venusian atmosphere, nuclear reactors, and superlubricity applications. Due to the variety of conditions of each application, different approaches were taken to address these challenges.

NASA and other space agencies seek to explore the harsh atmosphere and surface of Venus by deploying balloons, rovers, and drills to exploit information of the atmospheric composition and the soil and. To this end, a systematic study was carried out with the selection, testing, and characterization of advanced coatings, including a plasma sprayed (PS) NASA-developed nickel-based alloy, namely PS400. It was found that diamond-like carbon (DLC) coating significantly enhanced the tribological properties of PS400 at room temperature conditions (RT). Also, the main lubricating mechanism of PS400 is due to the generation of oxide glazes when subjected to high temperature (HT) oxidative environments. However, under Venusian environment the wear performance degrades. Furthermore, DLC and titanium-doped molybdenum disulfide ($TiMoS_2$) can be used as sacrificial coatings when paired with PS400 for lower temperatures (i.e., during descending on Venusian surface), and initial operation. Another significant finding is that DLC and $TiMoS_2$ depicted extreme chemical inertness when exposed to Venusian-simulated atmosphere for 72 hours, whereas PS400 and polycrystalline diamond (PCD)

formed dense adsorbed layers rich in sulfur. Also, the mechanical properties of PCD remained unaffected following Venusian aging, therefore, can be used as a structural material where dimensional precision is of a concern. Finally, the sulfur-rich layer appeared to have good lubrication properties when subjected to HT sliding.

ACKNOWLEDGEMENTS

I would like to express my deepest gratitude to my research advisor Professor Andreas A. Polycarpou for being an amazing mentor during my degree program and also supportive in my personal life. I would like to thank my committee members Professor Ali Erdemir, Professor Matt Pharr, Professor Miladin Radovic, Professor Spyros Tseregounis, and particularly my advisor Professor Andreas A. Polycarpou, for their valuable guidance, support, and encouragement throughout the course of this research.

Thanks also go to my friends and colleagues, especially my research group members in the Microtribodynamics laboratory, for their work and friendship. I would also like to thank the department faculty and staff for making my time at Texas A&M University a great experience.

I would like to acknowledge the support from Small Business Innovation Research (SBIR) by NASA for providing the financial support for this research. In addition, I would like to thank Dr. Pixiang Lan, Dr. Saifur Rahman, Dr. Malcolm Stanford, and Dr. Samuel A. Howard for their valuable suggestions during this research. I would like to also acknowledge the use of the Texas A&M Materials Characterization core Facility (RRID:SCR_022202), for the access to SEM, EDS, and Raman Spectroscopy, and XPS Instruments.

Finally, my warmest thanks to my parents and family for their supportive role, unconditional love, and encouragement thought my education journey.

CONTRIBUTORS AND FUNDING SOURCES

Contributors

This work was supervised by a dissertation committee consisting of Professor Andreas A. Polycarpou and committee members Professor Ali Erdemir and Professor Matt Pharr of the Department of Mechanical Engineering, Professor Spyros Tseregounis of the Department of Chemical Engineering and Mechanical Engineering, and Professor Milan Radovic of Materials Science & Engineering. The studies in **Chapters 2-6** were conducted with the help of Dr. Pixiang Lan, Dr. Saifur Rahman, and Dr. Kian Bashandeh from ATSP Innovations as the intermediate SBIR sponsor. The studies in **Chapter 7** were conducted with the guidance of Dr. Ali Beheshti of George Mason University and Dr. Richard Wright of Idaho National Lab for providing samples and valuable information. The studies in **Chapter 8** were conducted with the help of Dr. Saifur Rahman from ATSP Innovations. The development of the high temperature stage in **Appendix A.2** was contacted by Dr. Pixiang Lan from ATSP Innovations. All other work conducted for the dissertation was completed by the student independently.

Funding Sources

Funding of the studies in **Chapter 2-6** was provided by Small Business Innovation Research (SBIR) under Grant Number 80NSSC19C0517 and 80NSSC20C0180 from the NASA Glenn research center. The works in **Chapter 8** were partially funded by the Advanced Manufacturing program of the National Science Foundation award CMMI-AM #2029059.

NOMENCLATURE

A_c	Contact area
a-C:H	amorphous hydrogenated
AP	Ambient pressure
ATSP	Aromatic thermosetting co-polyester
COF	Coefficient of friction
CVD	Chemical vapor deposition
d	Sliding distance
DLC	Diamond-like carbon
EDS	Energy dispersive X-ray spectroscopy
E_r	Reduced modulus
F	Normal force
FIB	Focused ion beam
GEER	Glenn extreme environments rig
h	Wear depth
H	Hardness
h_c	Contact depth
h_{max}	Maximum depth
HP	High pressure
HPHT	High pressure-high temperature
HPP	High performance polymer

HT	High temperature
HTGR	High temperature gas-cooled reactor
HTT	High pressure tribometer
HVAF	High velocity air fuel
INC	Inconel
INL	Idaho national lab
LP	Laser peening
MPCM	Microencapsulated phase-change material
p	Hertzian pressure
PCD	Polycrystalline diamond
PCM	Phase-change material
PEEK	Polyether ketone
P_{max}	Maximum load
PS	Plasma spray
PTFE	Polytetrafluoroethylene
PVD	Physical vapor deposition
R	Radius of curvature
r_i	Inner radius of the wear track
RMS	Root-mean-square
r_o	Outer radius of the wear track
RT	Room temperature
S	Initial slope of unloading curve

Sa	Average absolute roughness
SEM	Scanning electron microscopy
Sku	Kurtosis
Sp	Highest mean-to-peak distance
Sq	Root-mean-square roughness
Ssk	Skewness
Sv	Highest mean-to-valley distance
Sz	Highest peak-to-valley distance
TEM	Transmission electron microscopy
TME	Thermal microstructure engineered
UHPT	Ultra-high pressure tribometer
V	Wear volume
VHTR	Very high temperature reactors
$\dot{W}$	Wear rate
XPS	X-ray photoelectron spectroscopy
Δr	Step increment
ε	Geometric constant

TABLE OF CONTENTS

Page

LIST OF FIGURES

Page

LIST OF TABLES

Page

1. INTRODUCTION AND OBJECTIVES

1.1. Introduction

Tribology, the study of friction, wear, and lubrication between interacting/rubbing surfaces is a major concern in a plethora of engineering applications (i.e., bearing systems, valves, pumps, bushings, gas turbine engines etc.) wherein unwanted energy loss is dissipated to the environment in the form of frictional heat and material removal (wear). It was reported that 11% of the total energy consumption in transportation, power generation, and machinery industries in the United States can be harvested through tribology [1]. Therefore, the minimization of such energy losses can increase the efficiency of the systems significantly, and ensure operational stability and longevity, omitting frequent maintenance and the associated costs. However, the consideration of tribology is sometimes downgraded or even neglected due to the interdisciplinary and complex nature of the subject, which includes engineering, physics, metallurgy, and chemistry. The effect of each discipline on the tribological response of an engineering system is intensifying when harsh environments prevail, for example high temperatures (HTs) and high pressures (HPs).

The widely used friction-reducing polymers are not suitable for HT applications (> 300°C), as their mechanical properties deteriorate, therefore the use of ceramic and metallic alloys is imposed. Furthermore, the application of thin coatings on metallic surfaces is becoming more and more prevalent in the industry, where there is a huge demand for particular surface characteristics, while the parent metallic substrate cannot be

change due to regulatory and operational concerns. The coatings technology is a mature, well-developed field, driven by the dimensional accuracy and the numerous deposition techniques, including physical vapor deposition (PVD), chemical vapor deposition (CVD), electrostatic spray deposition (ESD) etc., which allow the modification of almost any substrate. Another advantage of coatings is the utilization of them as sacrificial layers for particular operations, for example running-in or starting periods in interacting friction surfaces. Also, the coatings can be re-applied on damaged surfaces without the need to replace all the equipment (i.e., rotating shafts in engines, and bearing systems), therefore reducing maintenance costs. However, there are a few technical concerns that should be met for the successful implementation of substrate-coating systems. For example, the coatings should be well-adhered to the substrate, and there must be no thermal property "mismatch" that might cause delamination of the coating. The best way to accommodate these concerns is with the use of a bonding interlayer between the coating and the substrate.

Diamonds and their constituents, for example amorphous hydrogenated (a-C:H) diamond-like carbon (DLC) and polycrystalline diamond (PCD) coatings, demonstrated excellent tribological performance under different experimental conditions [2–5]. Plasma sprayed (PS) series 400, (PS400), a NASA-developed HT coating is considered a frontrunner among a series of PS coatings, and it is intended for HT and high speeds for turbine engine applications (coating material on the rotating shaft) [6]. Also, PS400 suffered from generating high friction and wear under RT conditions, attributed to the inability to form lubricious oxide glazes that would have mitigated the contact. In a study

by the author (as will be discussed in **Chapter 2**), the significance of selecting an "appropriate" mating surface to the PS400, in particular, was explored and suitable interfaces with enhanced tribological properties at RT and HT conditions is reported [7].

To illustrate the importance of the environment, a selected tribo-pair from **Chapter 2** was further examined under air and CO_2, as will be discussed in **Chapter 3**. It is widely accepted that at HT oxidative environments (i.e., in air), the formation of tribo-chemically induced oxide layers at the interface control the friction and wear, and it usually provides a buffer mechanism wherein the direct contact of metallic surfaces is avoided [8]. The selection of CO_2 environment was driven by the design of tribological materials for Venus bearing applications, as will be further discussed in **Section 1.2**. This study by the author was the first reported study towards suitable materials for Venus exploration [9].

Another important aspect of tribology is the effect of environmental pressure on the tribological performance of the materials under examination. The study of high CO_2 pressure is not adequately studied in the literature, as it only considers air-conditioning applications where CO_2 is being used as a refrigerant [10]. Also, when HT is included in the system the complexity is further compounded. The author studied the effect of HP and HT in a high pressure high temperature (HPHT) tribological setup pertaining to Venus future missions for surface and near-surface exploration using rovers, drills, and balloons, as will be discussed in **Chapter 4** [11].

The Venusian harsh environment can have an adverse effect on the exposed surfaces via different chemical interactions, for example oxidation and corrosion. While the effect of long-duration Venusian exposure is thoroughly studied by exposing sensors,

electronics and packaging in the Glenn Extreme Environments Rig (GEER) [12], where the exact composition of Venusian environment is simulated, the same effect on tribological materials is yet to be explored. In **Chapter 5** the effect of Venusian exposure on the chemical and mechanical properties of friction-reducing materials is studied, and in **Chapter 6** Venusian-aged bearing materials were subjected to a tribological study.

Another special HT environment is for nuclear power and generation wherein higher outlet temperatures of the reactors (>750 °C) will increase the efficiency of power plants [13]. Tribological parts in very-high temperature reactors (VHTR) and high-temperature gas-cooled reactors (HTGR), for example valves and control rods will encounter severe conditions and their contact behavior are of vital importance in maintaining reactor stability and operational integrity [14]. In **Chapter 7** a novel surface hardening technique is introduced and proved to have beneficial tribological effect of HT nickel-based alloys [15].

As mentioned earlier, the nature of polymeric materials prevents their more prevalent utilization in HT applications, and their operating temperature is up to 300°C, for high performance polymers (HPPs), as aromatic thermosetting coPolyester (ATSP) [16]. Such HPP are composite polymer blends wherein the matrix phase provides structural integrity and good accommodation to the lubricating additive phase. Again, the use of polymer coatings (instead of bulk composites) is beneficial mainly due to two reasons; (1) better heat dissipation and (2) higher bearing capacity. Among HPPs, ATSP and polytetrafluoroethylene (PTFE) blends depicted excellent tribological behavior in a wide range of temperatures, from RT to 300°C [16]. However, to further reduce the

coefficient of friction (COF) and to realize superlubricity, novel additives could be added. In **Chapter 8** the efficacy of a novel microencapsulated phase-change material (MPCM) additive in reducing the COF towards macro superlubricity is discussed.

This work studies the tribological performance of materials under extreme conditions. The main focus is related to bearing materials for Venus conditions and the results are discussed in **Chapters 2-6**. A unique surface technique targeting the betterment of the tribological behavior of HT alloys for nuclear reactor applications is proposed, and the results are discussed in **Chapter 7**. Another extreme condition is when tribological surfaces generate ultra-low frictional forces, and a novel phase-change additive is introduced and discussed in **Chapter 8**. In each chapter detailed information of the background and challenges is given and is also summarized in the following section.

1.2. Background and challenges

In this section a brief background and challenges associated with each application described in **Section 1.1** is discussed. Venus has been the topic of new exploration to investigate why the planet took such a different evolutionary path from accretion, compared to Earth, as it is believed that the atmospheres of both planets once had the same water and CO_2 levels [17]. Venus is similar to Earth in terms of size, distance from the sun, mass, and composition [18], however, significant technical challenges exist in Venus exploration. Compared to terrestrial conditions, the surface pressure is nearly 92 times higher, and the environment is primarily 96% CO_2 gas, and 3.5% N_2, and minute traces of Ar, H_2S, SO_2, HF, and HCl (with SO_2 being the dominant minor gas) with extremely hot (464°C mean surface temperature) and dry conditions [17]. The complexity of the

atmosphere is further compounded by the presence of dense sulfuric acid clouds above ~ 40 km from the surface [17]. In fact, previous planet Venus landers were able to transmit data for only a few hours, before succumbing to the harsh environment [19]. The successful accomplishment of future missions and in-situ investigation of Venus surface in a long-duration operation requires moving mechanical components that can withstand such extreme conditions [18]. For example, moving mechanical parts of entry probes, landers, sampling drills and balloons will encounter harsh environments and their continuous operation is vital for the successful accomplishment of long-duration missions to Venus. In addition to the HTs, the bearing materials will face lower temperatures while descending [20], therefore an enhanced tribological behavior at moderate and ambient temperatures (RT) should be demonstrated. In order to assess the tribological behavior of potential "candidate" materials, a specialized apparatus (called tribometer) should be designed and manufactured. In this work, an existing ultra-high pressure tribometer (UHPT) was modified to be able test specimens under Venus environmental conditions. Detailed design of the HPHT chamber of UHPT is provided in the **Appendix**.

For future generation nuclear reactors, the operating temperature of bearing materials, for example bushings in the controlling rods and valves is much higher than the mean surface temperature on Venus, that is 464°C (also the environment is different), therefore a different approach on the material selection and testing protocol should be taken. Besides, the starting point for material selection for nuclear reactors is already set, and there is regulatory scrutiny from the responsible commissions where the selection and testing of new materials could take 10+ years. At the same time, there is a need for low

friction and wear generation of the HT nickel-based alloys commonly used in nuclear reactors. Increasing demand for electricity production, coupled with more conservative regulations for clean and reliable energy have resulted in extensive research and development in nuclear power production during the past decade. The Generation IV International Forum has launched promising nuclear energy system concepts, seeking more sustainable, reliable, and efficient power plants [13]. A VHTR and HTGR are among the selected candidates to operate at high outlet temperatures (above 750°C) designed to reach 60-year operational lifespan [21]. Although helium is an inert gas, it inevitably contains impurities resulting in accelerated surface degradation for mechanical components in coolant circulation systems [22]. Besides exposure to harsh VHTR and HTGR environments, tribological parts in these reactors, in particular, undergo low speed sliding (e.g., valves and control rods under intermittent oscillatory motion and often combined with long idle times), or high frequency small vibratory condition (e.g., fretting in heat exchanger joints). Accordingly, their contact behavior are of vital importance in maintaining reactor stability and operational integrity [14]. Previous studies on the commonly used HT nickel-based alloys under He environment reported high friction and wear [23,24], due to a significant degradation of the mechanical properties (i.e., Young's modulus and hardness) and the failure to accommodate (due to low bearing capacity) any favorable tribo-chemically induced superficial oxide layer during sliding [25]. Therefore, a surface hardening modification technique was implemented in this study to enhance the surface properties of HT Ni-based alloys.

As seen in the previous paragraphs, the HT and the environment add complexities either in the form of material limitations or experimental capabilities. However, another kind of intricacy can come from extremely low friction requirements for the development of smart surfaces and multifunctional structures for engineering applications. While superlubricity (COF < 0.01) can be realized at the nano-micro level via an incommensurability phenomenon and using exotic materials [26], generating superlubricity at the macro level is intricate due to the presence of structural defects and a lattice disorder of the contacting surfaces. This is evident by the sparse literature wherein superlubricity was achieved in the macro-level [27,28]. In this study, a novel phase-change additive is proposed for ultra-low macroscopic friction engineering applications. A summary of the applications and indicatives COF values with the corresponding studies of each chapter is schematically given in **Figure 1.1**.

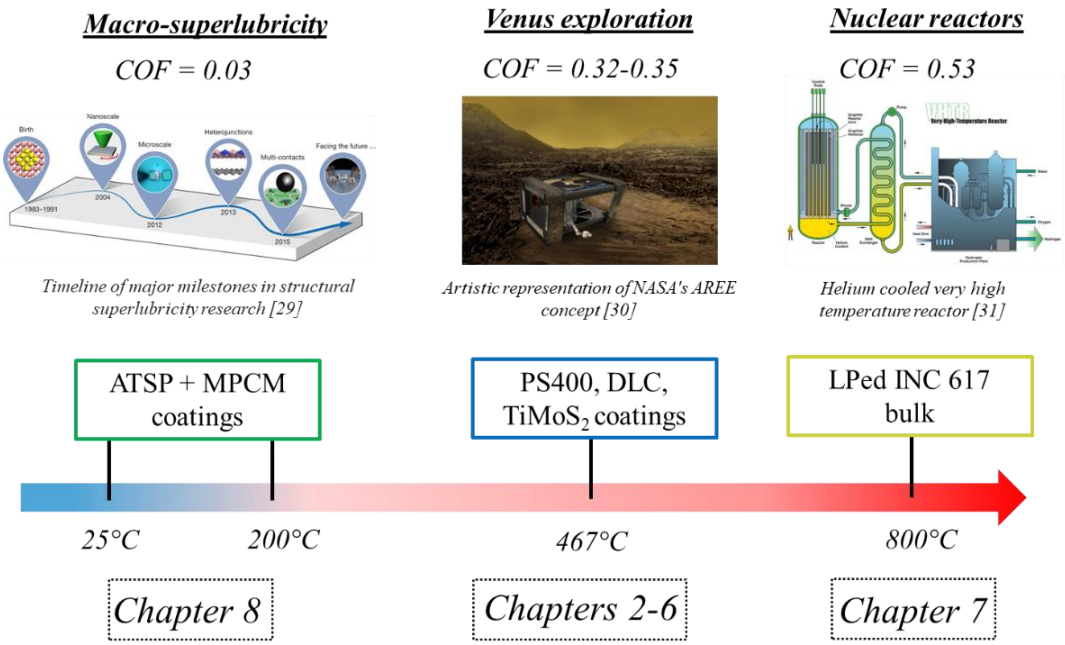

Figure 1.1 Summary of applications and challenges and the corresponding studies of each chapter [29–31].

1.3. Objectives and outline

An overall research outline of the different studies and the corresponding approaches of investigating suitable materials for (1) Venus, (2) nuclear reactors and (3) superlubricity extreme condition applications is shown in **Figure 1.2**. Also, the need, limitations, and contribution for each application is shown in the flow chart. As mentioned in **Section 1.1**, there is a need for the development of advanced materials which can withstand harsh Venusian conditions, however, this requires specialized testing at HTs and HPs. While there is a plethora of tribological studies under CO_2 environment, the addition of HT has not been extensively studied, as most of the applications are for compressors in refrigeration systems [10,32–34].That was also the driving force of this study, with the goal/contribution of developing interfaces for Venusian conditions. In the 1st approach (**Chapter 2**) potential coatings seeking low friction and wear at low and HT under ambient environment were introduced. It is generally true that every new material is tested in ambient conditions first, followed by more specialized testing. If adequate behavior was observed, then the 2nd step was followed, otherwise new materials were introduced. In the 2nd step (**Chapter 3**) the environment was changed to ambient pressure (AP) CO_2, and an additional intermediate temperature was added. At the 3rd step (**Chapter 4**) the tests were performed under HP CO_2 atmosphere and at the exact surface temperature of Venus, that is 464°C. During the 4th step selected tribo-surfaces were subjected to short-duration Venusian aging and the chemical/mechanical and tribological properties were

examined, as discussed in **Chapter 5** and **Chapter 6**, respectively. At each iteration the tested samples were characterized by analytical techniques, and appropriate connections with the tribological behavior were made.

The motivation, approach, limitations, and contribution regarding the implementation of a surface technique that can enhance the mechanical and tribological attributes of tribological HT alloys, for example mechanical parts in the controlling rods and valves of nuclear power plants is shown in the right-hand side of **Figure 1.2**. While there are several surface hardening techniques, for example shot peening, the resulting surface of the treated samples is such that generates high frictional forces due to high roughness. Herein, a novel laser peening method was introduced that can enhance the tribological and mechanical properties of a HT alloy, under 800°C He nuclear reactor environment, as discussed in **Chapter 7**.

Finally, the respective flowchart of realizing superlubricity is also presented in **Figure 1.2**. Driven by the motivation of the development of ultra-low friction-generating materials, a novel phase-change additive was added to an advanced polymeric matrix for engineering practical applications. The results are presented in **Chapter 8**.

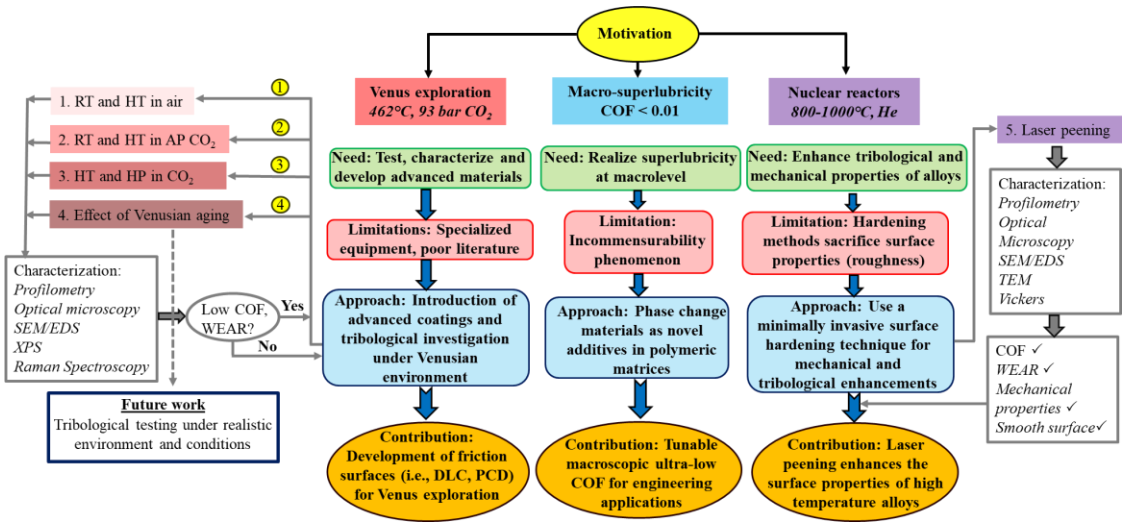

Figure 1.2 Flowchart of PhD dissertation.

2. TRIBOLOGICAL BEHAVIOR OF PS400-RELATED TRIBO-PAIRS FOR SPACE EXPLORATION[*]

2.1. Introduction

Maintaining low COF and low wear between sliding interfaces at HT is a major challenge in tribology, due to changes in the mechanical and chemical properties of the rubbing surfaces [23]. Many bearing systems such as in space applications [35], gas turbine engines [6], and power generation and conversion in nuclear reactors [24], operate at HT harsh environments. In such environments, conventional liquid lubricants are infeasible due to thermal degradation above 250°C [36], thus, the utilization of solid lubricants is inevitable. As the contribution of individual solid lubricants is limited in a narrow range of temperatures, and seeking to expand the applicability range, Sliney introduced different solid lubricants, such as silver and fluorides [36]. Scientists implemented such solid lubricants into intermetallic matrix composites [37,38], ceramic matrix composites [39], and self-lubricating composite coatings [40].

Metal alloys have also been investigated for HT applications, which their acceptable tribological behavior relies on an oxide layer formation at the interface [24,41–43]. Scientists at NASA Lewis Research Center advanced Sliney's work PS100 [36] and developed a series of self-lubricating HT coatings belonging to the PS-family [6,44–46].

[*] Reprinted with permission from "Tribological behavior of PS400-related tribopairs for space exploration" by Vasilis Tsigkis, Kian Bashandeh, Pixiang Lan, Andreas A. Polycarpou, 2021. Tribology International, 153, 1-13, Copyright 2023 by Vasilis Tsigki.

The latest reported version of the coating, namely PS400 is constituted of a Ni-based matrix, a hardener oxide phase, and solid lubricants. Specifically, Ni-Mo-Al acts as a supportive matrix and provides strength and creep resistance. Chromium oxide is added to the matrix as a hardening agent to further increase the wear resistance of the composite. Silver and barium/ cadmium fluorides eutectic act as low and HT solid lubricants, respectively.

DellaCorte et al. tribologically tested PS400 up to 650°C in ambient conditions and high sliding speeds (3 m/s), and low COF and wear at HT were reported. However, when sliding at RT (25°C) a significant increase in the COF was observed, associated with the inability of PS400 to form lubricious glazes at low temperatures [6]. Radil et al. examined the tribological performance of PS400 from 260 to 927°C and showed significant softening of the nickel-based matrix at 760°C, whereas the coating was thermally unstable at 927°C. The beneficial contribution of the lubricious transfer film was clearly detectable from 538 to 760°C. However, at 260°C, the absence of an oxide glaze film, and the low lubricating performance of the solid lubricants resulted in high COF and wear [47].

Li et al. modified the PS400 Ni-based matrix and increased the concentration of the solid lubricants. The bulk composite prepared by sintering demonstrated a low COF from RT to 800°C at moderate sliding speeds (1 m/s). Silver and fluorides provided adequate lubrication, still without the formation of a glaze oxide film [48]. Nonetheless, previous studies on PS400 were focused on tribologically testing the coating against nickel-based [6,35] and cobalt-based [47] superalloys, targeting HT applications. Also,

high sliding speeds were prevailed, associated with turbine engine application, as a coating material on the rotating shaft [6], or as sliding bearing composite [47]. However, several low-speed space-related applications, such as bearing components on the entry probes and long-lived balloons for future missions to Venus, will operate in the upper atmosphere where similar to Earth temperatures prevailed [20]. Thus, there is a need for a new counter-surface material, which can enhance the tribological behavior at RT conditions, and expand the operation range of PS400.

Typically, sliding at RT exhibits less challenges. Ceramics are favored materials for tribological applications due to their high hardness, corrosion resistance, low thermal expansion, and low density [49,50]. In fact, crystalline carbon-based materials, such as PCD, or the DLC family of coatings are excellent candidates for ultra-low friction and wear [2,3]. PCD coatings are prepared by sintering resulting in a coarse micro-crystalline structure. Qin et al. tested sintered PCD in nitrogen atmosphere and varying relative humidity (RH) content and reported a reduction on the COF with decreasing RH, but longer run-in periods occurred [3]. The same authors explored the performance of PCD at low RH content and nitrogen environment, against different ceramic mating surfaces and measured a low steady-state COF due to graphitic or amorphous carbon structures and material transfer to the counter-surface [4]. However, limited literature exists on the tribological performance of PCD under HT. Erdemir et al. tested PCD and DLC up to 400°C and reported the integrity of PCD with a deterioration of COF and wear up to 400°C, and thermal degradation of DLC above 300°C [5].

DLC has superior performance at RT conditions, but its mechanical properties severely degrade above 500°C [51] due to graphitization. Wang et al. investigated the influence of annealing temperature on the tribological performance of a-C:H DLC coatings and an increasing trend of COF up to 300°C, with a subsequent decrease from 400 to 600°C, due to graphitization was reported. In the case where DLC slid against a hard ceramic counter-surface, when annealed at 600°C, the coating was penetrated [52]. Deng et al. showed that regardless of the penetration of the a:C-H DLC film at 200°C, it can still maintain low friction due to the formation of graphite-rich transfer layer [53].

Besides diamond and its different forms, cermet coatings are being used for several industrial wear protection applications due to their intrinsic characteristics of combining a hard ceramic with a ductile metal that gives high hardness and toughness, respectively [54,55]. Khan et al. investigated the friction and wear mechanisms of molybdenum boride cobalt chrome (MoB/CoCr) for die-casting applications and reported low COF and "zero wear" after sliding for a very short time at RT [56]. However, a broader application range requires prolonged sliding time.

Adequate tribological behavior of PS400 at low temperatures has been a challenge and high values of COF and wear were reported [6,35,47]. In this chapter, the tribological performance of several metallic alloys and ceramic coatings was investigated against PS400 coating, at 25 and 500°C, and at low sliding speeds ranging from 0.05-0.25 m/s in ambient environment. The ambient atmosphere does not replicate non-terrestrial conditions, where vacuum, or other gases (CO_2, N_2, O_2) prevail. Besides, the current study focused on a downselection of different mating surfaces against PS400, targeting the best

tribo-pair at 25, and 500°C. The tribological behavior of a selected tribo-pair at an intermediate temperature was examined in the next chapters to capture any radical shifts on the COF. The worn surfaces and transfer films were studied, and correlations were found to the tribological performance.

2.2. Experimental

2.2.1. Materials and sample preparation

4130 steel disk substrates (25.4 × 25.4 × 6.35 mm) and cylindrical titanium pins with hemispherical face and diameter of 6.35 mm were coated with the desired materials. The pins were coated via PS with PS400 coating (Adma Products Inc). The chemical composition of the PS400 coating, a multi-component alloy, is provided in **Table 2.1**. The as-deposited coating had a thickness of 250 μm and the coating was polished down to 1.3 μm root-mean-square (RMS) surface roughness by a sequence of silicon carbide sandpapers down to 800 grit size. Then, the coating thickness reduced to about 200 μm. The disks were coated with three different materials: Balinit® DLC, PCD, and MoB/CoCr, which were prepared by Oerlikon Balzers, USSynthetic, and Kermetico, respectively.

The DLC coatings were deposited by CVD with a thickness of 2 μm and hydrogen content of 20-40 at%. The as-received coating featured a surface roughness of 0.35 μm RMS. Below the DLC and on top of the 4130 substrate a 9 μm thickness Cr-N inter-layer was deposited for better adhesion of the DLC coating. PCD was prepared by sintering small diamond particles at HP and HT in the presence of a liquid metal catalyst (cobalt) and bonded to a tungsten carbide inter-layer. The diamond and carbide were adhered to 4130 steel substrate by HT brazing. The total thickness of the two layers was 5 mm and

the RMS roughness of the as-received diamond coating was 0.3 μm. MoB/CoCr coatings were sprayed by high velocity air fuel (HVAF) onto the 4130 steel-substrate with a total coating thickness of 300 μm. A metal mixture of nickel, silicon, and boron was first sprayed by HVAF to enhance bonding with the substrate and the roughness was 0.24 μm (RMS) after grinding.

The tribological performance of tribo-pair PS400 coating vs. bulk 4130 steel substrate (RMS 0.75 μm) was served as the baseline, and PS400 coating vs. other coatings were used to identify a better tribo-pair for the Venus application: at both low and HT. The mechanical properties of the samples are presented in **Table 2.2** and were acquired either from the vendors or the literature. The mechanical properties of PS400 are dictated by the Ni-Mo-Al supportive matrix that gives a hardness of 2 GPa, similar to the mild 4130 steel. On the other hand, diamonds are extremely hard, especially in their polycrystalline form with a hardness up to 50 GPa, whereas DLC has a maximum hardness that is half that of PCD. MoB/CoCr has lower hardness than diamonds but is around 5 times harder than the PS400. Clearly, all the coated counter-surfaces of PS400 possess significantly higher values of both hardness and Young's modulus.

Table 2.1 Chemical composition of PS400 provided by the manufacturer (units are in wt.%). Reprinted with permission from [7].

PS400					
Binder matrix			***Hardener***	***Solid lubricants***	
Ni	Mo	Al	Cr_2O_3	Silver	BaF_2/CaF_2
63	3.5	3.5	20	5	5

Table 2.2 Mechanical properties of samples. Reprinted with permission from [7].

Material	Hardness (GPa)	Young's modulus (GPa)	Poisson's ratio
PS400	2±0.16*	83[57]	0.28 [57]
4130 Steel	2.03	205	0.29
DLC	15-25**	170 [58]	0.2 [59]
PCD	49.8**	810 [3]	0.07 [3]
MoB/CoCr	9.8-11.8**	100 [60]	0.3 [60]

*Measured using Vickers' indentation, **Provided by the vendor.

2.2.2. Experimental procedure

Four different pairs were tribologically tested. PS400 spherical pins were slid against bare 4130 steel substrate disks, and against DLC, PCD, and MoB/CoCr coated disks. Before each experiment, the samples were ultrasonically cleaned for 10 minutes in an acetone bath at 40°C. Then, they were rinsed with isopropanol to remove any remaining debris that may stick to the surface, before forced dry with hot air. Thereafter, the pin was fixed on the pin holder, and the disk was placed on the disk holder. For HT experiments, the furnace was heated up to 500°C, while the temperature was recorded using a thermocouple placed close to the contact region. After five minutes of constant temperature inside the furnace, the pin and disk were brought into contact and the experiment was initiated by rotation of the disk. The relative humidity (RH) was measured as 42%. The recorded in-situ normal and friction forces were used to calculate the in-situ COF.

The experimental conditions are shown in **Figure. 2.1**. The speed curve resulted in 240 m sliding distance and 2,970 cycles after 25 minutes of running time. A normal constant force of 5 N induced an initial maximum Hertzian pressure (p) of 462.5, 440.6, 540.4, and 388.8 MPa between the PS400 pins and 4130 steel, DLC, PCD, and MoB/CoCr disks, respectively. The circular wear track on the disk shown in **Figure. 2.1(b)** had a mean diameter of 17.5 mm. Each tribo-pair was first tested under RT and successively at 500°C in ambient environment. The worn surfaces of the samples were examined after the end of the experiments at both 25, and 500°C. After HT experiments, the samples were let to cool naturally. Then, the samples were removed, rinsed with isopropanol, dried under hot air, and stored in a desiccator. A minimum of three experiments for each tribo-pair were carried out to assure repeatability.

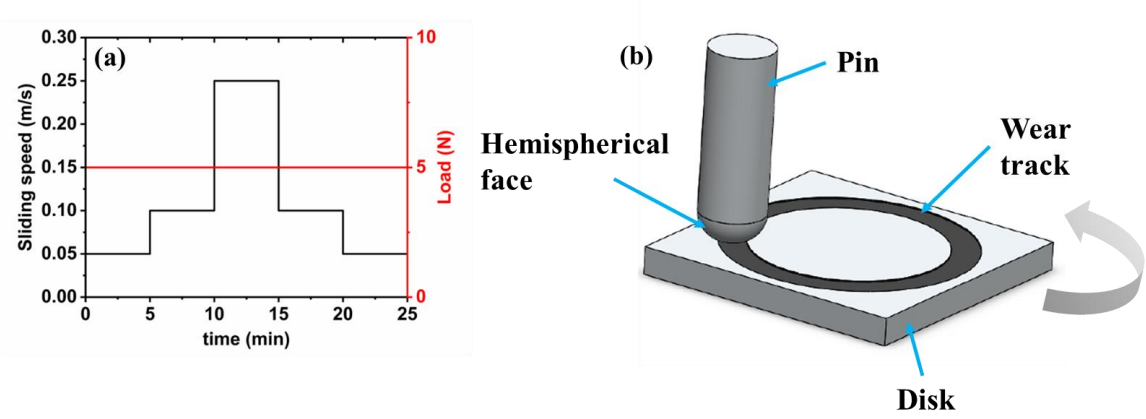

Figure 2.1 Experimental details. (a) Experimental conditions showing sliding speed and normal load versus time, and (b) pin-on-disk contact configuration. Modified with permission from [7].

2.2.3. Characterization

To measure the depth of the wear track and the resulting wear volume of the disks, a Dektak (Bruker) stylus profiler was used. The wear volume (*V*) for each disk was calculated by:

$$V = \int_{ri}^{ro} 2\pi \times r \times h \times dr = \sum_{i=1}^{n} 2\pi \times r \times h\, \Delta r \quad (1)$$

And the wear rate ($\dot{W}$) by:

$$\dot{W} = \frac{V}{F \times d} \quad (2)$$

Where r_i and r_o are the inner and outer radii of the wear track, respectively, h is the measured profilometric wear depth, Δr is the step increment of radius, F is the applied normal force, and d the total sliding distance, as shown in **Figure. 2.2(a, b)** [38]. The wear scans were performed perpendicular to the wear tracks, and four measurements for each sample were carried out at four different locations to obtain the average wear volume on the wear track. The wear volume on the spherical pins was calculated by:

$$V = \frac{\pi}{6} \times h'(3r'^2 + h'^2) \quad (3)$$

Where h' is the height of the worn spherical pin and r′ the radius of the scar measured by the optical image of the pin (using an Olympus DSX510 optical microscope), as illustrated in **Figure 2.2(c, d).** The height, h' can be calculated by:

$$h' = R - \sqrt{R^2 - r'^2} \quad (4)$$

Where R is the radius of curvature of the pin [4].

Optical microscopy was employed on the worn pins and disks after testing at RT, and 500°C. Scanning Electron Microscopy (SEM) was performed on the unworn and worn areas of the disks after the HT experiment to examine the topography of the surfaces. EDS was used to measure the chemical composition of the material transfer for some of the samples. SEM and EDS analyses were performed in a Vega II LSU SEM that was equipped with EDS detector. All the SEM images and the EDS scan were acquired using 5KV and 20KV operational voltages, respectively.

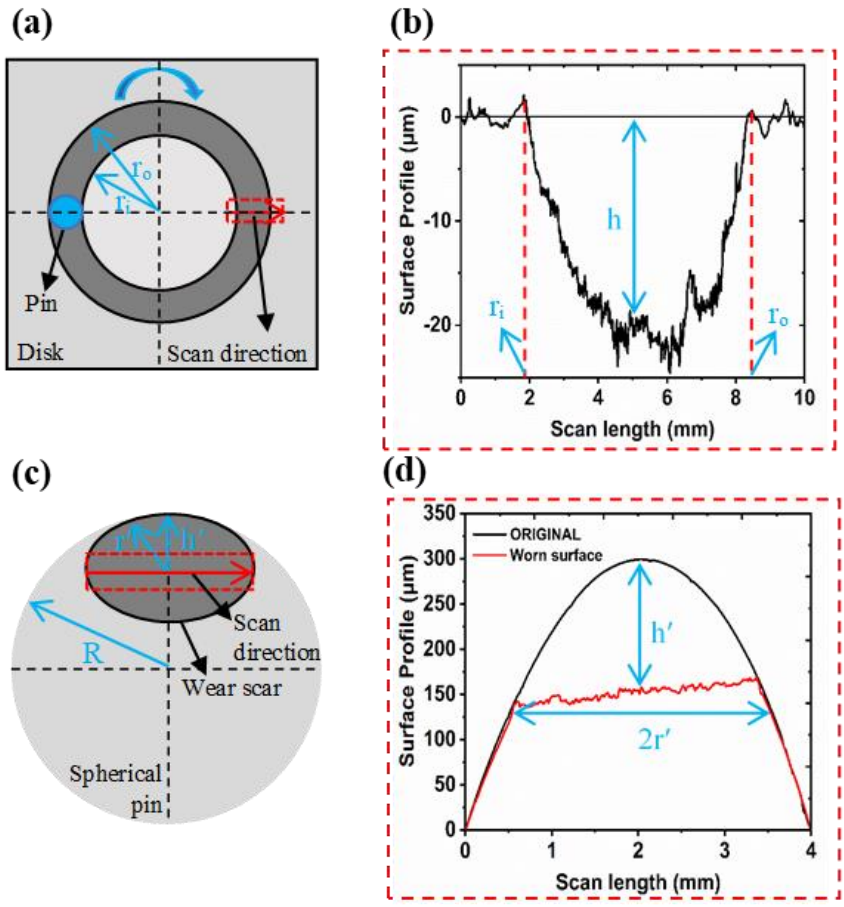

Figure 2.2 Schematics and measurements of worn disk and pin: (a) top view of a worn disk; (b) typical cross-section of the worn area on the disk (a); (c) 3D representation of a worn pin; (d) typical cross-section of the worn area on the pin**.** Reprinted with permission from [7].

Raman Spectroscopy was carried out to examine the graphitization of DLC coating after the experiment at 500°C, by employing a Horiba Jobin-Yvon LabRam HR Raman. It is equipped with an Olympus BX 41 confocal microscope, and a laser source of 633 nm wavelength was used for Raman scattering excitation in the wavenumber range of 500-2000 cm^{-1}.

2.3. Results and discussion

2.3.1. COF

To examine the tribological performance of the samples at both 25 and 500°C, experiments of PS400 pins against four mating surfaces, namely 4130 steel, DLC, PCD and MoB/CoCr disks, were performed. **Figure 2.3(a)** shows typical in-situ COF of all tribo-pairs at 25°C, and the corresponding average COF values are given in **Figure 2.3(c)**. The average COF values at both temperatures were calculated from the data acquired during the last 40% sliding of each speed step. The error bars represent ± 1 standard deviation of the average COF between repeated experiments. The evolution of the in-situ COF of 4130 steel, PCD, and MoB/CoCr was unstable, with no distinct trend with sliding speed or time. The values were scattered between 0.5 and 0.85 and resulted in high average COF values of 0.65 ± 0.07, 0.66 ± 0.04, and 0.76 ± 0.07, respectively. A fluctuation in the friction of PCD from 15 to 20 minutes can be observed and could be associated with the generation of regions with high amounts of accumulated debris at the interface [41].

DLC showed a constant region for the first 10 minutes of low COF, around 0.2 followed by a rapid increase at 0.26 for 5 minutes and then smoothly decreased to 0.25, at the end of the experiment, resulting in a low average COF of 0.24 ± 0.03. The intrinsic characteristics of DLC dominated the contact and a low COF was measured. The lubricating mechanisms of a-C:H DLC coating are as follows: the chemisorbed hydrogen that is incorporated into the coating during the deposition process or the oxygen present in the air can passivate the dangling bonds formed at the surface by the continuous rubbing and prevent strong bond formation with the counter-surface [2,52]. In fact, both mechanisms could have been in effect since the a-C:H DLC samples had a hydrogen concentration of 20-40 at%, and all experiments were carried out in ambient atmosphere, thus the presence of oxygen. The DLC coating exhibited a significant decrease in the average COF of 63%, compared with the uncoated 4130 steel.

Figure 2.3(b) depicts the in-situ COF of the four tribo-pairs at 500°C and the respective COF values are shown in **Figure 2.3(d)**. 4130 steel had a moderate average COF of 0.5 ± 0.04, a 23% decrease compared with RT, associated with the activation of the solid lubricants of PS400 at HT [6,35,47,61]. DLC and PCD exhibited low average COF of 0.4 ± 0.04 and 0.36 ± 0.02, respectively. For the case of DLC, a run-in period for 2.5 minutes with high friction, at 0.53 ± 0.04, can be observed, followed by a monotonic decrease at 0.34 after 25 minutes of sliding time. When PS400 slid against PCD, a constant COF for the first 20 minutes of 0.37 ± 0.02 was observed, followed by a decrease to 0.3 during the last 5 minutes of the experiment. MoB/CoCr followed a similar trend as RT by demonstrating high COF with an average value of 0.73 ± 0.04.

Figure 2.3(e, f) summarize the variation of the COF against sliding speed for the four tribo-pairs at 25 and 500°C, respectively. Small dependence of the COF with sliding speed can be seen, especially at RT where the fluctuations of COF were less pronounced, and the values are falling within one standard deviation. At 500°C, 4130 steel followed a monotonic increase of friction with increasing speed, whereas MoB/CoCr showed a decreasing trend with higher sliding speed. DLC depicted the smallest/negligible variation in COF at both temperatures, and thus demonstrating independence of COF with sliding speed.

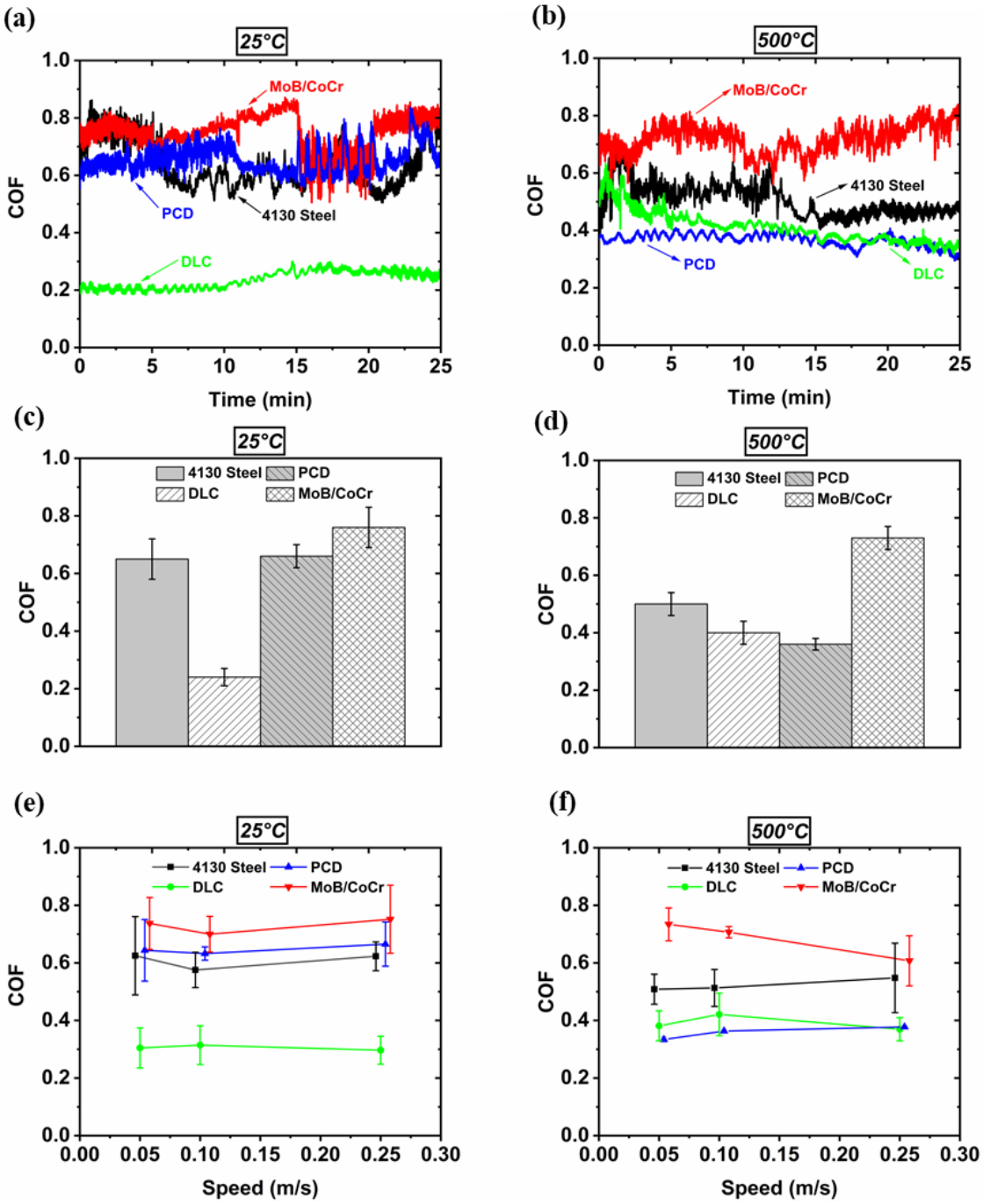

Figure 2.3 COF: (a) 25; (b) 500°C, and corresponding average values at (c) 25; (d) 500°C. COF versus sliding speed at (e) 25; (f) 500°C of the four tribo-pairs. Reprinted with permission from [7].

2.3.2. Wear

Typical wear profiles for the uncoated and the three coated disks, when slid against PS400 pin at 25 and 500°C, are presented in **Figure 2.4**. The wear scans of 4130 steel served as a reference. The uncoated surface showed a wear depth of around 0.5 μm at 25°C, whereas at 500°C moderate and deep grooves of a maximum 8 μm depicted the severity of the contact and an indication of abrasion, as shown in **Figure 2.4(a)**. DLC demonstrated immeasurable "zero wear" at RT, whereas at 500°C, a sharp peak in the profile shows that material transfer from PS400 was piled-up along the narrow contact region, as illustrating in **Figure 2.4(b)**. PCD also depicted material transfer from the pin to the disk at both temperatures. At RT, a uniform thin film of 0.5 μm formed on the surface of the disk within the sliding contact. At 500°C, an additional 2 μm material transfer was seen, as shown in **Figure 2.4(c)**. MoB/CoCr disk at RT showed a narrow wear track of 1 μm in depth, whereas at 500°C a wide valley of 1.5 μm in depth, can be observed, as shown in **Figure 2.4(d)**. This depth corresponds to 0.4% of the total coating thickness.

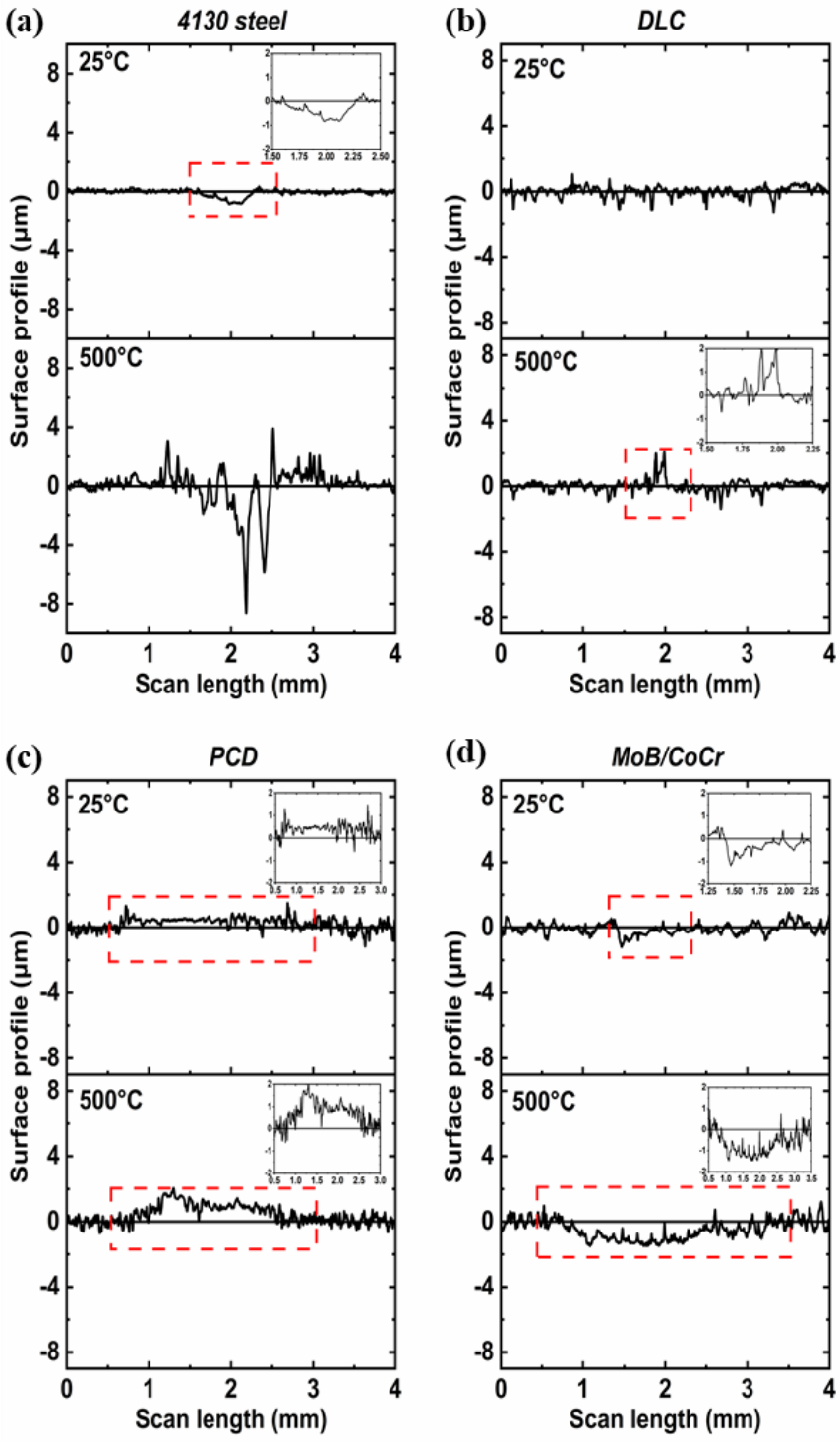

Figure 2.4 Typical wear scans: (a) 4130 steel; (b) DLC; (c) PCD; (d) MoB/CoCr disks at 25 and 500°C. Reprinted with permission from [7].

The corresponding wear profiles of the pins are presented in **Figure 2.5**. PS400 pin when slid against 4130 steel showed considerable wear, especially at 500°C, where a slice of a maximum height of 50 μm was worn off. Also, the worn surface at 500°C went through some light plowing, as **Figure 2.5(a)** depicts. **Figure 2.5(b)** shows the wear scan of the pin slid against DLC. It is clear that at both temperatures the coating experienced negligible wear and the effectiveness of the DLC coating in reducing the wear is demonstrated. The pin against PCD depicted similar wear profiles at both temperatures, as illustrating in **Figure 2.5(c)**. However, a slightly higher wear depth of the pin at 500°C, compared with RT, can be observed. The flat profiles of the pins within the contact region (1-3 μm) at both temperatures indicate a filling effect where some loose wear debris from the PS400 pin were "trapped" between high asperities and reduced the surface roughness from 1.3 to 0.2 μm RMS. The extreme hardness of the PCD disk, was compensated by the uniform film transferred on its surface at the early stages of sliding and no further wear of the pin occurred.

The pin slid against MoB/CoCr experienced significant wear, especially at 500°C, where the original curved profile flattened and a considerable amount of material was removed from the tip. The worn surface at 500°C demonstrated high roughness, indicating intense abrasion, as seen in **Figure 2.5(d)**. The high wear values are associated with the high hardness of MoB/CoCr, compared to PS400 that led to the removal of material during sliding. In fact, the inability of PS400 to be transferred onto MoB/CoCr and form a uniform glaze film, resulted in the direct contact of the sliding surfaces. The Ni-Mo-Al matrix of PS400 dictates the mechanical properties of the composite and its maximum

operating temperature is below 600°C [47]. It is plausible that at 500°C, the alloy matrix experienced some deterioration of its mechanical properties. On the other hand, MoB/CoCr has a maximum working temperature of 900°C. Thus, the difference in hardness between the two coatings is more pronounced at 500°C, than at RT and a higher wear was seen.

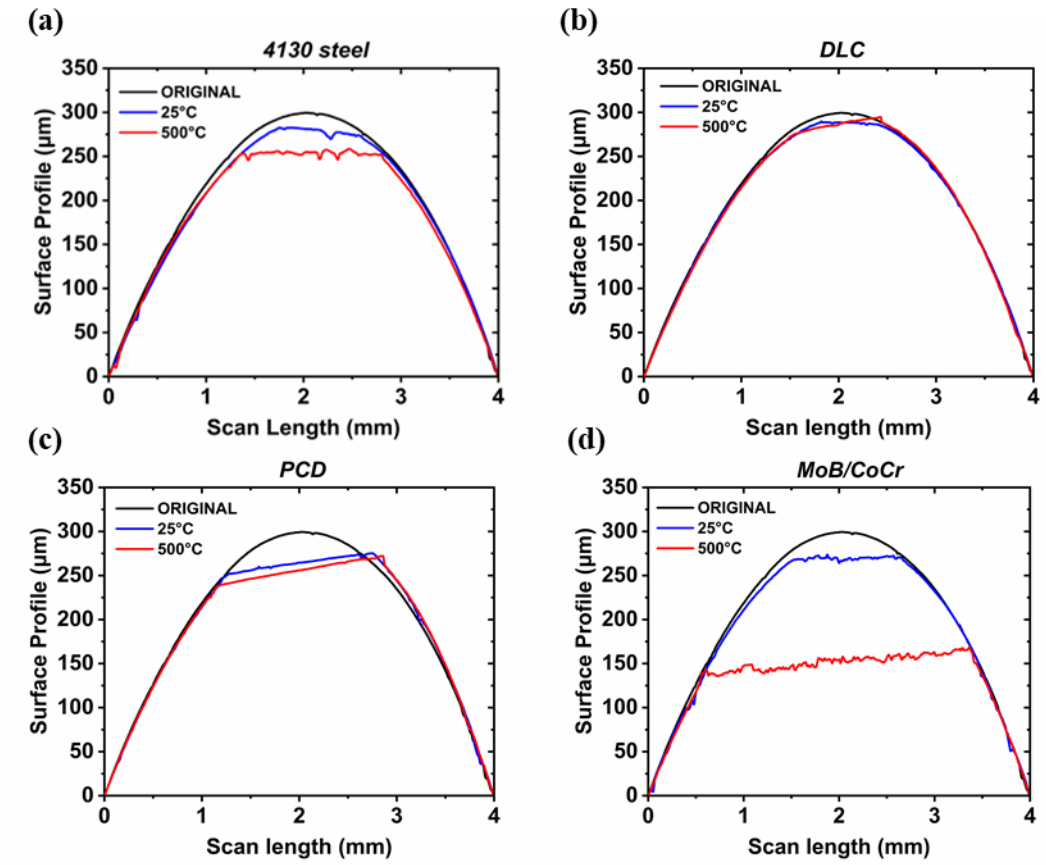

Figure 2.5 Typical wear scans of corresponding PS400 pins slid against (a) 4130 steel; (b) DLC; (c) PCD; (d) MoB/CoCr disks at 25 and 500°C. Reprinted with permission from [7].

The wear rates of the four tribo-pairs are summarized in **Figure 2.6**, which were calculated using equations (1) to (4). **Figure 2.6(a, b)** show the wear rate of the disks and pins, respectively. Note that the negative values in **Figure 2.6(a)** represent material gain (transfer) on the surface of the disks. The uncoated 4130 steel and MoB/CoCr disks had the highest wear at both 25 and 500°C, and an increasing trend with increasing temperature can be observed. This is in accord with the wear profiles shown in **Figure 2.4(a, d)** at 500°C, where moderate and deep grooves at RT and a wide shallow valley at 500°C, were present. The lower wear rate of MoB/CoCr is associated with its higher hardness. The wear values of 4130 steel and MoB/CoCr at both temperatures fall into moderate wear (10^{-5} $mm^3N^{-1}m^{-1}$ range), according to the criterion of DellaCorte et al. [62]. The absence of DLC value at RT indicates "zero wear," whereas at HT, "negative wear" was observed due to the transfer film, which protected the DLC coating from wearing off. PCD had a significant material gain from the pin, especially at RT, where a uniform film was initially formed.

Figure 2.6(b) summarizes the wear of PS400 pins when slid against the four mating surfaces at 25, and 500°C. The corresponding pins when rubbed against PCD and MoB/CoCr demonstrated the highest wear rates at both temperatures. Moderate wear of the pins against PCD at both temperatures was maintained. On the other hand, the pin against MoB/CoCr depicted significant wear at 500°C, rising from moderate values at RT to high values at 500°C (10^{-4} $mm^3N^{-1}m^{-1}$ range) [62]. Also, this value was almost one order of magnitude higher than the respective pin wear rate against PCD at 500°C. Direct contact between the sliding materials was detrimental for the softer PS400 surface. The pin against

4130 steel had a transition from low (10^{-6} $mm^3N^{-1}m^{-1}$ range) to moderate wear at HT [62]. The only time when the PS400 pin experienced low wear rate values at both temperatures it was when slid against DLC, with 2.73×10^{-6} and 9.98×10^{-6} $mm^3N^{-1}m^{-1}$ at 25 and 500°C, respectively.

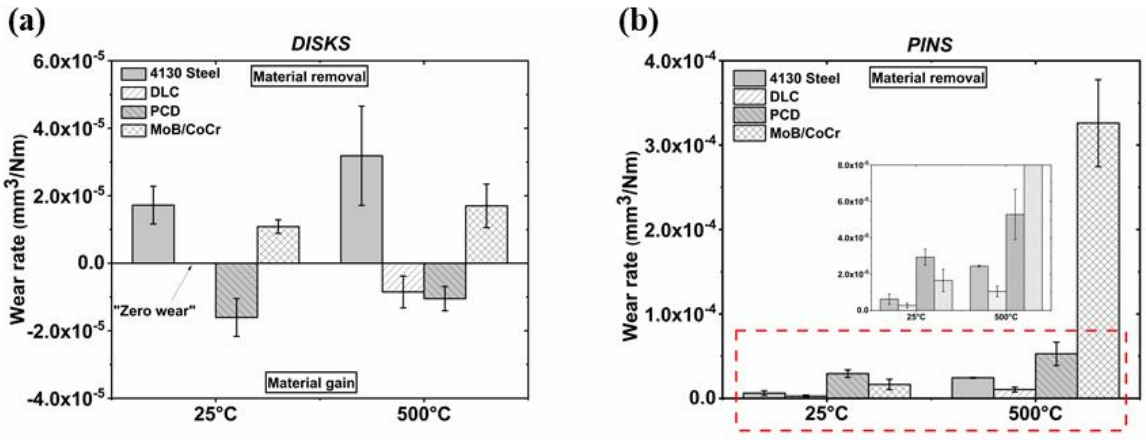

Figure 2.6 Wear rates of the four tribo-pairs at 25 and 500°C: (a) disks; (b) pins. Reprinted with permission from [7].

Figure 2.7 shows the COF against wear rate for the four disks at 25 and 500°C. The COF was measured from the highest sliding speed, that is 0.25 m/s. At 25°C, 4130 steel, PCD and MoB/CoCr showed high COF values of 0.62, 0.67, and 0.89, respectively. 4130 steel had the highest wear rate, followed by MoB/CoCr, whereas PCD experienced significant material gain, thus negative wear. DLC possessed the lowest COF of 0.3 and "zero wear." At 500°C, 4130 steel and MoB/CoCr possessed the highest friction but with 11% and 45% lower values, compared to RT. Also, their wear values did not change significantly. The COF of PCD was also reduced by 44% and at a value of 0.38. On the

other hand, DLC experienced a 24% increase and had a COF slightly less than PCD. Both PCD and DLC demonstrated negative wear values.

Comparing the average COF values of the four tribo-pairs, the only remarkable difference is that the tribo-pair PS400 against MoB/CoCr demonstrated a favorable behavior, in terms of friction, when slid at the highest speed and at 500°C. In fact, a reduction of the COF by 33% between the two COF values occurred. DLC had the lowest COF values at both temperatures and zero wear, thus making this material combination favorable and applicable at both RT and 500°C.

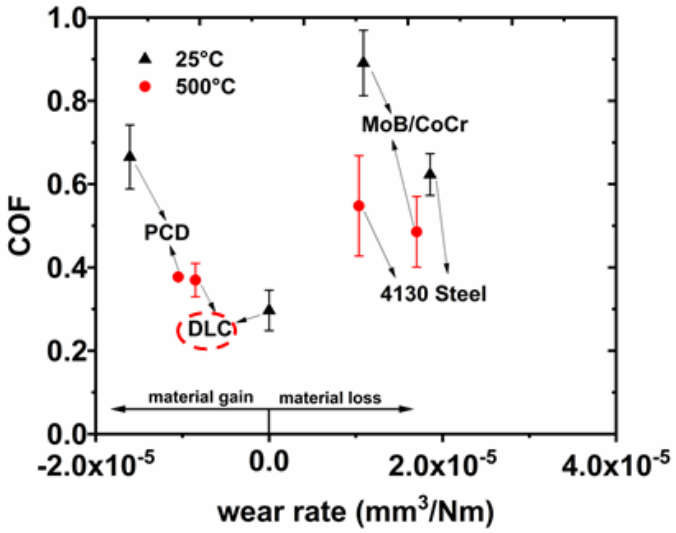

Figure 2.7 COF: (a) 25; (b) 500°C, and corresponding average values at (c) 25; (d) 500°C. COF versus sliding speed at (e) 25; (f) 500°C of the four tribo-pairs. Reprinted with permission from [7].

2.3.3. Optical microscopy

Figure 2.8 presents the optical images of the worn surfaces of the disks and pins at RT, and 500°C. At RT, 4130 steel showed a distinct wear track with mild contact, and

no indication of transfer film. The corresponding PS400 pin went through some burnishing. PS400 generates high COF at RT, as in Ref. [6,35], attributed to its inability to form a tribo-chemically oxidized glaze film on the counter-surface. Hence, the tribo-pair relied solely on the low temperature solid lubricant (silver) for lubrication. The low concentration of silver in the composite (5wt%), was inadequate for effective lubrication [47], resulting in high COF. Li et al. increased the concentration of silver from 5 to 12 wt% in a similar Ni-based matrix and reported a lower COF [48].

The DLC demonstrated extreme wear resistance and low COF. In fact, the wear track was barely visible, and the counter-surface experienced mild contact. The absence of a glaze oxide transfer film was compensated by the excellent lubricious characteristics of DLC at RT conditions, resulting in low COF. PCD gained significant material from PS400, and a uniform film was formed on the sliding surface. The pin exhibited significant wear, as this material was "consumed" on PCD to form a uniform dense film. However, this film had poor lubrication performance, as the glazed oxides are only formed when sliding at HT (in air) [6]. Thus, high friction was observed. The lubricating mechanisms of PCD were also terminated by the formation of the transfer film on the surface. MoB/CoCr experienced mild contact at 25°C with some polishing on the surface. The corresponding pin had higher wear than the pins against 4130 steel and DLC, but lower than the respective pin against PCD. No evidence of transfer film of PS400 to MoB/CoCr was found, similarly to 4130 steel, and high COF was reported.

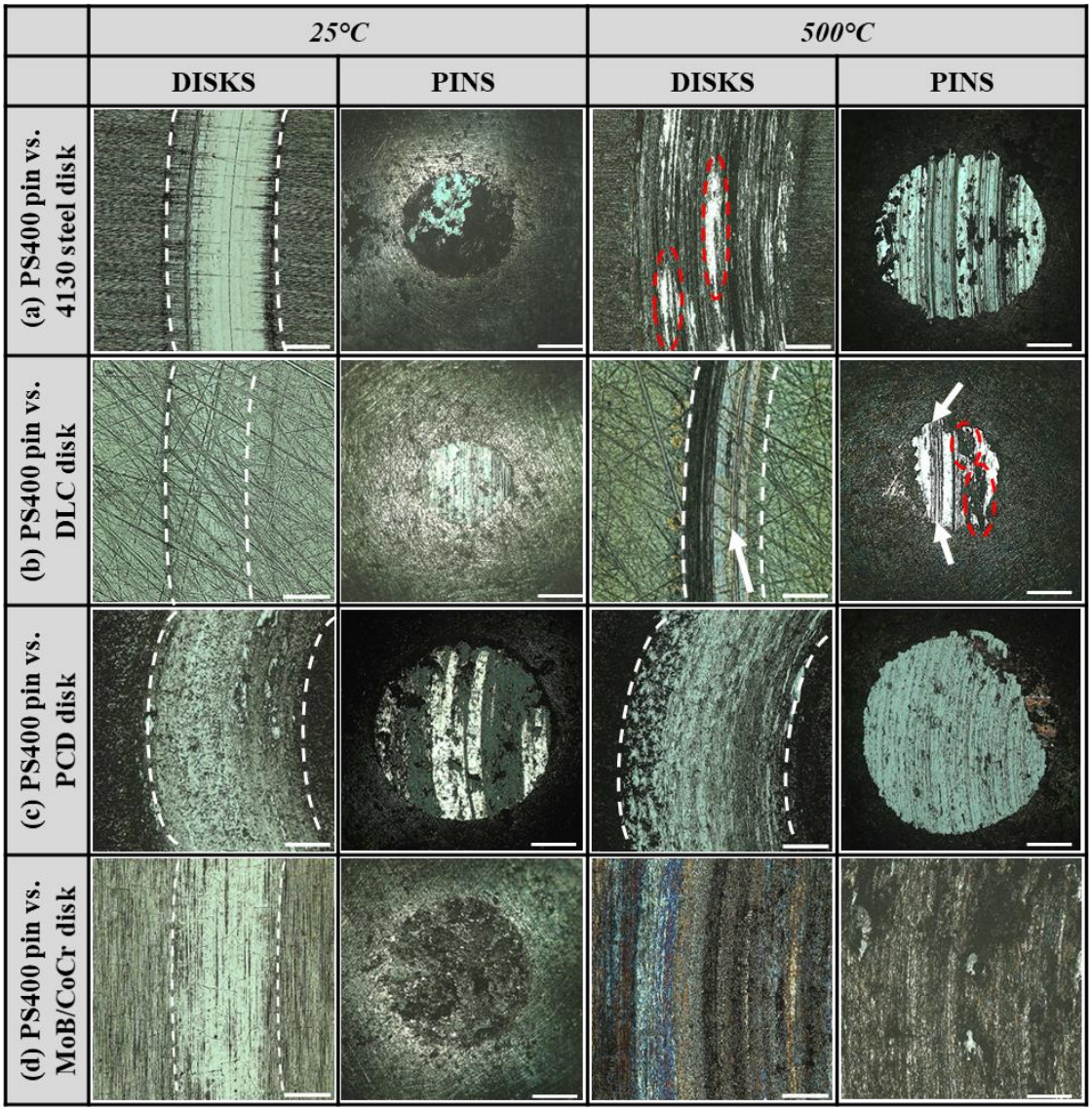

Figure 2.8 Optical microscopic images of worn areas of disks (left) and pins (right) at 25, and 500°C. PS400 pin vs.: (a) 4130 steel; (b) DLC; (c) PCD; (d) MoB/CoCr disks (400 μm scale bar). Reprinted with permission from [7].

At 500°C, 4130 steel experienced severe contact, with deep and long cavities appearing along the wear track (shown with red dashed circles). Also, the width of the wear track was considerably increased, compared with RT. The pin depicted long parallel grooves, indicating three-body abrasive wear mechanism. The glazed oxide film failed to

form, however, the activation of the fluorides in PS400 at HT resulted in a lower COF [62]. DLC depicted two regions of contact. A black track indicating material transfer from the counter-surface and the formation of a glazed oxide film. In the other half of the wear track (marked with arrow), mild polishing of asperities occurred. The worn surface of PS400 pin featured some grooving areas (shown with arrows), along with black attached regions (shown with red dashed circles). Surface plowing was induced by the sharp asperities of the accumulated material on the disk, as shown in **Figure 2.8(b)**. The black regions are linked to graphite structures which were worn off from the DLC and adhered to the surface of the pin during rubbing, as will be confirmed with EDS thereafter.

The moderate hardness of PS400 protected the graphitized DLC coating from penetration. Also, the glazed oxide film provided additional protection and lubrication, and a low COF was maintained. The uniform transfer film induced on PCD at RT was also evident at 500°C. The scar of PS400 was slightly increased, and a uniform and smooth wear scar with some indication of light abrasion can be observed. The inter-film mitigated the contact between the hard diamond and PS400 and protected the pin from significant wear. Unlike DLC, PCD can withstand higher temperatures without degradation and significant deterioration of its mechanical properties [5], thus the hard diamond could have easily worn off the counter-surface, with direct contact. At HT, the transfer film oxidized significantly and increased the lubricating performance resulting in COF reduction, compared with RT. The wear track on MoB/CoCr and wear scar on PS400 were increased, compared with the corresponding ones at RT, and thus the severity of the contact was pronounced. Essentially, the continuous wear of PS400 pin hindered the effect of both

lubricating mechanisms: glazed oxide transfer film formation, and activation of fluorides [63]. Hence, high friction and wear were observed.

2.3.4. SEM-EDS analysis

The topography of the three coatings, namely DLC, PCD and MoB/CoCr after sliding firstly at RT and subsequently at 500°C was further examined via SEM, and it is presented in **Figure 2.9**. The unworn surfaces after the test are shown in the left column, and the direction of sliding is shown with white arrows at the low magnification images. DLC in its as-received condition featured a smooth and uniform surface, whereas after the test at 500°C the DLC was graphitized, as will be seen with Raman Spectroscopy analysis thereafter. Graphitized DLC can be easily worn off, especially when sliding against a hard-mating surface such as a ceramic, as in Ref. [52], where an annealed DLC coating at 600°C was removed from the surface when slid against alumina. However, as seen in **Table 2.2**, the moderate hardness of PS400 can protect the graphitized coating from wearing off.

The transfer oxide film depicted two distinct regions: as agglomerated particles (indicated with P) and as densely uniform films (indicated with F). The texture remained smooth, as bulky formations or sharp-edge agglomerations were not present, as shown in **Figure 2.9(a)**. Elemental examination was carried out on the PS400 pin counter-surface by EDS and is presented in **Figure 2.10(a)**. Except from the intrinsic elements of PS400, C and Fe were also detected. C was attributed to graphite traces that were worn off and transferred from the DLC. Interestingly, the presence of Fe showed that the graphitized DLC was penetrated at localized points at the uncovered area, where mild polishing took place. Material from the steel substrate was then plowed and transferred to PS400.

Nevertheless, the overall performance of the tribo-pair did not deteriorate, and a low COF was maintained. PCD showed a uniform distribution of diamond grains, from small (<5 μm) to medium size (~ 5-10 μm) in its as-received condition. The contact area was fully covered with a glaze oxide transfer film, resulting in a homogenous, dense, and smooth surface. Moreover, small, propagated cracks along the transfer film were visible, which are not expected to deteriorate the integrity of the film, as illustrated in **Figure 2.9(b)**.

The transfer film was further examined via EDS analysis (acquired from the blue square area on high magnification image) and indicated the presence of all the elements of PS400's matrix, as well as the lubricious phases, especially BaF_2/CaF_2, and a high peak of oxygen, as shown in **Figure 2.10(b)**. It is noted that cobalt served as the bonding agent of PCD, and thus appeared in the spectrum. The fluorides, which were activated at HT, and experienced a transition from brittle to ductile behavior, and thus easier shearing [62], were expected to have a significant contribution in lowering the COF, along with the formation of metal oxides. The as-received MoB/CoCr showed a uniform surface with small particle accumulations induced from the spraying process during deposition. The magnified images illustrated some bulky transferred formations from PS400 that were patchy and spread within the contact surface. Each bulky formation contained smaller accumulated particles with sharp edges that can generate high friction and wear of the counter-surface. Also, during sliding the abrasive formations can harden and expedite the wear process of the counter-surface. As stated earlier, the continuous wear of PS400 was devastating for the lubricating mechanisms to be in effect, and thus high values were observed.

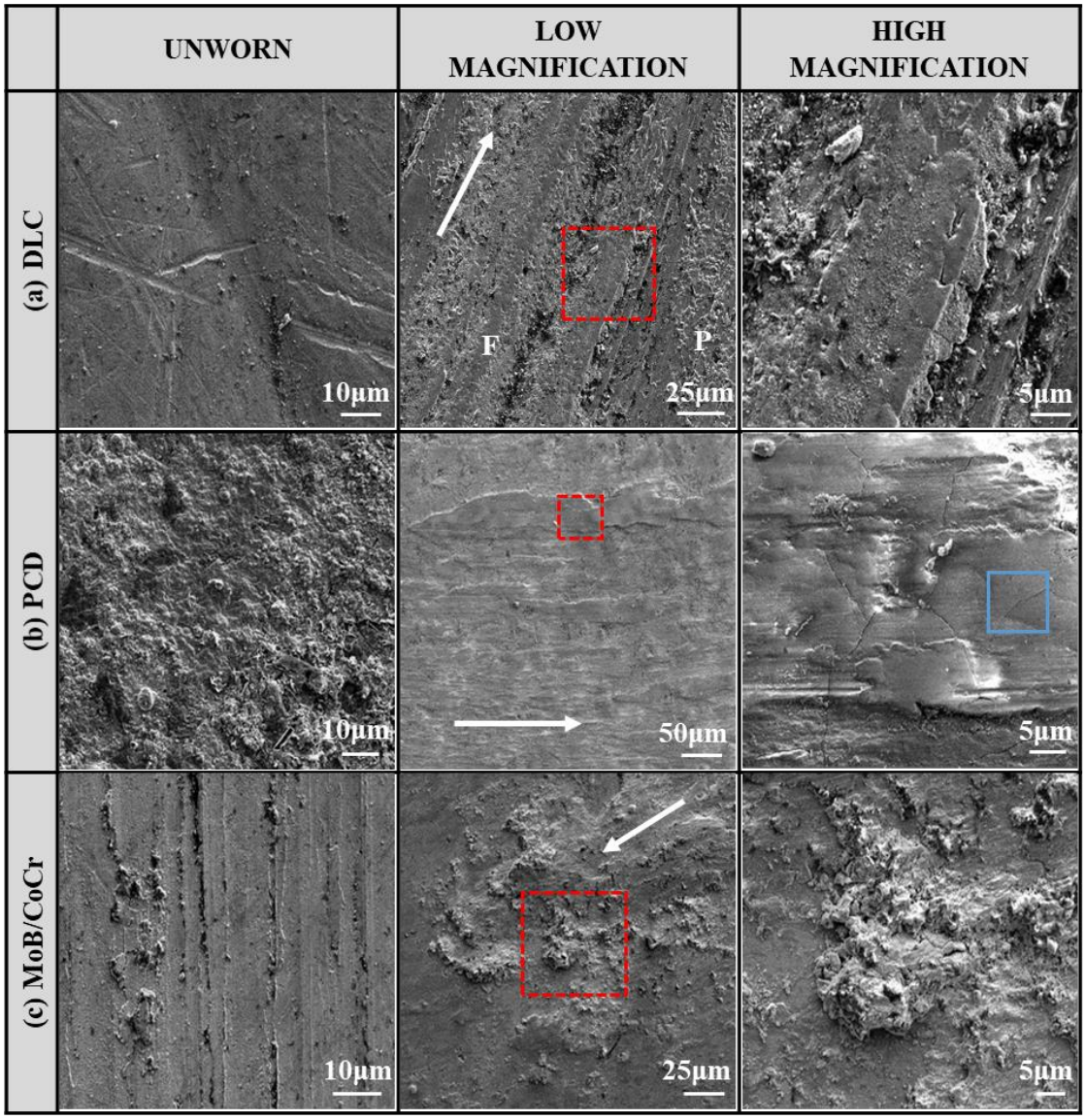

Figure 2.9 SEM micrographs on coated disks of unworn regions (left column), low magnification (middle column), and high magnification of worn tracks (right column). PS400 pin vs.: (a) DLC; (b) PCD; (c) MoB/CoCr. Reprinted with permission from [7].

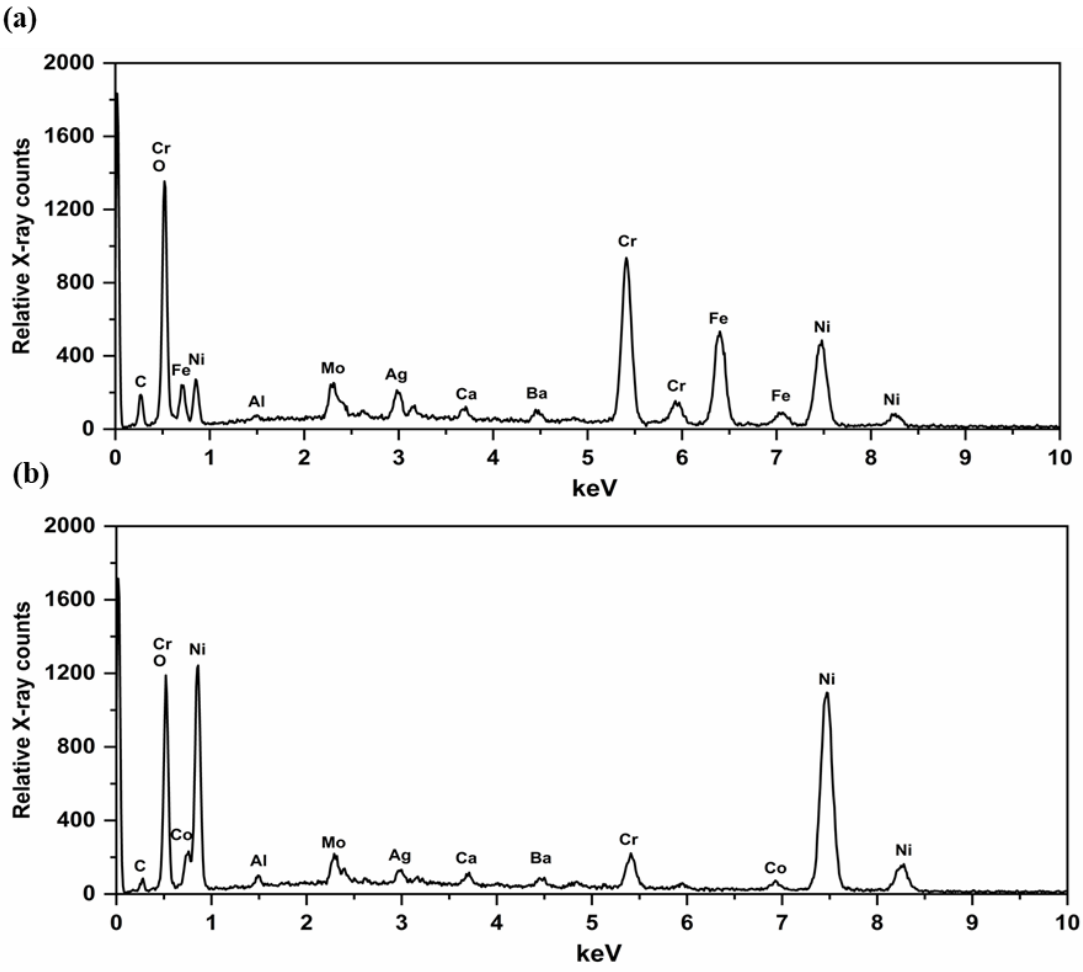

Figure 2.10 EDS spectra of (a) black region of PS400 pin when slid against DLC, and (b) transfer film on PCD disk after sliding against PS400 pin at 500°C. Reprinted with permission from [7].

2.3.5. Raman Spectroscopy

To investigate the amount of graphitization/functionalization/surface oxidation of the DLC coating before and after the experiment at 500°C, Raman spectroscopy was employed. **Figure 2.11** shows the Raman spectra of the DLC coating before and after the HT experiment (unworn area), that can be considered as a short annealing process. The as-received DLC led a wide spectrum with the typical G band. Obvious peak splitting

appeared only after exposing the coating at 500°C. The peak intensities centered at ~1330 cm^{-1} and ~ 1540 -1580 cm^{-1} represent the D and G bands, respectively, and were divided to calculate the height-based I_D/I_G ratio. This ratio indicates the changes in the structural integrity of the samples after testing. The as-received sample (before HT experiment) possessed a low I_D/I_G = 0.65, dominated by a diamond-like structure with some portions of sp^2 hybridized carbon atoms. However, after the experiment, the intensity ratio significantly increased to 1.01, due to the initiation of a number of defects or disorders with the initiation of the breathing mode of sp^2 carbon atoms. This can be caused by the functionalization of the sp^2-hybridized carbon, which caused a reduction in G mode and a higher I_D/I_G ratio was observed, thereby a significant structural transition from diamond-like to a graphite-like structure was seen.

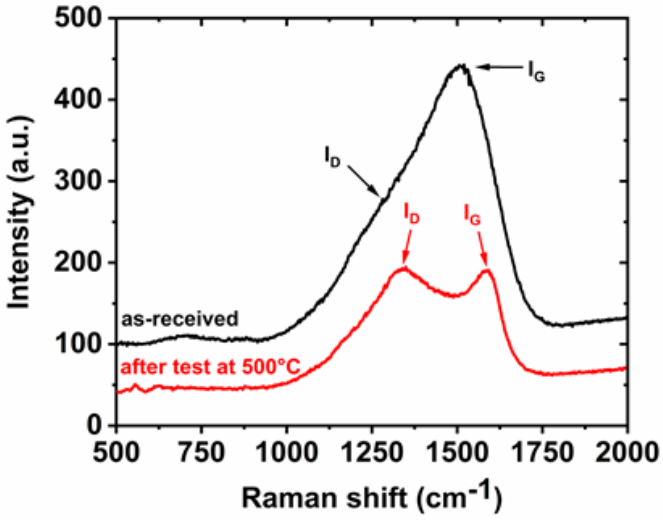

Figure 2.11 Raman spectra of DLC coating, as-received, and after the experiment at 500°C. Reprinted with permission from [7].

2.4. Summary

In this chapter the tribological performance of four different mating surfaces of PS400 pins, namely 4130 steel, DLC, PCD, and MoB/CoCr disks were examined through pin-on-disk experiments at 25, and 500°C under air environment. The mating surfaces were meant to contribute in enhancing the performance at low temperatures, whereas at HT PS400 demonstrates good lubrication. The variation of the COF and wear with temperature of the four tribo-pairs are summarized in **Figure 2.12**. The topography of the worn surfaces and the chemical composition of the transfer films were studied, and the following conclusions could be drawn:

- At RT, 4130 steel, PCD, and MoB/CoCr exhibited high COF. A uniform transfer film was only found with PCD, which, however, showed pour lubrication performance, as the lubricating mechanism of PCD was passivated. DLC maintained low COF of 0.24 ± 0.03, due to its excellent lubricating mechanism.
- At 500°C, 4130 steel experienced a significant decrease in COF due to activation of the solid lubricant in PS400. During the HT experiment DLC graphitized. The moderate hardness of PS400 counter-surface protected the coating from being worn off. The transfer oxide film provided additional protection and lubrication, and a low COF of 0.4 ± 0.04 was maintained. A uniform transfer oxide glaze film on PCD was generated, with the metal oxides and fluorides providing excellent lubrication, and thus low COF. MoB/CoCr depicted similar high friction, as in RT. The continuous wear of PS400 pin inhibited the lubrication mechanism.

- The uncoated 4130 steel and MoB/CoCr disks exhibited the highest (moderate) wear at both RT and 500°C, with an increasing trend with increasing temperature. DLC demonstrated zero wear at RT and negative wear (material transfer) at 500°C. PCD was readily covered by a uniform transfer film at both temperatures.
- The best performing tribo-pair, in terms of friction and wear is PS400 vs. DLC, followed by PS400 vs. PCD, whereas PS400 vs. MoB/CoCr is the worst performing pair.
- The DLC as a mating surface for PS400 tackled the negatives of PS400 of exhibiting high friction at low temperature. PS400 vs. DLC demonstrated favorable tribological behavior at 25 and 500°C, at low sliding speeds, expanding the applicability of the tribo-pair to space-related applications, for example the bearings of probes for future missions to Venus.

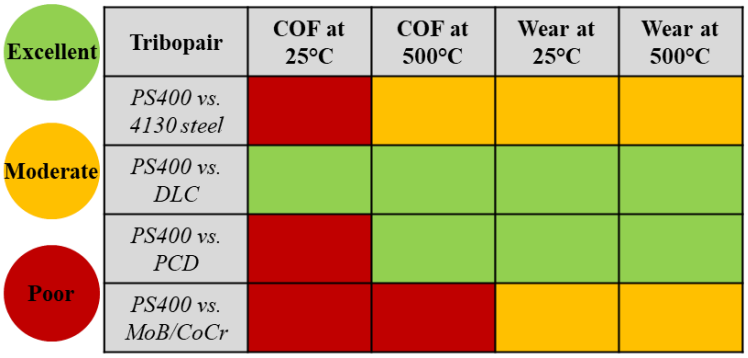

Figure 2.12 Summary of tribological performance of the four tribo-pairs at 25 and 500°C. Reprinted with permission from [7].

In this chapter different tribological interfaces were tested under generic conditions (ambient environment) for down selecting the best pair. In the next chapter the selected tribo-pair was examined under CO_2 and air atmosphere (at near AP). Also, an intermediate temperature was added at the experimental protocol and the same samples were used at each temperature to replicate a continuous operation of the tribological components during descending towards the Venusian surface [20].

3. DYNAMIC TRIBO-PAIR OF PS400 AND DLC FOR PLANET VENUS APPLICATION[†]

3.1. Introduction

Venus, which is also called Earth's twin has been the topic of new explorations to understand and investigate our planet and the feasibility of the existence of other habitable planets. Venus is similar to Earth in terms of size, distance from sun, mass, and composition [18]. However, significant technical challenges exist in Venus exploration. Compared to Earth conditions, the surface pressure is nearly 92 times higher, and the environment is primarily 96% CO_2 gas, and 3.5% N_2, and minute amounts of Ar, H_2S, SO_2, HF, and HCl (with SO_2 being the dominant minor gas) with extremely hot (mean temperature over the whole surface is 464°C) and dry conditions [17]. The successful accomplishment of future missions and in-situ investigation of Venus surface in a long duration operation requires moving mechanical components, for example bearing materials in the landers, that can withstand such extreme environmental conditions [18]. In addition to the HT, the bearing materials will face lower temperatures while descending [20], therefore an enhanced tribological behavior at moderate and low temperatures (i.e., RT) should be demonstrated.

[†] Reprinted with permission from "Dynamic tribo-pair of PS400 and DLC for planet Venus application" by Vasilis Tsigkis, Pixiang Lan, Andreas A. Polycarpou, 2021. Tribology International, 164, 1-11, Copyright 2023 by Vasilis Tsigki.

In **Chapter 2** we demonstrated that PS400 vs. DLC coating showed the most promising tribological behavior among other materials, with low COF and wear at RT, and 500°C under air environment [7]. Therefore, a hypothesis of the working mechanism of the tribo-pair was drawn: DLC coating provides adequate lubrication at RT while PS400 coating controls the friction and wear at 500°C. It was not surprising that DLC generated low friction and wear at RT, even when it was coupled with the HT super-alloy, namely PS400. In abundant studies [52,53,64,65] a:C-H DLC is exhibiting excellent tribological performance at RT air atmosphere, due to the successful termination of the dangling bonds forming during rubbing against the counter-surface [2,52]. However, some of the mechanical properties (i.e., hardness) of DLC deteriorate at temperatures above 300°C [66], thus sliding under such conditions is challenging. On the other hand, PS400 is specialized for HT applications and low friction and wear are achieved by means of oxide surface glazes formed and transferred on the counter-surface [6,35,47]. It was demonstrated that when sliding at HT air, the most significant lubricating mechanism of PS400 is the generation of oxide layers at the interface, and that the solid lubricants (silver, calcium/barium fluorides) therein, do not play a key role in lowering friction and wear.

Literature is plenty with tribological studies under CO_2 environment for high contact pressure air-conditioning compressor applications [10,32–34]. Also, the effect of the environment on RT tribology is adequately studied [67,68]. However, HT tribology (up to 500°C) in CO_2 environment is yet to be explored, hence the tribological performance of tribo-materials under such conditions is not available.

In this chapter, the effect of the environment and temperature on the tribological behavior of PS400 vs. DLC coatings, at RT, 300, and 500°C was investigated. Pertaining to bearing tribo-surfaces for Venusian applications, most of the experiments were performed under CO_2 atmosphere at AP. Also, the selected range of testing temperatures covered a wide spectrum of operating temperatures that the tribological components (e.g., on the landers) will encounter during descending onto the Venusian surface [20].

3.2. Experimental

3.2.1. Materials and sample preparation

An Inconel (INC) 750X plate was purchased from Altemp Alloys, Inc. and machined into 25.4 × 25.4 × 6.35 mm disk specimens by electrical discharge machining (EDM). The chemical composition of the precipitation-hardened alloy is detailed in **Table 3.1**. The disks were mechanically ground to achieve RMS surface roughness of 0.19 ± 0.005 μm. The Inc750X disk substrates were coated with DLC (a:C-H) via CVD by Oerlikon Balzers with 20-40 at% H content. Cr was used as a bonding layer between the DLC and the Inc750X substrate. The total thickness of the as-received DLC coating was 2 μm and featured a roughness of 0.17 ± 0.02 μm RMS.

The titanium (Ti) pin substrates were machined from a Ti alloy, namely Ti-6Al-4V into 6.35 mm diameter, 20 mm length, and were hemispherical tipped with a tip radius of 6.35 mm. Ti-6Al-4V is extensively utilized in aerospace applications, due to being lightweight and its excellent mechanical properties up to 600°C. Some of the pins were coated with PS400 at Adma Products, Inc. via PS. The chemical composition of PS400 is listed in **Table 2.1** of **Chapter 2.** The thickness of the as-received coating was 250 μm

and reduced to around 200 μm after polishing. A sequence of silicon carbide sandpapers, from 240 to 800 grit size achieved a roughness of 1.3 ± 0.05 μm RMS on the PS400 coating. The roughness along with some of the mechanical properties of the specimens under examination are summarized in **Table 3.2**.

The low ratio of sp^2 to sp^3 hybridized bonding of carbon atoms within commercial a-C:H DLC coatings results in high hardness values ranging from 15 to 25 GPa, as provided by the vendor. The exact average hardness value was measured via nanoindentation and was 19.9 GPa. The multi-component Ni-based alloys, namely PS400 and Inc750X featured significantly lower hardness values than DLC, ranging from 2 to 3.7 GPa. Note that the hardness of PS400 was measured via micro Vickers' indentation to capture all phases exposed on the surface, therefore calculating a more representative averaged value. Ti has the lowest hardness value among the materials under examination, at an average of 1.25 GPa.

Table 3.1 Chemical composition of Inc750X as provided by the manufacturer (units are in wt.%). Reprinted with permission from [9].

Ni	**Cr**	**Co**	**Nb + Ta**	**Al**
70	16	<1	<1	0.8
Mn	**Si**	**Fe**	**Ti**	**Cu**
0.35	0.35	**8**	2.5	0.5

Table 3.2 Mechanical properties of samples. Reprinted with permission from [9].

Material	RMS (μm)	Hardness (GPa)	Young modulus (GPa)	Poisson's ratio
DLC	0.17	19.9 ± 3.9*	170**	0.2**
PS400	1.3	2 ± 0.16***	83**	0.28**
Inc750X	0.15	3.1-3.7**	213**	0.29**
Ti	1.8	1.2-1.3**	120**	0.34**

*Measure via nanoindentation, **As provided by the vendor, ***Measured using Vickers' indentation.

3.2.2. Experimental procedure

The experimental conditions are presented in **Table 3.3.** Ti pin vs. Inc750X disk (uncoated substrates) served as a benchmark and the contribution of PS400 and DLC coatings at each temperature in reducing the friction and wear was investigated. Note that a PS400 pin was used and slid against Inc750X disk. However high wear was generated on the pin and the coating was completely removed from the surface by the end of the RT experiment. For that reason, a PS400-coated disk specimen and an Inc750X pin were used instead. Also, tribo-testing of PS400 pin vs. DLC disk under air (RH 49%) was performed to explore the effect of the environment on the tribological behavior at the three selected temperatures.

To replicate a continuous operation of the bearing materials, the same disk and pin specimens were used in successive experiments, from RT to 500°C. The initial Hertzian contact pressure of each tribo-pair for a sphere-on-plane configuration (see **Figure 2.1(b)**) was calculated using the information from **Table 3.2**. A constant sliding speed of 0.25 m/s for 30 min at each temperature stage resulted in a total sliding distance of 1350 m at all temperatures. For the two selected tribo-pairs (PS400 pin vs. DLC disk and Ti pin vs. DLC disk) a prolonged sliding time of 1 hour at 500°C resulted in 1800 m total sliding distance.

Sliding at 500°C for a longer time provided more information on the durability and the wear resistance of the tribo-pairs subjected under surface Venusian temperature.

For the tribo-experiments under CO_2 environment, a medical grade CO_2 with 99.5% purity was used. The rest 0.5% contains impurities, such as O_2, CO, N_2, and CH_4. A vacuum/flashing protocol was implemented to achieve the minimum presence of air within the jar, as in Ref. [41]. For the HT experiments, following the vacuum/flashing procedure, the furnace was heated up to the desired temperature (300, 500°C). After 5 minutes of constant temperature, the pin and disk were brought into contact and the experiment was initiated by rotation of the disk. During the experiment, the pressure inside the jar was kept at 0.1 ± 0.02 psi higher than ambient air pressure, thus no air could leak into the jar. After the end of the experiment, the samples were let to cool under CO_2 with a continuous flow of 0.14 m^3/hr. A minimum of three experiments for each tribo-pair were carried out to assure repeatability. Before each tribo-experiment, the disk and pin specimens were ultrasonically cleaned for 10 min in an isopropanol bath at 40°C

Table 3.3 Experimental conditions. Reprinted with permission from [9].

Tribo-pairs		**T (°C)**	**Load**	**Initial Hertzian pressure (MPa)**	**Sliding speed (m/s)**	**Total sliding distance (m) [cycles]**	**Env.**
Pin	**Disk**						
Ti	*Inc750X*	25→300 →500	5 N	470	0.25	1350 [24300]	CO_2
Inc750 X	*PS400*			550			
Ti	*DLC*			490		1800 [32400]	
PS400	*DLC*			590			
PS400	*DLC*			470			Air

3.3. Results and discussion

3.3.1. COF

The in-situ COF and average values at 25, 300, and 500°C under CO_2 are exhibited in **Figure 3.1**. The average COF values for all tribo-pairs were calculated from the last 40% of the data acquired from the in-situ COF and the error bars represent one standard deviation of the mean values between repeated experiments. At RT, Ti vs. Inc750X (baseline) and Inc750X vs. PS400 depicted similar evolutions of COF, with values scattered between 0.4 and 0.6. In fact, Ti vs. Inc750X appeared with high spikes in the COF. When Ti and PS400 slid against DLC the evolution of friction was more stable after a run-in period of 3, and 2 min which resulted in 84 and 58% decrease of the average values (compared to baseline), at 0.08 and 0.21, respectively. At 300°C, Ti vs. Inc750X and Inc750X vs. PS400 experienced an increasing trend in COF with average values of 0.62, and 0.47, respectively.

Furthermore, the rapid increase in the COF for Ti vs. DLC after 7 min of sliding time may be associated with the onset of coating removal, as will be seen with profilometric scans and microscopic images in **Section 3.3.2**. The COF was reduced and stabilized after 20 min of experiment. PS400 vs. DLC experienced a smoother evolution of COF, depicting an increase from 0.10 to 0.27 after 5 min of sliding and remained constant until the end of the experiment. Despite the average COF values between Ti vs. DLC and PS400 vs. DLC were similar (0.26 vs. 0.27), the former depicted a noticeable deviation among repeated experiments, and can be postulated that the onset of DLC

coating removal from the Inc750X substrate resulted in different contact mechanisms between the sliding surfaces, therefore different friction values were observed.

Tribo-testing at 500°C of Ti vs. Inc750X and Inc750X vs. PS400 tribo-pairs resulted in similar average COF values, at 0.53 and 0.5, respectively. However, the latter experienced high fluctuations in the in-situ COF, due to generation of high amount of accumulated debris at the bearing interface [41]. The 1-hr sliding of Ti vs. DLC and PS400 vs. DLC followed a monotonic increase, before stabilizing at the last 15 min of experiment, where a constant region was reached. The stable state coincides with the complete removal of the DLC coating. The average COF values of Ti vs. DLC and PS400 vs. DLC were 0.38 and 0.45, respectively.

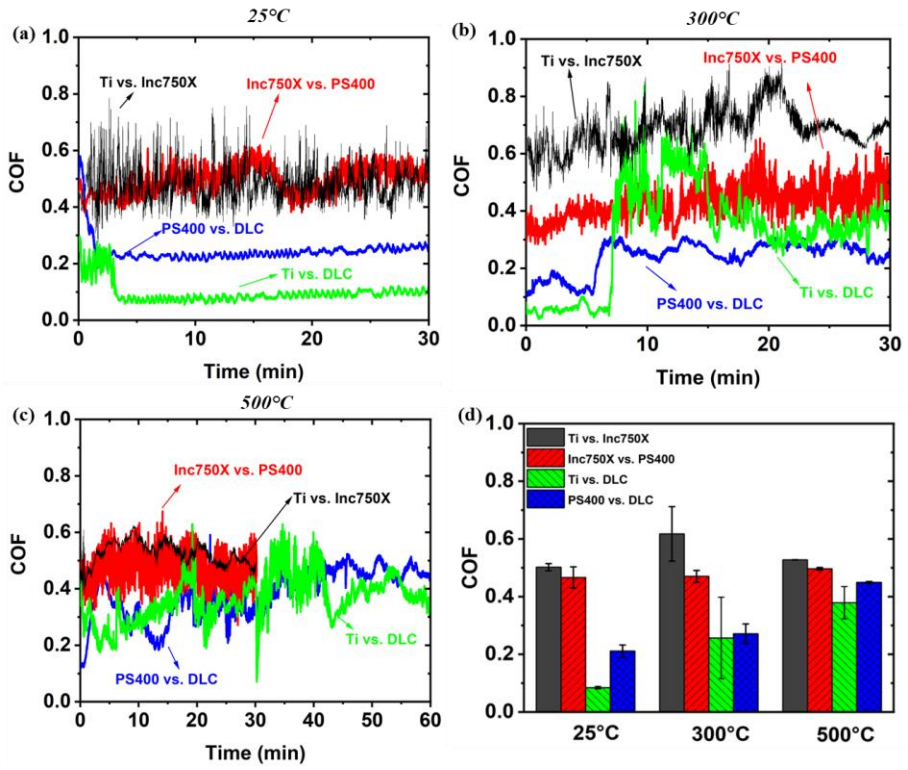

Figure 3.1 Evolution of COF with time of all tribo-pairs under CO_2 environment at (a) 25°C, (b) 300°C, (c) 500°C, and (d) corresponding average values with errors bars designating ± 1 standard deviation. Reprinted with permission from [9].

3.3.2. Wear

Figure 3.2 shows typical wear profilometric scans of both disk and pin specimens for all tribo-pairs following experiments at each temperature (25, 300, 500°C) in CO_2. Rubbing of the uncoated bare surfaces (Ti pin vs. Inc750X disk) resulted in severe wear at all temperatures on both contacting surfaces, which was mostly induced during RT sliding, as illustrated in **Figure 3.2(a)**. When PS400 disk slid against Inc750X pin, high wear on the disk was generated from RT sliding, and was successively increased with temperature, reaching a maximum wear depth of 60 μm. The pin counter-surface experienced a minute amount of wear at all temperatures, see **Figure 3.2(b)**. "Zero wear" on the DLC coating after sliding against Ti at RT can be observed, whereas at 300°C a maximum wear depth of 2 μm indicated that the pin reached the substrate, therefore the coating was penetrated due to wear. However, at 500°C the wear on the Inc750X substrate increased significantly and appeared with deep grooves with a maximum depth of 30 μm. The corresponding Ti pin specimen exhibited mild wear up to 300°C, whereas at 500°C severe wear occurred, as **Figure 3.2(c)** depicts. DLC disk also appeared with "zero wear" when slid against PS400 pin at RT, whereas at 300°C the wear depth was 0.5μm, yet not deep enough to reach the substrate. After sliding at 500°C, however, the coating was completely removed from the Inc750X substrate reaching a maximum wear depth of 20 μm. The corresponding PS400 pin demonstrated favorable wear resistance at 25, and 300°C, while at 500°C a deep wide groove was observed, see **Figure 3.2(d)**.

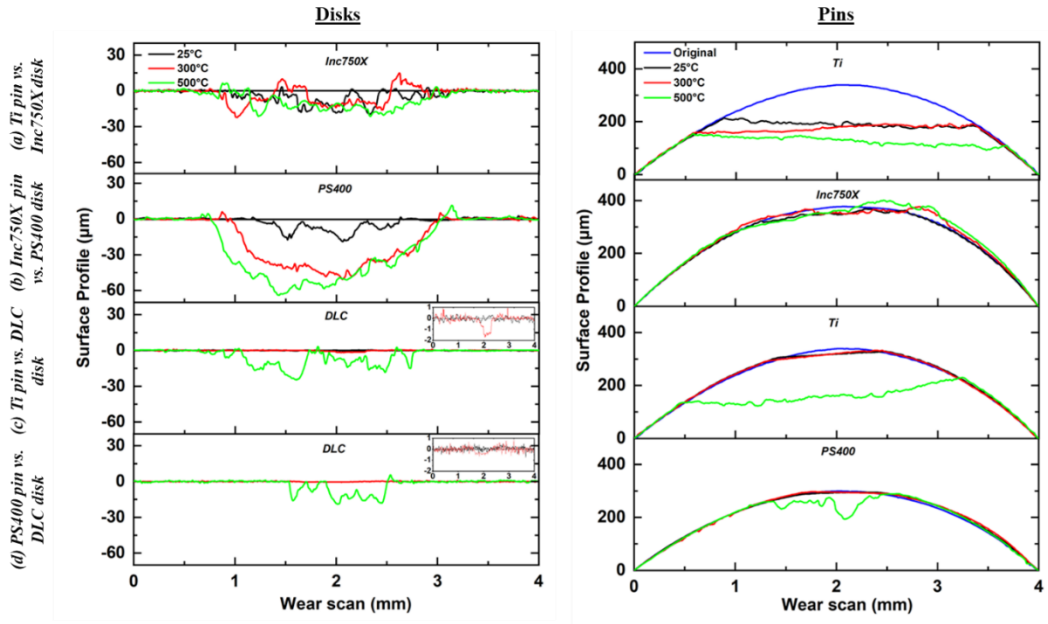

Figure 3.2 Typical wear scans of worn (a) disks and (b) pins following tribo-testing at 25, 300, and 500°C under CO_2. Reprinted with permission from [9].

Figure 3.3(a-c) summarize the COF and wear rate of the disk specimens following succesive experiments under CO_2 at 25, 300, and 500°C, respectively. **Figure 3.3(d)** excibits the COF and wear rate values of the two best-performing tribo-pairs under CO_2 at each temperature. Ti vs. Inc750X and Inc750X vs. PS400 showed similar tribological behavior with COF values around 0.5 and wear rate values of 2.8, and 2.7 $\times 10^{-4}$ mm^3/Nm, respectively. The tribo-pair Ti vs. Inc750X inevitably experienced poor tribological performance, since no lubricating mechanisms were in play. Inc750X and PS400 tribo-pair was extensively study by NASA scientists, targeting HT applications, depicting, however, poor performance at low temperatures, attributed to the innactivation of the low temperature solid lubricants of PS400 [47], and the absence of a glaze film at the interface

[6,35]. The extreme wear resistance of DLC coating at RT against both Ti and PS400 counter-surfaces is demonstrated with zero wear values on the plot, as shown in **Figure 3.3(a),** attributed to a hardness mismatch of the sliding surfaces, with Ti and PS400 being too soft to induce any wear on the hard DLC coating (see **Table 3.2**). In fact, the ultra-low COF (0.08) when DLC slid against Ti showed that the two surfaces are tribologically compatible and the bare Ti pin is not intervening in the lubricating mechanisms of DLC. Despite that when PS400 replaced the Ti pin a low COF was maintained, a higher average value at 0.21 was observed. Nevetheless, the lubricating mechanisms of DLC at RT were in effect and the contribution of DLC in decreasing the COF was successful [52,67].

At 300°C, the wear on the Inc750X disk against Ti pin did not change significantly from RT with a value of 3.26×10^{-4} mm^3/Nm, whereas the wear rate on PS400 disk when slid against Inc750X increased by a factor of 4, at 13×10^{-4} mm^3/Nm. Also, Ti vs. Inc750X experienced the highest COF at 300°C among all tribo-pairs with a value of 0.62. The DLC disks at both experiments (against PS400, and Ti) experienced mild wear described by the removal of superficial layers. In fact, at 300°C, DLC starts undergoing a structural transition from a diamond-like to a graphite-like structure inducing some degree of deterioration of its mechanical properties, such as hardness, and the coating is more prone to wearing off [52]. The wear rates for DLC disks were 14.7×10^{-6} and 5.67×10^{-6} mm^3/Nm, with Ti and PS400 pins as the counter-surfaces, respectively. The average COF values of both tribo-pairs were around 0.25. It can be concluded that at 300°C, DLC was still the dominant surface by providing good lubrication, especially for PS400 vs. DLC, whereas the DLC coating was partially removed, and the substrate was reached during sliding

against the Ti pin. This partial removal resulted in different contact mechanisms in every repetition, thus the high flactuation in the COF shown in **Figure 3.1(b)**.

The Ti vs. Inc750X tribo-pair experienced the highest COF, and a moderate wear of 3.4×10^{-4} mm^3/Nm at 500°C. On the other hand, Inc750X disk vs. PS400 tribo-pair generated the highest wear on the disk with a value of 22.8×10^{-4} mm^3/Nm. Furthermore, a temperature of 500°C is well above the transitional temperature of DLC into graphite [2,66,69], wherein the complete removal of the coating during sliding is inevitable. The wear on the DLC disks of both experiments (Ti vs. DLC, PS400 vs. DLC) increased significantly (compared to RT and 300°C) at values of 4.26×10^{-4} and 1.62×10^{-4} mm^3/Nm, respectively. The COF values also increased by 46 and 66% compared to 300°C, respectively.

Figure 3.3(d) shows that both tribo-pairs, namely PS400 vs. DLC, Ti vs. DLC had similar tribological responses, at 25, and 300°C, with the former showing an "unreliable" tribological character with high flactuations of COF at 300°C. At 500°C, and when DLC disk slid against the bare Ti pin, the wear rate of the former was more than three times greater than when DLC slid against PS400. Besides, surface oxides were found at the interface and contributed in maintaining a milder contact with adequate lubrication, as will be illustrated with Raman Spectroscopy in **Section 3.3.4**. Also, the solid lubricants of PS400 were activated, in which silver has a low shear strength beyond 400°C [61], and the fluorides are experiencing a transition from a brittle-like behavior to a ductile behavior at around 400 to 500°C [62].

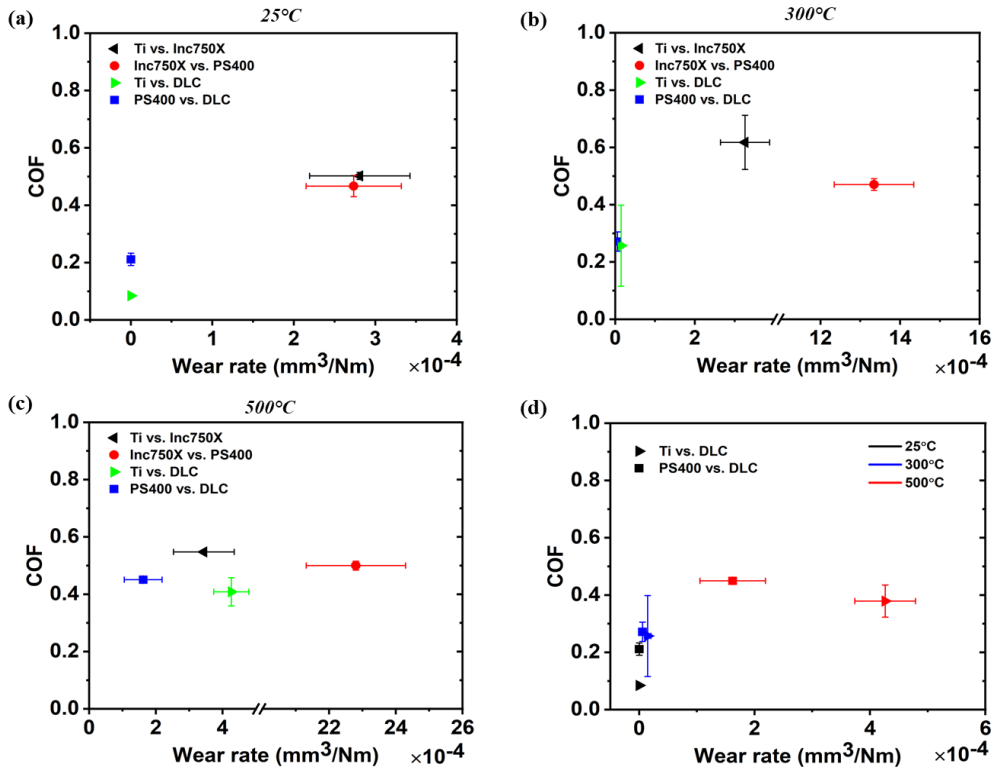

Figure 3.3 COF versus wear after tribo-testing in CO_2 at (a) 25, (b) 300, (c) 500°C, and (d) COF vs. wear of Ti vs. DLC, and PS400 vs. DLC at all temperatures under CO_2. Reprinted with permission from [9].

3.3.3. Optical microscopy

Figure 3.4(a-d) depict the microscopic images of the worn disks and pins following each successive experiment at 25, 300, and 500°C under CO_2. Note that the length and the diameter of the wear tracks and scars gives an indication of the wear on the disks and pins, respectively. Sliding Ti against Inc750X (**Figure 3.4(a)**) resulted in high wear at all three temperatures, with most of the wear being generated at RT. Inc750X vs. PS400 generated high wear on both surfaces, especially at RT, which was successively increased with increasing the temperature (**Figure 3.4(b)**). Typically, a lubricious transferred oxide layer is formed at the interface when sliding Inc750X vs. PS400 at HT

air, which reduces friction and wear significantly [6,47]. Herein, such a layer was not generated under CO_2 environment as it restricted surface oxidation, as will be seen by the elemental surface analysis via EDS in **Section 3.3.7**.

The DLC disk experienced excellent wear resistance when slid against Ti at RT (**Figure 3.4(c)**). However, after 300°C sliding, patches of the DLC coating were removed from the surface (shown with red circles). The rapid increase of the in-situ COF at 300°C can be attributed to the onset of DLC coating removal until steady state was reached. Nevertheless, the wear on the pin was low up to 300°C. After 500°C sliding, the DLC coating was completely removed, and a metal-on-metal harsh contact led to a severe abrasive wear mechanism on both sliding surfaces. Following tribo-experiments of PS400 vs. DLC, the DLC disk depicted excellent wear resistance at RT with mild asperity burnishing (**Figure 3.4(d)**). Also, the small diameter of the wear scars on the corresponding pins illustrates a well-lubricated contact. At 300°C, a clear wear track can be observed, yet not deep enough to reach the substrate, as illustrated with a maximum wear depth of around 0.5 μm in **Figure 3.2(a)**. At the temperature of 500°C, accompanied with a sliding contact allowed the PS400 pin to penetrate through the graphitized DLC coating. Also, abrasive wear on the pin can be observed, demonstrated with numerous parallel furrows. As it will be seen with Raman spectra of DLC coating in **Figure 3.5(a)**, the amount of graphitization (therefore softening) was significantly higher when exposing the DLC coating at 500°C, compared to 300°C.

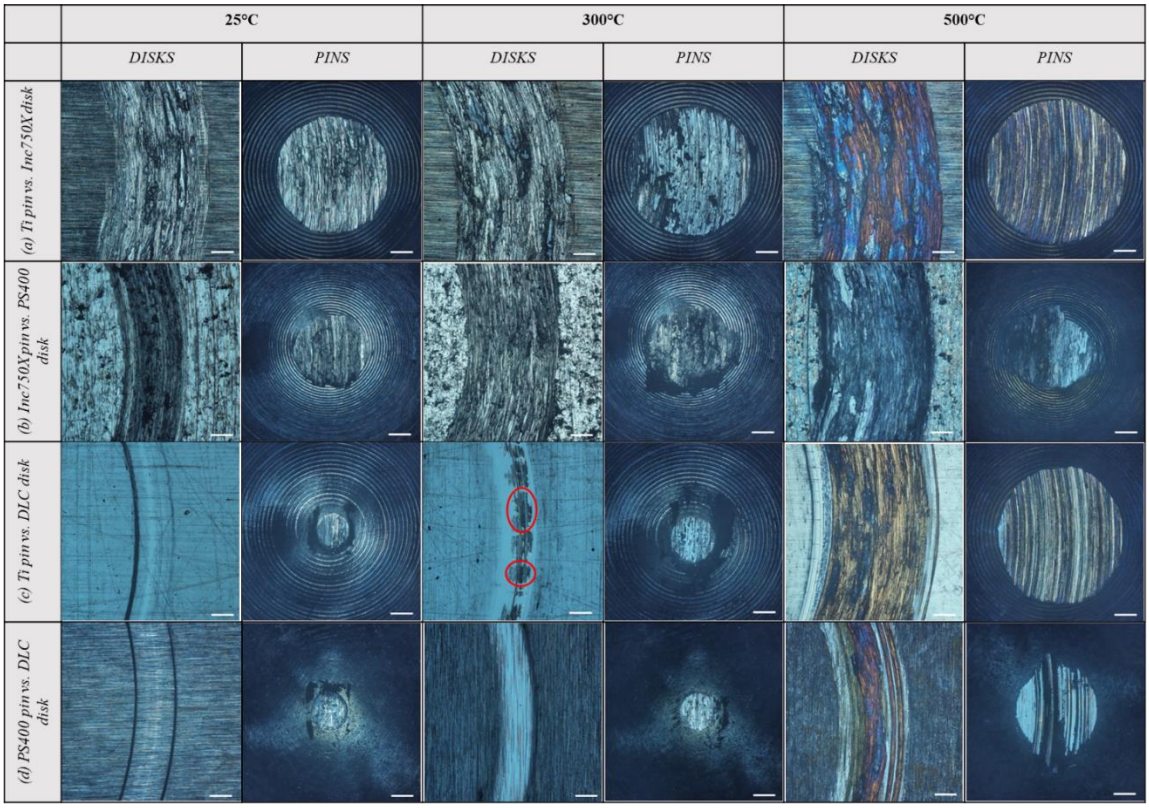

Figure 3.4 Optical microscopic images of worn disks and curved pins after the tribo-experiments in CO_2 (500 μm scale bar). Reprinted with permission from [9].

3.3.4. Raman Spectroscopy

Raman spectroscopy was employed to investigate the amount of graphitization and structural distortion of the DLC coating when exposed at 300 and 500°C under CO_2 during tribo-testing, and it is presented in **Figure 3.5(a)**. The worn area was also investigated to obtain information on the chemical composition of the interface (**Figure 3.5(b)**). The "as received" DLC specimen served as the benchmark. The amount of graphitization of DLC coatings can be qualitatively expressed with the I_D to I_G intensity ratio, and the value is low when the DLC specimen follows a diamond-like structural behavior [64].

The ratio was measured by dividing the intensities centered at I_D and I_G bands, as in **Section 2.3.5**. The as-received DLC coating appeared with a wide spectrum, with the typical G band centered at 1540 cm^{-1} corresponding to the majority of stable sp^3 clusters, with a low I_D/I_G of 0.65. After exposing the sample to 300℃, the intensity ratio did not change significantly, with a ratio of 0.66. It was only after exposing the sample to 500℃ that a clear "shouldered" peak centered at 1330 cm^{-1} (I_D band) was evident, and the intensity ratio was significantly increased to 1.15, demonstrating functionalization/graphitization of the DLC coating. At such structural conditions, the coating can be easily worn off during sliding contact [52], however, at 300℃ the amount of distortion of the DLC coating was such that no significant structural transition took place, as can be seen in **Figure 3.5(a)**.

The spectrum of the worn area at 300℃ appeared with a weak I_D and a dominant I_G peak, as shown in **Figure 3.5(b)**. In fact, I_D/I_G was calculated at 0.7, compared to 0.66 that was found outside the wear track. It is plausible that the frictional heat generated higher contact temperature which promoted some distortion and graphitic contributions on the DLC coating. Nevertheless, the DLC coating was not penetrated, confirming the assumptions on the structural integrity stated above. Finally, after 500℃ tribo-testing, the Inc750X substrate was reached, and new peaks appeared on the spectrum, while the I_D and I_G bands were very weak. The peaks centered at around 580, and 850 cm^{-1} correspond to different metal oxides, which were transferred from the PS400 counter-surface onto the Inc750X substrate. Specifically, the peaks were identified as Cr_2O_3 and Ag_2MoO_4 and played a key role in enhancing the wear performance at 500°C in CO_2 [48,70,71]. The

main contribution in maintaining the friction and wear low at 500°C was the sliding of two HT alloys, namely PS400 and Inc750X and the generation of metal oxides at the interface.

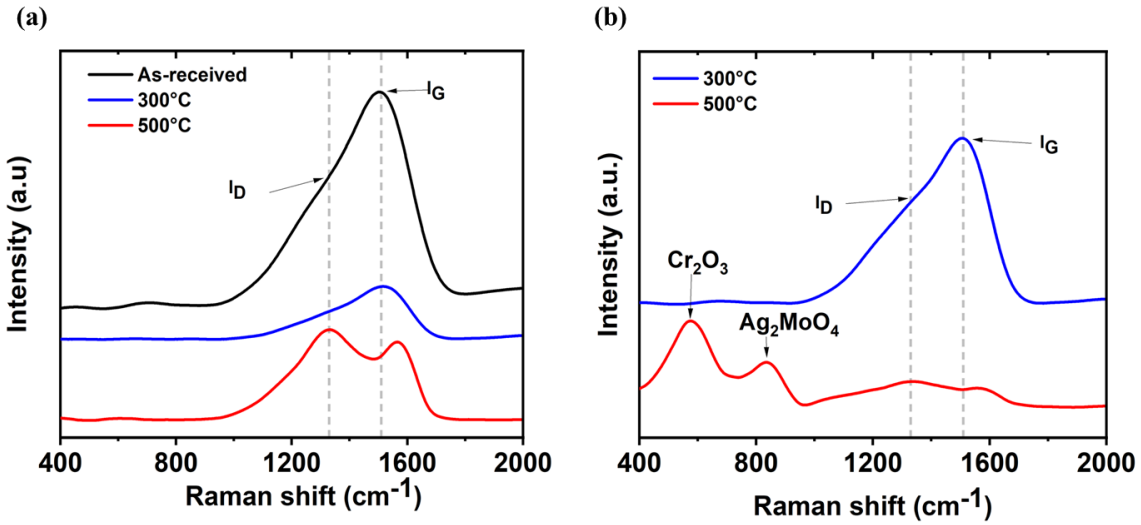

Figure 3.5 Raman spectra of DLC coating/Inc750X substrate of (a) unworn and (b) worn areas following tribo-testing in CO_2. Reprinted with permission from [9].

3.3.5. Effect of the environment

PS400 vs. DLC tribo-pair showed the best and most stable tribological behavior, especially at 300, and 500°C. To that end, experiments under air were also carried out to capture the effect of the environment on friction and wear. **Figure 3.6(a-c)** present the in-situ COF at 25, 300, and 500°C, in both environments, respectively. The corresponding average values are plotted versus the wear rate in **Figure 3.6(d)**. The COF results in CO_2 are reproduced from **Figure 3.1** and are presented in **Figure 3.6** for direct comparison. At 25°C (RT), the evolution of the COF in CO_2 and air was similar, following a slight increasing trend with sliding distance. The experiment under CO_2 resulted in a sudden

drop of the COF after the first few minutes of the experiment (running-in) before stabilizing. The average COF value in air was 67% higher than the experiment in CO_2, with a value of 0.35.

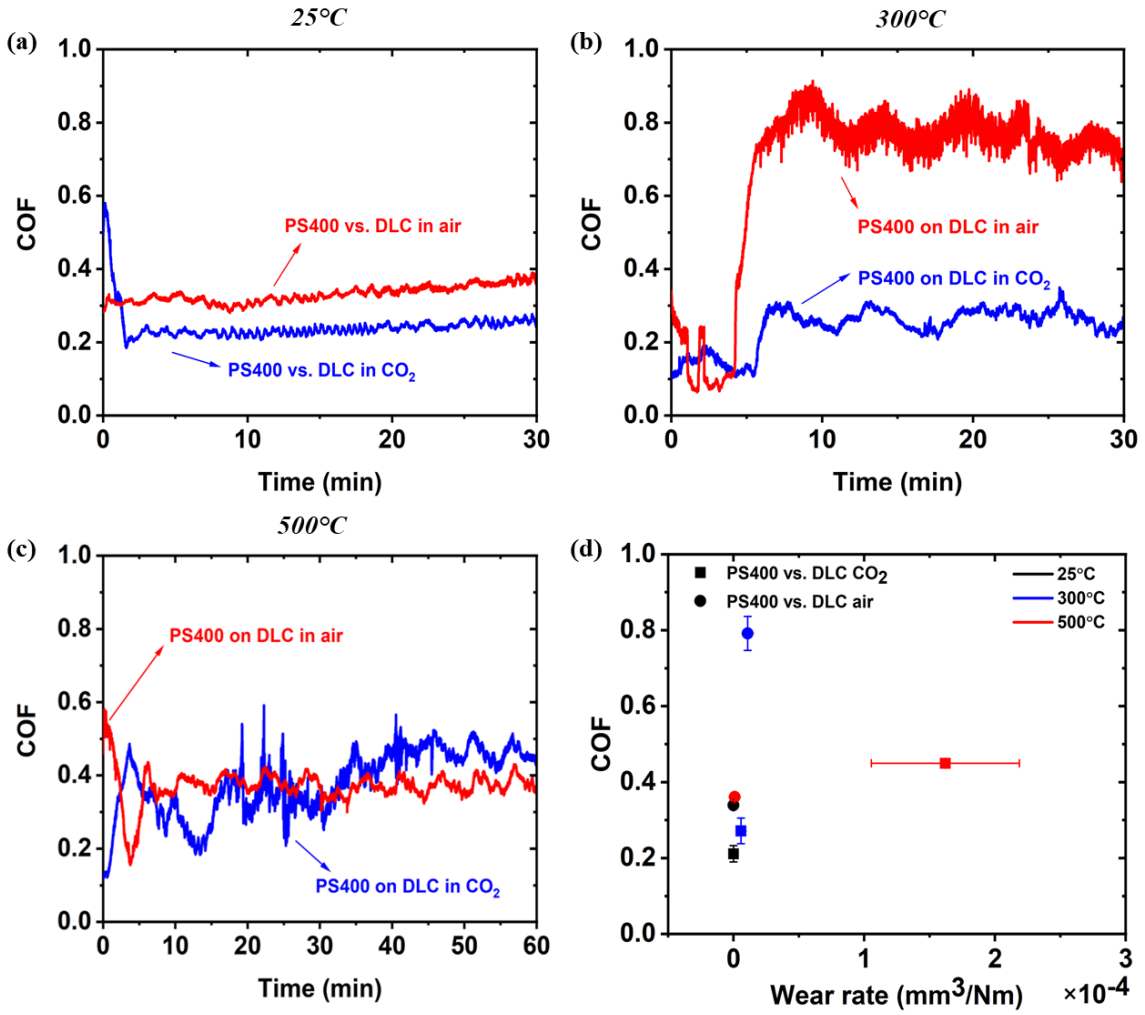

Figure 3.6 In-situ COF under CO_2 and air environments for PS400 vs. DLC tribo-pair at (a) 25°C, (b) 300°C, (c) 500°C, and (d) corresponding average values. Reprinted with permission from [9].

At 300°C, the effect of the environment was more pronounced, with the COF possessing an average value of 0.79 in air, in contrast to the experiment in CO_2 that yielded an average value of 0.27. In fact, a sharp increase in the COF after 5 min of experiment in air can be observed. It can be postulated that at higher temperatures (i.e., 300°C), the surrounding atmosphere is more prone to react with the sliding surfaces, form bonds, and alter the frictional behavior. The experiments at 500°C under both environments resulted in steady-state average COF values, of 0.36 (air) and 0.45 (CO_2). **Figure 3.6(d)** summarizes the average COF and wear rate values in a cumulative COF vs. wear plot. The most remarkable observations are the high friction at 300°C under air and the high wear at 500°C under CO_2.

Figure 3.7 shows the microscopic images of PS400 vs. DLC tribo-pair, along with profilometric scans following successive experiments from RT to 500°C in air. The same wear pattern as the experiments in CO_2 was also observed under ambient atmosphere up to 300°C, that is "zero wear" at RT and low wear with a maximum wear depth <1 μm at 300°C (no penetration of the coating). Interestingly, at 500°C, an oxide transfer film was found on the DLC disk that "filled" the wear track, which was previously induced at 300°C (see **Figure 3.7(c)**) and terminated further wear and provided low friction. Also, mild wear on the pin can be seen, which was mainly generated at RT and remained constant up to the 500°C experiment. Notably, the tribo-pair subjected to tribological testing under CO_2 atmosphere at 300°C demonstrated significantly lower COF than that under air. Therefore, the chemical structure of the sliding interface must play a key role in driving the frictional performance at both environments. XPS analysis on the worn tracks of both DLC coatings

following tribological experiments under CO_2 and air at 300°C was performed, and the results are presented in the following section.

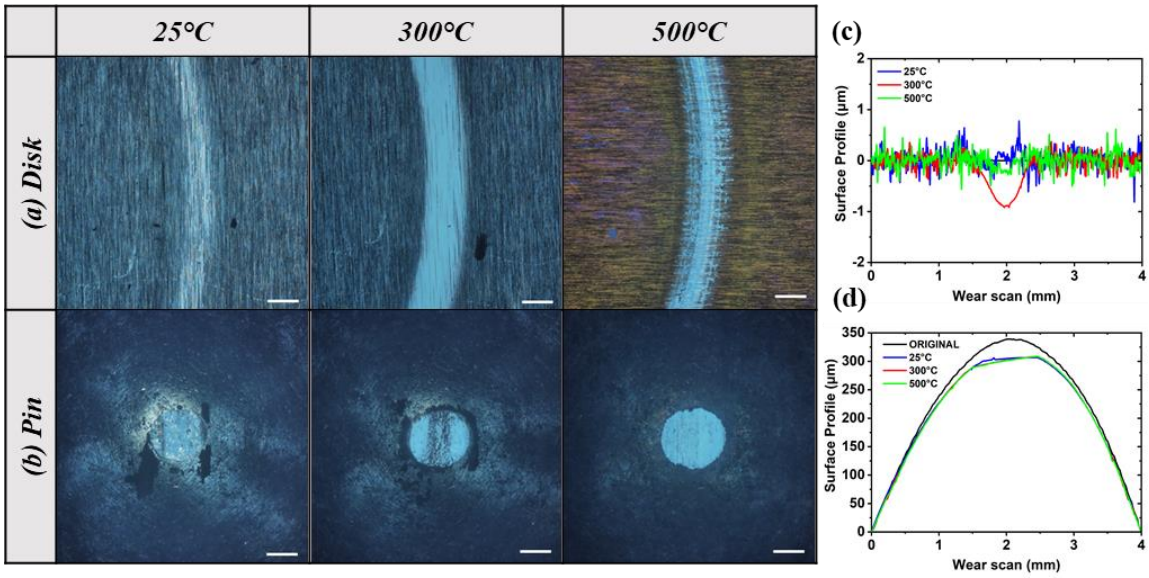

Figure 3.7 Optical microscopic images after tribo-experiments at each successive temperature in air of the worn (a) disk and (b) pin (500 µm scale bar). Corresponding profilometric scans of (c) disk and (d) pin. Reprinted with permission from [9].

3.3.6. XPS analysis

The elemental analysis (**Table 3.4**) of the wear tracks shows that the DLC sample subjected to CO_2 tribo-testing had a higher percentage of O, F, and Ca than the one under air. The high-resolution C 1s spectra of the DLC samples tested in air and CO_2 atmospheres are respectively shown in **Figure 3.8(a, e)**. The C1s spectra in both cases are fit deconvoluted into three peaks at 284.8, 286.5, and 288.5 eV, which correspond to C-C, C-O, and C=O/O=C-OH bonds, respectively. The lower friction coefficient in the presence of CO_2 is partially attributed to higher percentage of chemisorbed oxygen-

containing functional groups, which reacted and passivated the dangling bonds formed on the hydrogenated DLC surface during sliding [67,72].

Moreover, the PS400 includes 5 wt% CaF_2 and BaF_2 solid lubricants in its composition. The XPS results confirmed the presence of elemental Ca and F in the wear track. Interestingly, the percentage was higher for the samples tested in CO_2 atmosphere. Therefore, the lower COF in the presence of CO_2 can also be attributed to the higher percentage of CaF_2 solid lubricant at the interface. In addition, **Figure 3.8(b, c, f, g)** show that the transferred CaF_2 from PS400 disks maintained its chemical structure/composition and did not debone during experiments under both atmospheres. The O 1s spectra of the DLC samples tested in air and CO_2 atmospheres are respectively shown in **Figure 3.8(d, h)**. In accord with C 1s spectra, the O 1s spectra includes two main bonds, which are associated to C-O and C=O terminal groups.

Table 3.4 Atomic percentage (at%) of worn areas of DLC disks following tribo-testing at 300°C. Reprinted with permission from [9].

Elements	**C**	**O**	**F**	**Ca**
Worn area of DLC under CO_2 at 300°C	76.2	19.85	1.33	2.62
Worn area of DLC under air at 300°C	81.87	15.65	0.75	1.73

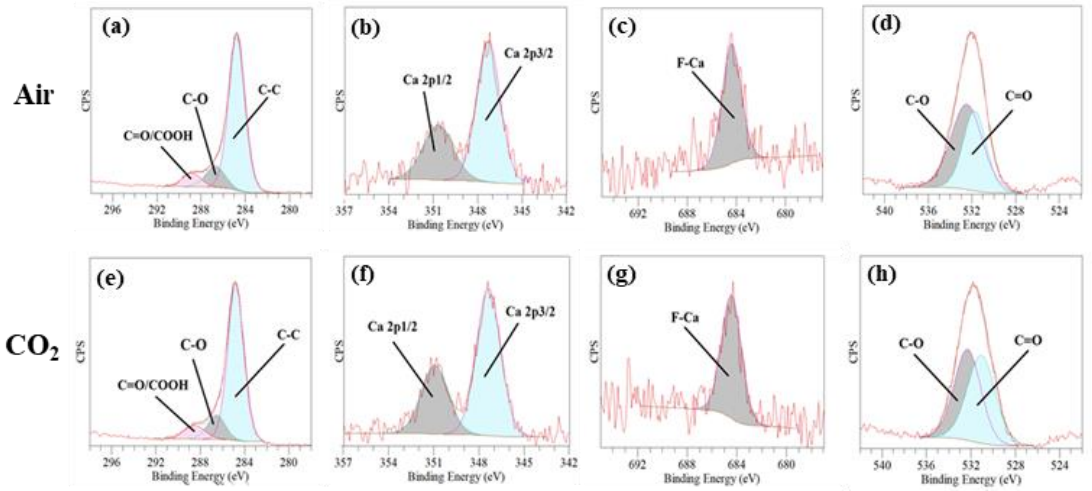

Figure 3.8 XPS spectrums on worn areas of DLC specimens following 300℃ tribo-experiments under air ((a)-(d)) and CO_2 ((e)-(h)). Reprinted with permission from [9].

3.3.7. SEM/EDS analysis

Figure 3.9 depicts the SEM micrographs of the unworn and worn areas of DLC-coated disks after successive experiments from RT to 500℃ of PS400 vs. DLC tribo-pair in CO_2 and air environments. The red dashed squares indicate the area from which the EDS spectra were acquired. Note that the 20 kV electron beam penetrates through the few microns layer (i.e., unworn DLC coating, ~2 μm thick), therefore the elements of the underlayer/substrate are also detected. Herein, EDS was used as a complementary analytical technique to Raman Spectroscopy. **Table 3.5** lists the composition of the elements found on the six designated areas. Area 1 is predominantly composed of graphitized DLC, therefore the high amount of C, with a minute presence of O illustrating that surface oxidation on the exposed unworn area was significantly retarded under CO_2 environment. On the other hand, the exposed DLC coating in air (area 4), demonstrated

significantly higher amount of surface oxidation, as was also seen from the yellow color of the microscopic images of **Figure 3.7(a)**.

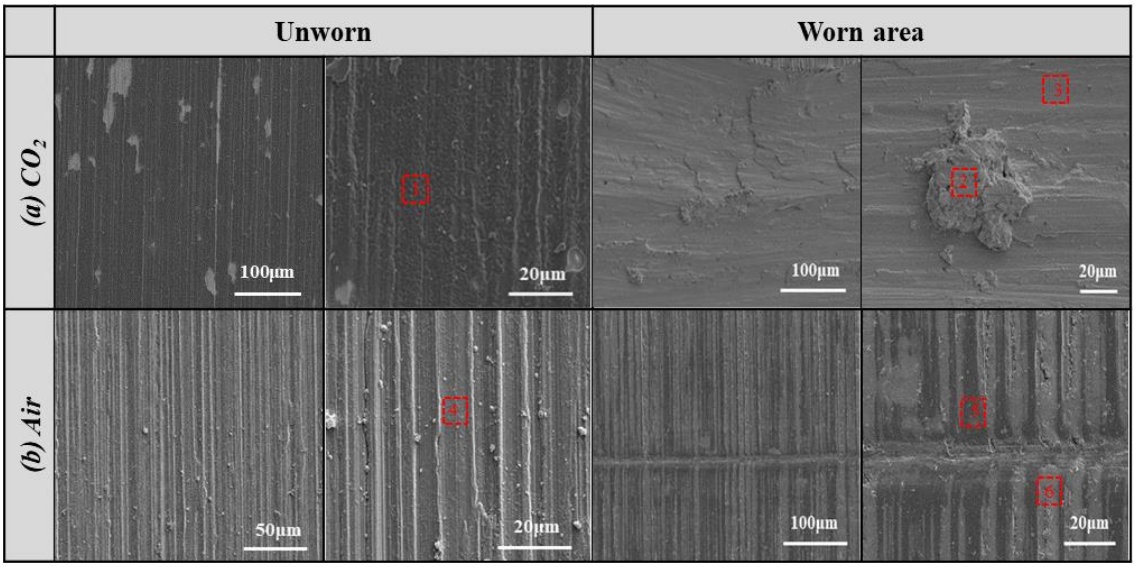

Figure 3.9 SEM micrographs on the unworn and worn areas of DLC specimens after the end of successive tribo-experiments from 25 to 500°C in (a) CO_2, and (b) air. Reprinted with permission from [9].

Table 3.5 Atomic percentage (at%) of DLC disks following tribo-testing at 500°C. Reprinted with permission from [9].

Elements (at%)		**C**	**O**	**Al**	**Ti**	**Ca**	**Cr**	**Fe**	**Ni**	**Mo**	**Ag**	**Ba**
CO_2	**1**	90.4	1.1	-	0.03	-	8.2	0.04	0.2	-	-	-
	2	22.8	39.5	0.7	-	0.6	5.2	0.6	27	2.3	0.8	0.6
	3	18	25.6	0.8	1.5	-	10.6	3.6	39.6	-	0.3	-
Air	**4**	33	27.6	0.2	0.2	-	37	0.3	1.8	-	-	-
	5	9.5	47.6	0.5	0.2	-	30.1	0.1	11.4	0.4	0.3	-
	6	28.9	28	0.2	0.2	-	37.8	0.4	4.5	-	0.1	-

As demonstrated in **Figure 3.4**, the DLC coating was penetrated and the Inc750X substrate was reached after sliding at 500°C in CO_2 environment. The worn area is

characterized by adhesive wear, along with accumulated debris, wherein small traces of the PS400 solid lubricants were found (area 2). Apparently, the low and HT solid lubricants, namely silver and barium/cadmium fluorides were activated and transferred onto the counter-surface. Hence, it is plausible that the softer phases smeared during HT sliding and accumulations of solid lubricant were adhered onto the disk surface, thus lubricating the interface and contributed in maintaining low friction and wear [36]. More importantly, and as seen in **Figure 3.5**, different kinds of oxides were detected on the worn surface of Inc750X substrate via Raman Spectroscopy and provided wear resistance. Furthermore, a considerable amount of C was found in areas 2 and 3, capturing traces of the coating, in accordance with the Raman spectrum of **Figure 3.5(b)**. Comparing the frictional and wear results between PS400 vs. DLC and Ti vs. DLC of **Figure 3.3**, it can be postulated that PS400 is mainly contributing in enhancing the wear performance, whereas the frictional behavior does not change significantly with the presence of PS400 as a counter-surface.

The worn region of DLC-coated specimen following tribo-testing in air at 500°C appeared with a Cr-rich glaze oxide transfer film. Dark and light patterns can be observed, that represent peaks (transfer oxide layer) and valleys (graphitized DLC underlayer). In fact, area 5 demonstrated a significantly higher amount of O compared to area 6, which was not in contact with the counter-surface, and therefore similar chemical composition with area 4 was observed. Also, the detection of C on graphitized DLC underlayer (area 6) was more pronounced, compared to area 5. Minute presence of Ag is also observed, which supports the activation of the solid lubricants. The main lubricating mechanism in

HT air was the formation of Cr-rich oxide glazes at the interface during sliding, which enhanced the frictional and wear performance of the PS400 vs. DLC tribo-pair, as in Refs. [6,7,35,47]. The main findings and the tribo-mechanisms at each temperature and environment are schematically summarized in **Figure 3.10**.

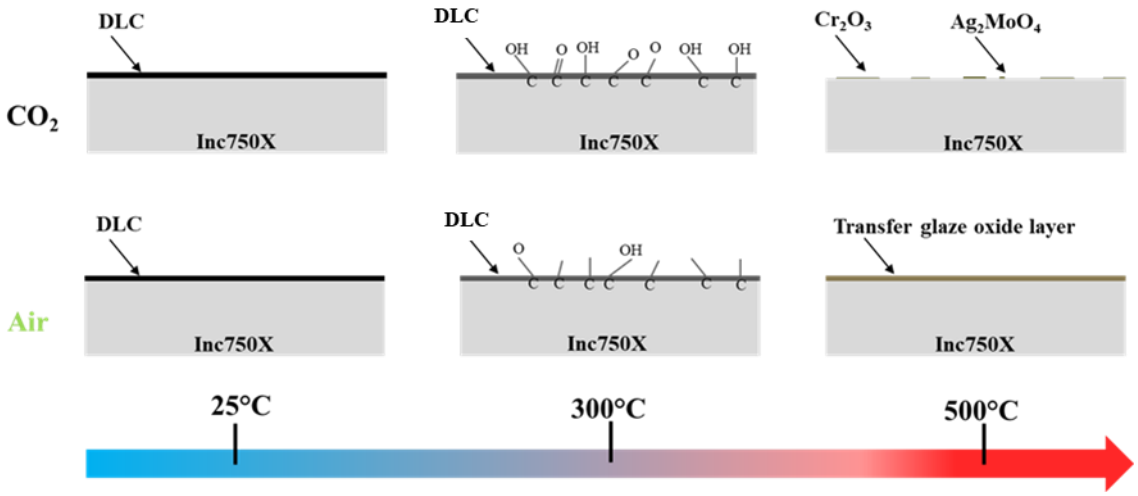

Figure 3.10 Schematic representation of disk tribo-surface at 25, 300, and 500°C under CO_2 and air environments. Reprinted with permission from [9].

3.4. Summary

In this chapter a parametric study was carried out to investigate the effect of each coating (PS400, DLC) at 25, 300, and 500°C under Venusian CO_2 atmosphere and air. The following conclusions could be drawn:

- At 25, and 300°C tribo-testing DLC is the dominant surface and provides excellent lubrication with low friction and high wear resistance. The DLC coating experienced a moderate amount of graphitization at 300°C.

- At 500°C, the graphitized DLC coating was removed from the substrate. Transferred metal oxide layers (Cr_2O_3, Ag_2MoO_4) were found on the worn area of Inc750X and offered enhanced wear resistance. The solid lubricants of PS400, namely silver and fluorides were also detected onto the Inc750X substrate and provided further lubrication.
- PS400 vs. DLC is a dynamic tribo-pair which depicted enhanced tribological performance at low, moderate, and HTs under Venusian-simulated environment. Testing at higher environmental pressures would be of paramount importance before launching the tribo-materials in future missions to Venus.

From **Chapter 2** and **3** it was apparent that the environment plays a significant role in the tribo-chemical and therefore tribological response of the friction surfaces. In the next chapter the effect of environmental pressure was investigated, targeting the pressure found on the surface of Venus. Additionally, two new coatings were added and tested against PS400.

4. TRIBOLOGICAL INVESTIGATION OF ADVANCED COATINGS SUBJECTED TO VENUSIAN ENVIRONMENT OF 2.4 MPA CO_2 PRESSURE AND 464°C[‡]

4.1. Introduction

Venus has been the topic of new explorations to investigate why the planet took such a different evolutionary path from the Earth, as it is believed that the atmosphere of both planets once had the same water and CO_2 levels [17]. Venus is also similar to Earth in terms of size, distance from the sun, and mass; however, the extreme conditions on the surface make it inhabitable [18]. The extreme surface temperature, with mean temperature of 464°C), dense atmosphere (92 times of that on Earth), accompanied by the presence of sulfuric clouds add more challenges to the mechanical equipment for exploitation of the surface and the atmosphere of Venus [17]. For example, moving tribological components in the entry probes, landers, sampling drills and balloons will encounter harsh environments and their continuous operation is vital to ensure successful accomplishment of long-duration missions to Venus. Herein, the surface of INC 718, a HT alloy was modified by the application of a NASA-developed coating, namely PS400, and coupled with advanced hard coatings to form a coating-on-coating contact configuration able to enhance the lubricating performance at the interface. In addition to DLC that was previously tested by the author [7,9], new HT coatings, namely titanium-doped

[‡] Reprinted with permission from "Tribological investigation of advanced coatings subjected to Venusian environment of 2.4 MPa CO_2 pressure and 464°C" by Vasilis Tsigkis, Kian Bashandeh, Pixiang Lan, Andreas A. Polycarpou, 2022. Surface and Coatings Technology, 441, 1-10, Copyright 2023 by Vasilis Tsigki.

molybdenum disulfide (referred as $TiMoS_2$ hereafter), and Nedox PF-F^{TM} (referred as Nedox hereafter) were introduced and their tribological response was investigated when sliding against PS400 under HPHT CO_2 Venusian atmosphere.

In **Chapter 2** and **3** the tribological performance of hard coatings with the prospect of maintaining low friction and wear at both RT and HT was investigated. Among the coatings tested against PS400, DLC yielded the most promising tribological behavior and thus, was flagged for further investigations [7]. In a subsequent study, a PS400 vs. DLC tribo-pair was subjected in a CO_2 Venusian-simulated environment as the dominant gas composition (96.5%), seeking to replicate the conditions on the surface. It was demonstrated that the testing environment controls the tribo-chemical interactions and the lubrication mechanisms at PS400/DLC interface, particularly at HT sliding [51]. Nevertheless, PS400 vs. DLC showed a dynamic tribological character where each coating controlled the friction and wear at different temperatures.

MoS_2 is being used as a solid lubricant due to its hexagonal basal crystalline chemical structure that provides easy shear between layers [73]. Several studies have been focused on the tribological performance of $TiMoS_2$ coatings under different atmospheres and temperatures [74–76], Ti-content [77], mating surfaces [78], and excellent lubricating properties are reported. Sun et al. studied the effect of temperature on $TiMoS_2$, demonstrating that above 400°C the coating started to wear off from the substrate when tested under dry N_2 environment [79].

Nedox SF-2^{TM}, and Nedox FM-5^{TM}, which are electroless Ni-plated fluorine-impregnated coatings, were tribologically evaluated as sleeves and washers for wear reduction in valves

and bearings applications, respectively [80,81]. HT Venusian environment requires polymer-free coatings that can withstand sliding at elevated temperatures, and therefore Nedox PF-F^{TM} was selected among the Nedox^{TM} family. In this chapter, the tribological behavior of metal-on-metal, metal-on-coating, and coating-on-coating contacts subjected to Venusian-simulated HPHT CO_2 environment utilizing the above-mentioned materials was systematically investigated.

4.2. Characterization

4.2.1. Materials and sample preparation

The disk and pin substrates were machined out of an INC 718 rod (Onlinemetals.com). The pin specimens were coated with PS400 and the disk specimens with Nedox, $TiMoS_2$, and DLC. PS400 was applied onto INC 718 pins by PS at ADMA Products Inc., Hudson, Ohio, USA, with an initial thickness of 250 μm. Nedox coating was applied onto INC 718 disk substrates by electroless nickel plating followed by an oven bake at 340°C for 2 hours, at General Magnaplate, Arlington, Texas, USA, with a thickness of ~ 17 μm. $TiMoS_2$ was coated onto INC 718 disk substrates at IBC Coatings Technologies, Lebanon, Indiana, USA, by simultaneous magnetron sputtering PVD of Ti and MoS_2 until the thickness of the coating reached 2 μm. A thin pure Ti interlayer was first sputtered to enhance the adhesion between the substrate and $TiMoS_2$ coating. The resulting coating was doped with ~ 10 at% Ti. The DLC (a:C-H) coating was deposited by CVD with a thickness of 2 μm, and hydrogen content of 20-40 at% at Oerlicon Balzers, Liechtenstein.

The chemical composition of INC 718 is listed in **Table 4.1**, and the chemical composition of PS400 is listed in **Table 2.1** of **Chapter 2**. INC 718 is a Ni-based multicomponent alloy and is being used for HT applications such as mechanical components of fluid-fueled rockets. PS400 is also a Ni-based alloy developed by NASA intended for HT tribological applications, reinforced by its unique composition of hardener and lubrication phases. Nedox is a polymer-free Ni-P alloy with high operating temperature up to 650°C, while maintaining low friction and wear. $TiMoS_2$ comprises of MoS_2 as the main lubricating phase, and it is doped with Ti to improve hardness and thermal stability. DLC is a carbon-based material structured in a diamond-like configuration that gives the coating extreme hardness and lubricating properties.

The RMS surface roughness and hardness values of the samples are listed in **Table 4.2**. The INC 718 substrate passed through mechanical grinding to remove machining marks and the RMS roughness was measured to be 0.55 ± 0.08 μm. The PS400 coating in its as-received form is very rough, therefore it was ground using a carbide wheel until ~ 50 μm of material was removed (~200 μm final thickness), and the RMS roughness was reduced to 0.4 ± 0.1 μm. Nedox, $TiMoS_2$, and DLC coatings were not subjected to post-polishing and hence, the specimens were tested in their as-received form, with RMS roughness values of 1.44 ± 0.19, 0.26 ± 0.06, and 0.26 ± 0.004 μm, respectively. The hardness values of INC 718 and Nedox were provided from the vendors and the corresponding values of PS400, $TiMoS_2$, and DLC were measured with Vickers' and nanoindentation, as shown in **Table 4.2**. DLC has the highest hardness corresponding to a majority of sp^3 bonds and a diamond-like structure of the commercialized coating.

Nedox and $TiMoS_2$ coatings have similar high hardness values around 8.5 and 6.1 GPa, respectively. PS400 has the lowest hardness value, and it was measured at 2 ± 0.2 GPa, in agreement with Ref. [47].

Table 4.1 Chemical composition of INC 718, provided by the manufacturer (units are in wt.%). Reprinted with permission from [11].

INC 718							
Ni	**Co**	**Cr**	**Fe**	**Mo**	**Al**	**C**	**Ta**
50-55	1	17-21	Balance	2.8-3.3	0.2-0.8	0.08	0.05
Cu	**B**	**Ti**	**Nb**	**P**	**Mn**	**Si**	**S**
0.3	0.006	0.65-1.15	4.75-5.5	0.015	0.35	0.35	0.015

Table 4.2 Surface roughness and hardness values. Reprinted with permission from [11].

Sample	***INC 718***	***PS400***	***Nedox***	***$TiMoS_2$***	***DLC***
Roughness RMS (µm)	0.55 ± 0.08	0.4 ± 0.1	1.44 ± 0.19	0.26 ± 0.06	0.26 ± 0.004
Hardness (GPa)	3.3*	2 ± 0.2**	8.5*	6.1 ± 0.5***	19.9 ± 3.9***

*Provided by the vendor; **Measured using Vickers' indentation, ***Measured via nanoindentation.

4.2.2. Experimental procedure

Five different tribo-pairs were selected for evaluation under 2.4 MPa CO_2 atmosphere, nominal contact pressure of 3.5 MPa (resulting from 89 N applied load and total nominal contact area of 25.7 mm^2), sliding speed of 0.2 m/s, and sliding duration of 30 min resulting in 6000 cycles. The tribo-pair INC 718 vs. INC 718 served as the benchmark to gauge the effect of each of the tested coatings. Medical grade CO_2 with

99.5% purity was used to replicate the Venusian CO_2 atmosphere. A flashing/venting procedure was followed to achieve the minimum presence of air within the chamber. Specifically, the chamber was flashed six times by pressurizing the chamber up to 1.4 MPa, with the relief valve closed, followed by intervening venting. At the last flashing step, the valve remained closed and the chamber was pressurized to 2.41 MPa. Next, the heating stage was heated to the target temperature (464°C), and after five min of constant temperature, the pin and disk testing specimens were brought into contact and the experiment was initiated by rotation of the 3-pin sample against the disk (**Figure 4.1**). After the end of the experiment, the samples were let to cool to RT under CO_2 at 2.41 MPa. A minimum of three experiments for each coated tribo-pair were carried out to assure repeatability. Before each experiment, the samples were ultrasonically cleaned for 10 min in an acetone bath at 40°C, rinsed with isopropanol alcohol, and forced dried with hot air.

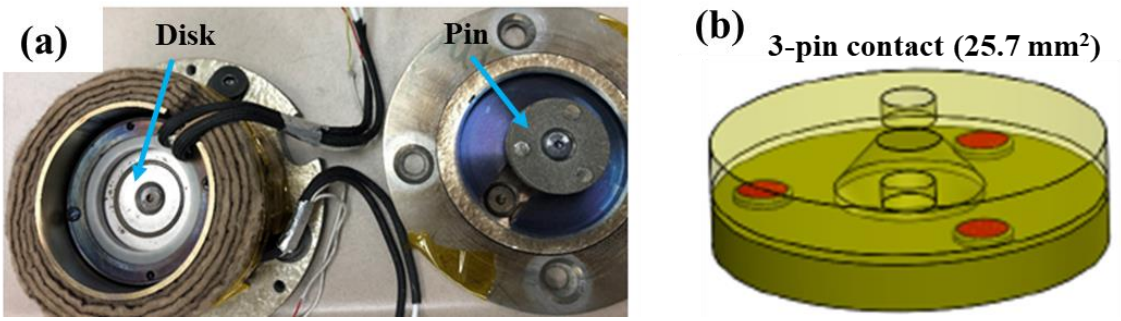

Figure 4.1 Experimental set up: (a) photograph of pin and disk, and (b) contact configuration. Modified with permission from [11].

4.3. Results and discussion

4.3.1. COF

Figure 4.2 presents in-situ and average COF of the five different tribo-pairs under the conditions described above. The pair INC 718 vs. INC 718 demonstrated high friction from the initial stages of the experiment with values ranging between 0.5 and 0.6, and remained constant for the duration of the experiment, as shown in **Figure 4.2(a)**. Metal-on-metal harsh contact in the absence of a mitigating coating led to high friction. When PS400 coating was deposited on the pin and tested against an INC 718 disk (**Figure 4.2(b)**), the COF was reduced to 0.35 with a rapid jump after 180 m of sliding distance. Following the transient zone, the COF remained constant at a value of 0.5, similar to the INC 718 vs. INC718 tribo-pair. The rapid jump of the COF might be attributed to the "runout" of the solid lubricant from the interface, due to the complete removal of PS400 coating, manifested with the high wear rate, as shown in **Figure 4.2(b)**. PS400 vs. Nedox appeared with a low running-in COF, with values ranging between 0.3 and 0.4, followed by a rapid increase at 60 m of sliding, and then remained stable around 0.7 (**see Figure 4.2(c)**). The pair PS400 vs. $TiMoS_2$ revealed a weak peak in the in-situ COF, with a value of 0.4 at 30 m of sliding distance, and then remained at lower values until the end of the test, as shown in **Figure 4.2(d)**. PS400 sliding against DLC (**Figure 4.2(e)**) showed a somewhat erratic nature with low values around 0.3. The hardness, and subsequently the wear resistance of DLC start deteriorating at temperatures above 300℃ due to graphitization, therefore sliding under such conditions is critical for the integrity of the coating [82]. However, when the coating remains at the interface, it can maintain low

friction and lubrication. Following "running-in," the values were around 0.3 with a sudden drop at 240 m of sliding distance. At the last cycles of the experiments, the COF was around 0.25.

Figure 4.2(f) summarizes the average COF and ± 1 standard deviation. The sliding of PS400 vs. Nedox resulted in the highest average COF, followed by the uncoated INC 718 vs. INC 718 tribo-pair. As both PS400 and Nedox are tribologically similar materials (Ni-based), it is plausible that strong adhesive frictional forces between the rubbing surfaces resulted in high friction. Comparing the average COF between INC 718 vs. INC 718 and PS400 vs. INC 718, a 25% reduction can be observed. The reduction in COF is attributed to the beneficial effect of the lubricating phases of PS400, evident from the EDS analysis shown in **Table 4.3** thereafter. The tribo-pairs PS400 vs. $TiMoS_2$ and PS400 vs. DLC yielded the lowest average COF values, at 0.35 and 0.32, respectively. However, the high standard deviation of PS400 vs. DLC due to the behavior of graphitized DLC coating overshadows the respective average value of PS400 vs. $TiMoS_2$.

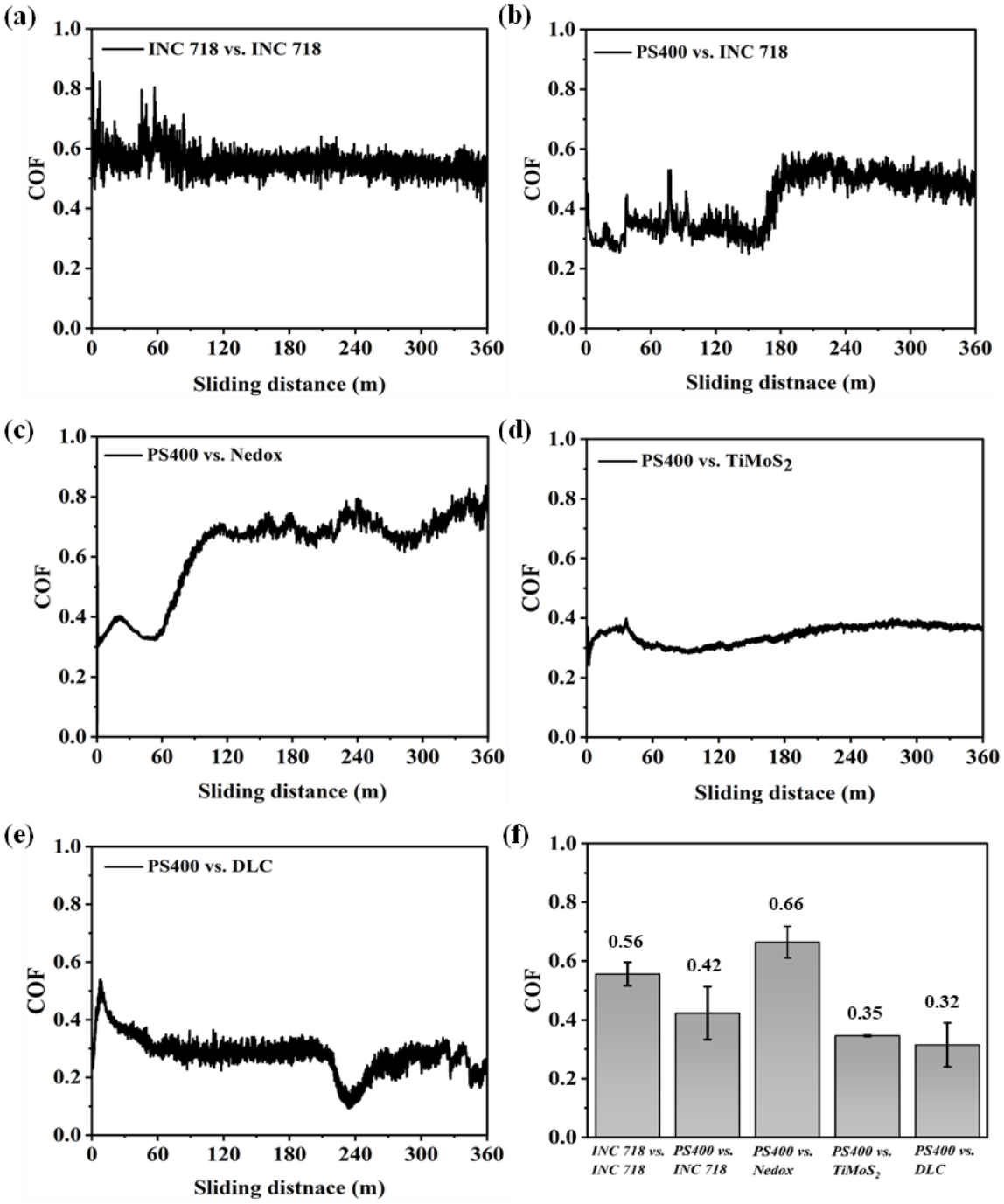

Figure 4.2 Evolution of COF with sliding distance under CO_2 environment and 464°C for (a) INC 718 vs. INC 718, (b) PS400 vs. INC 718, (c) PS400 vs. Nedox, (d) PS400 vs. $TiMoS_2$, and (e) PS400 vs. DLC, and (f) respective average COF values. Reprinted with permission from [11].

4.3.2. Wear

Figure 4.3 shows wear profilometric scans of the disk specimens, following tribological experiments. The 3D scans with 8 mm × 4 mm area captured both the unworn and worn regions, and the vertical distance of the uncoated disks spans from -70 μm to 40 μm (**Figure 4.3(a, b)**), and -10 μm to 10 μm range that represents the vertical distance of the scans on the coated disks (**Figure 4.3(c-e)**). The 2D line scans were performed perpendicular to the wear tracks and the wear depths are further illustrated, as shown on the right-hand side of **Figure 4.3**. The uncoated INC 718 disk experienced severe wear when slid against the uncoated INC 718 pin and induced deep scratches (~ 60 μm) on the surface. Rubbing of two metallic surfaces without internal or external lubrication results in harsh contact whereby adhesive wear tends to produce wear debris that can be trapped at the interface and subsequently plow the counter-surface and induce abrasive marks and deep scratches. When the PS400-coated pin was tested against an uncoated INC 718 disk it resulted in a lower degree of abrasive wear on the disk surface, and the wear depth was maintained at 20 μm.

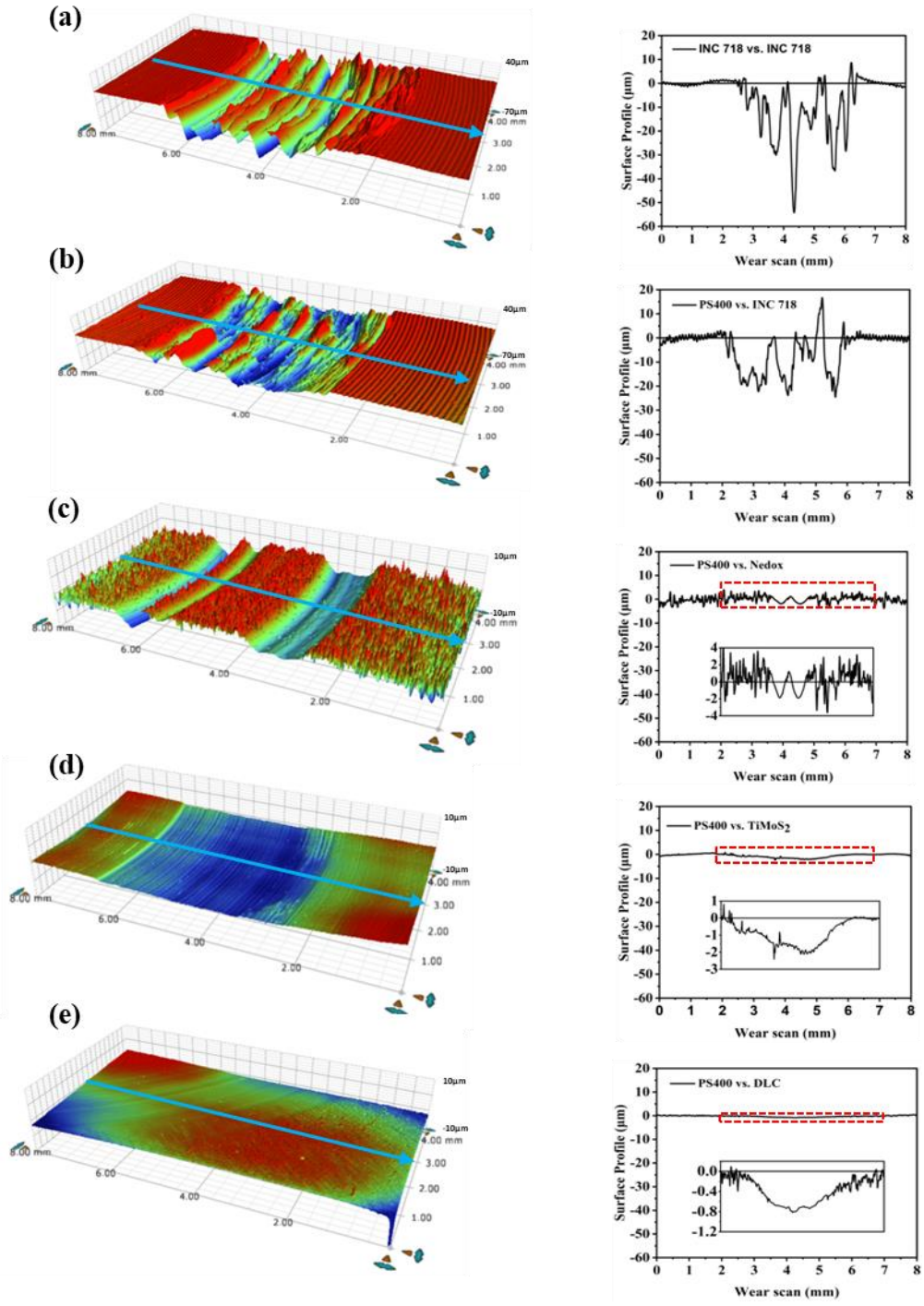

Figure 4.3 3D wear representation (8mm × 4mm area) and corresponding 2D scans of disk specimens of (a) INC 718 vs. INC 718, (b) PS400 vs. INC 718, (c) PS400 vs. Nedox, (d) PS400 vs. $TiMoS_2$, and (e) PS400 vs. DLC tribo-pairs. Arrows show the direction of the 2D scan. Reprinted with permission from [11].

Coating-on-coating contact configuration further increased the wear resistance of the contacting surfaces and the wear depth remained shallow. The worn surface of Nedox appeared with two distinct plows, rather than a uniform wear depth, indicating that during sliding against PS400 the pin deformed in an ambiguous manner, which resulted in a non-uniform contact between the surfaces. Although the resulting pressure was higher, it was not sufficient to plow the coating all the way through to the substrate, and the wear depth remained at ~ 2 μm (see inset of **Figure 4.3(c)**). It is noted that the thickness of Nedox coating is about 17 μm. In contrast, the few micrometers thick $TiMoS_2$ coating was penetrated through to the substrate at some areas, as can be observed from the 2 μm maximum wear depth. Thus, Nedox appeared to have higher resistance to wear compared to $TiMoS_2$, despite their similar maximum hardness values of 8.5 and 7 GPa, respectively. However, the thermal stability of Nedox is higher than that of $TiMoS_2$ (650 vs. 500°C), and since the testing temperature of 464°C approached the stability limit of $TiMoS_2$, the mechanical properties of the coating deteriorated, and the wear process was expedited as described in Ref. [79]. Sliding of PS400 vs. DLC induced light polishing and removal of superficial layers, with the maximum penetration depth remaining less than 1 μm, so that the coating was not penetrated (2 μm thick). It was previously demonstrated that DLC undergoes a significant structural transition at 500°C, from a diamond-like to a graphite-like structure that is more prone to wear [9]. The penetration was limited to shallow depths and the graphitized DLC coating remained at the interface until the end of the experiment, however it can be assumed that prolonged testing would eventually wear off the coating.

Figure 4.4(a-c) illustrates the wear performance of the five tribo-pairs and the tribological performance is summarized in **Figure 4.4(d**) in a COF vs. wear plot. High wear was observed on both INC 718 disks when slid against INC 718 and PS400 pin specimens, with similar wear rate values at 6.5×10^{-5} mm^3/Nm, as seen in **Figure 4.3(a)**. In contrast, the three disk surfaces coated with Nedox, $TiMoS_2$, and DLC demonstrated enhanced wear resistance, with wear rate values significantly lower than those of the uncoated INC 718 disk specimens. The lowest wear rate was obtained for the DLC disk at 3×10^{-6} mm^3/Nm. Sliding of a PS400 pin against an INC 718 disk was detrimental for the pin surface as the coating was penetrated down to the substrate (**Figure 4.4(b)**). In fact, the PS400 pin experienced the highest wear rate (4.34×10^{-4} mm^3/Nm) among the pin materials. The wear of the INC 718 pin when rubbed against INC 718 was low, as most of the wear was induced on the disk mating surface. The lowest wear rate was seen on PS400 pin when slid against $TiMoS_2$ (0.05×10^{-4} mm^3/Nm), followed by PS400 pin sliding against Nedox and DLC.

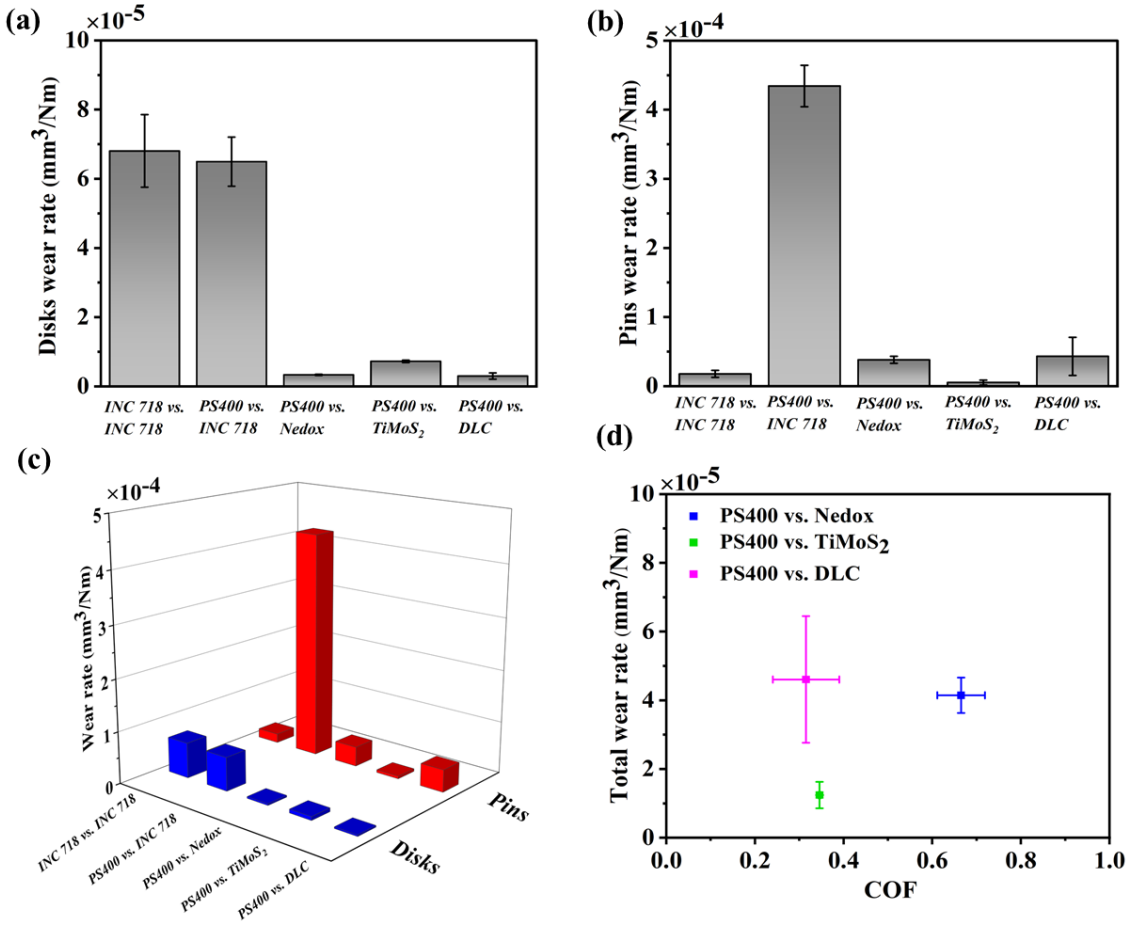

Figure 4.4 Wear performance of (a) disks, (b) pins, (c) combined 3D representation, and (d) summary of the tribological performance of the coated tribo-pairs in a wear vs. COF plot. Reprinted with permission from [11].

Overall, PS400 vs. INC 718 produced the highest total wear (sum of disk and pin wear) on the contacting surfaces, followed by INC 718 vs. INC 718, as illustrated in **Figure 4.4(c)**. Sliding of coating-on-coating resulted in a significantly lower total wear on the rubbing surfaces compared to metal-on-metal, or metal-on-coating. In summary, the best tribological performance among the tribo-pairs was demonstrated by PS400 vs. $TiMoS_2$, as seen in **Figure 4.4(d)**. Despite the fact that the average COF value of PS400

vs. DLC was lower than that of PS400 vs. $TiMoS_2$, the high data scatter results in overlapping of the two values. Also, the total wear of PS400 vs. $TiMoS_2$ was less than that of PS400 vs. DLC, therefore PS400 and $TiMoS_2$ was the optimum material combination under HPHT conditions.

4.3.3. SEM/EDS analysis

The SEM micrographs of the worn pins (left) and disk (right) following tribological experiments appear in **Figure 4.5** and magnified images are shown on the sides (see red squares). The orange squares represent the areas from which the EDS spectra were acquired and the results are presented in **Table 4.3**. INC 718 pin experienced significant adhesive wear, due to the metal-on-metal sliding of similar tribo-surfaces that led to a harsh contact in which both contacting surfaces were severely deformed. In fact, the INC 718 disk was plastically deformed with microcracks and grooves with high adhesion points, or dents, visible on the surface (**Figure 4.5(a)**), which resulted in high friction and wear. When the PS400 pin was tested against INC 718 disk, significant deformation also appeared, manifested as plastic flow and abrasive wear. The wear rate of the PS400 pin was significantly higher than that of the INC 718 pin when they both slid against INC 718 disk, as shown in **Figure 4.4(b)**. It can be postulated that a thermal softening "mismatch" between PS400 and INC 718 promoted high wear on the PS400 pin, which resulted in a penetration of the coating. At RT, the hardness values of INC 718 and PS400 are around 3.3 and 2 GPa, respectively. Also, INC 718 maintains its strength and structural integrity up to 700℃, while the maximum operating temperature of PS400 is below 600℃ [47], being more vulnerable to wear when sliding at the testing temperature

of 464°C. In addition, the INC 718 disk experienced lower plastic deformation, when the INC 718 pin was replaced with PS400, as seen in **Figure 4.5(b)**. The topography of the PS400 pin after sliding against Nedox confirmed the formation of "islands" of material accumulation. The "island" of **Figure 4.5(c)** appeared flattened, with sharp edges and a high amount of material debris was trapped between high contact points. The Nedox counter-surface appeared "fresh," with merging and burnishing of high asperities. Rubbing of the PS400 pin vs. $TiMoS_2$ produced a polished smooth surface on the pin, evidence of mild contact. However, the surface of the $TiMoS_2$ disk experienced adhesive wear, in which the substrate was reached in some areas, as shown in **Figure 4.5(d)**. Oxide particles up to10 μm in diameter are also visible in the magnified image and were identified as nickel oxides via EDS, as shown in **Table 4.3**. A smooth worn surface with mild wear is observed on PS400 vs. DLC tribo-pair, with some local exfoliation (micro-pitting) and polishing of superficial layers (see black strips) on PS400 and DLC coatings, respectively, (**Figure 4.5(e)**).

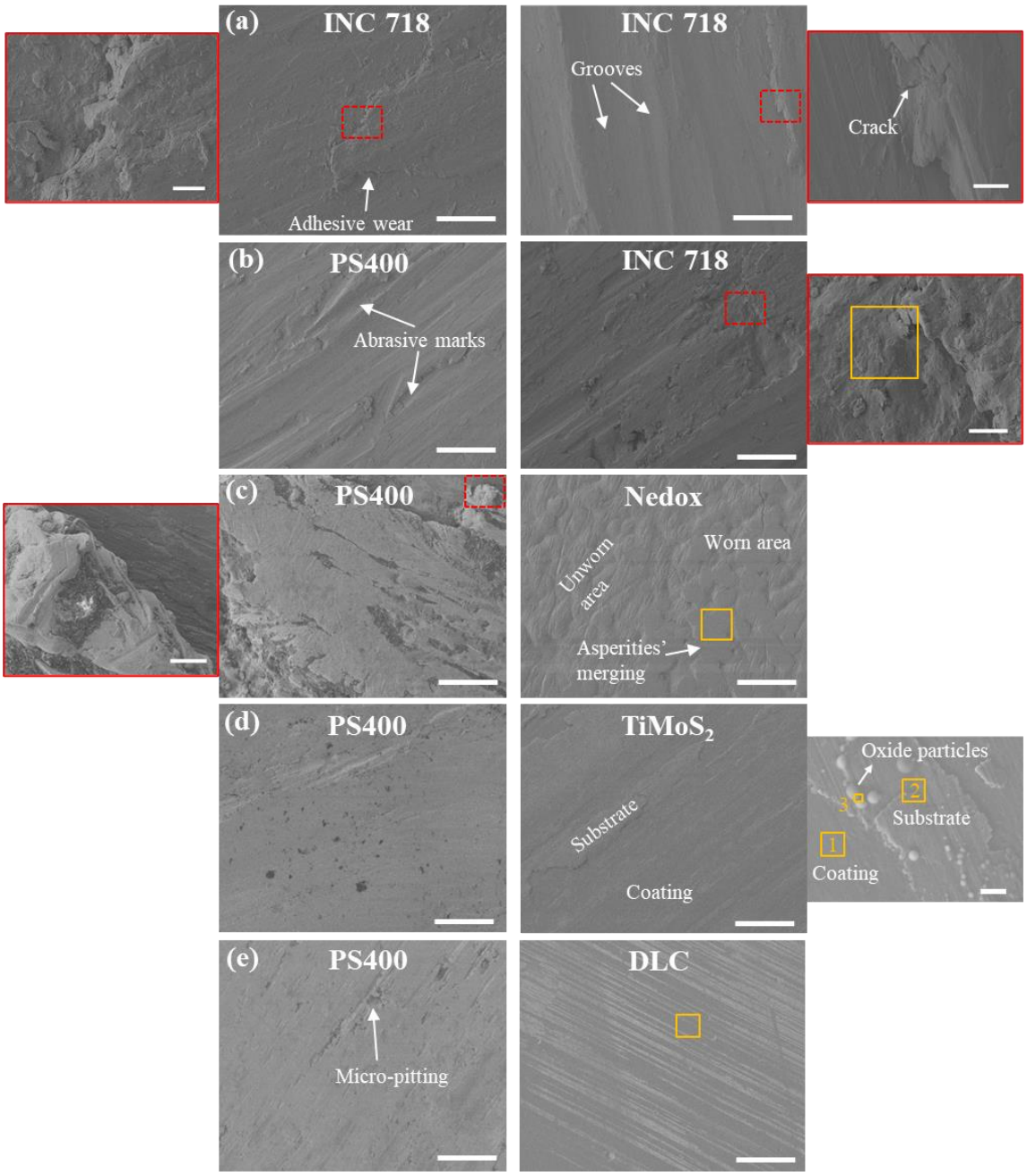

Figure 4.5 SEM micrographs of worn areas of pin (left) and disk (right) specimens of (a) INC718 vs. INC718, (b) PS400 vs. INC718, (c) PS400 vs. Nedox, (d) PS400 vs. $TiMoS_2$, and (e) PS400 vs. DLC tribo-pairs. The magnified area is shown with dashed squares, and the solid sections indicate the EDS area. Scale bars represent 100 μm for low and 10 μm for high magnification images, respectively. Modified with permission from [11].

Table 4.3 shows EDS analyses of the worn surface of the disk specimens after sliding against PS400 pins. The chemical composition of the worn surface gave information on the integrity of the coatings, material transfer from the PS400 counter-surface, and the degree of oxidation allowing correlation with the tribological performance. Note that for very thin coatings (2 μm) of $TiMoS_2$ and DLC, the electron beam can penetrate through the thickness and information on the substrate elements is also acquired. Also, the detection of C (if any) was removed from the chemical composition of the samples, except for DLC, as there is not a component of the rest of the tribo-surfaces, and detection of C is due to contaminants. In addition to the intrinsic elements of INC 718 (see **Table 4.1**), the solid lubricants from PS400 were also detected on the worn surface of INC 718.

Table 4.3 Elemental analysis via EDS of uncoated and coated disks following tribo-testing against PS400. Modified with permission from [11].

(at%)	C	O	Al	Ti	Cr	Fe	F	Ca	Ni	Mo	Ag	P
INC 718	-	18.4	2.8	0.9	13.9	10.5	7.7	0.36	43.6	1.3	0.6	-
Nedox	-	3.2	0.6	-	-	-	-	-	76.05	-	-	20.2
1. $TiMoS_2$	-	37.3	0.8	14.6	5.6	4.5	-	-	23.9	13.3	-	-
2. $TiMoS_2$	-	13.8	1.3	3	2.8	2.3	-	0.5	67.9	6.5	1.9	
3. $TiMoS_2$	-	75.4	0.4	0.4	0.5	0.6	-	-	21.6	0.9	0.2	-
DLC	90	1.1	-	-	8.4	0.1	-	-	0.3	-	0.1	-

The solid lubricants of PS400, CaF_2, BaF_2 (fluorides) and Ag, have an "activation point" between 400-500°C, at which low shearing strength and favorable ductility can provide a degree of lubrication [61,62]. When PS400 and INC 718 are slid against each other in a HT air environment, oxide "glaze" films are formed on the counter-surface [6,35,47]. Such oxide films adequately lubricate the interface, hence diminishing the contribution of the PS400 solid lubricants. However, similar uniform oxide films were not detected, as the CO_2 environment restricts surface oxidation, as mentioned in Ref. [51], and the only lubricating mechanism was due to the presence of transfer solid lubricants. In fact, a high amount of F and a minute amount of Ag were found on INC 718, which lubricated the interface and lowered the COF, until the full removal of the PS400 coating (see **Figure 4.2(b)**). Nedox appeared with its intrinsic elements only, indicating that the solid lubricants from PS400 were not transferred onto the counter-surface. The Ni-based coating contains a significant amount of P originating from the plating process, and a controlled balance between Ni and P provides the alloy with high hardness and subsequently good wear resistance and low friction when sliding against itself at ambient conditions. However, the observed COF for PS400 vs. Nedox was the highest among all tribo-pairs revealing an incompatible tribological character between the two contacting surfaces. It was evident that the PS400 was worn out in a non-uniform way that produced "islands" of accumulated material, probably due to the fact that Nedox is much harder than PS400 (8.5 vs. 2 GPa), and this difference resulted in high COF. Although the thermal stability of the PS400 and Nedox coatings is similar and around 600°C, the hardness difference is more pronounced.

The chemical analysis on $TiMoS_2$ was derived from three different areas, as indicated in **Figure 4.5(d)**. In area 1 the coating remained on the surface, as evident by the small amount of Ni (main element of INC 718 substrate), and the detection of Ti and Mo. Note that the characteristic X-ray signals of Mo and S overlap, therefore only Mo is shown in **Table 4.3**. In area 2, the substrate was reached, and the detection of Ni was significantly higher compared to area 1, and accordingly the amount of Ti, and Mo are lower. Regarding area 3, the EDS spectrum was acquired from oxide particles that were formed on top of the INC 718 substrate, due to chemisorption of oxygen atoms from the surrounding CO_2 environment. Since the most dominant elements were O and Ni, the oxide particles can be identified as a type of nickel oxide (Ni_xO_y). Under certain conditions, for example at prolonged sliding and a plethora of oxide particles will result in the formation of oxide layers by accumulation and compaction with excellent lubricating characteristics [15]. Hence, the adequate lubrication of the PS400 vs. $TiMoS_2$ tribo-pair can be partially ascribed to the beneficial formation of lubricating Ni-oxide particles on the substrate. In addition, $TiMoS_2$ coating (the MoS_2 phase in particular), contributed to lubricating the interface, therefore the observed low COF and wear. Also, a minute amount of Ag and F solid lubricants was detected that can further contribute to lubrication of the interface. The majority of C found on the DLC coating confirmed the integrity of the coating after the end of the experiment, and the graphitized DLC (presented thereafter) provided adequate lubrication. Some of the main elements of the INC 718 substrate were also detected, due to the beam penetrating through the coating.

4.3.4. Raman Spectroscopy

Raman spectroscopy was employed to identify the oxides formed on top of the INC 718 substrate after removal of the $TiMoS_2$ coating, and to qualify the amount of graphitization of DLC coating following HPHT tribological testing against PS400, as shown in **Figure 4.6**. The Raman spectrum of the worn area of $TiMoS_2$ captured both the intact coating and the areas where the coating was removed, and oxide particles were formed on the INC 718 substrate (see **Figure 4.5(d)**). The two Raman bands centered at 373 and 400 cm^{-1} were identified to belong to MoS_2 [83]. The Raman bands at 450 and 488 cm^{-1} correspond to Ni-O vibrations, for example NiO and Ni_2O_3 [84,85], as confirmed by the EDS analysis of area 3 (**Table 4.3**). The combination of MoS_2 and Ni-O lubricating phases at the interface controlled the friction and wear at low values.

The Raman spectrum on a fresh (as-received) DLC coating served as the reference point and direct comparisons were made with the worn area following HPHT testing, as shown in **Figure 4.6(b)**. The as-received DLC revealed a broad spectrum, with the typical G band of commercial diamond-like coatings with the majority of sp^3 bonds, and a low $I_D/I_G = 0.65$ (measured by height-based approach). Obvious peak splitting appeared only after exposing the coating at 464℃, with the presence of G band which is referred as the disorder or defect band. The intensity ratio increased to 0.83 due to the initiation of the breathing mode of sp^2 carbon atoms during functionalization/graphitization of the DLC coating. Also, comparing the intensities of the exposed DLC at 500°C under air (**Chapter 2**) and CO_2 (**Chapter 3**) environments at AP with the intensity ratio at 464°C HP CO_2 environment, at HPHT CO_2 environment the DLC coating experienced a lesser degree of

structural disorders, and the intensity ratio was lower and at 0.85, compared to 1.01 and 1.15 under AP air and CO_2, respectively. Therefore, the HP CO_2 could have an effect on the structural integrity of DLC coatings after exposure.

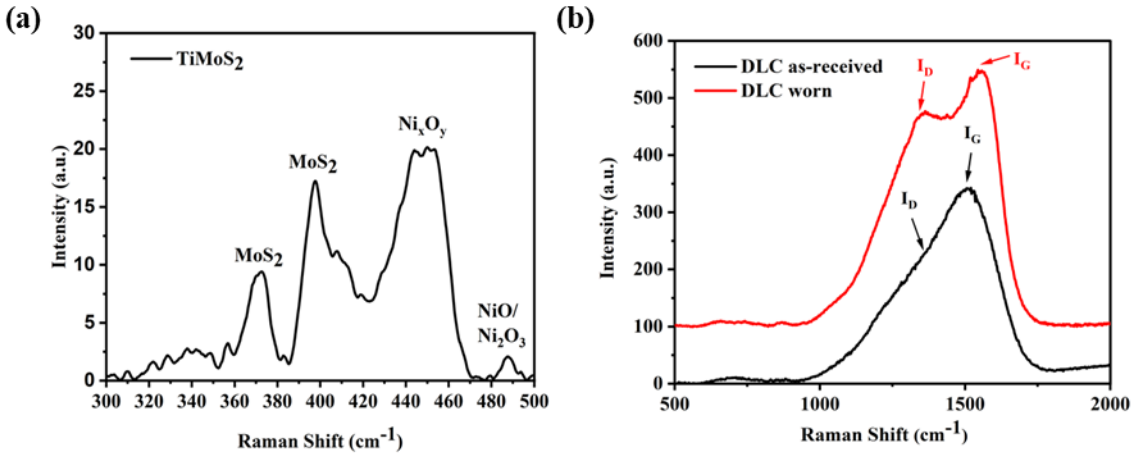

Figure 4.6 Raman spectra of (a) worn $TiMoS_2$ disk/INC 718 substrate, and (b) as-received and worn DLC, after tribo-experiments**.** Reprinted with permission from [11].

4.3.5. Summary

Five different tribo-pairs were tested under Venusian-simulated environment and characterized via different analytical techniques to investigate the wear mechanisms and to explain their tribological performance, as summarized in **Figure 4.7**. The uncoated INC 718 vs. INC718 tribo-pair was used as the baseline to gauge the contribution of each coating (PS400, Nedox, $TiMoS_2$, and DLC) on reducing friction and wear, and the following conclusions can be drawn:

- Modifying one of the contacting surfaces of INC 718 with PS400 coating (metal-on-coating) decreased the COF by 25%, due to the activation of PS400 solid

lubricants (CaF_2, Ag) that transferred onto the INC 718 counter-surface and lubricated the interface.

- DLC and $TiMoS_2$ coupled with PS400 (coating-on-coating) further decreased the COF up to 43%, compared to INC 718 metal-on-metal contact.
- PS400 vs. Nedox generated the highest COF (0.66), due to tribological "incompatibility" (due to significant hardness differential) at HT between the two contacting surfaces.
- The graphitization of DLC, and the partial removal of $TiMoS_2$ accompanied by the formation of Ni surface oxides on INC 718 substrate contributed in maintaining low COF.
- The observed total wear rates of coating-on-coating tribo-pairs were significantly lower than metal-on-metal or metal-on-coating. In particular, the total wear of PS400 vs. $TiMoS_2$ tribo-pair was ten times lower compared to INC 718 vs. INC 718.
- PS400/$TiMoS_2$ and PS400/DLC are a promising material combination for CO_2 HPHT environments, for example bearing materials on the rovers and sampling drills for future missions to Venus.

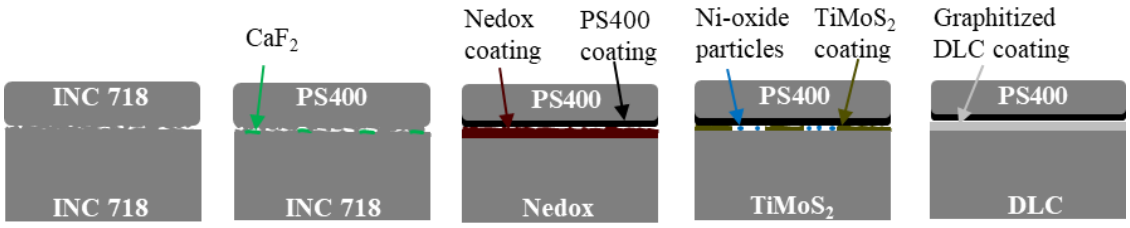

Figure 4.7 Schematic representation of the interfaces. Reprinted with permission from [11].

In this chapter the effect of high Venusian pressure was introduced to the tribological testing to further simulate the environment. In the next chapter the impact of Venusian exposure on the morphology and mechanical properties of selected friction-reducing coatings is explored.

5. CHEMICAL AND MECHANICAL ANALYSES OF HARD COATINGS EXPOSED UNDER THE VENUS ATMOSPHERIC SURFACE CONDITIONS

5.1. Introduction

Despite that Venus is called Earth's twin, due to similar size and distance from sun, its evolutionary path took a completely different trajectory from accretion, resulting in an inhabitable atmosphere with significant technical challenges for exploration [86]. In fact, previous planet Venus landers were able to transmit data for only a few hours, before succumbing to the harsh environment [87]. The surface pressure is 9.55 MPa, and the environment is 96% CO_2, 3.5% N_2, with traces of Ar, H_2S, SO_2, HF, and HCl (with SO_2 being the dominant minor gas) and 464°C mean surface temperature [17].

The survivability of future missions and in-situ investigation of the inhospitable surface of Venus in long-duration operations (of the order of days or weeks) requires knowledge of the impact of the environment on different surfaces, for example electromagnetic devices, structural and bearing materials in the probes and landers [18]. Recently, there was a twist in the future designs for surface exploration, with the latest artistic representations pointing towards rovers comprised of entirely mechanical parts [88]. This is due to the susceptibility of electronic and electromagnetic devices under HP and HT environments [89], and the minimization of their usage will decrease the complexity in the designs significantly. Several structural materials, for example pure metals, steels, and ceramics were exposed to Venusian-simulated environment in the GEER chamber [12,90–92] and their morphological changes were investigated. GEER is

located at NASA Glenn Research Center and the composition of the Venusian surface is simulated inside the chamber, that is 96.5% CO_2, 3.5%N_2, with 30 ppm H_2O, 150 ppm SO_2, 28 ppm CO, 15 ppm OCS, 3 ppm H_2S, 0.5 ppm HCl, and 5 ppb HF [92].

Costa et al. studied the effect of long Venusian exposure on 304 and 316 stainless steel for 42 days, and fast oxidation kinetics resulted in the formation of double-layered scales of iron and iron/chromium oxides. Nickel and molybdenum sulfides were also detected on the surface of 304 and 316 steels, respectively [91]. Lukco et al. investigated various materials used in fabricating sensors, electronics, and packaging after 42-days exposure in the GEER, and they reported high reactivity of sulfur-bearing atmospheric gas constituents (SO_2, H_2S) primarily with the materials composed of transition metals, for example Pt, Cu, and Ni [12]. In a subsequent study, Lukco et al. verified the adversity of the reactions between pure transition metals with the sulfur constituents in the Venusian atmosphere [90]. In the NASA report, the authors investigated the surfaces of different groups of materials, for example austenitic and carbon steels, nickel-based alloys (i.e., alloy 615), ceramics (i.e., SiC, SiO_2) and commercialized coatings (i.e., 4YSZ, Dursan®) following supercritical fluid pressures and temperatures mimicking the Venus lower atmosphere in the GEER chamber. It was found that steels formed double layers of magnetite and nickel sulfide oxides, nickel-based alloys formed nickel sulfide phases, and iron oxide phases were formed on top of some coatings, while ceramics were unreacted after 10 and 42 days of Venusian exposure [92].

It is therefore understood that the Venusian exposure has a significant effect on the surfaces of the exposed materials via different chemical reactions, for example oxidation

and corrosion. Despite that the effect on pure metals, metallic alloys and ceramics was adequately studied [12,90–92], the same effect on friction-reducing bearing materials, for example different forms of diamonds and NASA-developed HT alloys, is yet to be explored. The investigation of the Venusian exposure on frictional interfaces, for example shafts/bearing, and levers/gears systems is vital for designing future rovers, landers, probes, and drilling components. In **Chapter 3** and **4** different interfaces were tested under Venusian surface temperature in low and high CO_2 pressures and it was found that PS400, a NASA-developed HT alloy coating, generates adequate lubrication when is paired with DLC, PCD, and $TiMoS_2$ coatings.

In this chapter, morphological, chemical, and mechanical analyses on the above-mentioned friction-reducing coatings following 3-days Venusian exposure at NASA Goddard Space Flight Center were performed. Atmosphere-surface interactions were investigated and a starting point in designing mechanical and tribological components for future Venus exploration was established. Note that the pressurized chamber at NASA Goddard Space Flight Center does not fully replicate the composition of the lower atmosphere of Venus, as the GEER, and only the three more abundant gases (CO_2, N_2, SO_2) are considered instead. While each minor constituent can induce adverse atmosphere/surface interactions, it was demonstrated that sulfur constituents (i.e., SO_2), in particular, play the most significant role on altering the chemistry of the exposed surfaces by corrosion and the formation of sulfuric acids [90,91].

5.2. Experimental

5.2.1. Materials and sample preparation

DLC, PS400, PCD, and $TiMoS_2$ coatings were deposited onto INC 718 substrates (purchased from Onlinemetals.com). INC 718 is a HT nickel-based alloy and a good host of the above coatings when exposed to extreme environments. The a:C-H DLC coating was deposited by CVD with a thickness of 2 μm (**Table 5.1**), and hydrogen content of ca. 20-40 at% at Oerlicon Balzers. A thin chromium layer was used to enhance the adhesion between the coating and the substrate. PS400 was applied by PS at ADMA Products Inc. with a final thickness of ca. 200 μm after grinding using a carbide wheel for optimum morphology. The composition of PS400 and the role of each phase in enhancing the performance can be found in previous chapters. PCD was prepared by sintering small diamond particles at high pressure and temperature in the presence of a liquid cobalt catalyst at ChampionX. PCD was bonded to a tungsten carbide interlayer and the thickness of PCD was 1 mm, therefore it can be considered as thick coating or "bulk" material. $TiMoS_2$ was coated onto the substrate at IBC coatings technologies by simultaneous magnetron sputtering PVD process of Ti and MoS_2 until the thickness of the coating reached 2 μm. The resulting coating was doped with Ti at ca. 10 at% which enhanced the hardness and thermal stability of the composite. A thin pure Ti interlayer was first sputtered to enhance the adhesion between the substrate and the coating.

5.2.2. Aging protocol

Coupons of DLC, PS400, PCD, and $TiMoS_2$ coatings were subjected to Venusian aging at NASA Goddard Space Flight Center. The samples were fixed onto ceramic bars

separated by spacers, therefore the exposure of the surfaces was uniform, as shown in **Figure 5.1(a)**. The pressurized test chamber (**Figure 5.1(b)**) maintained a temperature of 464°C and a pressure of 9.55 MPa with a mixture of CO_2, N_2 and SO_2 gasses, as shown in **Figure 5.1(c)**. CO_2 was the major component inside the aging chamber with 96.5%, and N_2 at 3.5%. SO_2, which is the third most abundant gas below the clouds of Venus was injected in the chamber maintaining ca. 155 ppm. The aging duration was 72 hours, which would be adequate to simulate the exposure of tribological systems on the landers/probes during idle times before or during Venusian exploration.

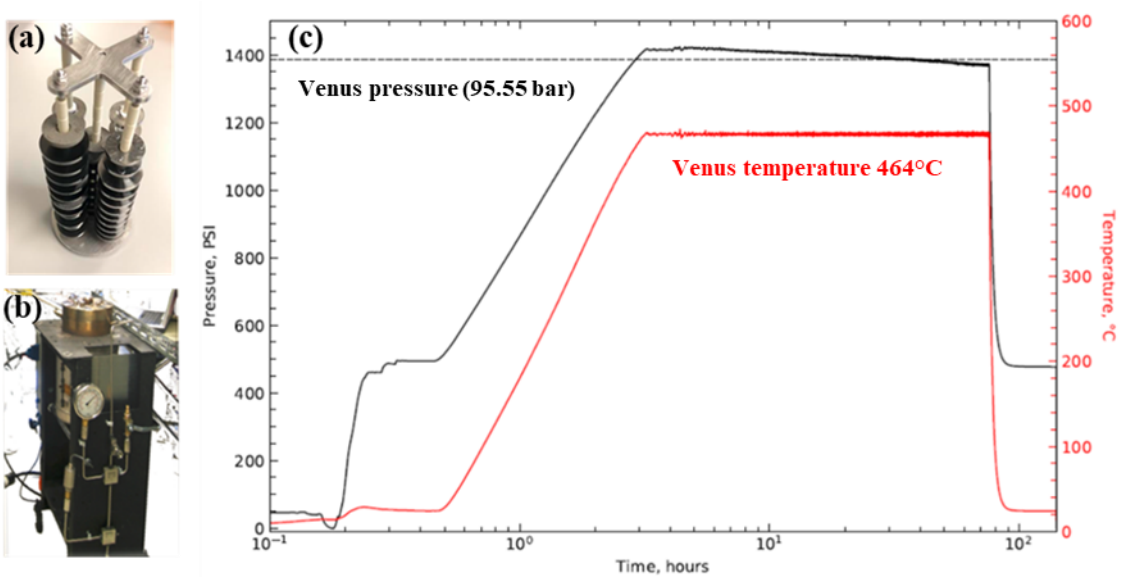

Figure 5.1 Setup for simulated Venusian surface aging, (a) coupons and fixture assembly for aging, (b) Venus pressure test chamber located at NASA Goddard Space Flight Center, and (c) aging protocol.

5.2.3. Characterization

A JEOL JSM-7500F SEM was employed to explore the surface of the as-received and aged specimens. Cross-section SEM and EDS analyses of the aged samples were performed to examine the near surface morphology and elemental composition.

The Omicron XPS system is equipped with an Argus detector, an excitation source of Mg Ka 1253.6 eV and the tests were performed in the X-ray power range of 180-250 W. The right angle for acquisition of the spectra was controlled by a computer-controlled stage. The surfaces of the aged samples were bombarded via an NGI3000 Argon ion sputter gun, and superficial layers of around 3 nm were removed, along with any contaminants that adhered on the surface during cleaning. CaseXPS software was used for deconvolution of the spectra, and the standard deviations for all the samples was kept less than ca. 1%.

A Bruker TI Premier® nanomechanical instrument was used for measuring the nanomechanical properties of the as-received and aged samples. The nanoindenter is equipped with standard and high load transducers. The standard transducer has a load limit up to 10 mN, whereas for the high load transducer, the maximum load is 1,000 mN (1 N) and was used for the PCD coating. Berkovich indenters were used to determine the hardness (H) and reduced modulus (E_r) of all samples. The nanoindentations were performed at room temperature following the loading/unloading curve of **Figure 5.2**. The hold time was introduced to reduce creep effects of the coatings, if any.

Note that several indents at different locations with varying loads were performed on each sample to assure homogeneity and therefore consistency of the calculated nanomechanical properties.

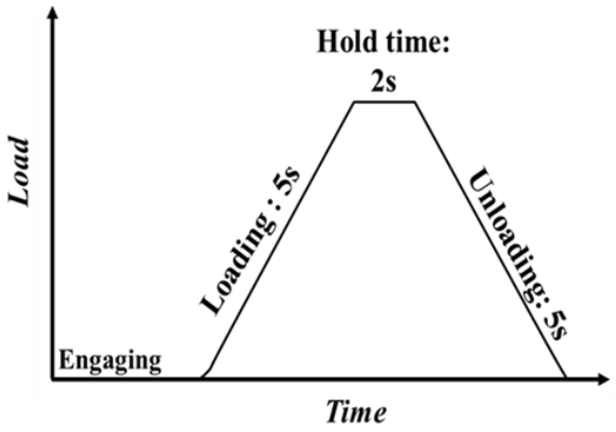

Figure 5.2 Nanoindentation loading/unloading curve versus time.

The Oliver-Pharr method was used to calculate H and E_r of the samples [93]. According to the method the contact depth (h_c) of nanoindentation can be calculated from Eq. (1),

$$h_c = h_{max} - \varepsilon \frac{P_{max}}{S} \quad (1)$$

where P_{max}, h_{max}, and S represent the maximum load, maximum displacement, and initial slope of the unloading section of the load-displacement curve, respectively. For Berkovich indenters, $\varepsilon = 0.72$. Using a predetermined areal calibration on a standard fused quartz, the contact area (A_c) was calculated from the contact depth (h_c). After that, H and E_r were determined using Eqs. (2) and (3), respectively,

$$H = \frac{P_{max}}{A_c} \quad (2)$$

$$E_r = \frac{\sqrt{\pi}\, S}{2\sqrt{A_c}} \quad (3)$$

Microhardness measurements were carried out using a Vickers microhardness tester (Wilson TUKON 1102) to measure the surface hardness of PS400, and to complement the results obtain from the nanoindentations on DLC and $TiMoS_2$.

5.3. Results and discussion

5.3.1. Surface SEM/EDS

Figure 5.3 depicts SEM images of the surface of the samples before aging (as-received). DLC appeared with parallel ridges of material formed from the deposition process. These higher points did not increase the surface roughness significantly, and the coating was fairly smooth, with root mean square (*Sq*) roughness of 0.38 μm, as shown in **Table 5.1**. Also, the maximum peak-to-valley distance (*Sz*) was 5.12 μm, capturing the height of the ridges. Different decolorizations can be seen in **Figure 5.3(b)**, corresponding to different phases of PS400 that are exposed on the surface, with Ni-Mo-Al being the dominant phase (shown with darker color). The localized concentration of different phases on the surface of PS400, its coarse microstructure, and residual porosity yield high surface roughness with *Sq* of 1.55 μm and *Sz* at 35.9 μm [6]. PCD appeared with two distinct surface morphologies induced from the sintering process (see black and white areas in **Figure 5.3(c)**), while the as-received $TiMoS_2$ had a smooth and uniform surface (**Figure 5.3(d)**) with a small degree of particles agglomeration, and the *Sq* values were 0.12 and

0.19 μm, respectively. The *Sz* values were also small depicting the smooth surface of PCD and $TiMoS_2$.

Table 5.1 Roughness parameters of as-received and aged samples using confocal microscopy (800 × 800 μm^2 image size). Thickness as provided by the vendor.

Parameters	**Sq (μm)**		**Sz (μm)**		**Thickness (μm)**
Condition	***As-received***	***Aged***	***As-received***	***Aged***	***As-received***
DLC	0.38 ± 0.0008	0.49 ± 0.06	5.12 ± 0.39	6.28 ± 1.17	2
PS400	1.55 ± 0.18	2.40 ± 0.48	35.9 ± 1.65	28.99 ± 0.66	200
PCD	0.12 ± 0.008	0.47 ± 0.07	2.38 ± 0.09	3.36 ± 0.37	1000
$TiMoS_2$	0.19 ± 0.01	0.20 ± 0.01	4.04 ± 1	4.07 ± 0.1	2

Figure 5.4 shows low and high magnification (inset) SEM images of the four samples after subjecting to Venusian aging according to the protocol in **Figure 5.1(c)**. The surface of DLC was characterized with the same parallel ridges seen on the surface of the as-received coating (**Figure 5.4(a)**), demonstrating that no morphological changes occurred after exposure. *Sq* and *Sz* were slightly increased to 0.49, and 6.28 μm, respectively. Exposing PS400 under supercritical pressures resulted in the full coverage of the coating with superficial particles of irregular shape and sharp edges, ranging from ca. 2 to 4 μm in size. Evidently, during the aging process atmosphere-surface interactions happened and chemically or physically adsorbed layers were formed on the surface which increased the *Sq* by 55% and decreased *Sz* by 29%.

Similarly, the surface of PCD was partially covered by nodular-like particles, forming islands of accumulated reactants following the aging process. These particles were smaller in size, compared to the particles observed on PS400, with diameters of less than 1 μm, and the measured *Sq* and *Sz* was 0.47 and 3.36 μm, respectively. Such a large increase in *Sq* was attributed to the formation of these islands composed of particles forming a rougher surface. Similar to DLC, $TiMoS_2$ appeared fresh and unreacted in the Venusian atmosphere, with marginal increases in *Sq* and *Sz*.

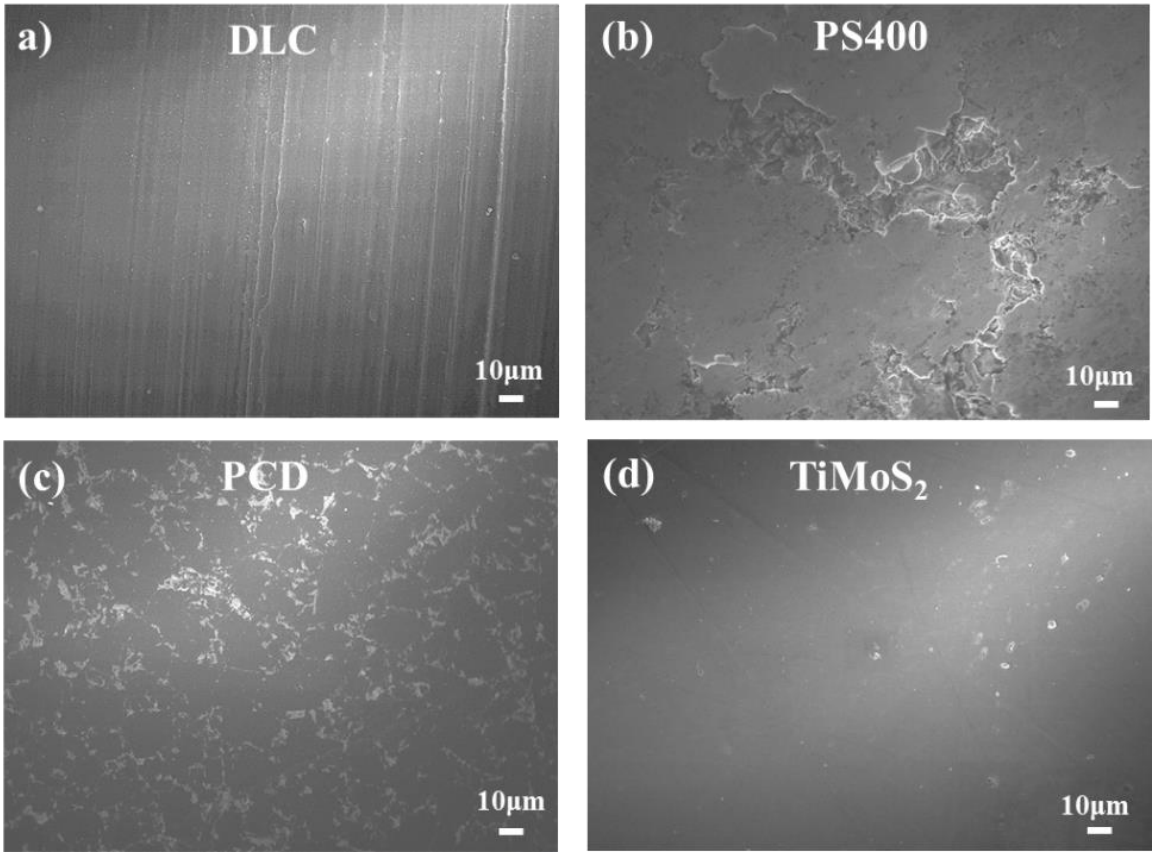

Figure 5.3 Surface SEM images of as received (a) DLC, (b) PS400, (c) PCD, and (d) $TiMoS_2$ coatings.

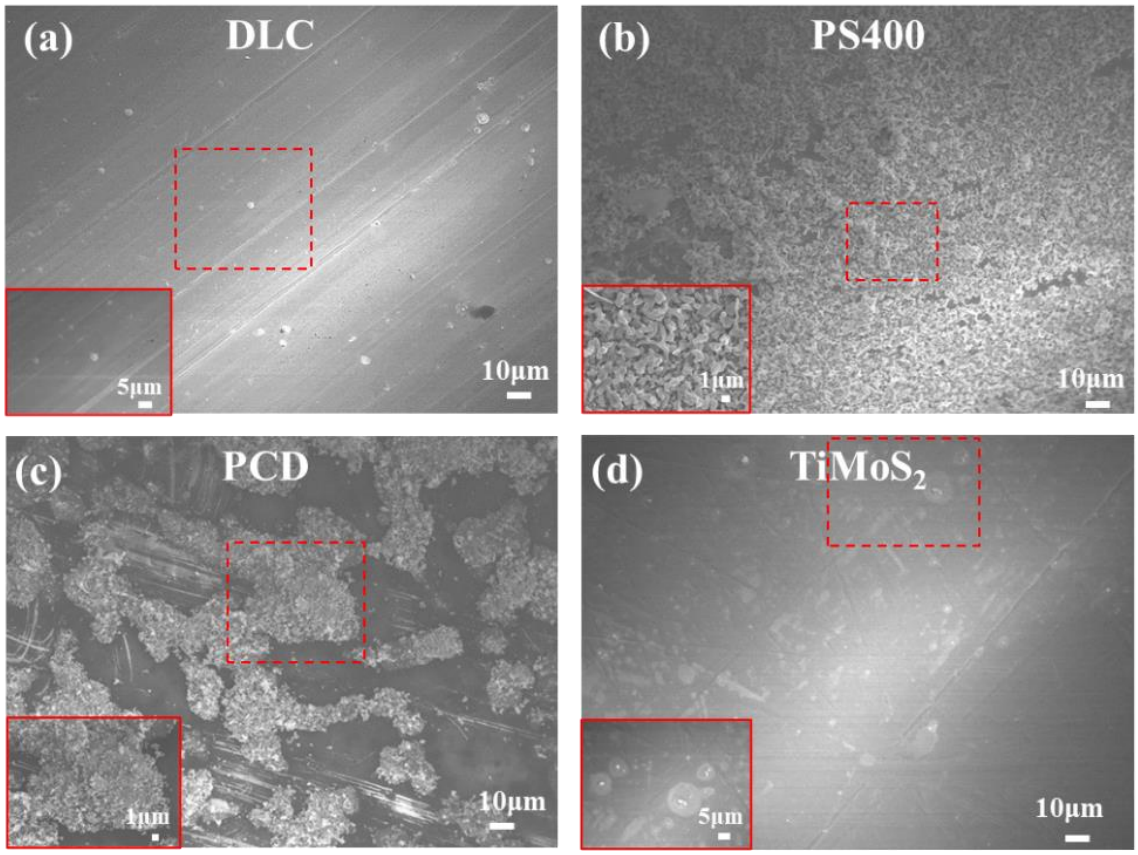

Figure 5.4 Surface SEM images after simulated Venusian aging of (a) DLC, (b) PS400, (c) PCD, and (d) $TiMoS_2$ coatings.

To further analyze the exposed surface of the samples, EDS mapping was carried out and information on the abundance of different elements on the surface was obtained, as shown in **Figure 5.5(a-d)**. Note that during EDS, information of the INC 718 substrate was also acquired but omitted from the analysis, for simplicity. As illustrated in **Figure 5.5(a)**, C was detected throughout the surface, corresponding to the sp^2 and sp^3 hybridized carbon bonds of DLC. A considerable amount of Cr is also detected, corresponding to the pure Cr interlayer between the DLC coating and the substrate. The concentration of O was insufficient to be detected from the EDS analysis. **Figure 5.5(b)** shows the EDS results

on the surface of PS400. As seen in the SEM image of **Figure 5.4(b)**, the surface of PS400 was covered by particles of irregular geometries. These adsorbed particles were rich in sulfur and were densely spread onto the surface. Their irregular shape promoted internal voids and therefore the newly formed layer showed a degree of porosity and the PS400 was exposed. Ni appears throughout on the EDS mapping image, demonstrating that the superficial S-rich film was thin, and easily penetrable by the EDS electron beam. Chromium was also detected with a marginal concentration. Note that the concentration of SO_2 inside the aging chamber was 155 ppm, yet adequate for energetic sulfur atoms to react with the exposed surface and form dense S-rich layers. O was also localized at the same areas of S with a small concentration, demonstrating that different types of sulfur oxides were formed. The porous structure of PS400 promoted the diffusion of sulfur and oxygen atoms found at the surrounding Venus atmosphere leading to oxidation, manifested as the formation of different types of sulfur oxides [92].

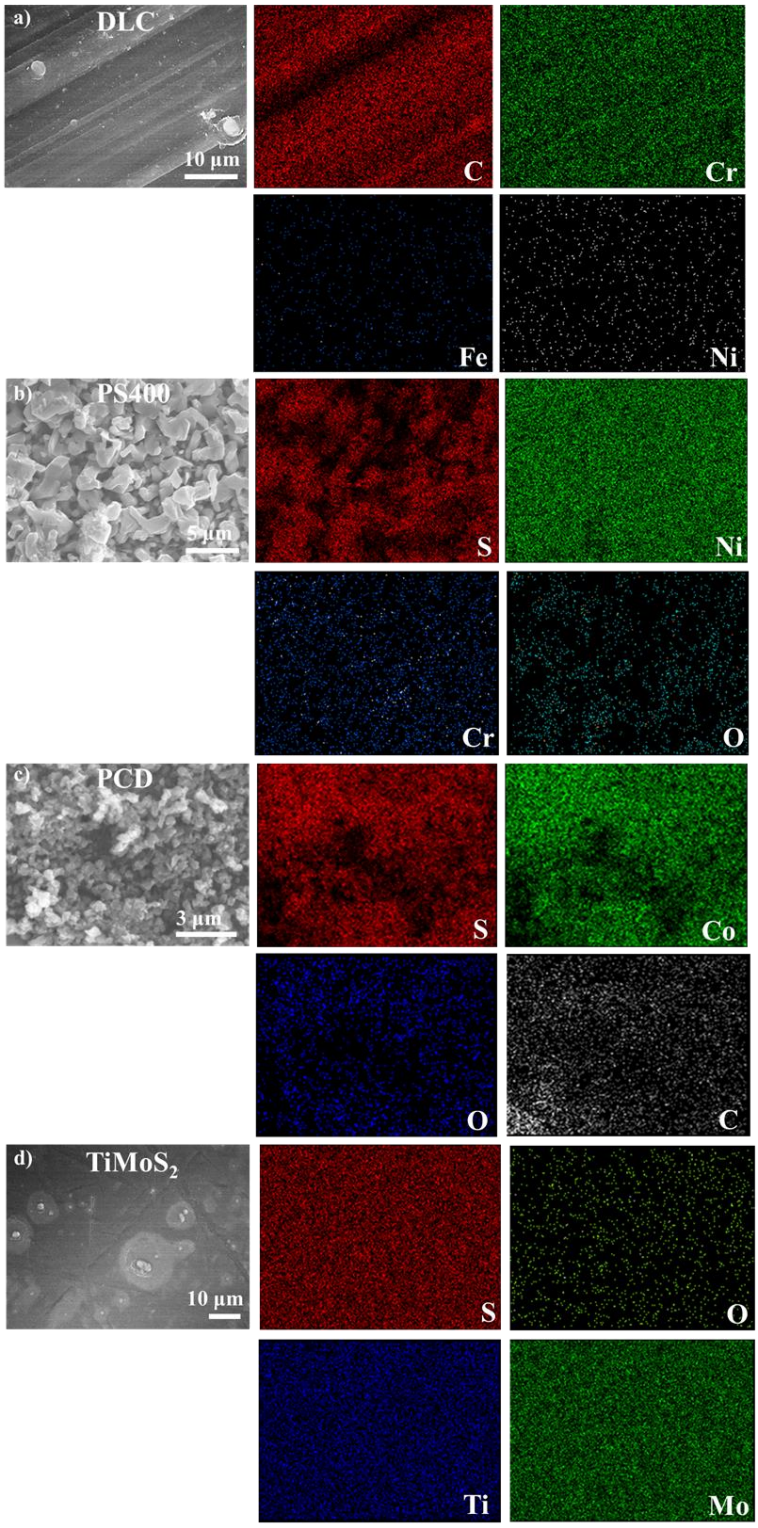

Figure 5.5 Surface EDS mapping of (a) DLC, (b) PS400, (c) PCD, and (d) $TiMoS_2$.

Figure 5.5(c) shows the corresponding EDS mapping of PCD. As seen from the SEM images of **Figure 5.4(c)**, PCD was partially covered by densely packed particles forming "islands" of adsorbed atoms following the aging process. EDS mapping was taken such both black and gray areas were covered and it was found that the black areas represented the PCD coating and the gray areas the accumulated particles formed during the aging process. Another EDS mapping of the accumulated particles was taken to acquire more information on the elemental analysis of the newly formed film, as shown in **Figure 5.5(c)**. S appeared as one of the main elements found on the surface, indicating that similar chemical interactions between the exposed surface and the surrounding environment took place, as in the case of PS400. Again, the S-rich layer was easily penetrable and the main elements of PCD were detected, namely C and Co. The presence of Co is attributed to the metal catalyst used during the sintering process. Traces of O were also found at the same areas where S was located, hence SO_x functional groups were formed on the surface, similar to PS400. The newly formed film was further chemically analyzed via XPS, and the results are presented in **Figure 5.7**. **Figure 5.5(d)** shows the EDS mapping of $TiMoS_2$. Similar observations as for PS400 and PCD, where S-rich adsorbed films were captured cannot be extrapolated for $TiMoS_2$, since S is intrinsically distributed throughout the surface. However, from the SEM images of **Figure 5.4(d)** no such film was observed, thus the detection of S corresponds to the as-received coating. Minute traces of O were also captured from the EDS analysis.

5.3.2. Cross-section SEM/EDS

As seen in **Section 5.3.1**, superficial adsorbed layers were formed onto the surface of PS400 and PCD. In this section, cross-section EDS was carried out to investigate the thickness of these layers and the abundance of the elements in the surface/subsurface area. For DLC (**Figure 5.6(a)**), C distributed everywhere along the top surface with a thickness of ca. 2 μm. Cr is detected below the coating, representing the interlayer used during the deposition process. A significant amount of O was also found below the DLC coating, depicting that O atoms were diffused through the DLC coating and reacted with Cr subsurface, while the top coating remained unreacted, as also seen with the surface EDS analysis in **Figure 5.5(a)**. In a previous study by the authors, it was reported that significant oxidation of DLC after short-time exposure only happened under air environment (and at 500°C), and not under CO_2 [51]. The elements found below the interlayer (Ni and Cr) correspond to the INC 718 substrate.

Figure 5.6(b) illustrates the splat-type morphology forming different phases of PS400 (thickness ca. 200 μm), in accord with Ref. [35]. PS400 is composed of a Ni-Mo-Al matrix, supported by Cr_2O_3 hardening phase, and Ag, BaF_2 and CaF_2 lubricating phases. In fact, all the main elements were scattered throughout the cross-sectional area. Most of the area is covered by nickel, with Cr_2O_3 phases “filling” the gaps and serving as the second most dominant phase of PS400 coating. The fluorides and silver phases were also detected. Most importantly, S did not only appear on the top surface of the coating forming a dense film of 2-5 μm in thickness, but it also diffused through the thickness due

to the high porosity of PS400 coating. O is also captured at the topmost surface (forming SO_x groups) and through the thickness because of intrinsic Cr_2O_3.

Figure 5.6(c) presents the EDS mapping of PCD, which had a thickness of 1 mm. C was the main element of the cross-sectional surface of PCD and appeared throughout. O was the second most abundant element which was also found through the thickness, revealing a degree of internal oxidization. S was also detected with a marginal concentration through the thickness, however, the accumulated S-rich islands seen in **Figure 5.4(c)** were not captured, possibly due to the unintentional removal of them during cutting for cross-section analysis. Specifically, electrical discharge machining was used to cut a cross-section of PCD, as opposed to dry cutting with diamond blade, which was used for the rest of the samples. As postulated earlier, the thickness of the S-rich islands observed in **Figure 5.4(c)** was smaller than the S-rich layer formed on PS400, as they were comprised of fine particles, in contrast to the larger particles seen in **Figure 5.4(b)** for PS400. **Figure 5.6(d)** shows the EDS mapping of $TiMoS_2$. The surface SEM/EDS on the coating demonstrated that no morphological and compositional alterations took place during the aging process and the coating appeared the same with as-received. The cross-section EDS confirmed the above-mentioned observations, with Ti, Mo, and S found on top of the INC 718 substrate with a thickness of 2 μm. O also appeared in the EDS mapping, with a slightly higher concentration towards the $TiMoS_2$ coating.

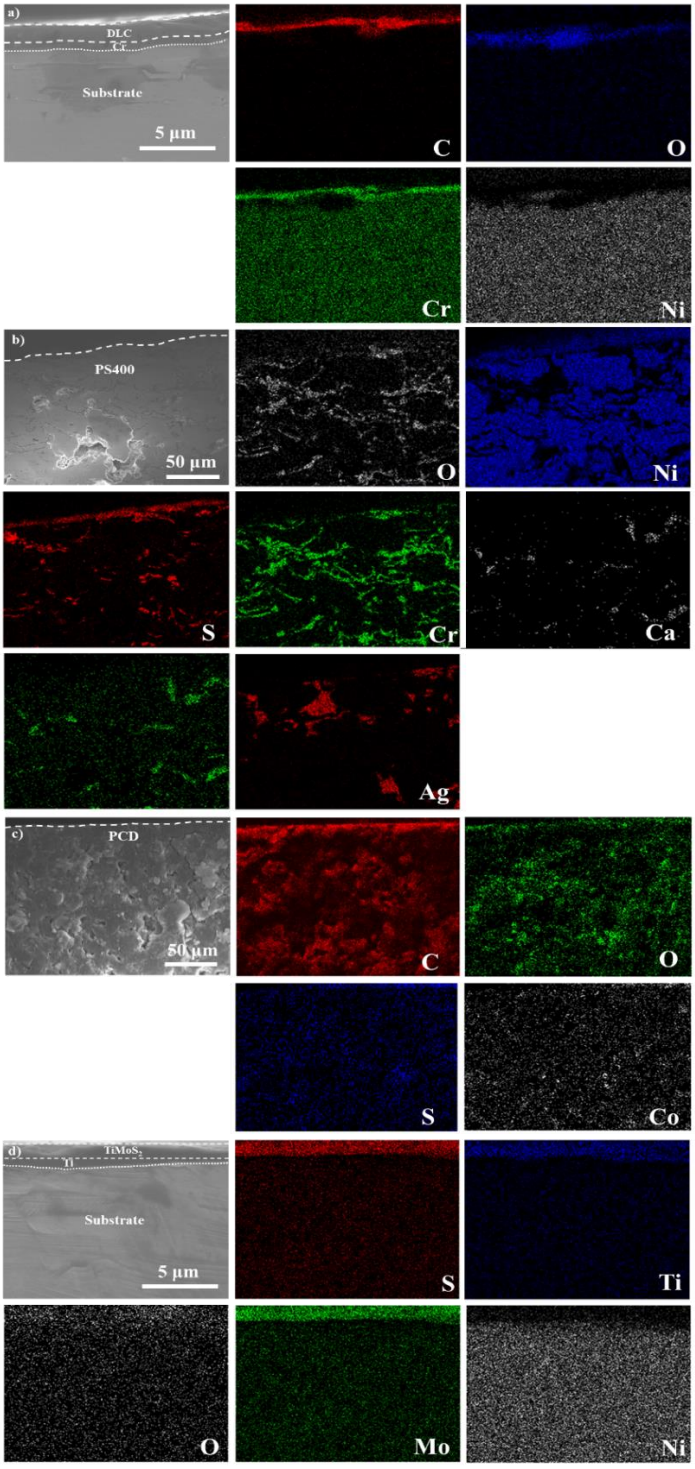

Figure 5.6 Cross-section EDS mapping of (a) DLC, (b) PS400, (c) PCD, and (d) $TiMoS_2$.

5.3.3. XPS analysis

Figure 5.7(a, b) show high resolution S2p spectra of PCD and PS400, respectively, which are the two coatings that experienced significant morphological and chemical changes following Venusian aging. The S2p spectra in both samples were fit deconvoluted into four peaks at 162, 164, 166, and 167 eV. The two intense peaks at lower binding energies represent S-S bonding, and the two weak peaks at higher binding energies represent sulfur oxide functional groups, presumably SO_4. The XPS spectra and the presence of S-S high peaks confirmed the formation of S-rich layers on top of PCD and PS400 coatings with a small degree of sulfur oxidization. Also, in both PCD and PS400 S did not react with the underlayers, therefore the S-rich particles were physically adsorbed on the surface.

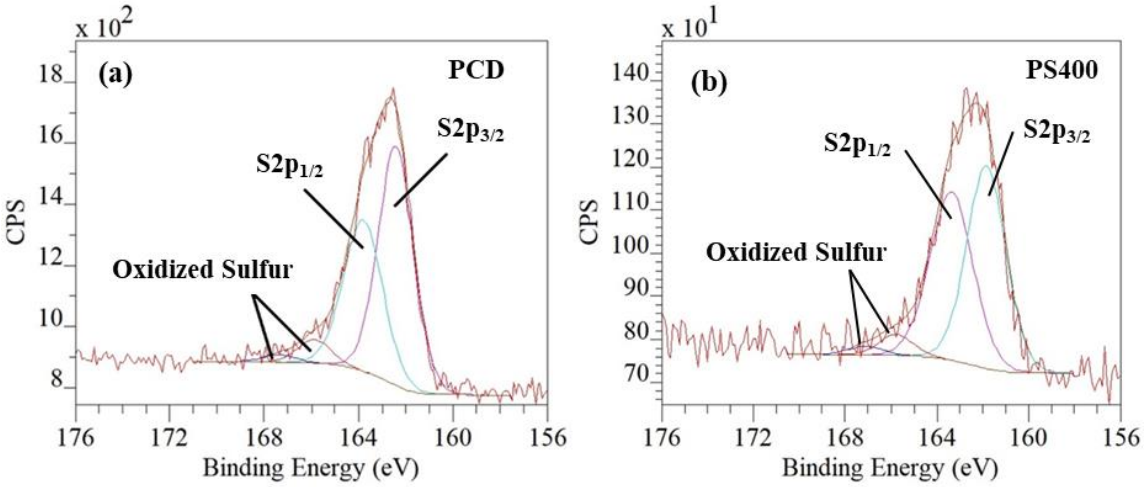

Figure 5.7 High resolution S2p XPS spectra of (a) PCD, and (b) PS400**.**

5.3.4. Micro and nanomechanical analysis

The same samples were subjected to nano and micro indentation measurements for mechanical evaluation before and after aging. It was previously found that PS400 and PCD experienced the most prominent morphological changes following Venusian-simulated aging, manifested as S-rich layers formed on the surface of the samples. It is widely understood that the chemical and mechanical properties of structural and frictional systems are dictated by their topmost surface, therefore such knowledge is very important. The newly formed layer on PS400 was 2-5 μm thick (see **Figure 5.6(b)**), and for PCD the thickness of the S-rich islands was ca. 1 μm, as measured by 3D profilometry (see *Sz* in **Table 5.1**). Therefore, to accurately measure the mechanical properties of such films the nanoindentation method was employed. Also, DLC and $TiMoS_2$ coatings were 2 μm thick, hence an accurate measurement of the mechanical properties of these coatings before and after Venusian exposure requires very shallow indentations to avoid substrate effects [94]. Vickers indentation was used to measure the hardness of as-received and aged PS400, as nanoindentation was not an effective method due to its multi-phase morphology, and localized indents would result in measuring the properties of the individual phases.

Figure 5.8 shows characteristic load-displacement curves of as-received and aged samples, therefore the effect of Venusian aging on the nanomechanical response and subsequently the mechanical properties were evaluated. Identical indentations on DLC yielded an increase in the h_{max} of around 50% compared to the corresponding aged coating (**Figure 5.8(a)**). At the same P_{max}, h_f was also increased from 20 to 35 nm, indicating a higher degree of plastic deformation. As discussed previously a dense S-rich film was

formed on PS400 and an attempt was made to measure the E_r and H via nanoindentation. However, as seen in **Figure 5.8(b)** the resulting load-displacement curve of the aged PS400 was of irregular shape and the Oliver and Pharr method was not suitable [93], due to surface/roughness effects and irregularities (i.e., defects) of the adsorbed S-rich film. Nevertheless, the corresponding penetration depths of the aged PS400 were significantly higher than those of the as-received sample, thus E_r and H were expected to reduce significantly. **Figure 5.8(c)** shows load-displacement curves of PCD, before and after aging. Note that the indents were performed on the PCD and not on the S-rich layer as an attempt to indent onto the S-rich particles resulted in erratic behaviors similar to PS400, and the measurement of E_r and H was infeasible. Interestingly, the h_{max} of the aged PCD was slightly lower than the corresponding as-received sample. Also, note that both indents were almost purely elastic, due to the extreme hardness of PCD, which is comparable with the hardness of the diamond Berkovich tip used for nanoindentation. Therefore, the extracted E_r and H value shown in **Figure 5.9** should be treated with care, and quantitative evaluations should be omitted. Herein, the indents on PCD were intended to capture any significant degradation of the nanomechanical response after Venusian aging. The h_f of aged $TiMoS_2$ increased from 125 to 150 nm, and h_{max} increased from 150 to 190 nm, revealing a degree of mechanical degradation after Venusian exposure (**Figure 5.8(d)**).

Figure 5.9 summarizes the average E_r and H values of $TiMoS_2$, DLC, PS400, and PCD calculated from multiple nanoindents before and after Venusian aging. For PS400 the average H value is only shown, and it was measured via Vickers indentation. DLC, which is generally understood that is not a very HT material, and its mechanical properties

are experiencing significant degradation due to structural transitions (i.e., graphitic contributions) starting at temperatures above 300℃ and intensifying at 500℃ [7,11]. Herein, the 72-hour exposure at 464℃ induced a significant reduction in E_r and H at 38 and 95%, respectively. Regarding PS400, the measured average Vickers hardness of the as-received PS400 was 2 GPa, in agreement with [47] and decreased to 1.6 GPa after exposure. Note that Vickers indentation is a suitable method for capturing the overall "combined" hardness of multi-phase materials.

Interestingly, E_r and H of PCD increased after the aging process, revealing high resistance to the Venusian environment. $TiMoS_2$ experienced some degree of degradation in E_r and H, manifested as 15 and 26% reduction, respectively. $TiMoS_2$ has a thermal stability up to 500℃, as given by the vendor. Therefore, it is plausible that by exposing the material under 464℃ (and 95.5 bar CO_2) for 72 hours resulted in degrading the mechanical properties of $TiMoS_2$ by lowering E_r and H. Also, Sun et al. reported a rapid jump on the wear of $TiMoS_2$ when the testing temperature was above 400℃, due to softening of the material [79].

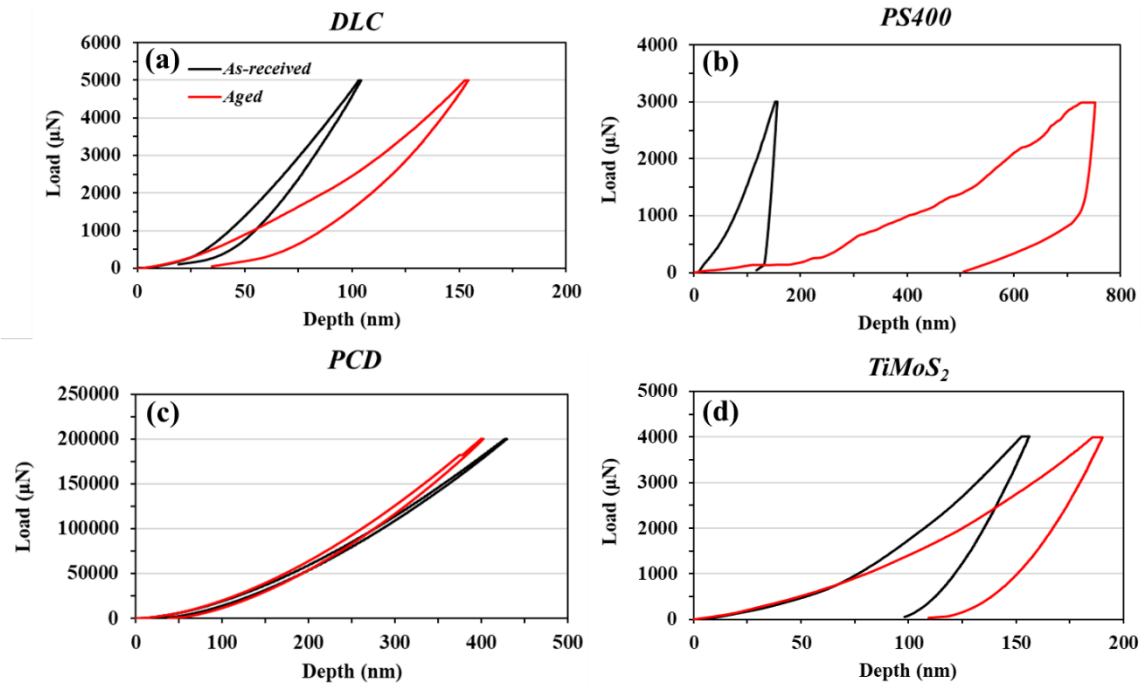

Figure 5.8 Representative load-displacement nanoindentation curves of as-received vs. aged samples (a) DLC, (b) PS400, (c) PCD and (d) $TiMoS_2$.

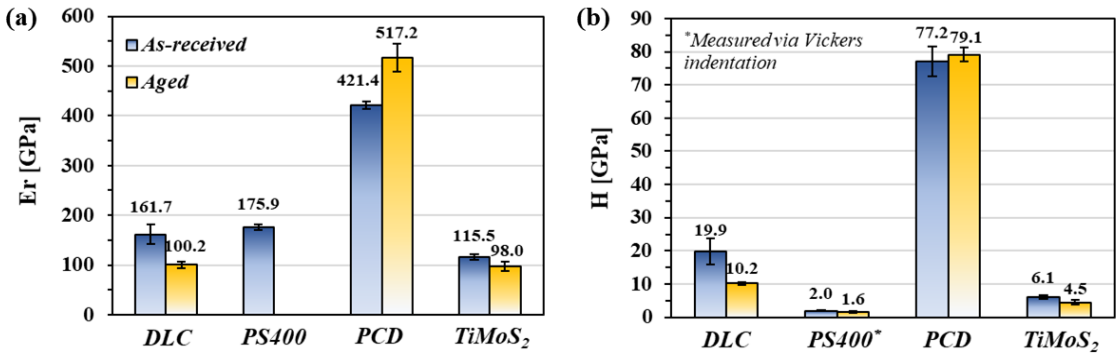

Figure 5.9 (a) Average E_r and (b) H of as-received and aged DLC, PS400, PCD and $TiMoS_2$. Error bars represent ± one standard deviation of multiple indents.

5.4. Summary

This chapter investigated the effect of 72-hour Venusian simulated exposure on the morphological, chemical, and mechanical properties of the surface of four friction-reducing coatings due to atmosphere-surface interactions. It was found that Venusian aging can have a significant effect on Ni-based alloys and diamond-like materials (DLC and PCD), and the following conclusions can be drawn:

- PS400 and PCD experienced a higher degree of morphological changes after Venusian aging with the adsorption of superficial layers of few microns in thickness, while DLC and $TiMoS_2$ exhibited chemical inertness. These layers were identified as S-rich with predominantly S-S bonds and a marginal presence of SO_4.
- The mechanical properties of DLC deteriorated the most after exposure to Venusian aging, whereas PCD demonstrated extreme structural resistance. The E_r and H values of $TiMoS_2$ decreased by 15 and 26%, respectively, and the corresponding H value of aged PS400 decreased by 20% after Venusian exposure.
- DLC, PCD, PS400, and $TiMoS_2$ could be candidate materials to coat structural and bearing systems for future missions to Venus.

In this chapter it was demonstrated that the Venusian environment can have an advert effect on the exposed surfaces by different chemical interactions. The mechanical properties can also be deteriorated, therefore the study of the tribological behavior of exposed specimens simulating idle times (before or between operation) after landing is paramount in designing and developing tribological surfaces for future missions to Venus.

Chapter 6 discusses the effect of Venusian aging on the tribological performance of these friction-reducing coatings.

6. EFFECT OF VENUSIAN AGING ON THE TRIBOLOGICAL PERFORMANCE OF FRICTION-REDUCING COATINGS

6.1. Introduction

As reported in the previous chapters, the adversity of the Venusian atmosphere can alter the chemistry, morphology, and mechanical properties of the topmost exposed surfaces. Therefore, information on how these surface changes can affect the performance of the coatings under tribological testing is very important.

6.2. Experimental

6.2.1. Materials and sample preparation

The same materials examined in **Chapter 5**, were subjected to tribological evaluation in this chapter. The sample preparation is reproduced from **Chapter 5,** and it is presented below for convenience. DLC, PS400, PCD, and $TiMoS_2$ coatings were deposited onto INC 718 substrates (purchased from Onlinemetals.com). INC 718 is a HT Ni-based alloy and a good host of the above coatings when exposed to extreme environments. a:C-H DLC coating was deposited by chemical vapor deposition with a thickness of 2 μm, and hydrogen content of 20-40 at% at Oerlicon Balzers. A thin chromium layer was used to enhance the adhesion between the coating and the substrate. PS400 was applied by plasma spraying at ADMA Products Inc. with a final thickness of ca. 200 μm after grinding using a carbide wheel for optimum morphology. The composition of PS400 and the role of each phase in enhancing the performance is described in previous chapters. PCD was prepared by sintering small diamond particles at

high pressure and temperature in the presence of a liquid cobalt catalyst at ChampionX. PCD was bonded to a tungsten carbide interlayer and the thickness of PCD was 1 mm, therefore it can be considered as thick coating or "bulk" material. $TiMoS_2$ was coated onto the substrate at IBC coatings technologies by simultaneous magnetron sputtering PVD process of Ti and MoS_2 until the thickness of the coating reached 2 μm. The resulting coating was doped with Ti at ca. 10 at% which enhanced the hardness and thermal stability of the composite. A thin pure Ti interlayer was first sputtered to enhance the adhesion between the substrate and the coating.

6.2.2. Aging protocol

The same aged materials examined in **Chapter 5**, were subjected to tribological evaluation in this chapter. The aging protocol is reproduced from **Chapter 5,** and it is presented below for convenience. Coupons of DLC, PS400, PCD, and $TiMoS_2$ coatings were subjected to Venusian aging at NASA Goddard Space Flight Center. The samples were fixed onto ceramic bars separated by spacers, therefore the exposure of the surfaces was uniform, as shown in **Figure 5.1(a)**. The pressurized test chamber (**Figure 5.1(b)**) maintained a temperature of 464℃ and a pressure of 9.55 MPa with a mixture of CO_2, N_2 and SO_2 gasses, as shown in **Figure 5.1(c)**. CO_2 was the major component inside the aging chamber with 96.5%, and N_2 at 3.5%. SO_2, which is the third most abundant gas below the clouds of Venus was injected in the chamber maintaining ca. 155 ppm. The aging duration was 72 hours, which would be adequate to simulate the exposure of tribological systems on the landers/probes during idle times before or during Venusian exploration.

6.2.3. Experimental parameters

Tribological testing was performed using fresh and aged specimens to capture the effect of aging on the tribological performance of three selected tribo-pairs in a ring on flat contact configuration, as shown in **Figure 6.1**. **Table 6.1** lists the experimental parameters. PS400 was the mating surface for all tribo-pairs, except PCD. Note that PS400 vs. PCD was previously tested in **Chapter 2** and generated high wear on the softer PS400 coating due to a hardness mismatch between the two contacting surfaces, therefore, PCD was self-tested. Also, a normal load of 178N resulted in 0.57 MPa contact pressure between the ring specimens and the corresponding disks. A pressure of 2.41 MPa CO_2 gas (99.5% pure) was developed inside the testing chamber. A flashing/venting protocol was used as described in **Section 4.2.2.** A linear speed of 0.2 m/s for 30 min test duration resulted in 360 m sliding distance. Fresh and aged samples were tested; hence the effect of aging was captured.

Table 6.1 Experimental parameters.

Tribo-pairs (ring vs. flat)	**T**	**Load (Pressure)**	**Sliding speed**	**Duration**	**Env.**
PS400 vs. DLC	464°C	178N (2.6MPa)	0.2m/s	30 min	2.41 MPa CO_2
PS400 vs. $TiMoS_2$					
PCD vs. PCD					

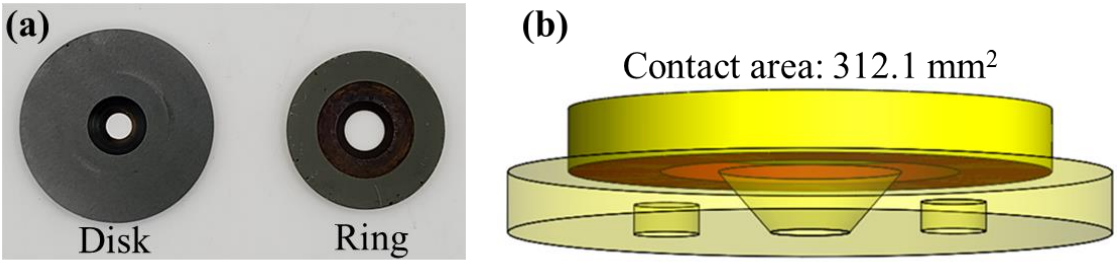

Figure 6.1 (a) Photograph of disk and ring and (b) contact configuration.

6.2.4. Characterization

Investigation of the pin and disk worn surfaces following tribo-testing was carried out with an Olympus DSX510 optical microscope. A Dektak (Bruker) stylus profiler was used to obtain the 3D topography of the wear track of the disks. A Tescan Vega SEM/EDS was employed to explore the topography and the elements found on the worn surfaces after tribological testing.

6.3. Results and discussion

6.3.1. COF – Fresh samples

The same tribo-pairs were previously subjected to tribological studies under different experimental conditions and contact configurations, as reported in **Chapter 4**. In this chapter, the contact configuration was changed from 3-pins on flat to ring on flat to ensure uniform wear of the rubbing surfaces. Therefore, the same experiments were repeated with the new configuration to allow direct comparison with the tribological performance of the corresponding aged samples and to capture the effect of thermal aging (see protocol in **Figure 5.1**). Each test was repeated twice to acquire an average trend of the frictional performance and to evaluate the degree of uncertainty. Note that under

special experimental conditions the tribo-surfaces generate more erratic responses, especially when are being tested close to their maximum operational capabilities.

Figure 6.2(a) shows the frictional response of PS400 vs. DLC, in which the COF was smoothly increasing until 15 min of experiment and remained fairly constant at around 0.35 thereafter. The sliding of PS400 vs. $TiMoS_2$ resulted in a rapid increase in the COF after 3 min of sliding, followed by a steady-state region with COF values around 0.35 (see **Figure 6.2(b)**). PCD vs. PCD generated a mild contact, evident by the smooth evolution and the absence of erratic changes of the in-situ COF, as seen in **Figure 6.2(c)**. **Figure 6.2(d)** shows the average values, calculated from the steady state COF of identical experiments. Despite that the sliding of PCD vs. PCD yielded the lowest average COF at 0.28, the high uncertainty (appeared with error bars) overshadows the corresponding average values of the other two tribo-pairs. PS400 vs. DLC generated an average COF of 0.34, whereas the average COF of PS400 vs. $TiMoS_2$ was 0.36.

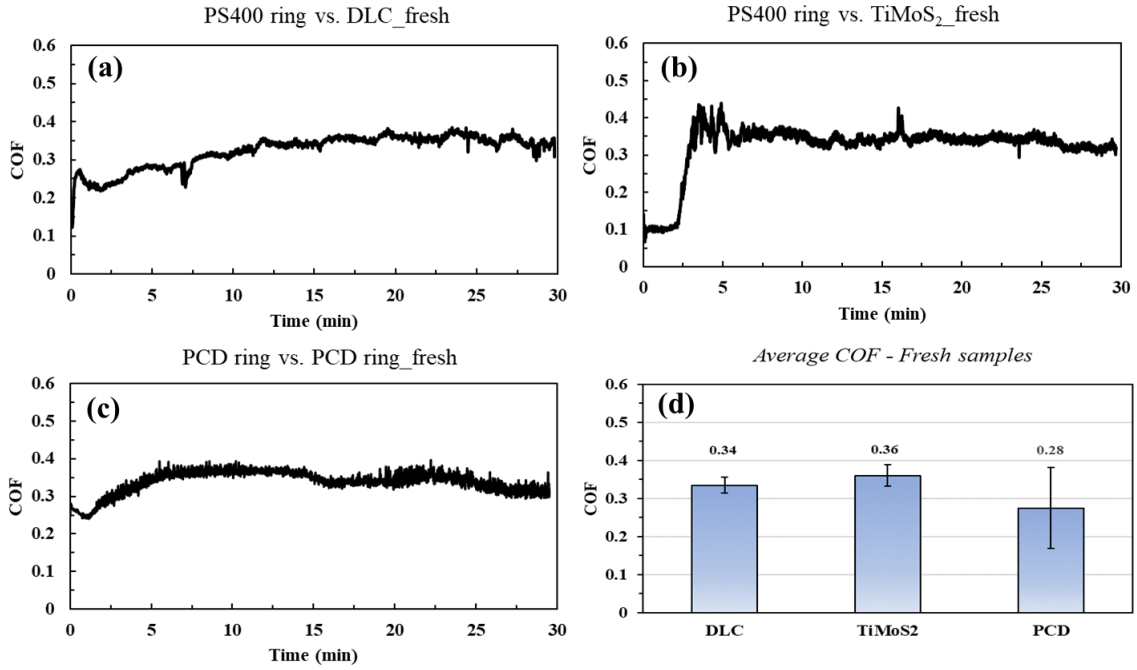

Figure 6.2 In-situ COF with time of ring tests of fresh (a) PS400 vs. $TiMoS_2$, (b) PCD vs. PCD, (c) PS400 vs. DLC, and (d) corresponding average COF values.

6.3.2. COF – Aged samples

Figure 6.3 shows the evolution of COF with time of the three aged tribo-pairs, as per the aging protocol of **Figure 5.1**. Note that the friction surfaces were tested as-aged and cleaning procedure with chemicals (i.e., isopropyl alcohol) was omitted, and the samples were soft cleaned with compressed dry air. As reported in **Chapter 5**, PS400 and PCD formed a compacted S-rich layer, therefore a sonication process would potentially remove it from the surface. PS400 vs. DLC appeared with a smooth increase from 0.1 to around 0.2 by the end of the experiment (see **Figure 6.3(a)**). **Figure 6.3(b)** shows the instantaneous COF with time of PS400 vs. $TiMoS_2$ tribo-pair, which depicted an initial decrease followed by a smooth increase in the COF until a fairly constant COF was

observed. By the end of the experiment the COF was 0.3. The interface between the self-made contact of PCD remained mild during the full duration of the experiment and the COF appeared unchanged and at a value of 0.2, as shown in **Figure 6.3(c)**. **Figure 6.3(d)** averages the values of the in-situ COF of repeated experiments. DLC depicted the lowest average COF value of 0.13, followed by PCD with a slightly higher value of 0.21. PS400 vs. $TiMoS_2$ appeared with the highest average COF of 0.3.

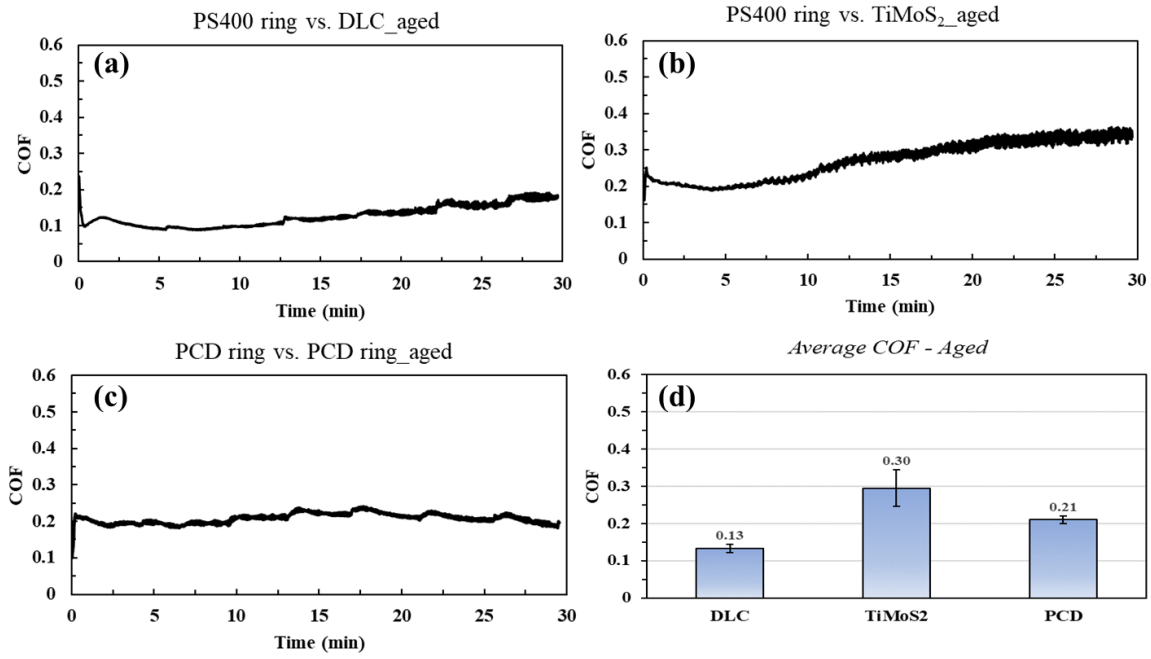

Figure 6.3 In-situ COF with time of ring tests of aged (a) PS400 vs. $TiMoS_2$, (b) PCD vs. PCD, (c) PS400 vs. DLC, and (d) corresponding average COF values.

6.3.3. Effect of aging on frictional performance

The corresponding in-situ and average COF values from **Figure 6.2** and **Figure 6.3** are reproduced in **Figure 6.4** to elucidate the effect of aging on the frictional

performance of PS400 vs. $TiMoS_2$, PCD vs. PCD and PS400 vs. DLC. Despite that the instantaneous COF values of fresh and aged PS400 vs. $TiMoS_2$ specimens overlapped at the last 10 min of the experiments, the transient zones demonstrated two different trends (see **Figure 6.4(a)**). A rapid increase was observed at the initial stages of the experiment for the fresh contacting surfaces, followed by high fluctuations attributed to different contact mechanisms formed by accumulated debris at the interface. In contrast, rubbing of the aged specimens resulted in a broad hump until 20 min of experiment, potentially due to a slower wear rate process of the contacting surfaces and a smoother interface. Both self-tests with fresh and aged PCD samples appeared with COF values remaining fairly constant, with the aged specimens generating a lower in-situ COF during the full duration of the experiment, as shown in **Figure 6.4(b)**. Similarly, the COF of fresh PS400 vs. DLC remained at higher values, while both evolutions stayed away from erratic changes and fluctuations (**Figure 6.4(c)**). Note that for the experiments with the aged PS400 against aged $TiMoS_2$ and DLC coatings the in-situ COF did not reach a steady-state, therefore prolonged tests should be performed until a constant interface is reached, if a durability study is of concern. $TiMoS_2$ and DLC coatings were 2 μm thick, and during the experiment were subjected to a progressive failure, until penetration into the substrate. Therefore, prolonged tests will also uncouple the durability behavior of the coatings and the steady-state COF and should be considered for future studies. **Figure 6.4(d)** shows the average COF values of the fresh and aged tribo-pairs; therefore, the effect of the aging process can be clearly captured. The thermal aging procedure had a positive effect on the frictional performance of the tribo-pairs, especially for PS400 vs. DLC, where a 62% reduction in

the average COF value was observed. PS400 vs. $TiMoS_2$ and PCD vs. PCD tribo-pairs experienced a 17 and 25% reduction, respectively. The high uncertainty of fresh PCD vs. PCD experiment overshadows the corresponding COF value seen in the aged samples, hence conclusive observations of the effect of aging on the frictional performance of PCD self-mate contact cannot be made.

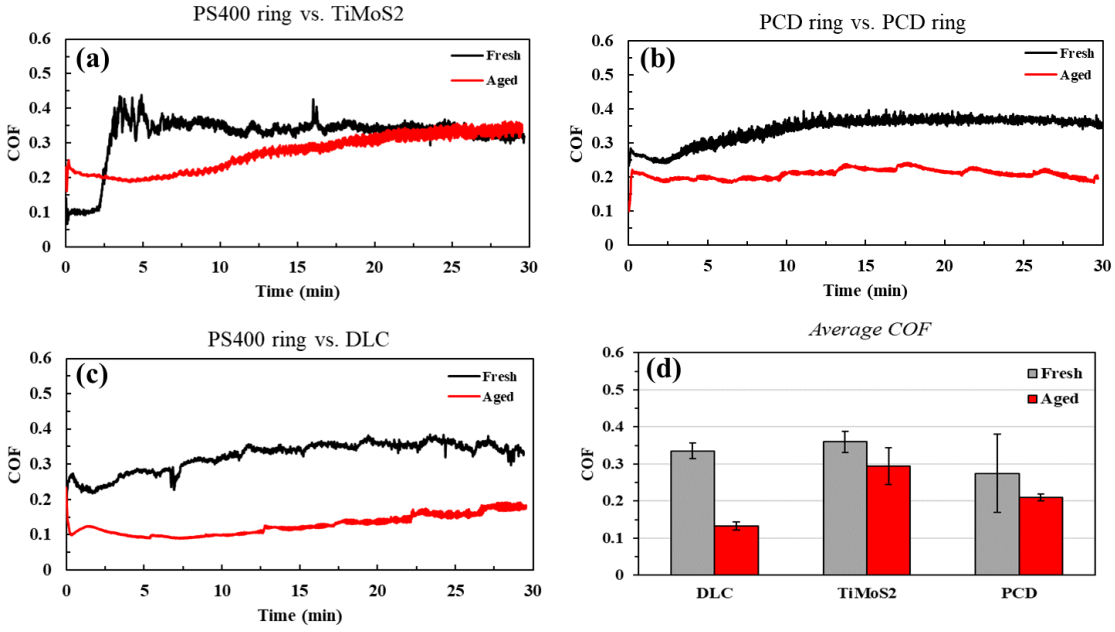

Figure 6.4 In-situ COF with time of ring tests with fresh and aged (a) PS400 vs. $TiMoS_2$, (b) PCD vs. PCD, (c) PS400 vs. DLC, and (d) corresponding average COF values.

6.3.4. Effect of aging on wear performance

Figure 6.5 demonstrates the severity of the wear in 2D and 3D profilometric scans. The line scan direction is shown with an arrow on the 3D images of **Figure 6.5(a2**, **a3**, **b2**, **b3)**.

Note that both the width and the depth of the wear track are good indicators of the amount of wear, that is higher the depth and broader the width of the wear track, higher the wear. **Figure 6.5(a1)** shows the wear profile of $TiMoS_2$ coating after fresh and aged experiments against PS400 coating. The wear track of fresh $TiMoS_2$ appeared wide with a maximum depth of around 1 μm, whereas the maximum depth of the coating after the aged test was almost 2 μm (coating thickness is 2 μm). The 3D scan of **Figure 6.5(a2)** also captures a significant amount of debris inside the wear track that can accelerate the wear on the counter-surface and generate higher friction (see COF value of fresh PS400 vs $TiMoS_2$ in **Figure 6.4(d)**). The wear track of the aged $TiMoS_2$ was smooth, indicating that a milder contact took place that yielded a lower COF, compared to the fresh specimens. The wear depth of DLC coatings after the fresh and aged tests remained at shallower depths (<1 μm) as can be seen in **Figure 6.5(b1)**, compared to $TiMoS_2$. The wear track on the fresh DLC was broader than aged DLC, indicating that a higher amount of material was removed from the surface. This is confirmed by the 3D profiles of **Figure 6.5(b2, b3)**.

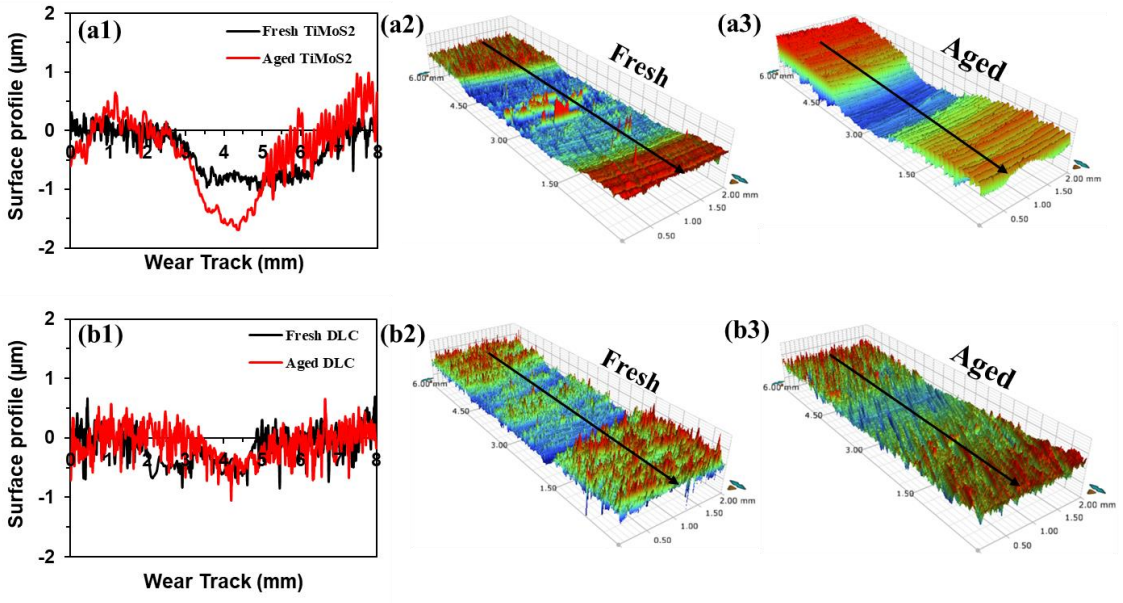

Figure 6.5 2D and 3D scans after tribological experiments with fresh and aged samples of (a) PS400 vs. $TiMoS_2$, and (b) PS400 vs. DLC.

6.3.5. Optical microscopy – Aged samples

Figure 6.6 illustrates optical micro-images of the worn disk specimens following ring on flat tribological testing with fresh and aged samples. **Figure 6.6(a)** shows the worn areas of PS400 rings and DLC disks. As-received PS400 is very porous, due to its coarse microstructure, with a high yielded surface roughness. **Figure 6.6(a1)** shows that the wear process of the softer phases of PS400 resulted in filling the porous and reducing the surface roughness via polishing. The DLC coating experienced mild wear and burnishing of high asperities. The aged PS400 ring experienced a similar "filling" process as the fresh sample (see **Figure 6.6(a2)**). However, the worn area was more compacted, uniform, and smooth, favorable for generating low frictional forces.

In **Chapter 5** it was shown that a dense, S-rich layer composed of particles of 2 to 4 μm in size was formed and physically attached on PS400 (and PCD) after exposure to the Venusian-simulated environment. Therefore, it is plausible that these particles were smeared and melted during HT contact forming a lubricious layer, thus a significantly lower COF was observed. The aged DLC disk had similar wear characteristics as the fresh sample, with mild wear appearing as discoloration. **Figure 6.6(b1)** shows that the pores of PS400 were filled, presumably with the softer silver and fluoride phases that are subjected to shearing during sliding. The $TiMoS_2$ had obvious wear marks, along with accumulated material, as indicated by an arrow in **Figure 6.6(b1)**. The PS400 aged ring of **Figure 6.6(b2)** was smooth and glazy, contributing to lowering the COF after the aging process. The $TiMoS_2$ counter-surface had different wear mechanisms, that is, towards the center the wear was more prominent, while at the edges of the wear track the coating experienced less wear. **Figure 6.6(c)** shows the micro-images after self-mate tribological experiments with fresh and aged PCD. Both contacting surfaces remained fresh and smooth with minor micro-pitting, demonstrating high wear resistance at the testing temperature of 464℃, as seen in **Figure 6.6(c1)**. **Figure 6.6(c2)** shows that the S-rich particles that formed from the aging process remained at the interface after tribological testing, demonstrating high affinity with the PCD underlayer. Also, material accumulation can be observed, probably due to compaction and melting of the S particles, as will be seen in **Section 6.3.6**. Nevertheless, the covering area with S-rich lubricious film on PCD was much less compared to PS400, therefore the effect of aging on the frictional performance was less pronounced, as seen in **Figure 6.4**.

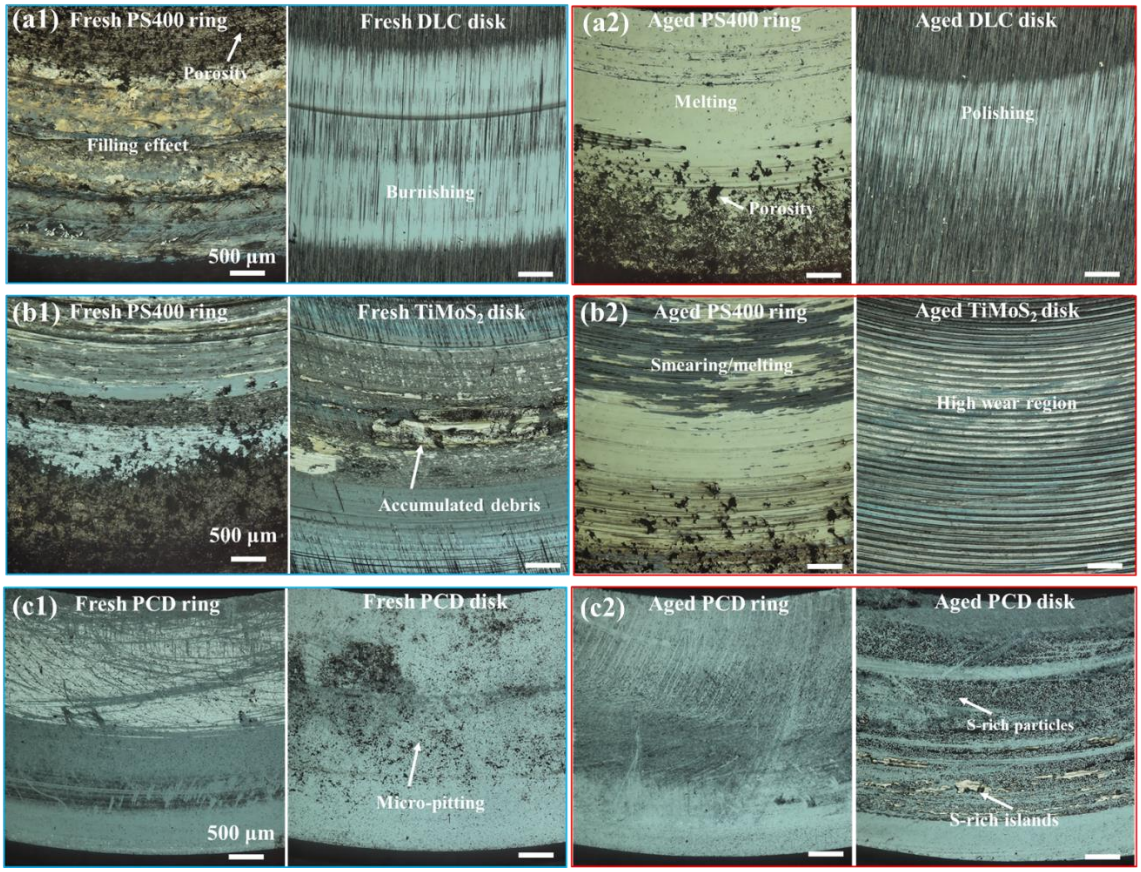

Figure 6.6 Optical images of worn rings and disks after fresh and aged experiments of (a) PS400 vs. DLC, and (b) PS400 vs. $TiMoS_2$, and (c) PCD vs. PCD.

6.3.6. SEM analysis – Aged samples

Figure 6.7 illustrates SEM images of the worn surfaces of fresh and aged DLC, $TiMoS_2$, and PCD disk surfaces. The surfaces of both fresh and aged DLC disks appeared smooth, with the wear mechanism happening mostly along the ridges of the surface, demonstrating that the coating retained its structural integrity after the HT test. The $TiMoS_2$ coating appeared more damaged compared to the DLC, following micro-pitting and adhesion wear mechanisms for the fresh and aged coating, respectively. The visible grains of fresh PCD demonstrate the extreme wear resistance of the coating when

subjected in tribological experiment under HPHT CO_2 environment. The grains are also visible on the aged PCD, with, however, most of the contacting surface covered with S-rich layers. As demonstrated in **Chapter 5**, following the aging process, S-rich physically adsorbed layers were formed on top of the PCD and PS400 coatings (see **Figure 6.8**). In this chapter, it was observed that these formations remained at the interface and acted as external liquid lubrication during testing at HT, passivating high frictional forces between the contacting surfaces, therefore the lower observed COF of **Figure 6.4** regarding the aged samples. The S-rich particles were subjected to smearing and melting during HT sliding contact and did not transfer on the counter-surfaces demonstrating good adhesion with the coatings. The most pronounced decrease in the COF was seen in PS400 vs. DLC tribo-pair, attributed to the generation of a favorable interface, on one hand the filling/polishing effect on PS400 and on the other hand the controlled wear process on DLC. However, $TiMoS_2$ experienced higher wear which almost caused the full removal of the coating, and this continuous wear process yielded a higher friction. It is expected that prolonged sliding of DLC and $TiMoS_2$ coatings will cause the complete removal from the interface, and their role can be sacrificial, in particular for long-duration mechanical contacts. In **Figure 5.9** it was shown that following Venusian aging DLC and $TiMoS_2$ had hardness values of 10.2 and 4.5 GPa, respectively. The addition of HT testing would further lower the hardness values of the coatings, thereby the wear resistance, with the DLC coating appeared to have higher resistance to wear compared to TiMoS2. HT nanoindentation on fresh and aged DLC and $TiMoS_2$ coatings should be implemented to

uncouple the effect of aging and HT testing on the mechanical properties and the wear resistance of the coatings, as discussed in **Chapter 9**.

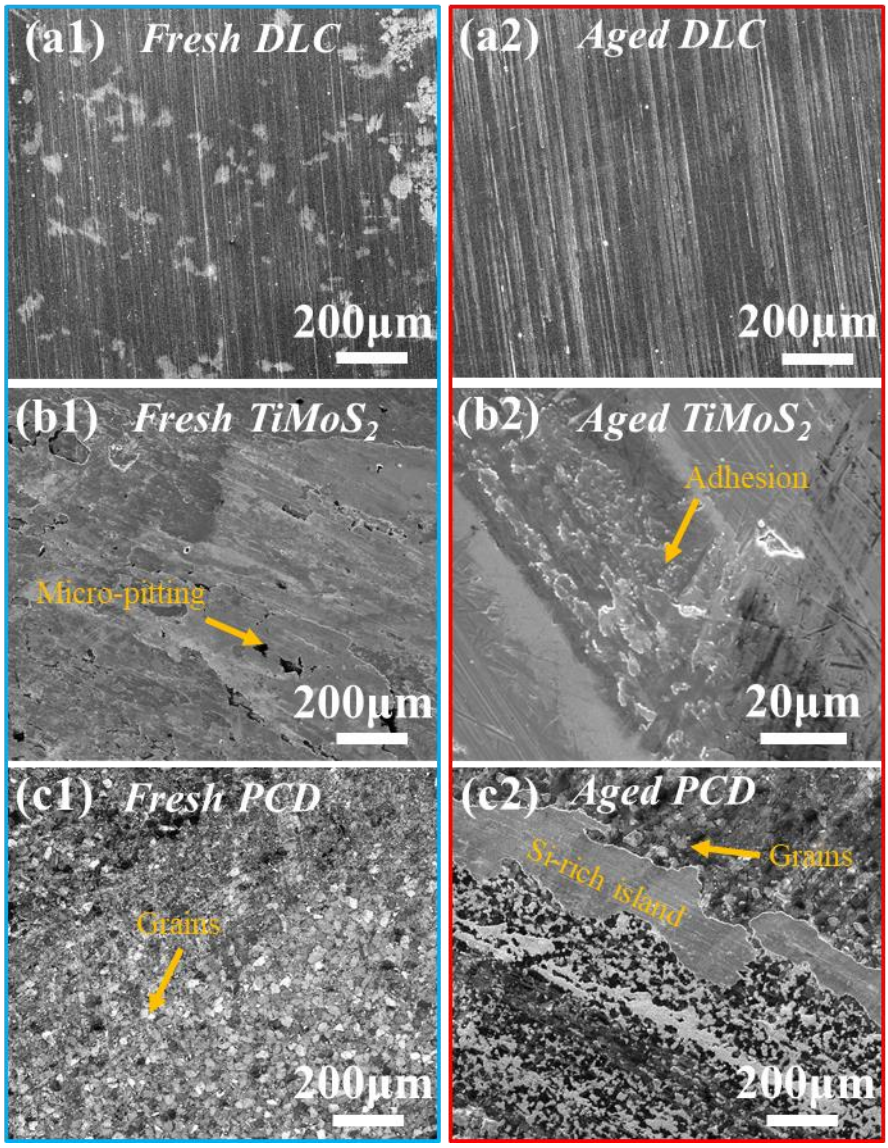

Figure 6.7 SEM micrographs following tribological experiments of fresh and aged (a) DLC, (b) $TiMoS_2$, and (c) PCD.

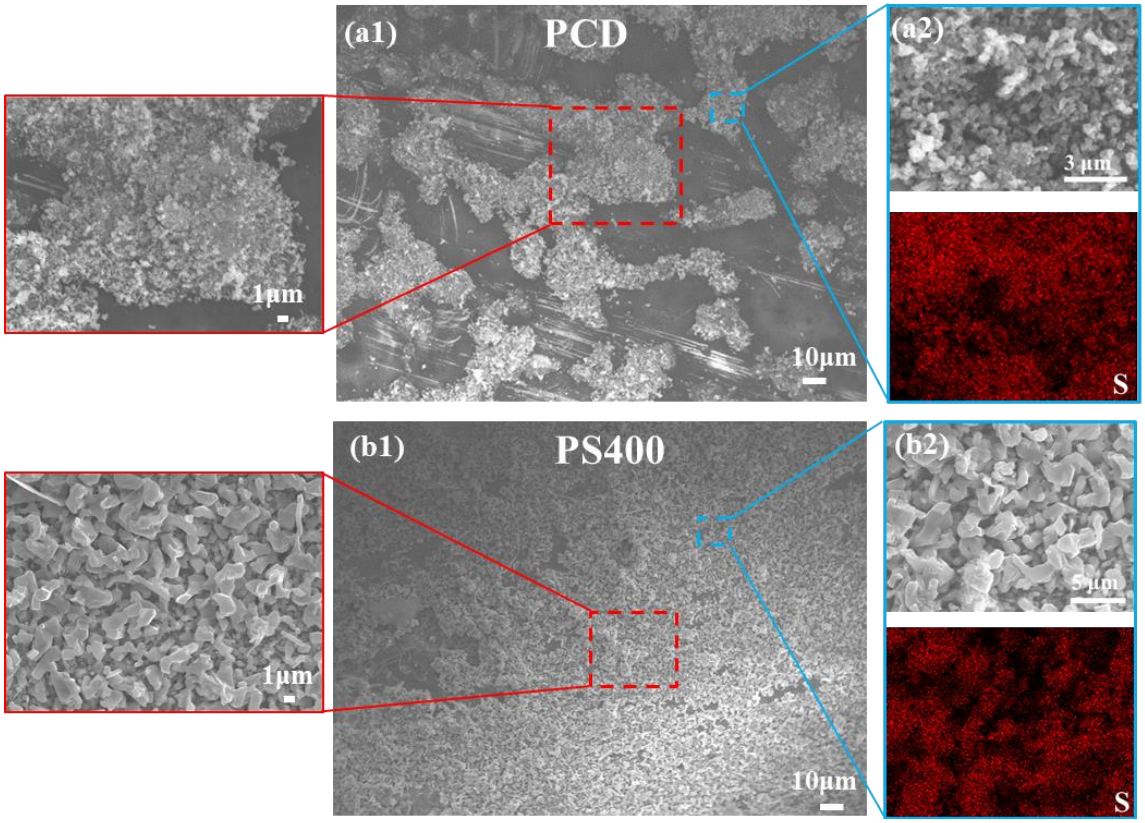

Figure 6.8 SEM/EDS analyses on untested aged (a) PCD and (b) PS400 coatings. High magnification images are shown on the left and EDS mapping appears on the right of the figure.

6.3.7. EDS analysis – Aged samples

Figure 6.9 shows EDS mapping of the pin surfaces following tribological experiments with the aged samples. In **Section 6.3.5** it was illustrated that S-rich particles were subjected to smearing and melting during sliding, hence lubricating the interface. Note that the testing temperature was significantly higher than the melting temperature of S. The EDS analysis confirmed the above-mentioned assumption with the detection of S-rich films on the surface of PS400 after sliding against DLC (**Figure 6.9(a)**) and $TiMoS_2$ (**Figure 6.9(b)**) and PCD self-testing (**Figure 6.9(c)**). These films had favorable flow

characteristics and load bearing capabilities, therefore lowering the COF and protecting the tribo-surfaces from excessive wear. Note that the most abundant element of the PS400 coatings, that is Ni, was also captured, and similarly C for PCD, as the EDS beam could penetrate the thin films. Also, minute traces of O were found in the same areas as S, especially for PS400.

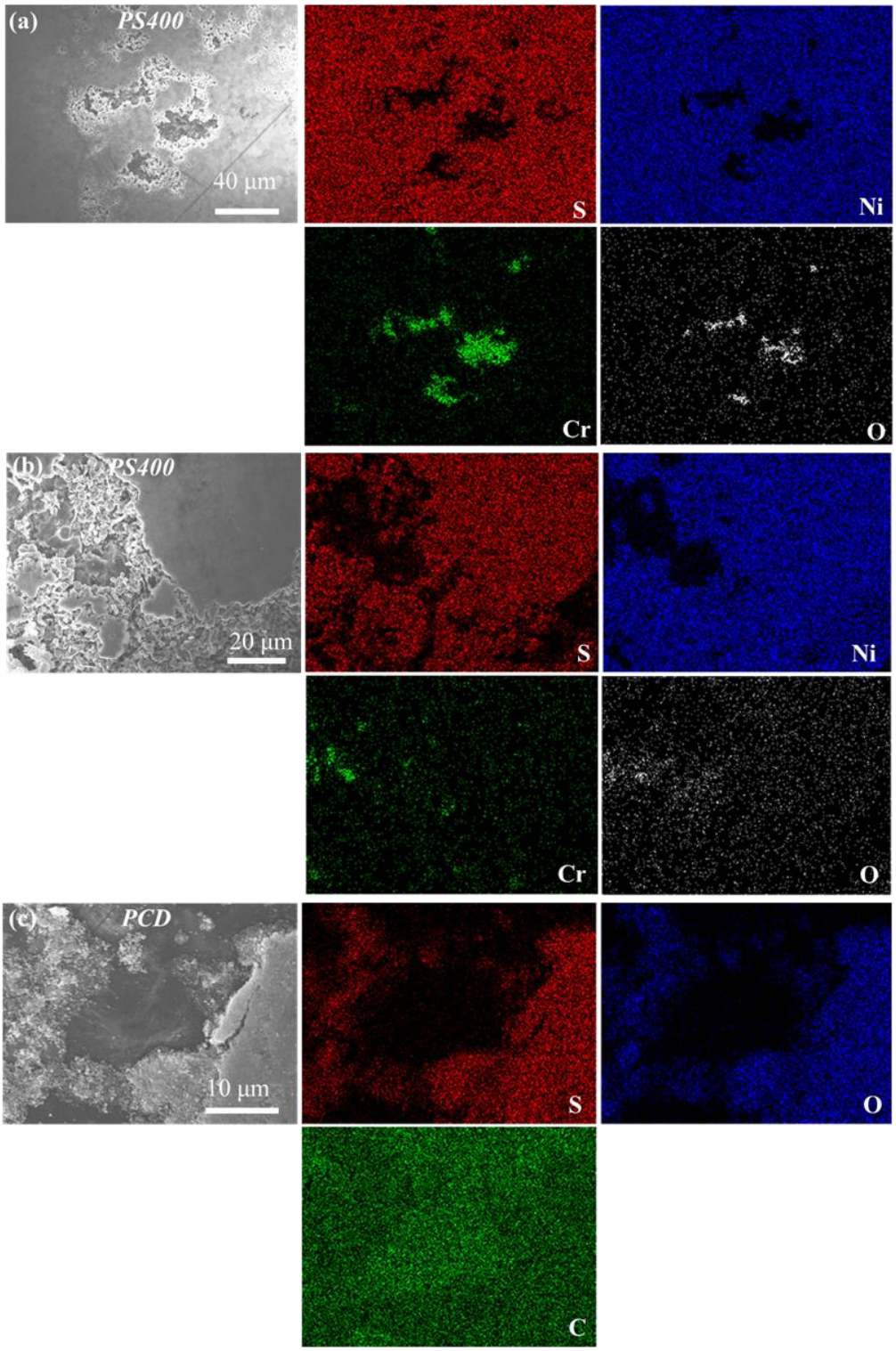

Figure 6.9 EDS analysis on pin surfaces of aged (a) PS400, (b) PS400, and (c) PCD following tribo-testing against DLC, $TiMoS_2$ and PCD, respectively.

6.4. Summary

In this chapter the effect of Venusian-simulated aging on the tribological performance on selected coatings was investigated and the following conclusions can be drawn:

- The aging process had a noticeable effect on the COF of the three tribo-systems, especially for PS400 vs. DLC, with a 62% reduction in the average value, whereas the wear did not change significantly.
- The S-rich layer that was formed on PS400 during the aging process was subjected to a smearing and melting process and acted as an external lubricant alleviating the friction between PS400 and $TiMoS_2$/DLC and PCD-self mate contact.
- PS400 and DLC coatings should be considered as candidate materials to coat bearing surfaces where low friction is concerned, and PCD where dimensional stability and structural integrity is dictated.

This chapter concludes the study on bearing surfaces for Venus exploration, such as in all-mechanical rovers, drills, balloons, probes, etc. Starting from a downselection of potential suitable interfaces for generic conditions to simulating Venusian aging and tribological testing in realistic conditions, this study provides significant results in the effort of launching future Venus missions. The next chapter makes a twist on the application to nuclear reactors, wherein higher temperatures and a different environment prevails, therefore a different approach on the material selection and processes was taken.

7. HELIUM TRIBOLOGY OF INCONEL 617 SUBJECTED TO LASER PEENING FOR 800°C HIGH TEMPERATURE NUCLEAR REACTOR APPLICATIONS[§]

7.1. Introduction

Increasing demand for electricity production, coupled with more conservative regulations for clean and reliable energy have resulted in extensive research and development in nuclear power production during the past decade. The Generation IV International Forum has launched promising nuclear energy system concepts, seeking more sustainable, reliable, and efficient power plants [95]. A VHTR and a HTGR are among the selected candidates to operate at high outlet temperatures (above 750°C) designed to reach 60-year operational lifespan [21]. Although He is an inert gas, it inevitably contains impurities resulting in accelerated surface degradation for mechanical components in coolant circulation systems [22]. Besides exposure to harsh VHTR and HGTR environments, tribological parts in these reactors, in particular, undergo low speed sliding (e.g., valves and control rods under intermittent oscillatory motion and often combined with long idle times), or high frequency small vibratory condition (e.g., fretting in heat exchanger joints). Accordingly, their contact behaviors are of vital importance in maintaining reactor stability and operational integrity [14].

[§] Reprinted with permission from "Helium tribology of Inconel 617 subjected to laser peening for high temperature nuclear reactor applications" by Vasilis Tsigkis, Md Saifur Rahman, Lloyd Hackel, Keivan Davami, Ali Beheshti, Andreas A. Polycarpou, 2022. Applied Surface Science, 577, 1-14, Copyright 2023 by Vasilis Tsigki.

INC 617 (Ni-Cr-Co-Mo solid solution alloy) is the main structural candidate for the construction of key components in VHTR/HTGR, due to its exceptional strength and corrosion resistance [14,96]. Furthermore, the literature is abundant with studies showing INC 617 to have superior oxidation and creep resistance, thermal fatigue performance, and phase stability [97–105]. Comprehensive comparative HT tribological studies in He and air environments were carried out on both alloys depicting that INC 617 outperforms alloy 800HT, in terms of tribological performance [14,21,41,106]. Still, the tribological studies of INC 617 at HT under nuclear reactor He environment showed high friction [23,24]. It was revealed that the absence of a mitigating compacted, and stabilized oxide layer leads to direct contact between metallic surfaces exposed to He environment promoting high friction and accelerated surface degradation and wear. Also, under HT He environment, INC 617 experiences a significant degradation of its mechanical properties (i.e., modulus and hardness) [25] that can result in accelerated wear and higher friction.

Although the widely used engineering technique of surface coatings can be developed to alleviate the friction and wear issues in reactor components, this should be the last resort as it can introduce other complexities in the reactor systems that require very high reliability and system integrity. This calls for a robust surface engineering technique that can enhance the tribological behavior and potentially other mechanical properties (e.g., creep and surface fatigue) and at the same time does not have regulatory concerns (as compared to, for example, to coatings as separate materials). LP is among those robust surface engineering techniques which induces high strain rate (up to 10^{-7} s^{-1}) plastic deformation on the surface (and deep into the subsurface), by means of short duration laser

pulses. Several mechanisms are in play during LP, for example the generation of high density tangled dislocations, and beneficial phase transformations, which generally result in high intensity compressive residual stresses, refined microstructures, and hardened regions for various alloys. It should be noted, however, that the surface modification benefit of LP is material dependent. For example, Kanjer et al. and Lavisse et al. reported almost negligible hardening effects on titanium and its alloys [107–109]. For the material studied here, there exists no report in the open literature on the effect of LP on INC 617 microstructure. Nonetheless, for superalloys with close microstructure to INC 617 such as INC 625 and INC 718, previous studies showed that LP generates promising structural modifications, compressive residual stresses and consequent hardening [110–113]. LP has also been proven to enhance corrosion resistance, fatigue life, and fracture resistance of INC 600 and INC 718 [114,115]. While the literature is abundant on the beneficial contribution of LP on the tribological performance of metallic surfaces, for example aluminum, magnesium, titanium and steel alloys [116–121], a few works are focused on nickel-based alloys [122,123]. In addition, no report exists in the open literature on the effect of LP on INC 617 friction and wear.

The successful implementation of LP in HT applications is, however, challenging due to diminishing effect of LP because of thermal relaxations and microstructure modifications at elevated temperatures manifested as defect annihilation and recovery, grain boundary migration, phase coarsening, and phase dissolution [124–127]. The relaxation of the LP induced stresses and microstructures at elevated temperatures is driven by the material softening (thermal mechanism), and external and internal stresses

of the material which induce plastic deformation (mechanical mechanism), or the combination of both [124]. For nickel-based superalloy, however, LP showed relatively good thermal stability and longer lasting effectiveness which makes it a potential for HT applications [112,126,128]. Munther et al. showed that the combination of cyclic thermal annealing and LP, called thermal microstructure engineered (TME) LP, substantially increases the thermal stability of LP induced microstructure in additively manufactured INC 718 after exposing the treated specimen to 600°C up to 350 hours. The repeated strain input achieved through cyclic LP and intermittent heat treatments encouraged the formation of γ' and γ'' phases which contributed in stabilizing the microstructures induced after the LP process [127].

The effects of LP on the tribological performance of several materials have been studied in the literature [116,117,119,121], and a decreasing trend of both friction and wear values of the treated specimens, compared to the as-received (untreated) specimens was observed. Regarding HT applications, Tong et al. investigated the tribological characteristics of LP specimens, by performing HT tribo-testing (up to 600°C) in an open environment utilizing a titanium alloy (TC11). Their findings pointed towards a lower degree of thermal softening of the LPed subsurface, which was able to maintain the integrity of the superficial oxide tribo-layer, and lower friction and wear were reported [129]. In spite of potential application of LP in enhancing the tribological behavior of superalloys, there are no studies on their tribological performance especially at HT. Also, the impact of LP+TME on friction and wear has yet to be explored, regardless of the surrounding environment and temperature.

In this chapter, the tribological behavior of INC 617 at an extreme temperature of 800°C under HTGR (99.999% He) environment following LP, and cyclic LP with intervening TME was investigated. Also, we simulate thermal aging under reactor conditions, by exposing the LP specimens in a HT (950°C) He environment to further study of how LP and TME processes affect the surface microstructure and the frictional/wear performance after aging.

7.2. Experimental

7.2.1. Materials and sample preparation

Disk specimens with dimensions of 25.4 × 25.4 × 15 mm as well as 19 mm long hemispherically tipped pins with tip radius of 8.15 mm were machined from INC 617 plate, provided by Idaho National Laboratory (INL). The chemical composition of INC 617 is presented in **Table 7.1**. The high concentration of nickel and chromium provide good oxidation resistance at HT, while chromium, cobalt, and molybdenum are the hardening/strengthening agents, which are dissolved into the solution matrix. After the LP and TME processes, the disks were polished down to 80 ± 5 nm RMS roughness using a sequence of 600, 800, 1200, and 2400 abrasive pads with a minimal layer removal. This was also followed by polishing with a 3 μm diamond suspension, and a final pass with a 0.05 μm colloidal silica. During the LP process and due to the very high local temperatures, a thin recast layer is formed on the surface. Also, during TME (600°C in air), the surface is subjected to some degree of oxidization. For example, Gill et al. demonstrated that a recast layer of ~5 μm in thickness was formed on the surface of INC 718, after the LP process without a protective layer [110]. Depending on LP process (laser

energy, cycles, etc.), CWST measurements after LP and LP+TME, showed oxide layer in the range of 5 to 20 µm for nickel-based superalloys. For consistency, in tribological tests and to eliminate the effect of this LP process-based transient layer and its material and topography, the samples LP-R and LP-TME were subjected to polishing, as explained above. Commercial abrasive pad polishing is a standard procedure after LP process. The samples were also sporadically examined during polishing, and the procedure was terminated as soon as the surface oxides were completely removed and were not optically visible on the surface. Also, optical microscopy was employed to further examine the polished surface to ensure no recast/oxide layer was present. Here, the polishing removed a layer thickness up to approximately 30 to 40 µm. It should be added that samples subjected to He aging were not polished following the aging process, however, they were polished prior aging.

Table 7.1 Chemical composition of INC 617 provided by the manufacturer (units are in wt.%). Reprinted with permission from [15].

Ni	**Cr**	**Co**	**Mo**	**Al**	**C**	**Fe**
53.27	22.02	11.91	9.38	1.1	0.08	1.46
Mn	**Si**	**S**	**Ti**	**Cu**	**B**	**P**
0.23	0.2	0.001	0.32	0.02	0.002	0.005

A schematic of the LP process is illustrated in **Figure 7.1**, wherein water was used as a confinement medium. The LP process was performed without a protective coating. However, the recast layer was removed with a very light polishing using 3M Scotch-Brite after the process. Fresh INC 617 disks were subjected to the LP process with a beam

irradiance of 7 GW/cm^2. To achieve that, a 1056 nm flash pumped Nd glass laser was used delivering 13 J per pulse on target. The spot size was 9 mm^2 square with 3% spot-to-spot overlap providing true 100% coverage for each layer. Laser pulse duration of 18 ns (full width half height) and 0.7 ns rise time were used. For preparation of regular LP specimens (symbolized by LP-R), the INC 617 disks were subjected to a 4-layer LP without an intervening TME or a post-treatment process. Regarding the LP annealed specimens (LP-TME), a combination of LP and intervening thermal treatment was carried out. Specifically, a sequence of 3 LP/TME processes was followed by a final LP, resulting in 4 LP events and 3 intervening TME surface treatments. Identical LP process parameters were used compared to LP-R samples, and each intermittent TME was carried out at 600°C (roughly 55% of material melting temperature, T_m) for 8 hours in air. The LP and TME treatments were performed with state-of-the-art laser and robotic positioning systems available at Curtiss Wright Surface Technologies (CWST), California, USA. Furthermore, some of the LP-R, and LP-TME, as well as INC 617 specimens were subjected to post-treatment thermal aging simulating HTGR/VHRT reactor environment, resulting in additional sample types referred to as LP-A, LP-TME+A, and INC 617-A (aged INC 617 with no peening), respectively.

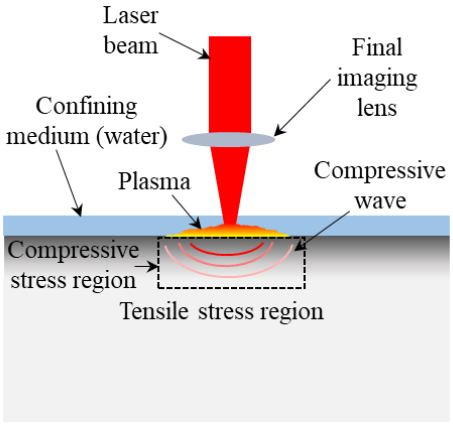

Figure 7.1 Schematic representation of LP process. Reprinted with permission from [15].

In an effort to simulate long-time exposure of the tribological components under HTGR/VHRT conditions, an aging process was implemented, following the LP and TME treatments. In the present study, He with purity of 99.999% was used where the concentration of the impurities, in parts per million (ppm), is as follows: O_2 (1), H_2O (1), total hydrocarbons, i.e., CH_4 (0.5), CO (1), CO_2 (1), and N_2 (5). These impurity levels are similar to the cooling medium of VHTR [22]. To assure the minimum presence of oxygen within the furnace, a vacuum/flashing protocol was used (see Ref. [130] for details). Afterwards, the furnace was set to the target temperature of 950°C, with 6°C/min ramping temperature, followed by constant temperature aging time of 10 hours. The samples were then cooled down to ambient temperature with a rate of 1°C/min or less. A constant He flow rate of 0.14 m^3/hour was maintained during heating, aging, and cooling.

7.2.2. Experimental procedure

The experimental conditions are outlined in **Table 7.2**. Five different tribo-pairs were selected to investigate the contribution of LP, TME and post processes (aging) on

INC 617 tribological performance. All tribo-pairs were constituted of an untreated INC 617 pin vs. different sample types, namely INC 617, INC 617-A, LP-R, LP-TME, LP-A, and LP-TME+A disks, and the resulting tribo-pairs are named as such for convenience. To have a better comparison and to further understand the involved wear and friction mechanisms, in addition to He environment, limited tribological tests were also performed in air. The linear velocity was set to 0.4 m/s, with a 30-minute duration resulting in 72 m sliding distance. The untreated INC 617 served as the baseline to gauge the effect of each treatment on the tribological behavior of the tribo-pairs.

For the experiments under He environment, a vacuum-flashing protocol was used to ensure minimum presence of contaminants within the chamber/jar, as detailed in Ref. [41]. Thereafter, the furnace was heated up to 800°C. During the experiment, the pressure was controlled at 0.1 ± 0.02 psi (gage). After the end of the experiment, the samples were let to cool in He with a continuous flow of 0.14 m^3/hour. A minimum of three experiments for each tribo-pair were carried out to assure repeatability.

Table 7.2 Experimental conditions. Reprinted with permission from [15].

Samples		**T**	**Load (Hertzian pressure)**	**Sliding Speed**	**Sliding Distance**	**Ambient**
Pin	***Disk***					
INC 617	INC 617	800°C	5N (580.7 MPa)	0.4 m/s	72 m	He
	INC 617-A*					He
	LP-R**					He
	LP-TME***					He, Air
	LP-A					He, Air
	LP-TME+A					He, Air

**A: aged; **R: regular peened with no TME or aging; ***TME: thermally engineered*

7.2.3. Characterization

Microhardness measurements were carried out using a Vickers microhardness tester (Wilson TUKON 1102) to measure the surface hardness following the LP and TME processes, and after aging. Investigation of the pin and disk worn surfaces following tribo-testing was carried out with an Olympus DSX510 optical microscope. A JEOL JSM-7500F SEM was employed to explore the topography of the unworn and worn areas of the untreated and treated disks. Cross-sectional SEM and EDS analysis of the unworn and worn surfaces were also performed to analyze the near surface oxide morphology and elemental composition. Transmission Electron Microscopy (TEM, Fei Tecnai F-20) foils were sectioned from the top (treated) surfaces through focused ion beam (FIB) milling. The foils were approximately 10 μm long and 5 μm wide, encapsulating the upper affected region of the material. A Dektak (Bruker) stylus profiler was used to measure the wear rate of the disks.

7.3. Results and discussion

7.3.1. Vickers hardness

Surface hardening is achieved by the high strain plastic deformation induced by the laser pulses, which result in an increase in the dislocation density, the generation of compressive stresses, and grain refinement [110,112,131]. The microhardness values of the disk specimens are depicted in **Figure 7.3**. Note that the penetration depth was maintained at 8-12 μm in all specimens to assure that the hardness levels of the specimens corresponded to the upper surface and well within the LP regions. It should be emphasized, nevertheless, that LP can induce surface modifications which result in considerably hardened regions. For instance, for INC 718, surface modifications more than ~ 500 μm depth, was reported [110]. The untreated INC 617 features the lowest microhardness value of 190 HV or 1.86 GPa. After 4 passes of LP the average surface microhardness experiences a 62% increase resulting in 3.03 GPa, confirming a successful implementation of LP in enhancing the microhardness of the treated sample (LP-R). The TME process (LP-TME) results in an additional increase on the average surface microhardness (7% at 3.22 GPa), compared with LP-R. It is noted that the LP-TME sample was polished after the LP+TME processes to remove any surface oxides formed when exposed at 600°C during TME.

The effect of LP+TME process on the surface enhancements of INC 718 was studied by Palma et al. and Munther et al. and was elucidated that the increase in hardness is related to a combined effect of precipitation hardening and microstructure pinning effect [127,132]. Generally, precipitation hardening of INC 617 is induced at temperatures of

650 to 760°C, by γ′ and γ″ phases, respectively. With the current TME procedure (600°C-8 hours), mild strengthening is expected, which is mainly attributed to the formation of fine γ′ particles [132]. More importantly, it is shown that cyclic LP and the subsequent plastic deformation can encourage the formation of γ″ phases at lower temperatures (650°C), that will cause a further increase in the material's hardness [127].

The LP specimens were also subjected to a post-aging thermal treatment of 950°C for 10 hours in He. LP-A and LP-TME+A appear to have similar microhardness enhancements, as LP-TME, showing after 10 hours of very HT aging, the LP effect was still preserved. It should be noted, however, that the microhardness values of LP-A, and LP-TME+A are also affected by superficial oxides (3-6 μm thick) following exposure at 950°C in He atmosphere (please see section 3.5 for cross-section EDS). Microhardness measurements of untreated INC 617-A show that the surface oxides increase the microhardness by 65%, compared to the unaged INC 617 specimen. Salari et al. measured the nanohardness of surface oxides (mainly Cr_2O_3) formed on He aged INC 617 by nanoindentation and reported high hardness values of 25 GPa at depth up to 200 nm [98]. Nevertheless, the indentations performed herein penetrated through the few microns-thick oxide layer, targeting the subsurface and as a result the effect of generated hard oxides on microhardness findings was reduced. The LP aged samples (LP-A, LP-TME+A) demonstrate a 17% higher microhardness value than INC 617-A, thus the further increase in hardness can be mostly attributed to LP and TME processes than the aging process. As depicted in **Figure 7.3**, by exposing the specimens to the VHTR/HTGR environment (950°C under He) for 10 hours, defect annihilation and thermal relaxation is prevented,

and the microhardness values are retained. Note that the thermal stability of LP specimens at long HT exposures does not fall into the scope of this study, nonetheless, to further evaluate the microstructural stability of LP and LP+TME processes, longer thermal exposure (60 hours) was performed followed by TEM imaging (see next section). It is, however, noted that the current study focuses on the tribological behavior of INC 617 treated by LP under VHTR/HTGR environments.

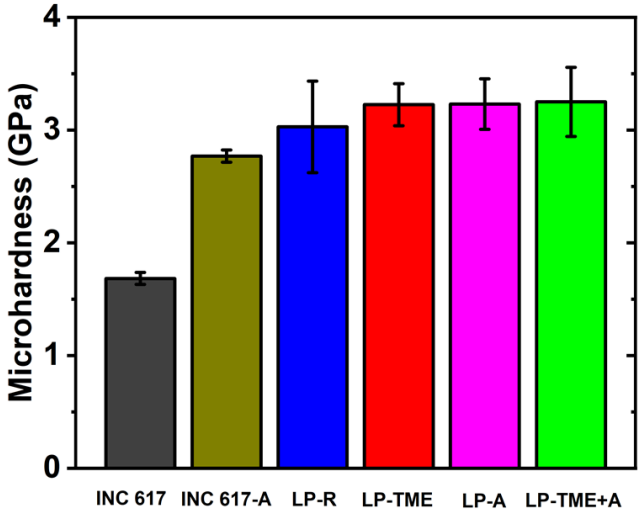

Figure 7.2 Surface microhardness values measured by Vickers indentation of the as-received disk specimens before HT sliding. Error bars designate ± 1 standard deviation. Reprinted with permission from [15].

7.3.2. TEM

LP and especially LP+TME processes provide enhanced microhardness results on treated INC 617. In this section, TEM imaging was performed to evaluate the stability of LP induced microstructures after long time HT exposure. Both LP and LP+TME samples were subjected to 60-hour, 800^{o}C exposure wherein subsequent TEM characterization was

carried out. Investigation of the treated surface of the material subject to each of the treatment schemes was carried out to discern relevant microstructural alterations known to play a role in influencing surface-level mechanical properties. Following thermal exposure and 4 subsequent layers of laser peening (LP-R sample), dense dislocation networks are observed occupying the immediate sub-surface, to a depth of 1 μm (**Figure 7.4(a)**). Above these dislocation networks, nanoscale subgrain structures are also found to dominate the microstructural changes occurring in the uppermost plastically deformed regions, occurring to a depth of 300 nm. The presence of subgrains is surmised to be a result of cyclic LP wherein repeated strain facilitates the transformation of defect networks into fine, subgrain structures [133]. With a buildup of sufficiently dense dislocations, defect networks then begin to organize into low energy configurations, or subgrains, under the influence of long-range stresses [134]. This mechanism has been proven to be favorable for the deformed microstructure as it enables further work hardening effects by impeding the motion of glissile dislocations.

Following LP+TME (**Figure 7.4(b)**), a similar microstructure is observed. Fine surface-level subgrain is seen with dense, core dislocation networks directly underneath. In this case, the presence of subgrain facilitates the effective "storage" of work hardening effects at HT as defect structures are organized into lower-energy configurations, promoting favorable microstructural and property modification retention when subjected to elevated temperature [135]. Additionally, nanoscale precipitates are found to be dispersed among surface-level subgrain networks providing another level of stabilization and strength for the deformed microstructure of LP+TME samples. These particles behave

as immobile barriers to the motion of strain-driven dislocation motion, and also pin the barriers of newly formed subgrain structures, preventing subgrain coarsening. These findings highlight the stability of the deformed microstructure and provide validity to the LP+TME process and its ability to impart thermally stable microstructural modifications. Typically, near complete defect annihilation would be expected through the use of conventional LP processes, but the addition of cyclic LP and the inclusion of intermittent thermal input promotes work hardening retention through the formation of subgrains and, especially, the precipitation of favorable nanoscale precipitates by modifying their precipitation kinetics. Application of thermal input following LP promotes the preferential nucleation of precipitates along defect sites which acts to not only strengthen the material matrix, but also provides an additional barrier against thermally activated dislocation motion.

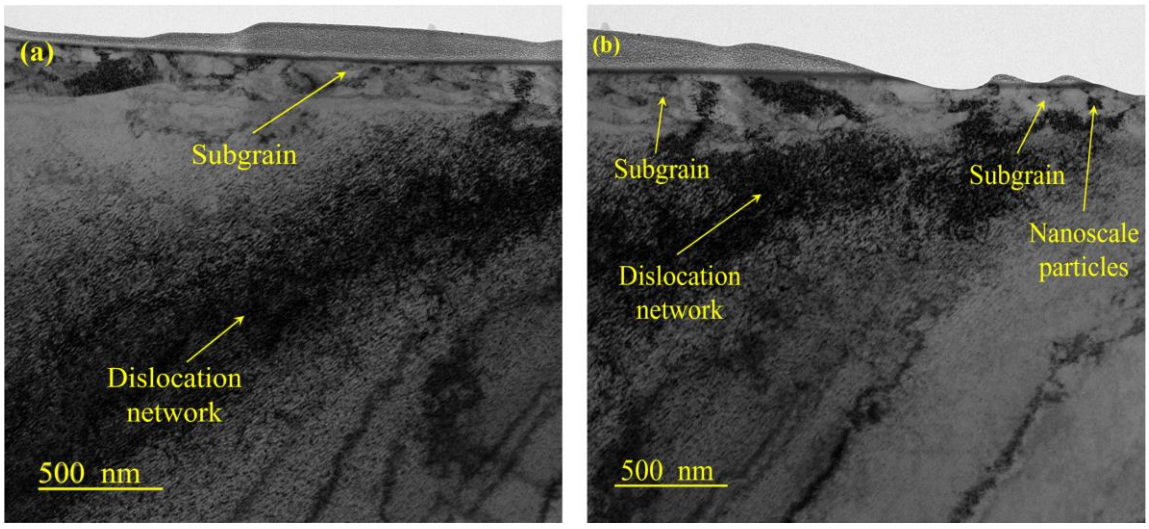

Figure 7.3 TEM micrograph illustrating the microstructure of INC 617 subjected to (a) LP and (b) LP+TME processes after 60-hour thermal exposure at 800°C. Reprinted with permission from [15].

7.3.3. COF

Figure 7.5 shows the evolution of the coefficient of COF under He (**Figure 7.5(a, b)**) as well as under air environments (**Figure 7.5(d, e)**) measured for several tribo-pairs under examination. The corresponding average values (**Figure 7.5(c, f)**) are also calculated from the data acquired during the last 40% of sliding distance to minimize running-in effects. The error bars represent the standard deviation of the mean COF values between repeated experiments. Tribo-pairs INC 617 and LP-R depict similar evolutions of the COF and average values. Noting the error bars, it can be concluded that the effect of LP on steady state HT COF is insignificant. However, LP+TME seems to slightly reduce the COF. The untreated INC 617 was extensively studied by Rahman et al. (800°C, He) and their tribological results are in accord with the present study [41]. INC 617-A (aged in He) appears with high fluctuations in the in-situ COF which result in an average COF value of 1.17. A complementary experiment was performed with INC 617 aged in air (INC 617-A-Air) to investigate the effect of aging environment on the frictional performance under He environment. It can be seen that during the first cycles of the experiment the COF is low, followed by a rapid increase to a COF of 1.71, due to the deterioration of the integrity of the pre-formed compact oxide layer and the subsequent detachment from the surface. Both LP samples followed by aging process (LP-A, LP-TME+A) feature a dramatic decrease in COF, after a running-in period of high friction and high fluctuations for 25 and 15 m, respectively, resulting in 0.53 average COF value.

LP and aging processes show a synergistic effect in the development of hard, well-supported oxides at the interface, that enhances the frictional behavior. This is also reinforced by the friction results of INC 617-A and INC 617-A-Air, showing that the aging process alone is inadequate to provide strong surface oxides to reduce the COF.

Under ambient atmosphere (air) and at 800℃, LP-TME, and LP-TME+A, experience an initial transition zone (running-in) for 10 and 5 m, before settling to a constant state that results in average values of 0.44, and 0.47, respectively. INC 617 and LP-A depict similar COF values of 0.47 and 0.44, respectively. It can be concluded that operating under HT air environment provides sufficiently strong compact oxide to the extent that it overshadows any enhancement by LP processes. It should be, however, emphasized that INC 617 is aimed to operate under He environment.

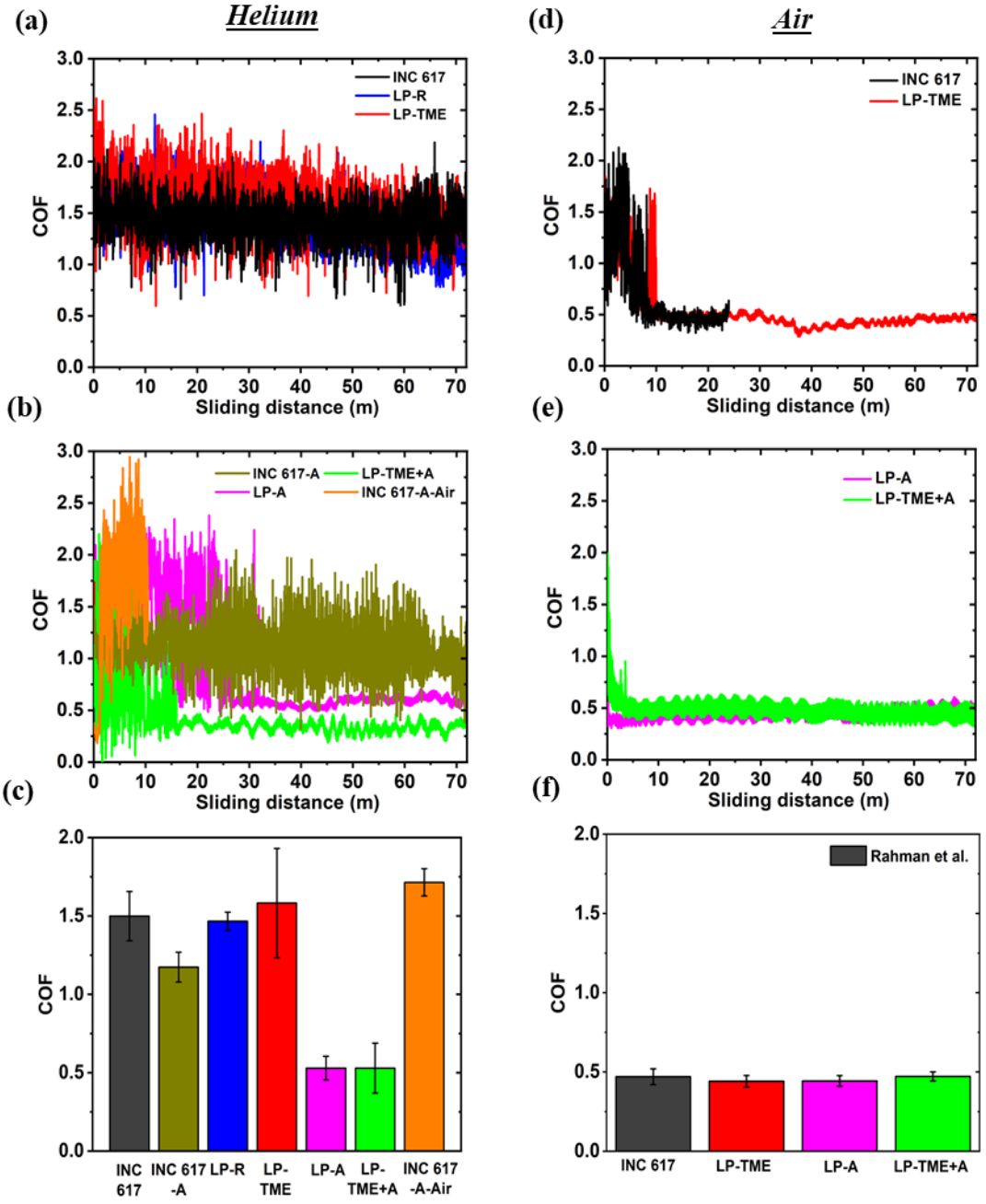

Figure 7.4 Evolution of COF with sliding distance in (a) and (b) He, and (d) and (e) air environment at 800°C, and the corresponding average values (c), and (f), respectively [24]. Reprinted with permission from [15].

7.3.4. Wear

Figure 7.6 shows 2D and 3D profilometric scans of the worn disks following tribo-experiments under He and air environments. Both the width and the depth of the wear track give a direct measurement of the wear and severity of the contact. INC 617, INC 617-A, and LP-TME specimens appear with a wear up to 50 μm in depth, while the penetration depth of LP-R is 80 μm. In sharp contrast, both LP aged disks, namely LP-A and LP-TME+A exhibit maximum wear depths of less than 20 μm as well as an indication of material piled ups. **Figure 7.6(b)** captures the 3D topography of the disk specimens and covers both the wear tracks and unworn areas. Accumulation of loose debris is evident on the worn surface of INC 617 and INC 617-A, along with a wide wear track, similar to LP-TME, whereas LP-R appears with a deep, yet narrow wear track. In agreement with the friction data, however, LP-A and LP-TME+A feature low wear and the formation of high peaks, which are identified as compacted islands of oxides, thereafter. Similarly, the disk specimens tested under air exhibit minute wear, and the wear tracks are mostly covered by surface oxides (see **Figure 7.6(c)**). It can be postulated that regardless of the surface treatment, the disk specimens are favorable in developing an oxide tribo-layer when exposed to HT air, which results in low friction and wear, however, it is not the case in He environment where only combined LP and aging process results in stable surface oxide.

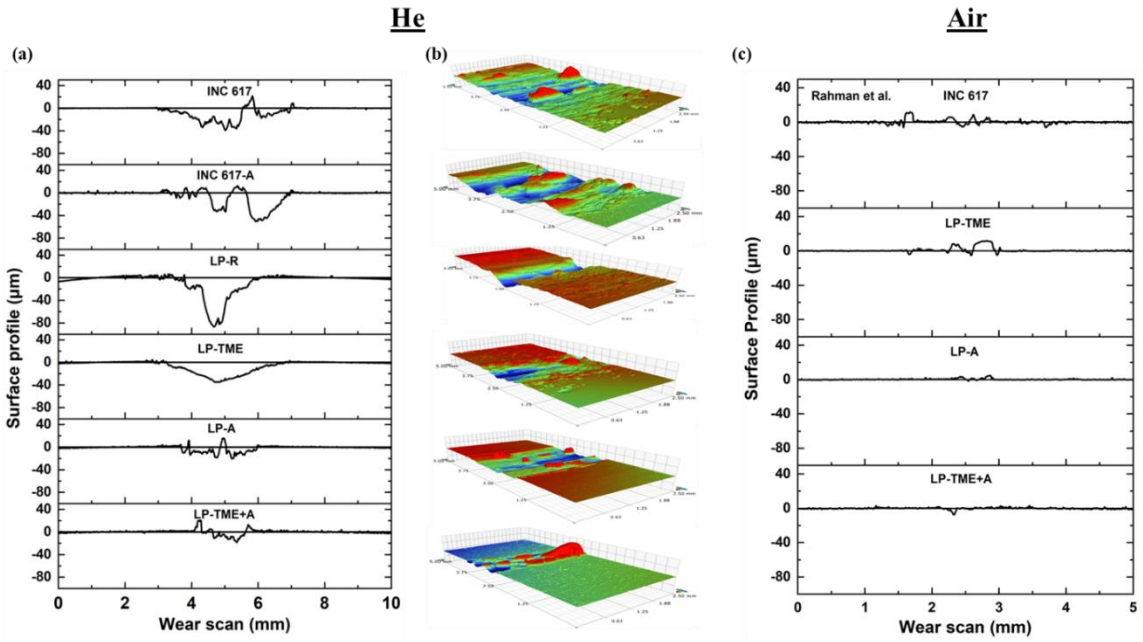

Figure 7.5 Typical (a) 2D, (b) 3D wear scans (5 × 2.5 mm area and -100 to 100 µm vertical range) of disk specimens following HT sliding in He, and (c) 2D scans after HT sliding in air. Reprinted with permission from [15].

Figure 7.7 illustrates the corresponding wear rates of the disk samples under He atmosphere. The worn volumes are approximated from multiple profilometric wear scans performed perpendicular to the wear track on each disk to obtain the average value, and the wear rates are calculated as described in Ref. [136]. As expected from wear track profilometry (**Figure 7.6**), the LP-A and LP-TME+A samples feature the lowest amount of wear followed by INC 617-A and LP-R. INC 617 and LP-TME possess the highest wear rate values among the specimens under examination. Given the erratic nature of HT wear and the error bars, we can conclude that INC 617-A, and LP-R, INC 617 and LP-TME wear in a similar fashion. Nonetheless, significant wear reduction for aged LP and LP-TME samples is evident. Tribo-testing under air, results in negative wear rate values,

as illustrated in **Figure 7.7(b)** showing that oxidation overshadows material loss due to wear. The highest amount of material gain occurred on INC 617, followed by LP-TME. LP-A and LP-TME+A experience the lowest amount of surface oxidation during tribo-testing.

Figure 7.7(c, **d)** summarize the tribological performance of each tribo-pair under He and air, in a cumulative COF vs. wear rate plot, respectively. Under He environment, the results are scattered around low COF/low wear, high COF/high wear, and moderate regions. The experiments with INC 617, LP-R, and LP-TME fall into the high COF/high wear region with average COF values around 1.5, and a maximum wear rate of 9.42×10^{-3} mm^3/Nm, corresponding to LP-TME. However, the experiments with the LP aged specimens, namely LP-A, and LP-TME+A experience low COF/low wear values, of 0.53, 0.65, and 2.61×10^{-3}, 0.8×10^{-3} mm^3/Nm, respectively. The tribological performance of the untreated aged sample (INC 617-A) falls into the moderate region, with an average COF value of 1.17 and wear rate at 6.8×10^{-3} mm^3/Nm, but still higher friction and wear is observed compared to LP-A, and LP-TME+A samples.

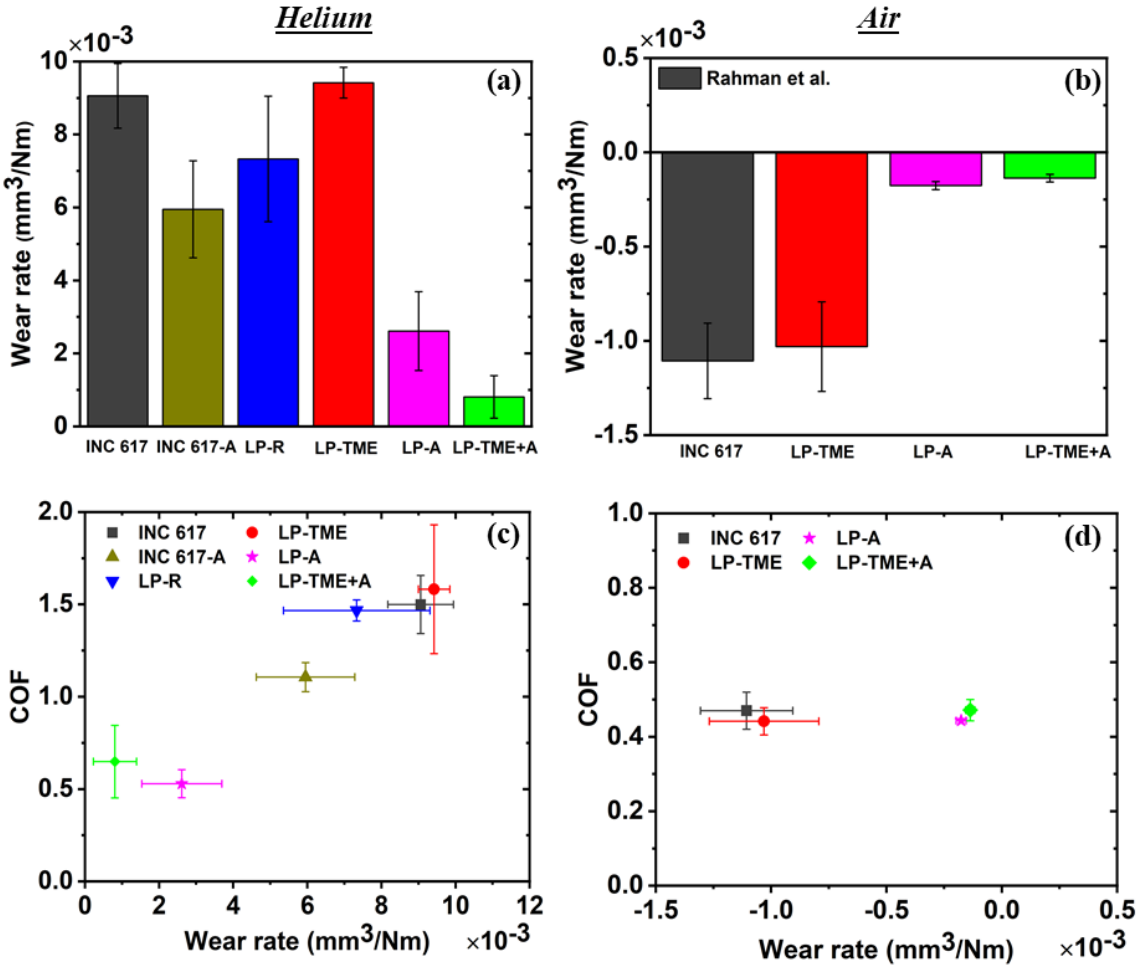

Figure 7.6 Wear rates of the disks following tribo-testing in (a) He and (b) air environment. Average COF vs. wear graphs after tribo-testing in (c) He and (d) air environment. Reprinted with permission from [15].

7.3.5. Surface SEM analysis

SEM micrographs of the unworn and worn surfaces of the disks after tribo-experiments in He are shown in **Figure 7.8**. The orange arrows on the images of the worn areas shown on the right-hand side indicate the sliding direction of the counter-surface. The left-hand side of **Figure 7.8** presents the morphology of the surface oxides developed on the matrix of the untreated and treated INC 617 disks following tribo-testing in 800°C

He environment. The magnified images are shown on the sides of **Figure 7.8**. **Table 7.3** details the elemental composition of the surface of both the unworn and worn regions of most of the disk specimens under examination. Despite the minute presence of oxygen-containing groups (O_2, H_2O, CO, CO_2) within the testing chamber and the aging furnace, it is sufficient to promote the formation of different types of superficial metal oxides on all specimens as reported in Refs. [23,24,41]. Note that the HT tribo-testing for 30 minutes at 800°C in He, can be considered as a short-time aging process, during which fast oxidation kinetics encourage the reactivity of surface atoms with the surrounding atmosphere. The INC 617 matrix appears full of uniformly distributed surface oxide particles. The unworn surface of LP-R shows similar surface oxide particles, as INC 617, with a diameter of less than 500 nm, but finer oxides are also observed in between (gray regions), thus the overall surface oxidation is reduced by the LP process, as also supported by previous studies (e.g., see Ref. [137]). The virgin area of LP-TME appears with larger oxides of around 1 μm in diameter and with a marginal increased percentage of surface oxidation, compared to LP-R. Furthermore, the unworn surface of the aged specimens, namely LP-A, and LP-TME+A feature homogeneous distribution of nodular-like oxides, where several oxides are merged forming long and continuous ridges along the grain boundaries (indicated with white arrows). Comparing the elemental composition of the LP aged specimens (LP-A, LP-TME+A) with the unaged ones (LP-R, LP-TME) of **Table 7.3**, it can be inferred that the surface of the specimens that underwent aging process was mainly covered by Cr-oxide, whereas a Ni-Cr-O mixed oxide layer appears on the unaged specimens. Also, the amount of O found on LP-A, and LP-TME+A specimens is

significantly higher than the amount of the unaged ones due to adequate surface oxidation that was promoted during the aging process.

Investigating the morphology of the worn areas allows correlations with the frictional and wear performance of the tribo-pairs. INC 617, LP-R, and LP-TME, depict similar wear modes, namely oxidative adhesion, and delamination. Deformed surface oxides are evident on the wear tracks of both specimens, without any indication of agglomeration. LP-R features the smallest amount of oxide particles, in accord with the quantitative analysis shown in **Table 7.3**. On the other hand, compacted oxide tribo-layers are found on the wear tracks of the aged samples (LP-A, LP-TME+A), and are identified as Ni-Cr-O mixed oxides. The accumulation and compaction of surface oxide particles result in a significantly higher amount of oxygen in these regions, which are characterized as islands of oxides. Such thick glazed oxides that evidently are further stabilized by the LP process provide an excellent protective layer with lubricating characteristics that results in low COF and wear [21,96]. Furthermore, the running-in period of the aged tribo-pairs, seen in **Figure 7.5(a),** describes the time needed for the compacted glazed oxides to be generated, until a constant zone is reached. In fact, some of the surface oxides are removed from the interface as loose debris, but more importantly some others undergone a shearing, compaction, and accumulation, and thus developing stabilized and strong oxide layers and islands. Longer running-in time for LP-A than LP-TME+A, indicates that more surface material was purged out, until compacted oxide layers were generated. Therefore, the wear rate of LP-A is higher than LP-TME+A as shown in **Figure 7.7**.

The pre-oxidation (aging) process contributes to the subsequent development of compacted surface oxides within the contact region during sliding, which results in enhanced tribological performance. As discussed, experiments following LP, LP+TME, and post aging processes were performed (e.g., see **Figure 7.5)** in an effort to further understand the contribution of each surface and thermal treatments on the tribological response of the tribo-pairs. A synergistic effect of the two surface treatment techniques, namely LP, and aging takes place herein, and eventually strong, well-supported compacted oxide layers are formed during sliding, significantly mitigating friction and wear (LP-A, LP-TME+A). The aging process by itself does not result in measurable tribological enhancements as poor tribological performance is observed for tribo-pair INC 617-A. Also, in a similar study on untreated aged alloy 800HT, high friction and wear values were observed due to the inadequateness of strong, well-supported oxides to be sustained at the interface [130]. It can be hypothesized that the load bearing capability of the subsurface is poor, due to thermal softening at HT, and the plastic deformation of the untreated subsurface induces delamination and removal of the surface oxides [138].

Herein, the LP process induces compressive residual stresses, plastic deformation, defects, and fine grains, resulting in an enhanced surface/subsurface structure, which is retained even after aging the specimens at 950°C (LP-A, LP-TME+A), as seen in **Figure 7.3**. As the LP process alleviates a degree of thermal softening of the subsurface, it is able to support the integrity of the superficial oxide tribo-layers, which provide low friction and wear [129]. Another influencing mechanism could be a stronger interfacial bond between the oxide and substrate promoted by the strengthening effect of the LP process.

Interfacial bond improvement is also reported by Kanjer et al. and Lavisse et al. [107–109] for titanium alloys. They concluded that LP could enhance the adherence of surface oxides by the formation of an intermediate nitride layer on titanium and titanium-based substrates following thermal aging (oxidation) in air environment. While interfacial bond improvement can be also a contributing factor in the current observation, intermediate nitride layer formation cannot be concluded as the aging process and the tribological tests were all carried out in an impure (99.999%) He environment. The chemical composition of the sample also does not show significant amount of N. Rather, here, the stronger interfacial bond is attributed to the microstructural improvements by LP process. In addition to LP process itself, the aging provides the surface with adequate pre-oxidation (**Table 7.3**), in which during sliding surface oxide layers and bulky oxide islands are formed, supported by the LP treated subsurface. Therefore, low COF and wear values are observed. Also, the wear resistance of the LP subsurface is enhanced [117,118,121] and the hard oxide particles are more likely to remain at the interface and form oxide layers, instead of plowing on the contacting surface.

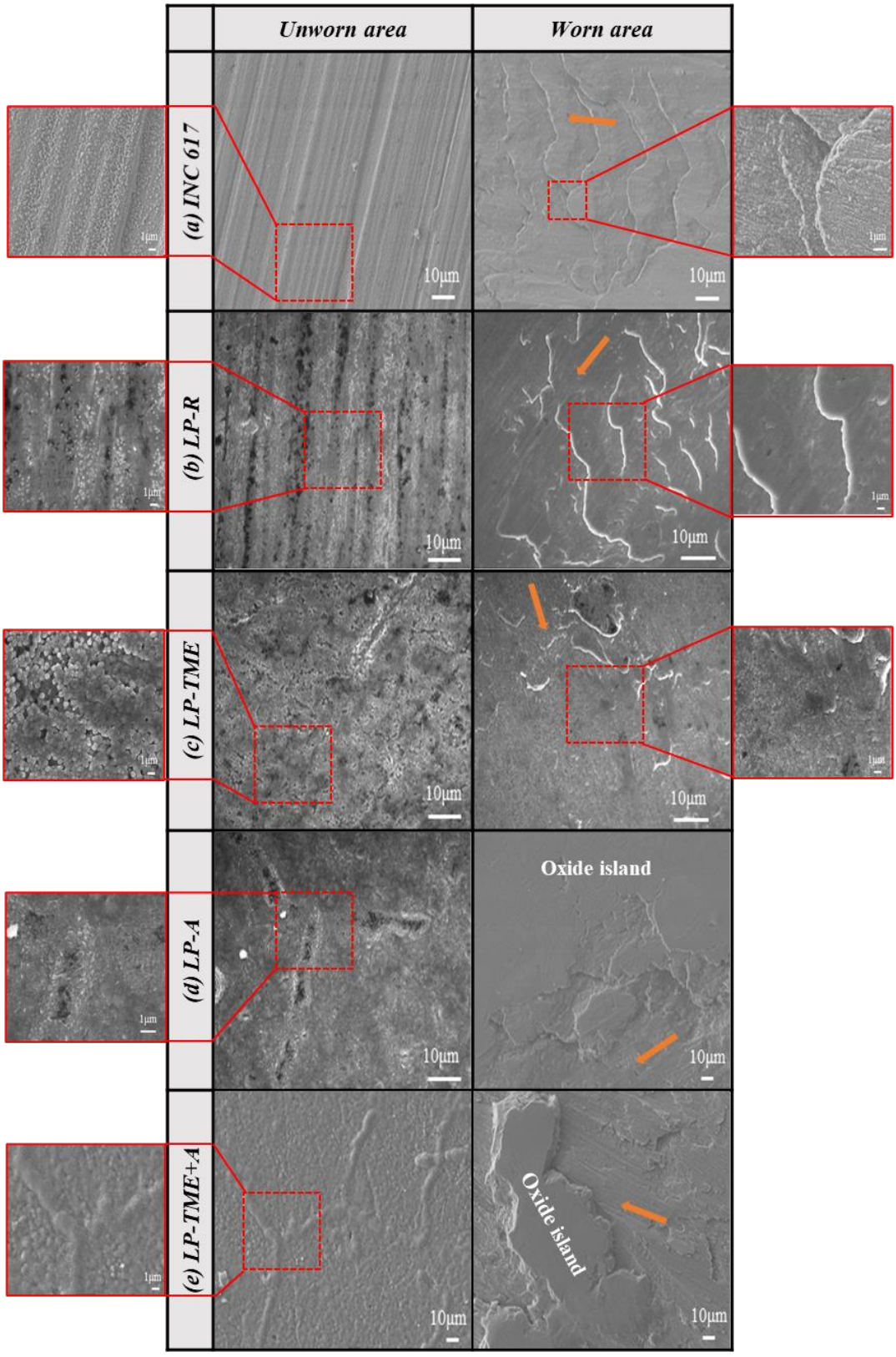
Unworn area
Worn area
(a) INC 617
(b) LP-R
(c) LP-TME
(d) LP-A
(e) LP-TME+A
Oxide island
Oxide island
10μm
1μm

Figure 7.7 SEM images of the unworn and worn surfaces of (a) INC 617, (b) LP-R, (c) LP-TME, (d) LP-A, and (e) LP-TME+A after the tribological experiments in He. Magnified images are shown on the sides of the figure. Orange arrows represent the sliding direction of the counter-surface. Reprinted with permission from [15].

Table 7.3 Chemical composition of INC 617 provided by the manufacturer (units are in wt.%). Reprinted with permission from [15].

	Elements (at%)	**O**	**Al**	**Ti**	**Cr**	**Fe**	**Co**	**Ni**	**Mo**
Unworn area	INC 617	50.4	2.7	0.3	14.4	0.8	5.3	23.2	2.9
	LP-R	45.1	3.1	0.4	15.2	1	5.9	25.8	3.6
	LP-TME	49.5	2.1	0.5	14.8	0.8	5.3	24.3	2.8
	LP-A	71.2	0.3	0.8	26.7	0.2	0.2	0.6	0.07
	LP-TME+A	66.1	0.2	1	30.3	0.3	0.3	1.6	0.2
Worn area	INC 617	43.2	1.9	0.2	15.5	0.9	6.4	28.7	3.2
	LP-R	25.8	1.7	0.4	18.9	1.6	8.6	39.3	4.3
	LP-TME	35.8	1.8	0.3	16.3	1.1	7.5	33.5	3.7
	LP-A	59.5	0.7	0.3	13.6	0.7	4.7	18.6	1.9
	LP-TME+A	66.5	1	0.3	16	0.6	2.9	11.7	1

7.3.6. Optical microscopy – Air environment

The same tribo-testing was repeated for the LP tribo-pairs by changing the environment to ambient air, so the effect of the atmosphere on the tribological performance can be further explored. **Figure 7.8** shows microscopic images of the worn regions of LP-TME, LP-A, and LP-TME+A disk and pin specimens, following sliding in air environment. It is apparent that surface oxides are respectively generated along the wear tracks and the wear scars of all disks and pins resulting in low COF and wear values. LP-TME (**Figure 7.8(a)**) demonstrates well-developed and more compacted oxide layers,

compared to LP-A (**Figure 7.8(b)**), and LP-TME+A (**Figure 7.8(c)**) disks. This is in accord with the longer running-in time of the former, whereas LP-A, and LP-TME+A appear with almost a constant COF from the beginning of the experiment, as shown in **Figure 7.4(b)**. Also, the wear scars of all pins appear to be mostly covered by a thick oxide layer. Several studies were carried out investigating the tribological behavior of metal alloys sliding in HT open environment. It is widely understood that the tribological performance is mainly driven by the oxidation of the rubbing surfaces, that is inevitably taking place in ambient air at HT [139]. In fact, the open environment gives a plethora of oxygen-containing sites that during sliding, tribo-chemical interactions are taking place at the interface, and new fresh oxides are formed continuously replacing the worn ones [23]. This is more pronounced during HT sliding in air, since in He the concentration of O-containing groups in the surrounding atmosphere is significantly lower, and tribo-chemical interactions are much slower, which hinders the formation of new oxides. This is also in line with the wear rate results shown in **Figure 7.76b)**, wherein significant surface oxidation resulted in "negative wear," or material gain in all disk specimens tested in ambient environment. As stated earlier, regardless of the surface modifications and post-aging processes on INC 617, enhanced tribological characteristics prevail in HT air, attributed to different surface oxides, mainly Cr_2O_3 [23,24,41].

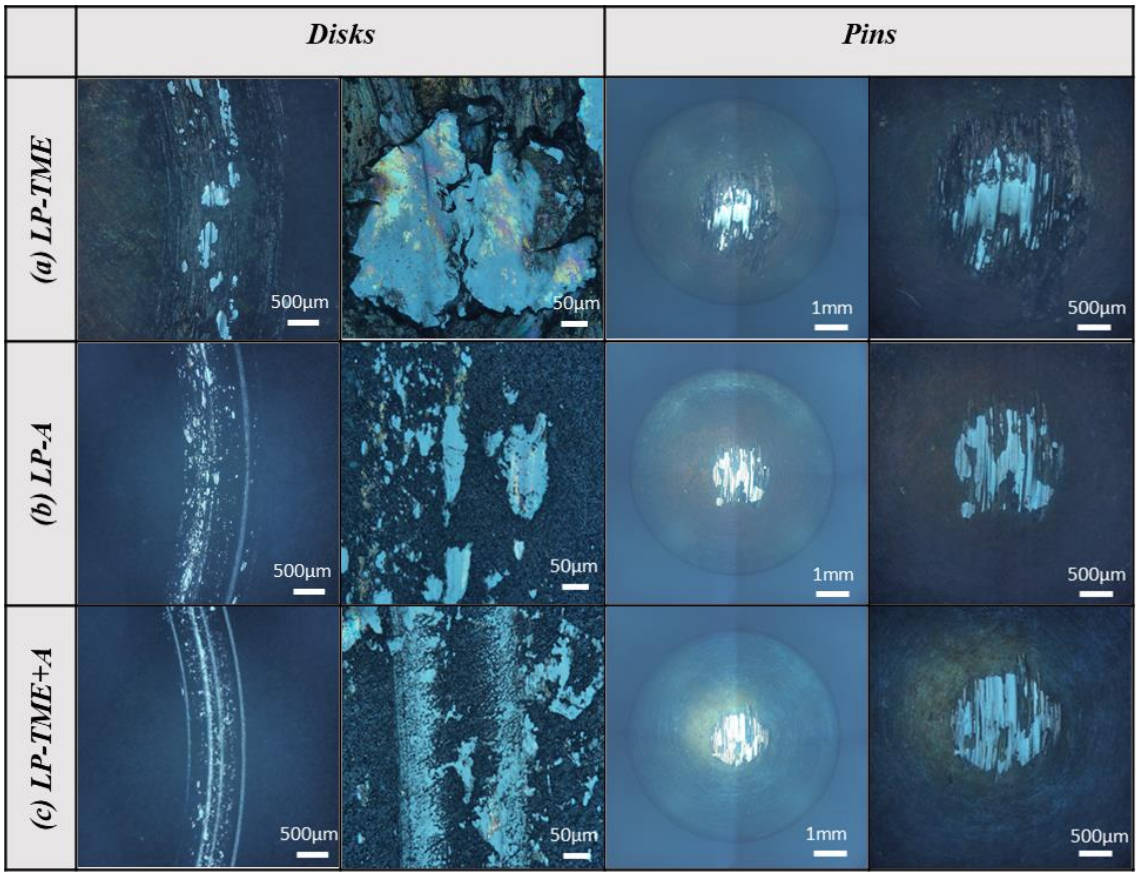

Figure 7.8 Optical microscopic images of the worn disks and pins of (a) LP-TME, (b) LP-A, and (c) LP-TME+A after sliding in air. Reprinted with permission from [15].

7.3.7. Cross section SEM/EDS – He environment

Figure 7.9 presents the cross-section EDS mapping of the unworn areas of the LP disk specimens, namely LP-R, LP-TME, LP-A, and LP-TME+A after the tribo-experiments in He atmosphere. **Figure 7.9(a)** depicts that the main elements were evenly distributed along the thickness of LP-R. The cross-section EDS mapping of LP-TME shows higher surface and subsurface oxidation with a partition of Cr, and Al respectively (**Figure 7.9(b)**). On the contrary, both aged samples, namely LP-A, and LP-TME+A appear with a superficial dense oxide layer of thickness around 6, and 3 µm, as shown in

Figure 7.9(c, **d)**, respectively. The thickness of the surface oxide also shows that our microhardness test depth was sufficient to penetrate deep into the materials reducing oxide effects. **Figure 7.9(c, d)** reveal the surface oxides to be predominantly Cr-oxides with a partition of Mn, and the presence of subsurface oxides of Al. Cr-rich surface oxides are formed on the surface of INC 617 during HT aging in He atmosphere [14,21,23,24,41]. Rahman et. al. investigated the surface of INC 617 aged in He for 100 hours via XRD, and identified the surface oxides to be mainly composed of Cr_2O_3, and $(Ni/Mn)Cr_2O_4$ [23]. Also, Al is found below the surface oxide suggesting that O is diffused into the matrix and reacts with Al, as also reported in Refs. [24,140].

Figure 7.10 maps the elements found on the cross-section of the worn regions of the disk specimens following tribo-sliding under He atmosphere. The topmost layers of LP-R had a marginal increase in the amount of O, and the main elements are evenly distributed within the subsurface, as shown in **Figure 7.10(a)**. **Figure 7.10(b)** demonstrates that LP-TME experiences a higher concentration of O at the topmost layer, where a uniform oxide layer is observed. The amount of surface oxidation on LP-R, and LP-TME disk specimens is not adequate to promote the development of compacted oxide glazes at the interface, hence, a high COF and wear values are observed. On the other hand, the worn area of LP-A appears with a Cr-rich oxide layer, around 6 μm thick with an apparent subsurface Al oxidation, as shown in **Figure 7.10(c)**.

During HT sliding, the pre-formed surface oxide particles are merged under pressure by compaction and maintained on the surface. More importantly, the superficial oxides, supported by the LP subsurface, develop bulky islands of oxides, of 40 μm thick,

which provided excellent lubrication at the interface with low COF and wear values. To further examine the strengthening effect of the islands of compacted oxides, Vickers microhardness measurements were taken targeting selected areas. The microhardness results ranged from 3.5 to 7.5 GPa, with a corresponding penetration depth of 6.3 to 3.4 μm. Such high hardness makes them highly durable during sliding, terminating further wear and maintaining low COF. Similarly, LP-TME+A appeared with mainly Cr-oxide on the surface and Al-oxide underneath. Again, islands of oxides up to 80 μm thick formed at the sliding interface, and efficiently separated the 2 metallic surfaces where a favorable tribological response was observed. The microhardness values ranged from 3.7 to 7.8 GPa, with maximum indentation depths of 5.5 and 3.8 μm, respectively.

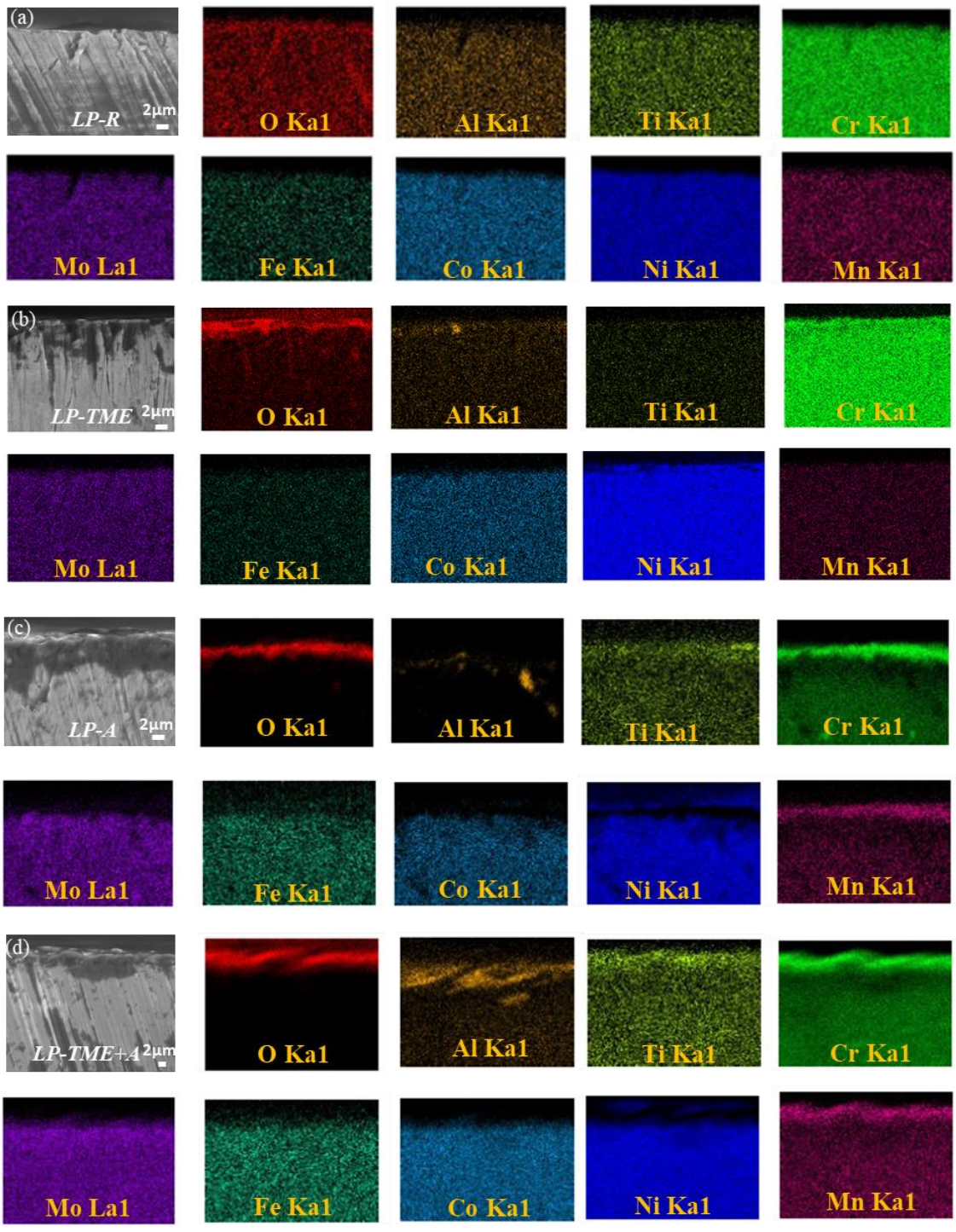

Figure 7.9 Cross-section SEM images and EDS maps of the unworn areas (matrix) after HT tribo-testing in He of (a) LP-R, (b) LP-TME, (c) LP-A, and (d) LP-TME+A. Reprinted with permission from [15].

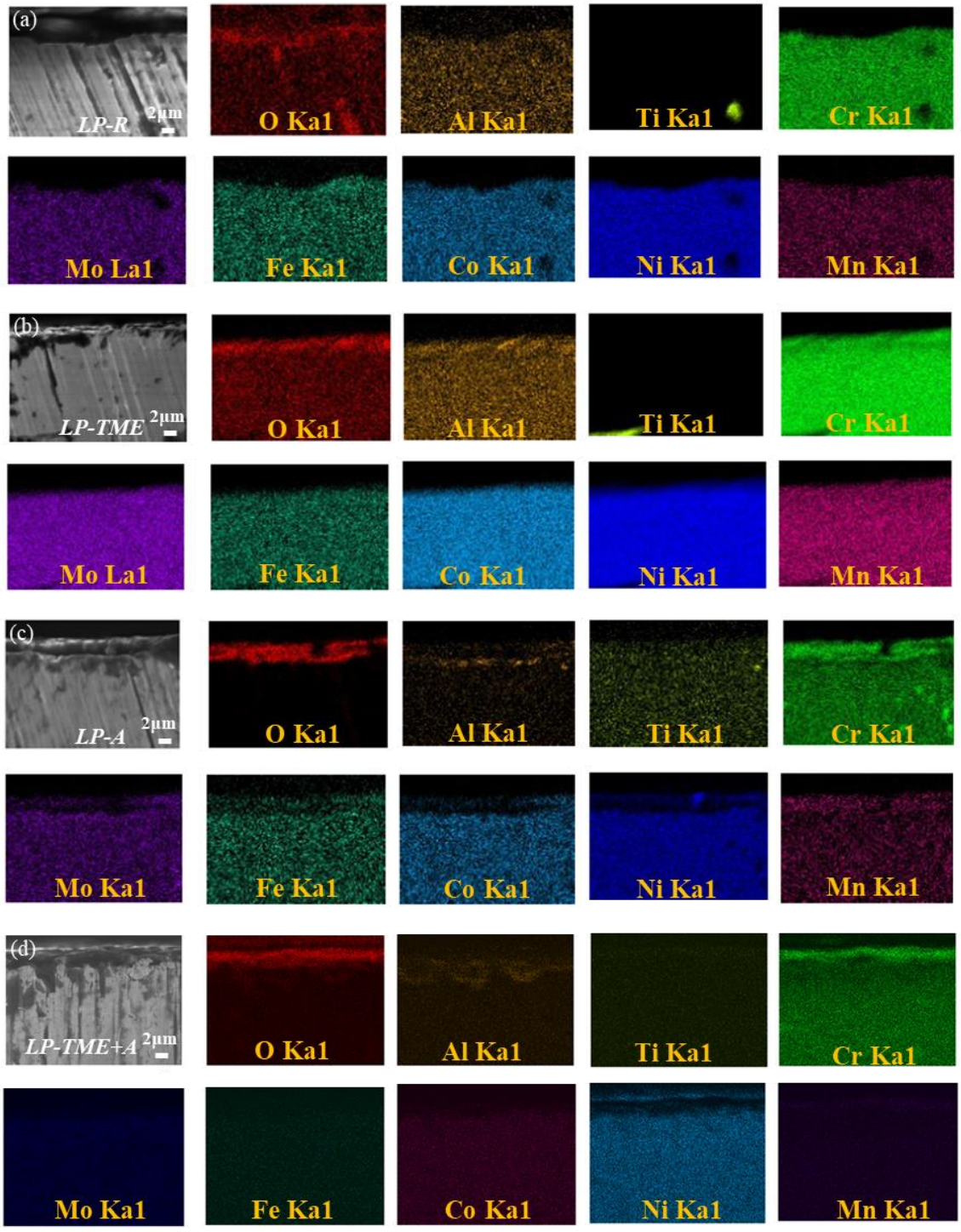

Figure 7.10 Cross-section SEM images and EDS maps of the worn areas after HT tribo-testing in He of (a) LP-R, (b) LP-TME, (c) LP-A, and (d) LP-TME+A. Reprinted with permission from [15].

7.4. Summary

In this chapter the effect of surface modifications, namely LP, TME and post-treatment aging on the tribological performance of INC 617 in HTGR/VHTR (He) and air environments investigated. The following conclusions can be drawn:

- The LP process itself increases the surface microhardness by 62%, whereas the TME process adds a marginal increase on the average microhardness, due to the additional effect of precipitation hardening. After the aging process (950℃-10 hours) relaxation and annihilation of the LP-induced stresses and microstructure are prevented as evident by relatively preserved hardness values. This is also supported by the stabilized microstructure captured through TEM imaging after 60 hours of thermal exposure.
- LP-A and LP-TME+A depicted excellent tribological behavior under impure He environment due to the high amount of pre-oxidation and the supportive role of the LP surface and subsurface to stabilized surface oxides, in contrast with INC 617-A.
- Tribo-testing in HT air environment diminished the effect of surface modifications since adequate continuous surface oxidation at the sliding interface results in low friction and wear overshadowing any other enhancement, if any.
- The findings of this work show that a post-treatment aging process can be coupled with a pre-treatment LP process on the HT superalloy, namely INC 617 to enhance the tribo-response of mechanical components in HT He applications (i.e., VHTR/HTGR). However, the underlying mechanism involved in the process

needs to be comprehensively studied in future works to enhance and optimize the process and to pave the way for effective commercialization of the LP process for HT nuclear reactor components under tribological and potentially tribo-corrosive environments.

This chapter concludes the study on a state-of-the-art surface hardening technique that can be implemented on a Ni-based alloy material used in key components of nuclear reactors. The next chapter introduces a novel additive for realizing superlubricity in practical engineering tribological applications.

8. REALIZING MACRO-SUPERLUBRICITY USING ENCAPSULATED PHASE-CHANGE MATERIALS

8.1. Introduction

Macroscopic friction and wear of tribological parts such as pumps, seals, gears, and bearing systems induce material losses and unwanted energy waste that can put the operation of major systems at risk due to malfunction and dimensional discrepancies of key components. Scientists have been implementing different ways to reduce friction and wear between tribological parts by developing advanced materials with enhanced lubricating properties, such as polymer composites [141]. Polymers, leveraged by their unique chemical configuration, outperform metallic and ceramic materials in terms of chemical inertness and structural stability during thermal shocks. Polymers are also lightweight, which makes them attractive for the automotive and aviation industries [142]. However, in their bulk form they suffer from high thermal expansion coefficient, low creep strength, and poor load-bearing capacity. These unfavorable intrinsic characteristics are mitigated by the use of thin polymer coatings (10's of micrometer thick) covering metallic structural parts, wherein heat dissipation and high load-carrying capability is achieved [143]. In particular, metallic substrates can accommodate high bearing loads by providing structural support to the coatings, and the generated frictional heat, or the temperature from the surrounding environment can be dissipated away from the coating through the metallic substrate [143]. Despite the fact the mechanical and thermal performance can be enhanced by the utilization of thin coatings, the tribological properties

remain poor. Therefore, the use of compounding polymers, or additives with intrinsic lubricating properties is of paramount importance in tribological and bearing applications [144].

Different types of additives have been introduced into polymeric matrices, for example nanoparticles, nanofibers [145,146] and various solid lubricants such as graphite, graphene, MoS_2 and PTFE [16,147–149] to enhance the tribological performance by lubricating the interface. PTFE additive is being widely used by researchers and in industry as a commercial low-friction solid lubricant due to the ease of sliding between its polymeric chains [150]. PTFE can serve as an additive into different polymeric matrices, for instance polyether ether ketone (PEEK), wherein it enhances the tribological response of the composite, compared to unfilled PEEK [151,152]. The polymeric matrix plays a vital role in tuning the wear performance of the composite; therefore a "suitable" selection should be made. It was demonstrated that ATSP provides an accommodative matrix to PTFE. ATSP/PTFE compounding coatings were investigated in an extreme range of temperatures in a self-mate (coating-on-coating) contact configuration, from RT to 300°C. The reported steady-state COF values varied from 0.15 at RT to 0.08 at 300°C. The tested tribo-pairs depicted favorable wear resistance, manifested as "zero wear" under the tested conditions [149]. Therefore, ATSP/PTFE blend is a good material combination wherein ATSP provides structural integrity and controls the wear, and PTFE lowers the friction. However, to further reduce the COF at both RT and HT conditions (i.e., up to 200°C), novel additives or super-lubricative liquids could be added.

Ultra-low friction, or superlubricity (COF < 0.01), is achieved by sufficiently separating the two sliding surfaces with liquid molecules (hydrodynamic lubrication). For example, Raviv et al. developed polymer brushes that were attached onto the rubbing surfaces via an aqueous medium and yielded a COF of 0.0006-0.001 [153]. Also, ceramic materials like SiC and Si_3N_4 were self-tested in water and resulted in super-low COF [154]. Zhou et al. reported COF values in the range of 0.01 to 0.02 for SiC and Si_3N_4 balls sliding against a-CN_x coatings in water [155]. Glycerol-based lubricants were added to steel and ta-C self-mate tribo-systems and tested at 25 and 80°C, yielding COF values up to 0.025 and 0.01, respectively [156]. However, in numerous applications, i.e., in the space industry the use of liquid lubricants is infeasible [157]. Therefore, solid lubricants should be used to deliver adequate lubrication at the interface.

Superlubricity under dry conditions is more complex, and in the nano or micro level it is achieved via an incommensurability phenomenon, wherein the orientation of the surface lattice of one of the contacting surfaces is misaligned with respect to the corresponding lattice of the other surface, thereby preventing the interlocking of atoms and stick-slip phenomena, and an ultra-low frictional force is generated [26]. This is also called structural lubricity, and the concept of a theoretically zero friction (practically COF < 0.01) was proposed by Hirano and Shinjo [158]. Superlubricity was realized by Erdemir et al. a:C-H DLC coatings prepared by plasma assisted CVD under a dry nitrogen environment, yielding a COF of 0.002 [159]. MoS_2 coatings were also tested against steel under high vacuum and the generated COF of 0.001 was attributed to the easy-to-slide of its basal plane and a favorable orientation disorder resulted from sliding [160]. The

interpretation of the superlubricity in the above studies was based on lubricating mechanisms at the micro/nano level. However, realizing superlubricity at the macro level is intricate due to the presence of structural defects, therefore the incommensurability phenomenon is very challenging to be achieved. To that end, the literature is sparse and the studies are limited to obtainable superlubricity under nano and micro-scale normal forces, by developing advanced materials in the macro level, of few cm characteristic dimensions [27]. For example, Zhang et al. reported pioneered superlubricity on macroscale surfaces under ambient environment, by introducing graphene-based coated surfaces, i.e., plates, and microspheres that resulted in an ultra-low COF of 0.006 after sliding under 35 mN and 0.2 mm/s [27]. Also, Berman et. al. generated superlubricity in engineering-scale conditions by invoking carbon-based exotic materials (i.e., graphene, nanodiamond), with the working lubricating mechanism being applied in the nanoscale, uncoupled with computational simulations [28].

While the above state-of-the-art studies realized superlubricity and the corresponding materials can be applied in macro-level surfaces, their more prominent utilization in tribological applications will require higher, engineer-bearing capacities and simplicity of synthesis, therefore low fabrication cost for mass production. Furthermore, frictional surfaces are often subjected to higher temperatures, either due to the generation of frictional heat under high-speed applications, or their presence in HT environments. Superlubricity at HTs, for example up to 200°C, is yet to be explored and the realization of such will pave the way towards the development of novel materials with additives operating at non-generic conditions.

The use of MPCMs is a technology where the core material is enclosed within a surrounding shell, which acts as a protective agent that monitors the release of the core material. The mechanism of encapsulation of lubricating agents is not new, and many researchers have been studying the effect of encapsulated ionic liquids (ILs) and waxes on enhancing the tribological behavior of polymer composites [140,161]. However, the use of phase-change materials (PCMs) as a friction reducer agent is novel, yet the lubricating mechanism of MPCM is simple; the polymeric shell provides structural stability and thermal protection to the core PCM material. Above a critical applied pressure, the shell brakes open and releases the lubricating PCM (mechanical stimulus) at the interface. Also, the PCM undergoes a phase transition from solid to liquid in an endothermic process wherein it absorbs heat from the environment, or the frictional heat generated from sliding contact (thermal stimulus). In a previous work, it was demonstrated that ATSP + MPCM blends generate ultra-low COF (0.05) at high sliding speeds of 1 m/s under ambient temperature [162].

In this chapter, a systematic study towards realizing superlubricity at the macroscopic scale for practical engineering applications up to 200°C was carried out. The surface of structural steel was modified with ATSP + MPCM composite coating deposited by conventional electrostatic powder spraying (EPS) process. The tunability of the generated COF was systematically examined via cyclic temperature, short-duration experiments to expand the applicability of the coatings for smart surfaces and multifunctional structures. The durability of the coatings was also examined via prolonged sliding until failure, manifested as a rapid increase in the in-situ COF.

8.2. Experimental

8.2.1. Materials and sample preparation

To synthesize ATSP resins, two aromatic copolyester systems, namely CB2 and AB2, were crosslinked to form CB2AB2 oligomer system. CB2 and AB2 are decorated with carboxylic acid and acetoxy functional end groups, respectively. During curing, CB2 and AB2 end groups react and the crosslinked aromatic polyester backbone along with acetic acids by-products are generated. Detailed synthesis method of the oligomers is described in Ref. [163]. The CB2 and AB2 oligomers were then ground and sieved into fine particles of a maximum 90 μm size. ATSP powder was blended with 10 wt% MPCM additive. The MPCM additive was purchased from Mikrotek Laboratories, Inc and is identified as Nextek®43D, with a melamine-based wall and paraffin-based core materials. The exact composition of the MPCM is in the proprietary position of the vendor. The 43D designation corresponds to the melting temperature of the core PCM, that is 43 ± 2°C, while the polymeric shell provides thermal stability during curing. The blended powder was directly sprayed onto the sandblasted 52100 square steel plate disks (25.4 mm × 25.4 mm) using EPS. The coated samples were then cured at 245°C for 15 min in a conventional oven, which resulted in the ATSP + MPCM coating. The same procedure was used to prepare neat ATSP, without adding MPCM into the mixture. Note that the standard cure temperature of ATSP coatings is 270°C (and 1 hr), however, as per vendor's recommendation ATSP and MPCM blends should be partially cured to tailor the activation of MPCM and subsequently generate optimum tribological performance. The pins were machined out of a 5.2 mm in diameter 52100 steel rod into 6 mm long cylinders with

round edges of 0.1 mm radius of curvature and a final flat contact of 5 mm diameter. The pins were hand-polished on a Buehler polishing machine using a sequential pass of 600, 800, and 1200 grit size, followed by a final pass of cloth under colloidal silica suspension until the RMS roughness was 0.0727 ± 0.005 μm.

8.2.2. Experimental procedure

A commercial tribometer (Rtec, MFT 5000), was used to perform the flat, pin-on-disk experiments. The setup involved a rotary platform that spins the disk while a fixed pin holder applies load on top of the sample. This pin holder is able to apply equal load on the sample due to the horseshoe-shaped self-alignment holder, which allows for a plane contact configuration. The pin holder is connected to a load cell with a maximum capacity of 220 N normal force. **Table 8.1** outlines the parameters and tribopairs of pins and disks for the experiments. The only parameters changing throughout the experiments are the environmental temperature and duration. Two different tribopairs were subjected to tribological testing under RT, 100, and 200°C environments. The application of 20 N normal force generated 1 MPa nominal contact pressure, while a sliding speed of 0.25 m/s was calculated based on a test radius of 7 mm and 340 revolutions per minute. Multiple tests were conducted using identical experimental parameters to ensure repeatability. Before each test the samples were cleaned with isopropyl alcohol in an ultrasonic bath for 10 min, then dried with hot air. For the temperature testing at 100°C and 200°C, an in-built furnace was used, with a maximum temperature of 1000°C. Each temperature test was allowed five min of heating once the desired temperature of the furnace was reached

and stabilized, to allow for the samples to achieve thermal equilibrium with the environment.

Table 8.1 List of tribo-pairs and experimental parameters.

Study	**Tribo-pair (flat pin vs. disk)**	**T (°C)**	**Load, (Pressure)**	**Speed (m/s)**	**Duration**
Effect of temperature	52100 steel vs. neat ATSP	RT	20 N, 1 MPa	0.25	30 min
	52100 steel vs. ATSP + MPCM	RT, 100, 200			
Tunability	52100 steel vs. ATSP + MPCM	RT→100→RT →100 RT→200→RT →200			10 min at each step
Durability	52100 steel vs. ATSP + MPCM	RT, 100, 200			Until MPCM is depleted

Tunability testing was designed to test how well the COF can be monitored via external thermal stimulus and whether this is a reversible process. This was done by running short, cyclic tests at RT for 10 minutes, then ramping the temperature up to either 100 or 200°C while the samples were idle, and then running for 10 minutes. This cycle was performed twice for each tribo-pair, resulting in a total runtime of 40 minutes. The durability testing involved prolonged running of the ATSP + MPCM disks against the 52100 steel pins at RT, 100, and 200°C. This was to test how long the MPCM within the ATSP matrix would provide lubrication before its complete consumption and the

subsequent increase in the COF. For the RT tests, the contact temperature was routinely measured via an infrared (IR) thermometer during the experiment.

8.2.3. Characterization

A Dektak (Bruker) contact profiler was used to measure the 3D topography of the as-received neat ATSP and ATSP+MPCM specimens with a 12 μm tip radius. Multiple 2D line scans were performed to measure the wear rate of the disks, as described in Ref. [7]. The diameter of the MPCM capsules was measured via optical microscopy using a DSX (Olympus) microscope by dispersing the MPCM particles on a double-face carbon tape. A Tescan FERA-3 model GMH SEM was used to monitor the morphology of the worn areas of the coated disk specimens. The samples were sputtered with a 5 nm palladium and platinum to enhance the electrical conductivity of the samples and to avoid charging effects. The SEM images were acquired using 5 kV acceleration voltages.

A Bruker TI Premier® nanomechanical instrument was used for measuring the nanomechanical properties of neat ATSP and MPCM capsules. The nanoindenter is equipped with a standard transducer which is able for 100 μN to 10 mN normal force indentations. A Berkovich diamond indenter with a tip radius of 320 nm was used to determine the H and E_r of the samples. The nanoindentations were performed at room temperature following the loading/ unloading curve of **Figure 8.1**, with linear loading and unloading at the peak load in 5 sec and hold time 2 sec to reduce creep effects. Note that several indents at different locations with varying loads were performed on each sample to assure homogeneity and therefore consistency of the calculated nanomechanical properties. As for measuring the nanomechanical properties of the MPCM, the

indentations were directed on single isolated capsules exposed on the surface of ATSP+ MPCM composite (and not on free-standing capsules), allowing replication during actual operating conditions where the MPCM is supported by the matrix.

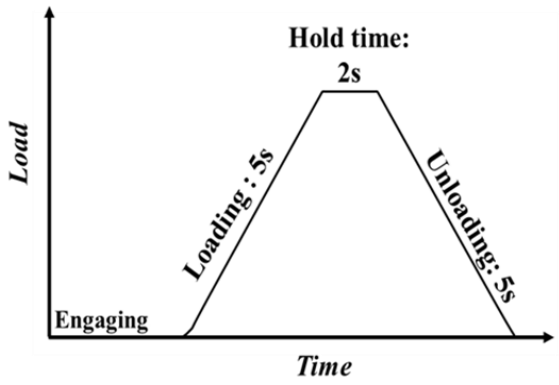

Figure 8.1 Nanoindentation loading/unloading curve versus time.

The Oliver-Pharr method was used to calculate H and E_r of the samples [93]. According to the method the h_c of nanoindentation can be calculated from Eq. (1),

$$h_c = h_{max} - \varepsilon \frac{P_{max}}{S} \quad (1)$$

where P_{max}, h_{max}, and S represent the maximum load, maximum displacement, and initial slope of the unloading section of the load-displacement curve, respectively. For Berkovich indenters, $\varepsilon = 0.72$. Using a predetermined areal calibration on a standard fused quartz, A_c was calculated from h_c. After that, H and E_r were determined using Eqs. (2) and (3), respectively,

$$H = \frac{P_{max}}{A_c} \quad (2)$$

$$E_r = \frac{\sqrt{\pi} S}{2\sqrt{A_c}} \quad (3)$$

8.3. Results and discussion

8.3.1. Surface parameters

Figure 8.1 shows the surface topography of neat ATSP and ATSP + MPCM samples in a 3D representation of a 1 mm × 1 mm area on the samples. The neat ATSP sample appeared relatively smooth, with occasional hills and valleys caused by the deposition process. In comparison, the ATSP + MPCM shows high peaks and deep valleys. These peaks are caused by MPCM accumulation, which are spheres mixed within the ATSP powder during the coating process, as shown in the optical images of **Figure 8.3(a, b)**.

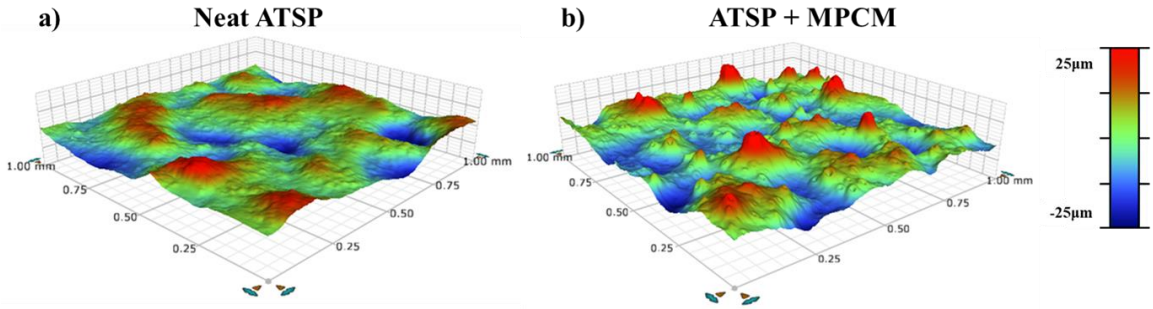

Figure 8.2 3D representation (1 mm x 1 mm) of (a) neat ATSP and (b) ATSP + MPCM samples.

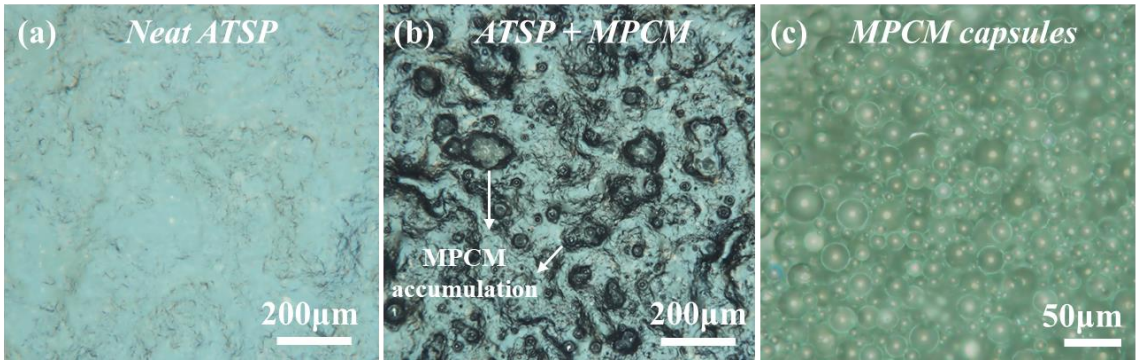

Figure 8.3 Optical microscopic images of (a) neat ATSP, (b) ATSP + MPCM, and (c) MPCM capsules.

Table 8.2 Surface parameters of the samples measured via contact profilometry of 1 mm × 1 mm area.

Roughness parameters	**Sa (µm)**	**Sq (µm)**	**Ssk**	**Sku**	**Sp (µm)**	**Sv (µm)**
Neat ATSP	2.69	3.36	-0.16	3.04	10.32	-11.97
ATSP+MPCM	3.5	4.48	0.26	4.38	18.23	-21.89

Table 8.2 lists some of the surface parameters of the two samples. The neat ATSP showed a lower average absolute roughness (*Sa*) and a lower RMS roughness (*Sq*) than the ATSP + MPCM sample. Typically, a lower surface roughness would provide a lower COF and shorter running-in periods, however the peaks on ATSP + MPCM are lubricating "reserves" which during sliding are subjected to shearing and the capsules breaking open and release the PCM lubricant, allowing for the reduction in the generated friction force. Also, a negative skewness (*Ssk*) was observed for neat ATSP, demonstrating a higher average depth of the valleys than the average high of the peaks, in contrast with ATSP + MPCM which a positive *Ssk* was seen due to the high peaks of accumulated MPCM. The kurtosis (*Sku*) measures the peakedness of the height distribution of profile shape, and a value of *Sku* = 3 describes an ideal Gaussian surface (follows Gaussian distribution), which was the case of neat ATSP. However, ATSP + MPCM appeared with slightly deviated value (>3) attributed to a narrower shape of the distribution of the surface profile. The highest mean-to-peak (*Sp*) and highest mean-to-valley (*Sv*) values of the ATSP +

MPCM clearly captured the effect of MPCM in roughening the surface, by inducing the formation of deep valleys and high peaks.

The size distribution of the spherical MPCM particles was measured via optical microscopy (see **Figure 8.3.(c)**) and it can be divided into three groups: small, medium, and large size, with diameters of 15 ± 1.5, 25 ± 2, and 33 ± 1 μm, respectively. This is in accord with the data provided by the vendor that is 15-30 μm in diameter with a wall thickness of 0.4 to 0.8 μm. Various capsule sizes affect the surface properties of the disks, for example, larger capsules will yield a rougher surface while more lubricant can be encapsulated as core material, thereby having a controlled mixture of large and small sized capsules can help provide optimal topographical characteristics and amount of stored lubricant.

8.3.2. Nanoindentation

Figure 8.4 shows the load-displacement nanoindentation curves on the ATSP phase (matrix) and the capsules. Note that the exposed capsules were clearly observable from the optics, therefore the nanoindentations could be accurately directed at the center of the capsules. The nanoindentations were performed on single/isolated capsules to minimize the effect of uncertainties in the calculated mechanical properties. Also, the extremely low thickness of the shell (400-800 nm) omits quantitative analysis of the nanomechanical properties of the shell material, and the results should be treated with care as they represented an overall H and E_r from the combined effect of the shell and core materials. It was provided by the vendor that the protective melamine-based shell is much harder than the paraffin-based core, which provided structural and thermal stability.

Figure 8.4(a) shows typical load-displacement curves on ATSP matrix with different normal loads to ensure homogeneity of the mechanical properties through the thickness of the coating. The maximum penetration depth was limited to ca. 1 μm to avoid substrate effects (coating thickness was 30 ± 5 μm) [94]. The nanoindentations on the ATSP matrix yielded an average H of 257.5 ± 14.7 MPa and E_r was 3.96 GPa ± 0.07 GPa. **Figure 8.4(b)** shows the corresponding nanoindentation on the capsules with a much lower normal load of 500 μN to avoid rupturing the shell, evident as a pop-in during the loading stage. Also, identical indentations resulted in different h_{max} (hence H and E_r), that were higher than the thickness of the melamine-based wall therefore the overall H and E_r of the capsules was calculated. The yielded H and E_r of the capsules was 72% lower than that of the ATSP matrix meaning the ATSP phase is acting as a protective mantle and controls the activation during tribological experiments.

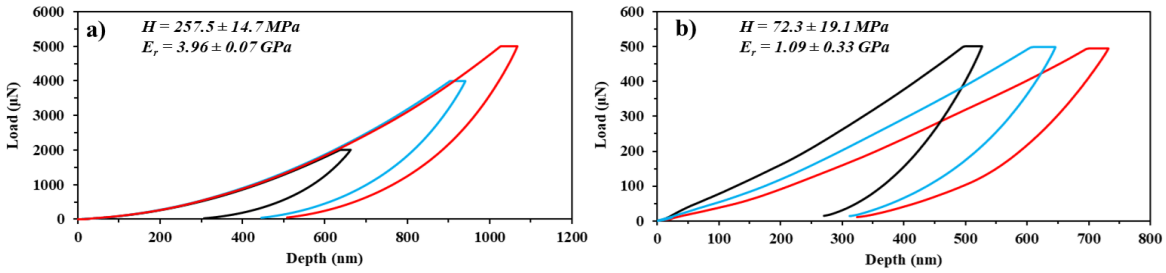

Figure 8.4 Typical load-displacement curves of (a) ATSP matrix and (b) directly in the MPCM capsules embedded in the ATSP matrix. Calculated mean and ± one standard deviation H and E_r are also shown.

8.3.3. COF and wear performance of neat ATSP and MPCM-filled ATSP

Figure 8.5(a) shows the in-situ COF with time and the corresponding average values from repeated experiments are depicted in **Figure 8.5(b)**. The test with the neat ATSP served as a benchmark to gauge the effect of MPCM additive incorporation on the frictional performance of the tribopairs. The reference experiment with the neat ATSP was only tested at RT and generated unstable evolution of COF with values ranging from 0.35 to 0.55 with high fluctuations, which attributed to a continuous wear process and the generation of accumulated debris at the interface that dynamically changed the contact mechanics during the experiment. The addition of 10 wt% MPCM resulted in an enormous reduction in the friction, with the in-situ COF appearing smooth and constant throughout the experiment, with instantaneous values below 0.1. With the addition of temperature, the COF was further decreased, inducing a positive effect on the lubrication efficiency of the MPCM. In fact, the ATSP + MPCM tribopair yielded the lowest COF values during the experiment when tested under 200°C, which was slightly lower than the corresponding experiment at 100°C. Note that there were no other additives in the ATSP matrix, other than the MPCM. **Figure 8.5(b)** shows the average COF values calculated from identical experiments, and the error bars represent ±1 standard deviation from the mean value. The experiment at RT with the neat ATSP yielded an average COF value of 0.46, and the incorporation of MPCM resulted in 83% reduction, at an average value of 0.08. Note that neat ATSP is a structural material which generates low COF values (< 0.2) only when is compounded with suitable additives, such as PTFE [162]. At 100 and 200°C, the COF was further decreased at 0.04 and 0.03, respectively, approaching the superlubricity regime

that is below 0.01 [158]. At 100 and 200°C environmental temperatures, that are beyond the melting temperature of the MPCM (43°C), the paraffin undergoes a phase change from solid to liquid, therefore the lubrication characteristics are changing. The paraffin in liquid form can act as an externally supplied lubricant that generates mixed lubrication at the interface. As liquid form paraffin can flow, instead of only shearing, therefore the "wetted area" and the lubrication efficiency is increasing, and a lower COF was observed, as described thereafter.

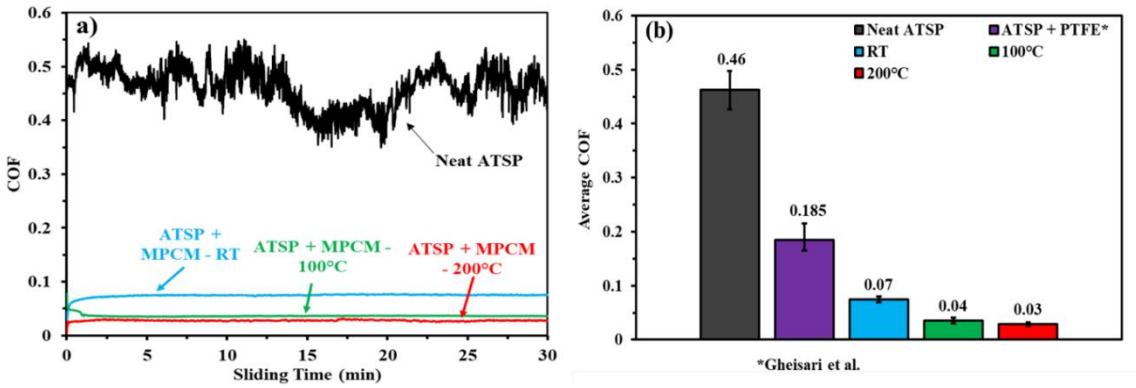

Figure 8.5 Comparison of COF for (a) in-situ monitoring and (b) average COF values of neat ATSP at RT, and ATSP+MPCM at RT, 100, and 200°C.

Figure 8.6 shows typical 2D and 3D wear profilometric scans of the tested samples following 30 min testing. Note that the scans covered both the unworn and worn areas, therefore information of the wear depth and the severity of the contact can be acquired. **Figure 8.6(a)** describes the wear on neat ATSP (unfilled) after RT tribological testing and a deep groove reaching 35 μm depth can be observed. The wear rate was calculated to be 7.96×10^{-5} mm^3/Nm based on the worn volume, the normal force and the sliding distance,

as described in Ref. [7]. As mentioned in **Section 8.2.1**, the curing temperature and time for ATSP was tailored to generate a control wear process in a way that more MPCM capsules would be activated through the depth, therefore the durability of the coatings is prolonged, as described in **Section 8.3.5**. The wear track shows two distinct wear modes, that is heavy burnishing of asperities (6-8 mm in 2D scan) and plowing of the surface due to a hardness mismatch between the metallic and the polymer tribo-surfaces. The addition of 10 wt% MPCM (**Figure 8.6(b)**) resulted in a significant decrease in the wear depth, and a change in the wear mode from severe plowing to mild asperities polishing. In fact, the RMS roughness of the worn area was reduced to be 3.09 ± 0.63 μm, compared to 4.5 μm for the as-received ATSP + MPCM coating. In order to express the amount of decrease in the height of the asperities, the ratio of the normalized (per lateral distance) summation of the profile peaks outside and inside the wear track was measured. After the RT testing, the ratio was found to be 2.5, meaning that the asperities inside the wear track were shortened by 2.5 times. At 100°C, the ATSP+MPCM was subjected to a mild degree of polishing, or "zero wear" (RMS roughness was 3.54 ± 0.16 μm and asperities ratio 1.05) indicating that the lubricating mechanisms of the PCM are temperature dependent, and therefore the amount of wear is different, compared to RT testing, as seen in **Figure 8.6(c)**. This is not surprising as the MPCM used in this study has a melting point at 43°C, therefore a testing temperature of 100°C would have caused the released PCM to melt. The contact temperature during the RT experiment was routinely (every 2 min) measured via an IR thermometer and it remained fairly unchanged after 30 min of testing. The thermal equilibrium is dynamically reached due to the melting (endothermic) process of the

exposed PCM at the interface, and the temperature is expected to increase with the full depletion of the capsules due to frictional heat. **Figure 8.6(d)** illustrates the wear profile of ATSP + MPCM following tribological testing at 200°C. A smooth surface can be observed (RMS roughness 2.72 ± 0.25 µm, and asperities ratio of 3.5), resulting from a burnishing and filling effect of the peaks and valleys, respectively. It can be postulated that the increase in testing temperature, close to cure temperature caused the shearing of high asperities, while the melted paraffin covered the valleys resulting in a favorable tribological interface and an ultra-low COF was observed.

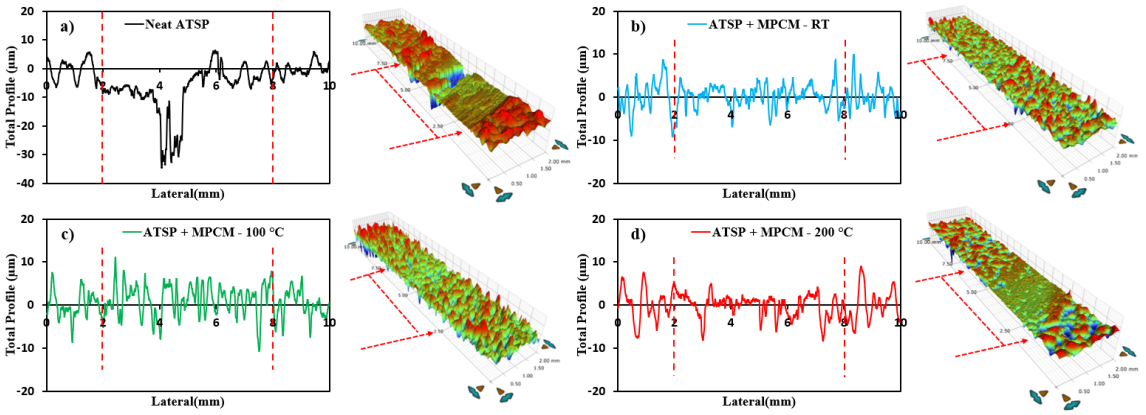

Figure 8.6 2D and 3D profilometric scans following tribological experiments of (a) neat ATSP at RT, and ATSP + MPCM at (b) RT, (c) 100°C, and (d) 200°C.

Figure 8.7 illustrates the SEM images of the worn ATSP + MPCM specimens after 30 min of experiments at the three selected temperatures, namely RT, 100°C, and 200°C. The sliding direction of the countersurface is shown with arrows. The surfaces of ATSP + MPCM samples appeared smooth at all temperatures, with, however, different lubrication mechanisms in place. **Figure 8.7(a)** shows that multiple capsules remained

intact, while other capsules were raptured, releasing the encapsulated PCM. The released PCM remained in solid "waxy" form and did not flow at the interface but was only subjected to shearing. However, at 100°C the surrounding environment could provide sufficient heat to the PCM to melt and flow, therefore wetting the interface. In fact, **Figure 8.7(b2)** shows wrinkled-like melted PCM from adjacent activated capsules, which generated mixed lubrication, hence the ultra-low COF. Similarly, **Figure 8.7(c)** depicts uniform "islands" of melted PCM covering the contact surface after testing at 200°C. Note that fresh capsules cannot be seen on the surface due to the full depletion from the surface or the covering of them due to the melted PCM. Compared to 100°C, these lubricating paraffin-based films were more compacted, smoother, and wrinkle-free, presumably due to better flow characteristics of the paraffin-based PCM at higher temperatures. Adequate lubrication will be generated at the interface until the full consumption of the PCM, as discussed in the durability study of **Section 8.3.5**.

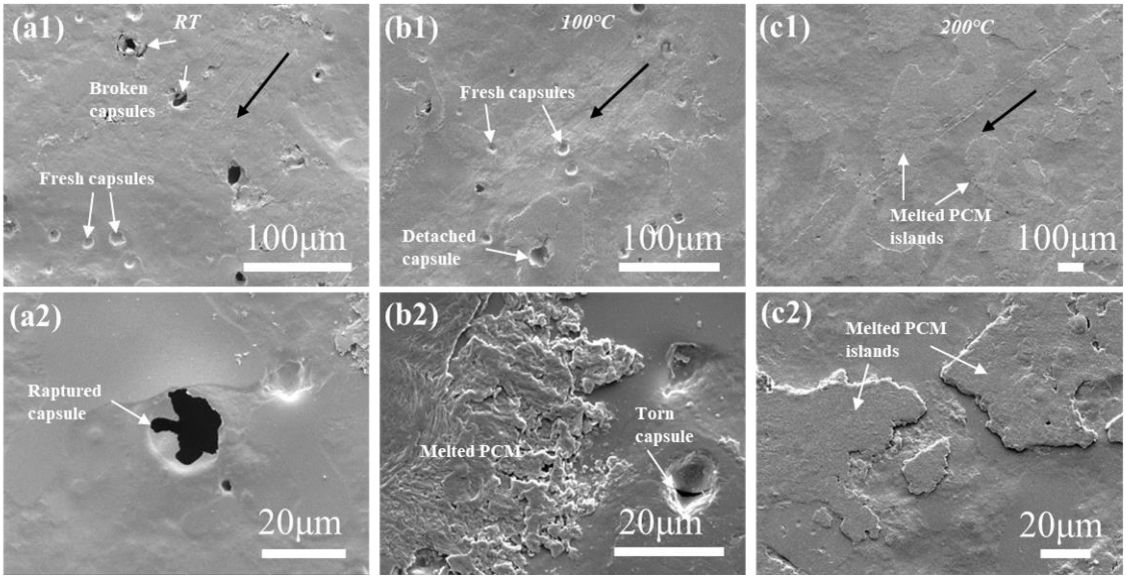

Figure 8.7 SEM micrographs of ATSP+MPCM after 30 mins tribological experiment at (a) RT, (b) 100℃, and (c) 200℃.

8.3.4. Tunability of MPCM-filled coatings

In this section the reversibility of the COF with thermal stimulus was examined via cyclic tunability experiments using the same tribo-surfaces, as detailed in **Table 8.1**. The average COF at each temperature for the two tests is shown in **Figure 8.8**. The error bars represent the deviation of the in-situ COF from the average value during the 10-min intervals. The initial contact at RT generated an average COF of 0.065, and with an increase in temperature to 100℃ the average COF value dropped to 0.034, due to the phase change of paraffin and the increased lubricating efficiency. The 2nd cycle of RT testing resulted in slightly lower COF, compared to the 1st cycle at a value of 0.057, presumably due to a higher coverage area of the contact surface by the previously melted and newly solidified paraffin. The 2nd reheating cycle yielded a COF of 0.018, demonstrating a good tunability of the COF by altering the surrounding temperature.

The same experiment with a fresh interface was performed with temperature increasing from RT to 200℃ to examine the reversibility of the COF at a wider range of temperatures. During the first contact at RT the generated average COF was 0.092, and with an increase in temperature to 200℃ the COF experienced a 32% decrease. Note that the difference between the average COF values of the two 1st cycle experiments at RT shows that the tribo-systems are vulnerable to surface characteristics of the contacting surfaces, predominantly the distribution of the capsules wherein unfavorable agglomerations/clustering disturb the uniformity on the surface (see **Figure 8.3(b)**),

thereby the lubricating efficiency. During the 2nd RT cycle the COF was returned to higher values, that is 0.1, before returning to 0.055 at 200°C. **Figure 8.8** uncoupled a novel capability of the MPCM, that is a good control of the frictional performance of MPCM-filled polymeric composites via thermal stimulus, which arise from the intrinsic characteristic of PCMs to change their physical properties at critical temperatures. Therefore, a proper selection of a particular type of PCM (i.e., with different melting temperatures) can be made to accommodate the use of polymeric and MPCM blends at different environmental conditions and tribological applications.

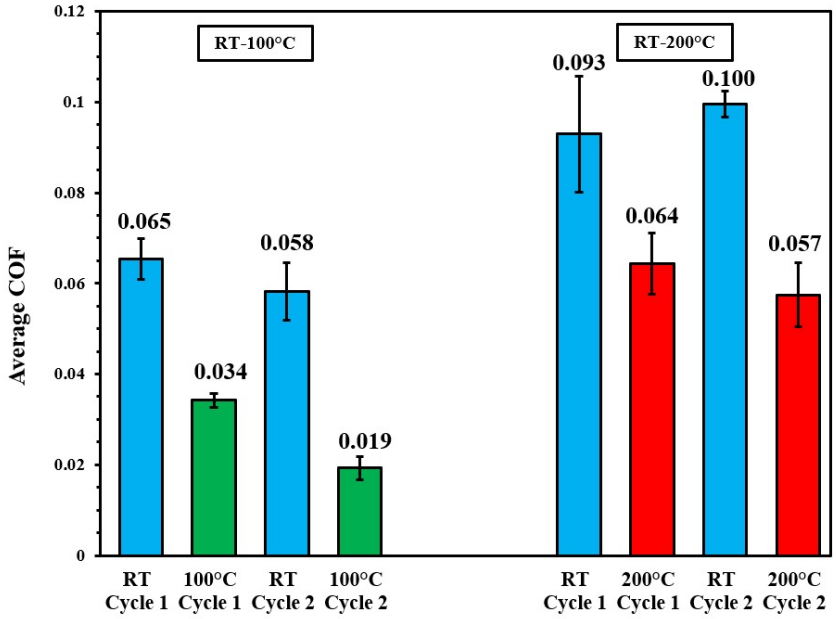

Figure 8.8 Average COF results from tunability study of cycle experiments at RT, 100, and 200°C.

8.3.5. Durability of MPCM-filled ATSP coatings

MPCM additive inside the ATSP matrix acts as a dynamic lubricating agent by the controlled rapture and activation of the capsules. The capsules are both exposed on the surface and through the thickness (capsules < 30 μm). It is therefore expected that with the full depletion of the MPCM the frictional performance of the composite will deteriorate. The durability of the capsules in providing ultra-low friction was examined via prolonged tribological testing, as shown in **Table 8.1**. **Figure 8.9** shows the overall tribological performance of ATSP + MPCM at RT, 100, and 200°C. The in-situ COF against time of **Figure 8.9(a)** reveals the critical time/sliding distance at which a full depletion of MPCM is taking place, manifested as a rapid increase in the COF, if any. **Figure 8.9(b)** shows profilometric line scans of the worn surfaces of the ATSP + MPCM composites, and **Figure 8.9(c)** illustrates the corresponding SEM images (insets represent high magnification images). The sliding of ATSP + MPCM at RT resulted in a fairly constant evolution of COF, after a mild hump at ca. 20 min of sliding time. The experiment was terminated after 160 min/2,400 m of sliding distance as a steady-state behavior was reached. The 2D scan of **Figure 8.6(b)** shows the burnishing of high asperities, and **Figure 8.9(c1)** illustrates a smooth surface formed from the overlaid paraffin wax that acted as a durable solid lubricant providing longevity at the interface. The cyclic stress concentration and fatigue initiated micro-cracks and minute platelet-like material removal [164], without altering the contact dynamics, enabling the COF to remain constant. It is expected that once a critical number of cycles is reached, the cracks will propagate and merge resulting in catastrophic failure of the film and the lubrication mechanisms will be terminated.

When the temperature was raised to 100°C the COF started increasing after 70 min or 1,050 m of sliding distance, attributed to the insufficient lubrication from the remaining capsules (if any). From the wear scan of **Figure 8.9(b)** it is apparent that the composite coating experienced some amount of material removal, with a wear depth reaching 7.5 μm, which was critical for the lubricating efficiency of the capsules. Also, the low magnification SEM image of **Figure 8.9(c2)** captured loose debris that is believed to be shell peels following the rupture of the vast majority of the capsules (see broken capsule at high magnification inset). The experiment at 200°C generated instantaneous COF values at 0.05-0.06 for 20 min, followed by a monotonic increase up to 0.1 at 30 min of sliding, which covered 450 m of sliding distance. The COF continued to increase beyond 0.1 and the experiment was terminated after 40 min. The wear depth remained shallow, yet critical at ca. 7 μm. The SEM image indicates mild adhesive wear and shell peels on the surface (as at 100°C), which could expedite the wear process.

It was seen that the lubrication mechanisms of the MPCM are temperature dependent. At ambient conditions, the frictional heat is not sufficient to melt the PCM, therefore the paraffin-based wax is only subjected to shearing, forming a passive and durable interlayer that alleviates the friction between the polymer and metallic counter-surface. While an extreme durability performance was observed (> 2,400 m), to achieve ultra-low COF approaching the superlubricity regime the PCM must be melted to generate mixed lubrication. However, as liquid lubrication is being generated internally, without continuous external supply, the interface will reach starved conditions due to the consumption of PCM which is being squeezed out of the contact (due to the act of

centrifugal forces) resulting in excessive wear and an increase in the COF. The durability at 200°C was deteriorated, due to ATSP softening (note ATSP curing at 245°C) and subsequently decreased wear resistance, thereby faster consumption of the MPCM.

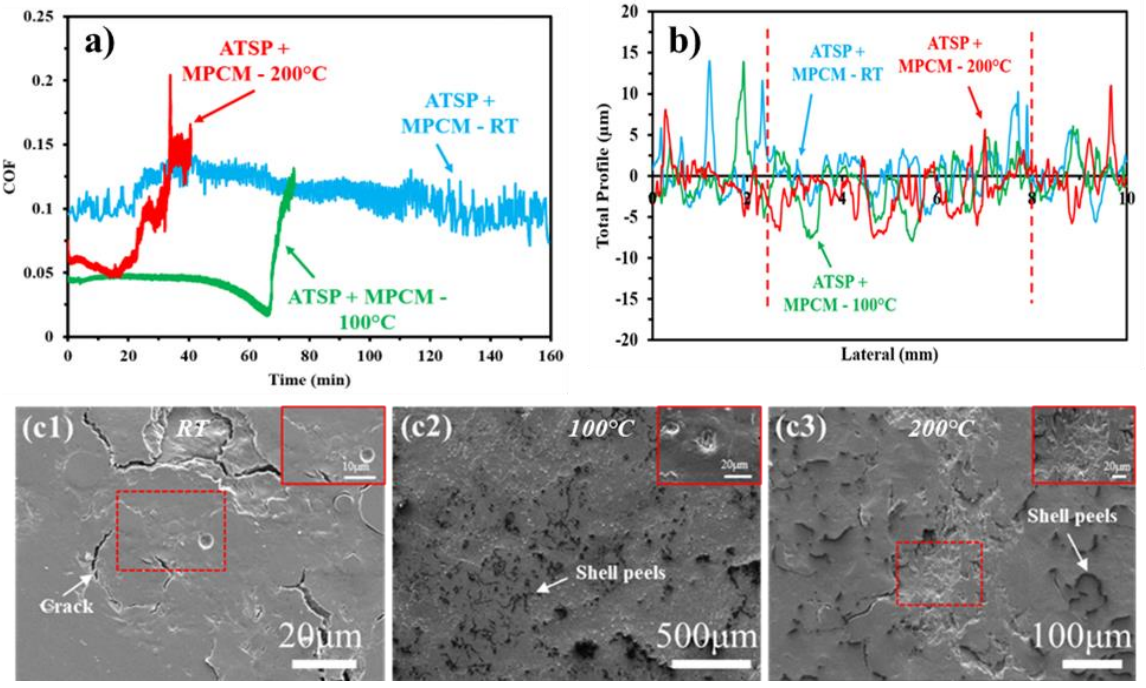

Figure 8.9 Tribological performance of ATSP + MPCM durability tests at RT, 100, and 200°C. (a) In-situ COF against time, (b) 2D wear profilometric scans, and (c) SEM images of worn surfaces. High magnification images are shown as insets.

8.4. Summary

A novel additive was introduced into an advanced polymeric matrix seeking superlubricity at the macroscale level for engineering practical applications. In this chapter the ATSP + MPCM composite was subjected under HT conditions, up to 200°C. Also, the tunability and durability characteristics were investigated, and the following conclusions can be drawn:

- The incorporation of MPCM additive reduced the COF by 85% and at 0.07 under RT conditions. At 100 and 200℃ an ultra-low COF was generated, at 0.04 and 0.03, respectively. The melted PCM realized mixed lubrication at the interface, whereas a passivated interlayer was formed from the paraffin wax at RT conditions.
- The frictional performance of ATSP + MPCM coatings can be tuned by thermal stimulus which changes the lubrication mechanisms.
- At 100 and 200℃ starved conditions are reached after 70 and 30 minutes, respectively, whereas at RT a fortified durability was observed.
- The findings in this study show that paraffin-based PCMs can generate tunable, ultra-low COF under engineering applications. However, the underlying lubricating mechanisms should be further studied experimentally and computationally to optimize the composite material and to pave the way for commercialization for practical superlubricity applications.

9. CONCLUSIONS AND RECOMMENDATIONS FOR FUTURE WORK

9.1. Conclusions

A comprehensive experimental tribological study was conducted in this research to systematically evaluate and compare the performance of different ceramic and alloy coatings, Ni-based HT bulks, and novel additives in polymeric matrices for use in bearing systems for Venus exploration, key components in nuclear reactors, and multi-functional structures for superlubricity, respectively. The main objective was to assess the feasibility of employing these materials and techniques to the specific applications discussed in each chapter. Most of the work done in this research covered the selection of materials, design of experiments and tribological evaluations of suitable interfaces for Venus exploration. However, the last two chapters enriched this work with similar studies for other extreme environments, for example very HTs in nuclear reactors and extreme operating conditions for macro-superlubricity applications. The scientific contributions and summary of the main findings are summarized below:

1. The latest version of PS coatings, namely PS400, suffered from generating high friction and wear at low temperatures, i.e., RT. Hence, the selection of a suitable mating surface could expand the applicability to a wider range of temperatures, for example during descending of the exploration equipment, i.e., probes and rovers onto the surface of Venus. As discussed in **Chapter 2**, DLC coating enhanced the RT friction and wear properties of the NASA-developed PS400 when selected as a tribo-pair, expanding the capabilities of the coating. PCD coating was not

tribologically compatible with PS400 due to a hardness mismatch that induced significant wear on the softer PS400 surface.

2. From the literature it was apparent that the lubricating mechanisms of PS400 are solely relied on the formation of oxide glazes at the interface during HT sliding in oxidative environments. In **Chapter 3**, PS400 vs. DLC tribo-pair was tested under air and CO_2 environments. It was shown that up to 300°C DLC coating controls the COF and wear mechanisms of the tribo-pair, and at 500°C DLC worn out due to significant structural changes (graphitic contributions) and PS400 provided adequate lubrication, either in the form of uniform transfer glaze oxide layer or minute oxide traces, under air and CO_2 environments, respectively. Reasonably, the formation of uniform oxide layer is favorable with better lubricating characteristics and wear protection. Also, CO_2 environment provided a plethora of functional groups to terminate dangling bonds of the DLC coating subjected in superficial layer removal. Therefore, PS400 and DLC is a dynamic tribo-pair from RT to 500°C (with intermediate temperature of 300°C), wherein each coating controls the friction and wear via different mechanisms.
3. Tribo-testing under Venusian-simulated environment is paramount for selecting potential interfaces for bearing application for surface exploration. In part of this study a HT stage was engineered and installed in an existing tribometer for testing under realistic conditions. To the author's knowledge, this is the sole device that can measure the COF and wear properties of materials under near-Venusian conditions. In **Chapter 4** different surfaces were selected and slid against PS400

coatings (coating vs. coating). It was found that $TiMoS_2$ and DLC coatings have a significant contribution in reducing the friction and wear compared to when PS400 is rubbing against a Ni-based metal (metal vs. coating). The $TiMoS_2$ and DLC can act as sacrificial layers, whereafter PS400 coating will provide adequate lubrication if prolonged sliding is required.

4. The effect of Venusian exposure on the morphology of exposed electronics, sensors, and structural surfaces was adequately studied. However, the effect on friction-reducing coatings on this aspect has yet to be explored. In **Chapter 5**, previously tested coatings were subjected to 74-hours Venusian aging and the topographical, chemical, and mechanical properties were investigated. It was found that the S-constituents of the Venusian atmosphere reacted with the surface of PS400 and PCD and formed S-rich particles that densely covered the coatings and changed the surface properties. DLC and $TiMoS_2$ experienced the highest reduction in their corresponding hardness values, followed by PS400, whereas the mechanical properties of PCD remained unchanged. Depending on the application (i.e., the mechanical part on a rover, drill, probe etc. of interest), the most "appropriate" material can be selected. For example, if chemical inertness to the Venusian environment is of interest, DLC and $TiMoS_2$ would be preferrable, whereas PCD would be favorable for mechanical parts wherein structural durability and dimensional stability are of high importance. Therefore, the new knowledge provided from this study is contributing to the development of future

probing equipment, such as all-mechanical rovers for exploiting the surface of Venus.

5. Following Venusian aging the above coatings were subjected under tribological evaluation and the results were presented in **Chapter 6**. On one hand, the Venusian exposure did not change the wear performance of the tribo-pairs significantly, and on the other hand the physically adsorbed S-rich particles improved the frictional performance, upon compaction and melting at the interface. This preliminary work on the tribological performance of friction materials revealed that the adverse atmosphere of Venus might not necessarily act negatively on tribological systems.
6. In **Chapter 7** a different application was considered, that is nuclear reactors. The high operating outlet temperatures (>800°C) do not suggest the utilization of the coatings examined in the previous chapters. Therefore, Ni-based HT alloys were introduced instead. However, the unmodified alloys exhibit high friction and wear in He HT nuclear environment. A state-of-the-art laser peening hardening process found to have a beneficial effect of the bearing capacity of oxide layers formed during He aging process (exposure), and hence lowering the COF and wear significantly. Therefore, a special treatment of Ni-based HT alloys with LP for surface and subsurface hardening and thermal aging for enrichment with beneficial oxides can be implemented to significantly enhance the tribological performance in extreme HTs.
7. In **Chapter 8** an approach in realizing superlubricity at the macro level for practical engineering application was made. Superlubricity is always linked to the

nano and micro level through the incommensurability phenomenon. A novel MPCM additive is proposed for tunable, ultra-low friction applications up to 200°C when added to an advanced polymeric matrix (i.e., ATSP) for controlled activation and lubrication.

9.2. Recommendations for future work

In the systematic studies of **Chapter 2-6** potential bearing materials were examined under different conditions, seeking realistic Venus operating environment. A big challenge in this study was to design and implement a unique specialized apparatus for tribological testing under Venusian-simulated conditions. While the pressurized chamber of UHPT is capable of hosting pressures up to 13.8 MPa, that is higher than the exact surface pressure on Venus (9.3 MPa), the introduction of HT (mean surface temperature on the surface of Venus is 464°C) added more complexity into the system. In other words, the supercritical CO_2 gas can absorb and dissipate enormous amount of heat away from the system, and the maximum pressure at which the sample could be heated up to 464°C was 2.4 MPa. Therefore, for a more accurate replication of the Venusian surface the testing apparatus should be upgraded with a higher power supply and perhaps better insulation. However, it should be noted that other complexities might arise regarding space limitations and safety concerns. Another recommendation would be to perform longer, prolonged tribological experiments. As seen in **Chapter 4** and **6**, the thin DLC and $TiMoS_2$ coatings started wearing off, reaching a critical depth where the complete removal of the coating was imminent. Despite the fact that their utilization could be sacrificial, until PS400 activates, information on their durability performance (until full depletion

from the contact) will be very important in designing the future Venus exploration equipment and identifying the durability of the system. Another recommendation would be the use of the GEER chamber for Venusian aging, instead of the Goddard Space Flight Center where only the main three constituents are considered, that is CO_2, N_2, and SO_2, The GEER chamber simulates the exact Venusian atmosphere, therefore it will give a better understanding on the effect of exposure on the topography, chemical, mechanical, and tribological properties. Also, longer duration exposures could be considered. Last but not least, different contact configurations, i.e., line and point contact should be tested to simulate ball bearing or bushings tribo-systems.

For nuclear reactors some general considerations could be about the underlying mechanism involved in the process (pre-treatment LP and post-treatment thermal aging) that needs to be comprehensively studied in future works to enhance and optimize the process and to pave the way for effective commercialization of the LP process for HT nuclear reactor components under tribological and potentially tribo-corrosive environments.

Regarding the use of MPCM for superlubricity applications, that is admittedly a new area of research, more PCMs with different melting temperatures could be incorporated in different polymeric matrices to explore a broader applicability. Also, the critical pressures at which the protective wall breaks open and releases the lubricant can be studied experimentally by employing the nanoindentation technique using an appropriate flat punch, complemented by computational studies.

REFERENCES

[1] Holmberg K, Andersson P, Erdemir A. Global energy consumption due to friction in passenger cars. Tribol Int 2012;47:221–34. https://doi.org/10.1016/J.TRIBOINT.2011.11.022.

[2] Liu Y, Erdemir A, Meletis EI. A study of the wear mechanism of diamond-like carbon films. Surf Coatings Technol 1996;82:48–56. https://doi.org/10.1016/0257-8972(95)02623-1.

[3] Qin W, Yue W, Wang C. Understanding integrated effects of humidity and interfacial transfer film formation on tribological behaviors of sintered polycrystalline diamond. RSC Adv 2015;5:53484–96. https://doi.org/10.1039/C5RA09327A.

[4] Qin W, Liu Y, Yue W, Wang C, Ma G, Wang H. Influence of Frictional Interface State on Tribological Performance of Sintered Polycrystalline Diamond Sliding Against Different Mating Materials. Tribol Lett 2019;67:1–9. https://doi.org/10.1007/S11249-019-1196-1/FIGURES/10.

[5] Erdemir A, Fenske GR. Tribological Performance of Diamond and Diamondlike Carbon Films at Elevated Temperatures. Tribol Trans 1996;39:787–94. https://doi.org/10.1080/10402009608983596.

[6] DellaCorte C, Edmonds BJ. NASA PS400 : A New High Temperature Solid Lubricant Coating for High Temperature Wear Applications. Nasa Tm-2009-215678 2009:1–15.

[7] Tsigkis V, Bashandeh K, Lan P, Polycarpou AA. Tribological behavior of PS400-related tribopairs for space exploration. Tribol Int 2021;153:106636. https://doi.org/10.1016/J.TRIBOINT.2020.106636.

[8] Pearson SR, Shipway PH, Abere JO, Hewitt RAA. The effect of temperature on wear and friction of a high strength steel in fretting. Wear 2013;303:622–31. https://doi.org/10.1016/J.WEAR.2013.03.048.

[9] Tsigkis V, Lan P, Polycarpou AA. Dynamic tribo-pair of PS400 and DLC for planet Venus application. Tribol Int 2021;164:107237. https://doi.org/10.1016/J.TRIBOINT.2021.107237.

[10] Nunez EE, Demas NG, Polychronopoulou K, Polycarpou AA. Tribological Study Comparing PAG and POE Lubricants Used in Air-Conditioning Compressors

under the Presence of CO_2. Tribol Trans 2008;51:790–7. https://doi.org/10.1080/10402000801911861.

[11] Tsigkis V, Bashandeh K, Lan P, Polycarpou AA. Tribological investigation of advanced coatings subjected to Venusian environment of 2.4 MPa CO2 pressure and 462 °C. Surf Coatings Technol 2022;441:128550. https://doi.org/10.1016/J.SURFCOAT.2022.128550.

[12] Lukco D, Spry DJ, Harvey RP, Costa GCC, Okojie RS, Avishai A, et al. Chemical Analysis of Materials Exposed to Venus Temperature and Surface Atmosphere. Earth Sp Sci 2018;5:270–84. https://doi.org/10.1029/2017EA000355.

[13] Cabet C, Terlain A, Lett P, Guétaz L, Gentzbittel JM. High temperature corrosion of structural materials under gas-cooled reactor helium. Mater Corros 2006;57:147–53. https://doi.org/10.1002/MACO.200503901.

[14] Pauly V, Tesch C, Kern J, Clark M, Grierson D, Singh D, et al. High-temperature tribological behavior of structural materials after conditioning in impure-helium environments for high-temperature gas-cooled reactor applications. J Nucl Mater 2019;522:311–23. https://doi.org/10.1016/J.JNUCMAT.2019.05.025.

[15] Tsigkis V, Saifur Rahman M, Hackel L, Davami K, Beheshti A, Polycarpou AA. Helium tribology of Inconel 617 subjected to laser peening for high temperature nuclear reactor applications. Appl Surf Sci 2022;577:151961. https://doi.org/10.1016/J.APSUSC.2021.151961.

[16] Bashandeh K, Lan P, Meyer JL, Polycarpou AA. Tribological Performance of Graphene and PTFE Solid Lubricants for Polymer Coatings at Elevated Temperatures. Tribol Lett 2019;67:1–14. https://doi.org/10.1007/S11249-019-1212-5/FIGURES/11.

[17] Taylor FW, Svedhem H, Head JW. Venus: The Atmosphere, Climate, Surface, Interior and Near-Space Environment of an Earth-Like Planet. Space Sci Rev 2018;214:1–36. https://doi.org/10.1007/S11214-018-0467-8/FIGURES/19.

[18] Rehnmark F, Cloninger E, Cody H, Bailey J, Traeden N, Zacny K, et al. High Temperature Electromagnetic Actuator and Sampling Drill for Venus Exploration. ESAMTS 2017.

[19] Kolowa et al. Extreme environment technologies for future space scinece missions. JPL D-32832. https://solarsystem.nasa.gov/resources/292/extreme-environment-technologies-for-future-space-science-missions-september-2007.

[20] Balint T, Thompson T, Cutts J, Robinson J. Venus Exploration opportunities within NASA's Solar System Exploration roadmap. JPL 2006.

[21] Pauly V, Kern J, Clark M, Grierson DS, Sridharan K. Wear Performance of incoloy 800HT and inconel 617 in various surface conditions for high-temperature gas-cooled reactor components. Tribol Int 2021;154:106715. https://doi.org/10.1016/J.TRIBOINT.2020.106715.

[22] Wright RN. Summary of Studies of Aging and Environmental Effects on Inconel 617 and Haynes 230. INL/EXT-06-11750 2006.

[23] Rahman MS, Polychronopoulou K, Polycarpou AA. Tribochemistry of inconel 617 during sliding contact at 950 °C under helium environment for nuclear reactors. J Nucl Mater 2019;521:21–30. https://doi.org/10.1016/J.JNUCMAT.2019.04.032.

[24] Rahman MS, Ding J, Beheshti A, Zhang X, Polycarpou AA. Helium Tribology of Inconel 617 at Elevated Temperatures up to 950°C: Parametric Study. Nucl Sci Eng 2019;193:998–1012. https://doi.org/10.1080/00295639.2019.1582315.

[25] Zhang Y, Mohanty DP, Seiler P, Siegmund T, Kruzic JJ, Tomar V. High temperature indentation based property measurements of IN-617. Int J Plast 2017;96:264–81. https://doi.org/10.1016/J.IJPLAS.2017.05.007.

[26] Vanossi A, Bechinger C, Urbakh M. Structural lubricity in soft and hard matter systems. Nat Commun 2020 111 2020;11:1–11. https://doi.org/10.1038/s41467-020-18429-1.

[27] Zhang Z, Du Y, Huang S, Meng F, Chen L, Xie W, et al. Macroscale Superlubricity Enabled by Graphene-Coated Surfaces. Adv Sci 2020;7. https://doi.org/10.1002/advs.201903239.

[28] Berman D, Deshmukh SA, Sankaranarayanan SKRS, Erdemir A, Sumant A V. Macroscale superlubricity enabled by graphene nanoscroll formation. Science 2015;348:1118–22. https://doi.org/10.1126/science.1262024.

[29] Hod O, Meyer E, Zheng Q, Urbakh M. Structural superlubricity and ultralow friction across the length scales. Nat 2018;563:485–92. https://doi.org/10.1038/s41586-018-0704-z.

[30] OHB. How do you explore one of the most hostile planets in our solar system. OHB 2020. https://www.ohb.de/en/magazine/destination-venus-part-6-mechanical-rover-or-atmospheric-probes-how-do-you-explore-one-of-the-most-hostile-planets-in-our-solar-system.

[31] Sevini F, Cojazzi GG, Renda G. Proliferation resistance and physical protection robustness characteristics of innovative and advanced nuclear energy systems. ESARDA Bulletin. 2008;39:3-20.

[32] De Mello JDB, Binder R, Demas NG, Polycarpou AA. Effect of the actual environment present in hermetic compressors on the tribological behaviour of a Si-rich multifunctional DLC coating. Wear 2009;267:907–15. https://doi.org/10.1016/J.WEAR.2008.12.070.

[33] Velkavrh I, Autserer F, Klien S, Voyer J, Ristow A, Brenner J, et al. The influence of temperature on friction and wear of unlubricated steel/steel contacts in different gaseous atmospheres. Tribol Int 2016;98:155–71. https://doi.org/10.1016/J.TRIBOINT.2016.02.022.

[34] Demas NG, Polycarpou AA, Conry TF. Tribological Studies on Scuffing Due to the Influence of Carbon Dioxide Used as a Refrigerant in Compressors. Tribol Trans 2005;48:336–42. https://doi.org/10.1080/05698190590970525.

[35] Dellacorte C, Stanford MK, Thomas F, Edmonds BJ. The Effect of Composition on the Surface Finish of PS400: A New High Temperature Solid Lubricant Coating. Nasa Tm-2010-216774

[36] Sliney HE. Wide temperature spectrum self-lubricating coatings prepared by plasma spraying. Thin Solid Films 1979;64:211–7. https://doi.org/10.1016/0040-6090(79)90511-X.

[37] Zhu S, Bi Q, Yang J, Liu W, Xue Q. Effect of particle size on tribological behavior of Ni3Al matrix high temperature self-lubricating composites. Tribol Int 2011;44:1800–9. https://doi.org/10.1016/J.TRIBOINT.2011.07.002.

[38] Zhu S, Bi Q, Niu M, Yang J, Liu W. Tribological behavior of NiAl matrix composites with addition of oxides at high temperatures. Wear 2012;274–275:423–34. https://doi.org/10.1016/J.WEAR.2011.11.006.

[39] Kong L, Bi Q, Zhu S, Yang J, Liu W. Tribological properties of ZrO2 (Y2O3)–Mo–BaF2/CaF2 composites at high temperatures. Tribol Int 2012;45:43–9. https://doi.org/10.1016/J.TRIBOINT.2011.09.008.

[40] Zhang S, Zhou J, Guo B, Zhou H, Pu Y, Chen J. Friction and wear behavior of laser cladding Ni/hBN self-lubricating composite coating. Mater Sci Eng A 2008;491:47–54. https://doi.org/10.1016/J.MSEA.2007.12.015.

[41] Rahman MS, Ding J, Beheshti A, Zhang X, Polycarpou AA. Elevated temperature tribology of Ni alloys under helium environment for nuclear reactor applications. Tribol Int 2018;123:372–84. https://doi.org/10.1016/J.TRIBOINT.2018.03.021.

[42] Inman IA, Datta PK, Du HL, Burnell-Gray JS, Pierzgalski S, Luo Q. Studies of high temperature sliding wear of metallic dissimilar interfaces. Tribol Int 2005;38:812–23. https://doi.org/10.1016/J.TRIBOINT.2005.02.007.

[43] Rahman MS, Ding J, Beheshti A, Zhang X, Polycarpou AA. Tribology of incoloy 800HT for nuclear reactors under helium environment at elevated temperatures. Wear 2019;436–437:203022. https://doi.org/10.1016/J.WEAR.2019.203022.

[44] Dellacorte C, Fellenstein JA. The Effect of Compositional Tailoring on the Thermal Expansion and Tribological Properties of PS300: A Solid Lubricant Composite Coating. Tribol Trans 2008;40:639–42. https://doi.org/10.1080/10402009708983703.

[45] Dellacorte C, Edmonds BJ. Preliminary Evaluation of PS300: A New Self-Lubricating High Temperature Composite Coating for Use to 800 C. Nasa Tm-1995-107056.

[46] Della Corte C, Sliney HE. Composition Optimization of Self-Lubricating Chromium-Carbide-Based Composite Coatings for Use to 760°C. Tribol Trans 2008;30:77–83. https://doi.org/10.1080/05698198708981733.

[47] Radil K, DellaCorte C. The Performance of PS400 Subjected to Sliding Contact at Temperatures from 260 to 927°C. Tribol Trans 2016;60:957–64. https://doi.org/10.1080/10402004.2016.1231357.

[48] Li F, Cheng J, Qiao Z, Ma J, Zhu S, Fu L, et al. A nickel-alloy-based high-temperature self-lubricating composite with simultaneously superior lubricity and high strength. Tribol Lett 2013;49:573–7. https://doi.org/10.1007/S11249-012-0101-Y/FIGURES/5.

[49] Niu M, Bi Q, Yang J, Liu W. Tribological performance of a Ni3Al matrix self-lubricating composite coating tested from 25 to 1000 °C. Surf Coatings Technol 2012;206:3938–43. https://doi.org/10.1016/J.SURFCOAT.2012.03.064.

[50] Wang C, Ye Y, Guan X, Hu J, Wang Y, Li J. An analysis of tribological performance on Cr/GLC film coupling with Si3N4, SiC, WC, Al2O3 and ZrO2 in seawater. Tribol Int 2016;96:77–86. https://doi.org/10.1016/J.TRIBOINT.2015.12.010.

[51] Tsigkis V, Lan P, Polycarpou AA. Tribology International Dynamic tribo-pair of PS400 and DLC for planet Venus application. Tribol Int 2021;164:107237. https://doi.org/10.1016/j.triboint.2021.107237.

[52] Wang L, Nie X, Hu X. Effect of thermal annealing on tribological and corrosion properties of DLC coatings. J Mater Eng Perform 2013;22:3093–100. https://doi.org/10.1007/S11665-013-0585-0/FIGURES/7.

[53] Deng X, Kousaka H, Tokoroyama T, Umehara N. Thermal Stability and High-Temperature Tribological Properties of a-C:H and Si-DLC Deposited by

Microwave Sheath Voltage Combination Plasma. Tribol Online 2013;8:257–64. https://doi.org/10.2474/TROL.8.257.

[54] Zhu H Bin, Li H, Li ZX. Plasma sprayed TiB2–Ni cermet coatings: Effect of feedstock characteristics on the microstructure and tribological performance. Surf Coatings Technol 2013;235:620–7. https://doi.org/10.1016/J.SURFCOAT.2013.08.040.

[55] Voyer J, Marple BR. Tribological performance of thermally sprayed cermet coatings containing solid lubricants. Surf Coatings Technol 2000;127:155–66. https://doi.org/10.1016/S0257-8972(00)00667-8.

[56] Khan FF, Bae G, Kang K, Kumar S, Jeong T, Lee C. Development of cermet coatings by kinetic spray technology for the application of die-soldering and erosion resistance. Surf Coatings Technol 2009;204:345–52. https://doi.org/10.1016/j.surfcoat.2009.07.033.

[57] PS400 Composite Solid Lubricant Plasma Coating. https://technology.grc.nasa .gov/documents/GRC_PS400_Plasma-Coating_DataSheet_2017-12-06.pdf.

[58] Meškinis Š, Tamulevičiene A. Structure, properties and applications of diamond like nanocomposite (SiO x containing DLC) films: A review. Medziagotyra 2011;17:358–70. https://doi.org/10.5755/j01.ms.17.4.770.

[59] Cho SJ, Lee KR, Eun KY, Ko DH. Measurement of elastic modulus and Poisson's ratio of diamond-like carbon films. Mat. Res. Soc. 2011;518. https://doi.org/ 10.1557/PROC-518-203.

[60] Lv H, Nie P, Yan Y, Wang J, Sun B. Characterization and adhesion strength study of detonation-sprayed MoB-CoCr alloy coatings on 2Cr13 stainless steel substrate. J Coatings Technol Res 2010;7:801–7. https://doi.org/10.1007/s11998-009-9189-x.

[61] Dellacorte C, Manco RA, Martin RA. Tribological Performance of PM400 Bushings in Oscillatory Sliding from 25 to 927 °C. Nasa Tm-2019-220038.

[62] Dellacorte C, Sliney HE. Tribological properties of PM212: A high-temperature, self-lubricating, powder metallurgy composite. Nasa Tm-1990-102355.

[63] DellaCorte C. The effect of counterface on the tribological performance of a high temperature solid lubricant composite from 25 to 650°C. Surf Coatings Technol 1996;86–87:486–92. https://doi.org/10.1016/S0257-8972(96)02959-3.

[64] Jongwannasiri C, Li X, Watanabe S, Jongwannasiri C, Li X, Watanabe S. Improvement of Thermal Stability and Tribological Performance of Diamond-Like

Carbon Composite Thin Films. Mater Sci Appl 2013;4:630–6. https://doi.org/10.4236/MSA.2013.410077.

[65] Niiyama Y, Shimizu N, Kuwayama A, Okada H, Takeno T, Kurihara K, et al. Friction and Delamination Properties of Self-Mating Diamond-Like Carbon Coatings in Water. Tribol Lett 2016;62:1–7. https://doi.org/10.1007/S11249-016-0682-Y/FIGURES/13.

[66] Ogwu AA, Lamberton RW, Morley S, Maguire P, McLaughlin J. Characterisation of thermally annealed diamond like carbon (DLC) and silicon modified DLC films by Raman spectroscopy. Phys B Condens Matter 1999;269:335–44. https://doi.org/10.1016/S0921-4526(99)00138-6.

[67] Huo L, Wang S, Pu J, Sun J, Lu Z, Ju P, et al. Exploring the low friction of diamond-like carbon films in carbon dioxide atmosphere by experiments and first-principles calculations. Appl Surf Sci 2018;436:893–9. https://doi.org/10.1016/J.APSUSC.2017.12.044.

[68] Wu X, Cong P, Nanao H, Minami I, Mori S. Tribological behaviors of 52100 steel in carbon dioxide atmosphere. Tribol Lett 2004;17:925–30. https://doi.org/10.1007/S11249-004-8101-1/METRICS.

[69] Tang XM, Weber J, Mikhailov SN, Müller C, Hänni W, Hintermann HE. Structure stability of hydrogenated amorphous carbon film during thermal annealing. J Non Cryst Solids 1995;185:145–50. https://doi.org/10.1016/0022-3093(95)00672-9.

[70] Zhen J, Li F, Zhu S, Ma J, Qiao Z, Liu W, et al. Friction and wear behavior of nickel-alloy-based high temperature self-lubricating composites against Si3N4 and Inconel 718. Tribol Int 2014;75:1–9. https://doi.org/10.1016/J.TRIBOINT.2014.03.005.

[71] An Y, Chen J, Hou G, Zhao X, Zhou H, Chen J, et al. Effect of Silver Content on Tribological Property and Thermal Stability of HVOF-Sprayed Nickel-Based Solid Lubrication Coating. Tribol Lett 2015;58:1–10. https://doi.org/10.1007/S11249-015-0489-2/FIGURES/15.

[72] Qi Y, Konca E, Alpas AT. Atmospheric effects on the adhesion and friction between non-hydrogenated diamond-like carbon (DLC) coating and aluminum – A first principles investigation. Surf Sci 2006;600:2955–65. https://doi.org/10.1016/J.SUSC.2006.05.008.

[73] Miyoshi K. Solid Lubricants and Coatings for Extreme Environments : State-of-the-Art Survey. Nasa Tm-2007-214668.

[74] Li Y, Xie M, Sun Q, Xu X, Fan X, Zhang G, et al. The effect of atmosphere on the

tribological behavior of magnetron sputtered MoS2 coatings. Surf Coatings Technol 2019;378:125081. https://doi.org/10.1016/J.SURFCOAT.2019.125081.

[75] Ding XZ, Zeng XT, He XY, Chen Z. Tribological properties of Cr- and Ti-doped MoS2 composite coatings under different humidity atmosphere. Surf Coatings Technol 2010;205:224–31. https://doi.org/10.1016/J.SURFCOAT.2010.06.041.

[76] Dunckle CG, Aggleton M, Glassman J, Taborek P. Friction of molybdenum disulfide–titanium films under cryogenic vacuum conditions. Tribol Int 2011;44:1819–26. https://doi.org/10.1016/J.TRIBOINT.2011.07.010.

[77] Hui Z, Jun Z, Qing-ping W, Zhi-hua W, Rui-peng S. The effect of Ti content on the structural and mechanical properties of MoS 2 -Ti composite coatings deposited by unbalanced magnetron sputtering system 2011;18:234–9. https://doi.org/10.1016/j.phpro.2011.06.087.

[78] Feng X, Zhou H, Zheng Y, Zhang K, Zhang Y. Tribological behavior and wear mechanism of Ti / MoS 2 films deposited on plasma nitrided CF170 steel sliding against different mating materials. Vacuum 2021;194:110623. https://doi.org/10.1016/j.vacuum.2021.110623.

[79] Sun G, Bhowmick S, Alpas AT. Effect of Atmosphere and Temperature on the Tribological Behavior of the Ti Containing MoS2 Coatings Against Aluminum. Tribol Lett 2017;65:1–13. https://doi.org/10.1007/S11249-017-0934-5/FIGURES/12.

[80] Bergseth E, Henriksson M, Dizdar S, Sellgren U. Effects of thrust washer bearing surface characteristics on planetary gear train wear. Wear 2019;432–433:202933. https://doi.org/10.1016/J.WEAR.2019.202933.

[81] Sakakibara K, Suzuki S, Shibata K, Sawada Y, Ashizawa S, Oomichi T. Development of the Servo Valve with High Durability Using Split-Type Sleeve – Reduction of Wear with Ceramic Material –. J Robot Mechatronics 2019;31:707–14. https://doi.org/10.20965/JRM.2019.P0707.

[82] Ogwu AA, Lamberton RW, Morley S, Maguire P, McLaughlin J. Characterization of thermally annealed diamond like carbon (DLC) and silicon modified DLC films by Raman spectroscopy. Phys B Condens Matter 1999;269:335–44. https://doi.org/10.1016/S0921-4526(99)00138-6.

[83] Radhakrishnan J, Biswas K. Facile synthesis of Ti doped MoS 2 and its superior adsorption properties. Mater Lett 2020;280:128522. https://doi.org/10.1016/j.matlet.2020.128522.

[84] Joya KS, Sala X. In situ Raman and surface-enhanced Raman spectroscopy on

working electrodes: spectroelectrochemical characterization of water oxidation electrocatalysts. Phys Chem Chem Phys 2015;17:21094–103. https://doi.org/10.1039/C4CP05053C.

[85] İmran Vaizoğullar A, Vaizo gullar I. Facile preparation and characterization of NiO/Ni2O3-decorated nanoballs and mixed phase CdS nano rods (CdS&NiO/Ni2O3) for effective photocatalytic decomposition of Congo red under visible light irradiation. J Dispers Sci Technol 2020;42:1408–18. https://doi.org/10.1080/01932691.2020.1814804.

[86] Johnson NM, Fegley B. Atmosphere-Surface Interactions on Venus. Adv Sp Resour 2002;29:233–41.

[87] Kolowa E et al. Extreme environement technologies for future space scince missions. JPL D-32832.

[88] Sauder J, Hilgemann E, Kawata J, Stack K, Parness A, Johnson M. Automaton Rover for Extreme Environments (AREE). JPL 2017. https://trs.jpl.nasa.gov/bitstream/handle/2014/47914/CL%2317-2311.pdf?sequence=1.

[89] Neudeck PG, Meredith RD, Chen L, Spry DJ, Nakley LM, Hunter GW. Prolonged silicon carbide integrated circuit operation in Venus surface atmospheric conditions. AIP Adv 2016;6. https://doi.org/10.1063/1.4973429.

[90] Lukco D, Spry DJ, Neudeck PG, Nakley LM, Phillips KG, Okojie RS, et al. Experimental study of structural materials for prolonged venus surface exploration missions. J Spacecr Rockets 2020;57:1118–28. https://doi.org/10.2514/1.A34617/ASSET/IMAGES/LARGE/FIGURE13.JPEG.

[91] Costa GCC, Jacobson NS, Lukco D, Hunter GW, Nakley L, Radoman-Shaw BG, et al. Oxidation behavior of stainless steels 304 and 316 under the Venus atmospheric surface conditions. Corros Sci 2018;132:260–71. https://doi.org/10.1016/J.CORSCI.2018.01.002.

[92] Costa GCC, Jacobson NS, Lukco D, Hunter GW, Nakley L, Radoman-Shaw BG, et al. Chemical and Microstructural Changes in Metallic and Ceramic Materials Exposed to Venusian Surface Conditions. Nasa Tm-2017-219437.

[93] Oliver WC, Pharr GM. An improved technique for determining hardness and elastic modulus using load and displacement sensing indentation experiments. J Mater Res 1992;7:1564–83. https://doi.org/10.1557/JMR.1992.1564/METRICS.

[94] Tayebi N, Conry TF, Polycarpou AA. Determination of hardness from nanoscratch experiments: Corrections for interfacial shear stress and elastic recovery. J Mater

Res 2003;18:2150–62. https://doi.org/10.1557/JMR.2003.0301/METRICS.

[95] Cabet C, Terlain A, Lett P, Guetaz L, Gentzbittel J. M. High temperature corrosion of structural materials under gas-cooled reactor helium. Mater Corros 2006;57, 147-153.

[96] Sun W, Tan AWY, King DJY, Khun NW, Bhowmik A, Marinescu I, et al. Tribological behavior of cold sprayed Inconel 718 coatings at room and elevated temperatures. Surf Coatings Technol 2020;385:125386. https://doi.org/10.1016/J.SURFCOAT.2020.125386.

[97] Salari S, Beheshti A. Asperity-based contact and static friction with provision for creep: A review. Surf 2021;24:101144. https://doi.org/10.1016/J.SURFIN.2021.101144.

[98] Salari S, Rahman MS, Polycarpou AA, Beheshti A. Elevated temperature mechanical properties of Inconel 617 surface oxide using nanoindentation. Mater Sci Eng A 2020;788:139539. https://doi.org/10.1016/J.MSEA.2020.139539.

[99] Morris B. The components of the wired spanning forest are recurrent. Probab Theory Relat Fields 2003;125:259–65. https://doi.org/10.1007/S00440-002-0236-0/METRICS.

[100] Birol Y. Thermal fatigue testing of Inconel 617 and Stellite 6 alloys as potential tooling materials for thixoforming of steels. Mater Sci Eng A 2010;527:1938–45. https://doi.org/10.1016/J.MSEA.2009.11.021.

[101] Osthoff W, Schuster H, Ennis PJ, Nickel H. Creep and Relaxation Behavior of lnconel-617. Nucl Tech 1984;66:296–307. https://doi.org/10.13182/NT84-A33433.

[102] Saber D, Emam IS, Abdel-Karim R. High temperature cyclic oxidation of Ni based superalloys at different temperatures in air. J Alloys Compd 2017;719:133–41. https://doi.org/10.1016/J.JALLCOM.2017.05.130.

[103] El-Awadi GA, Abdel-Samad S, Elshazly ES. Hot corrosion behavior of Ni based Inconel 617 and Inconel 738 superalloys. Appl Surf Sci 2016;378:224–30. https://doi.org/10.1016/J.APSUSC.2016.03.181.

[104] Akhiani H, Nezakat M, Penttilä S, Szpunar J. The oxidation resistance of thermo-mechanically processed Incoloy 800HT in supercritical water. J Supercrit Fluids 2015;101:150–60. https://doi.org/10.1016/J.SUPFLU.2015.03.019.

[105] Fulger M, Ohai D, Mihalache M, Pantiru M, Malinovschi V. Oxidation behavior of Incoloy 800 under simulated supercritical water conditions. J Nucl Mater

2009;385:288–93. https://doi.org/10.1016/J.JNUCMAT.2008.12.004.

[106] Ahmadi A, Sadeghi F, Shaffer S. In-situ friction and fretting wear measurements of Inconel 617 at elevated temperatures. Wear 2018;410–411:110–8. https://doi.org/10.1016/J.WEAR.2018.06.007.

[107] Kanjer A, Optasanu V, Lavisse L, Marco de Lucas M del C, Dejardin S, François M, et al. Influence of Mechanical Surface Treatment on High-Temperature Oxidation of Pure Titanium. Oxid Met 2017;88:383–95. https://doi.org/10.1007/S11085-016-9700-6/FIGURES/8.

[108] Lavisse L, Kanjer A, Berger P, Optasanu V, Gorny C, Peyre P, et al. High temperature oxidation resistance and microstructure of laser-shock peened Ti-Beta-21S. Surf Coatings Technol 2020;403:126368. https://doi.org/10.1016/J.SURFCOAT.2020.126368.

[109] Kanjer A, Lavisse L, Optasanu V, Berger P, Gorny C, Peyre P, et al. Effect of laser shock peening on the high temperature oxidation resistance of titanium. Surf Coatings Technol 2017;326:146–55. https://doi.org/10.1016/J.SURFCOAT.2017.07.042.

[110] Gill AS, Telang A, Vasudevan VK. Characteristics of surface layers formed on inconel 718 by laser shock peening with and without a protective coating. J Mater Process Technol 2015;225:463–72. https://doi.org/10.1016/J.JMATPROTEC.2015.06.026.

[111] Rozmus-Górnikowska M, Kusiński J, Cieniek Ł. Effect of Laser Shock Peening on the Microstructure and Properties of the Inconel 625 Surface Layer. J Mater Eng Perform 2020;29:1544–9. https://doi.org/10.1007/S11665-020-04667-3/FIGURES/7.

[112] Munther M, Martin T, Tajyar A, Hackel L, Beheshti A, Davami K. Laser shock peening and its effects on microstructure and properties of additively manufactured metal alloys: a review. Eng Res Express 2020;2:022001. https://doi.org/10.1088/2631-8695/AB9B16.

[113] Gill AS, Telang A, Ye C, Mannava SR, Qian D, Vasudevan VK. Localized plastic deformation and hardening in laser shock peened Inconel alloy 718SPF. Mater Charact 2018;142:15–26. https://doi.org/10.1016/J.MATCHAR.2018.05.010.

[114] Sheng J, Zhang H, Hu X, Huang S. Influence of laser peening on the high-temperature fatigue life and fracture of Inconel 718 nickel-based alloy. Theor Appl Fract Mech 2020;109:102757. https://doi.org/10.1016/J.TAFMEC.2020.102757.

[115] Karthik D, Swaroop S. Laser shock peening enhanced corrosion properties in a

nickel based Inconel 600 superalloy. J Alloys Compd 2017;694:1309–19. https://doi.org/10.1016/J.JALLCOM.2016.10.093.

[116] Trdan U, Skarba M, Porro JA, Ocaña JL, Grum J. Application of massive laser shock processing for improvement of mechanical and tribological properties. Surf Coatings Technol 2018;342:1–11. https://doi.org/10.1016/J.SURFCOAT.2018.02.084.

[117] Guo Y, Wang S, Liu W, Sun Z, Zhu G, Xiao T. Effect of laser shock peening on tribological properties of magnesium alloy ZK60. Tribol Int 2020;144:106138. https://doi.org/10.1016/J.TRIBOINT.2019.106138.

[118] Zhou J, Sun Y, Huang S, Sheng J, Li J, Agyenim-Boateng E. Effect of laser peening on friction and wear behavior of medical Ti6Al4V alloy. Opt Laser Technol 2019;109:263–9. https://doi.org/10.1016/J.OPTLASTEC.2018.08.005.

[119] Yakimets I, Richard C, Béranger G, Peyre P. Laser peening processing effect on mechanical and tribological properties of rolling steel 100Cr6. Wear 2004;256:311–20. https://doi.org/10.1016/S0043-1648(03)00405-8.

[120] Kumar D, Nadeem Akhtar S, Kumar Patel A, Ramkumar J, Balani K. Tribological performance of laser peened Ti–6Al–4V. Wear 2015;322–323:203–17. https://doi.org/10.1016/J.WEAR.2014.11.016.

[121] Siddaiah A, Mao B, Liao Y, Menezes PL. Surface characterization and tribological performance of laser shock peened steel surfaces. Surf Coatings Technol 2018;351:188–97. https://doi.org/10.1016/J.SURFCOAT.2018.07.087.

[122] Jinoop AN, Subbu SK, Paul CP, Palani IA. Post-processing of Laser Additive Manufactured Inconel 718 Using Laser Shock Peening. Int J Precis Eng Manuf 2019;20:1621–8. https://doi.org/10.1007/S12541-019-00147-4/METRICS.

[123] Anand Kumar S, Sundar R, Ganesh Sundara Raman S, Gnanamoorthy R, Kaul R, Ranganathan K, et al. Effects of laser peening on fretting wear behaviour of alloy 718 fretted against two different counterbody materials. Proc IMechE Part J: J Engineering Tribology 2017;231:1276–88. https://doi.org/10.1177/1350650117692707.

[124] Cao W, Khadhraoui M, Brenier B, Guédou JY, Castex L. Thermomechanical relaxation of residual stress in shot peened nickel base superalloy. Mater Sci Technol 1994;10:947–54. https://doi.org/10.1179/MST.1994.10.11.947.

[125] Li Y, Zhou L, He W, He G, Wang X, Nie X, et al. The strengthening mechanism of a nickel-based alloy after laser shock processing at high temperatures. Sci Technol Adv Mate 2013;14:55010. https://doi.org/10.1088/1468-

6996/14/5/055010.

[126] Zhou Z, Gill AS, Telang A, Mannava SR, Langer K, Vasudevan VK, et al. Experimental and Finite Element Simulation Study of Thermal Relaxation of Residual Stresses in Laser Shock Peened IN718 SPF Superalloy. Exp Mech 2014;54:1597–611. https://doi.org/10.1007/S11340-014-9940-9/FIGURES/13.

[127] Munther M, Rowe RA, Sharma M, Hackel L, Davami K. Thermal stabilization of additively manufactured superalloys through defect engineering and precipitate interactions. Mater Sci Eng A 2020;798:140119. https://doi.org/10.1016/J.MSEA.2020.140119.

[128] Kattoura M, Mannava SR, Qian D, Vasudevan VK. Effect of laser shock peening on residual stress, microstructure and fatigue behavior of ATI 718Plus alloy. Int J Fatigue 2017;102:121–34. https://doi.org/10.1016/J.IJFATIGUE.2017.04.016.

[129] Tong ZP, Ren XD, Zhou WF, Adu-Gyamfi S, Chen L, Ye YX, et al. Effect of laser shock peening on wear behaviors of TC11 alloy at elevated temperature. Opt Laser Technol 2019;109:139–48. https://doi.org/10.1016/j.optlastec.2018.07.070.

[130] Rahman MS, Polychronopoulou K, Polycarpou AA. Tribochemical changes of alloy 800HT under sliding contact at elevated temperature in impure helium environment. Wear 2020;462–463. https://doi.org/10.1016/j.wear.2020.203508.

[131] Mostafa AM, Hameed MF, Obayya SS. Effect of laser shock peening on the hardness of AL-7075 alloy. J King Saud Univ - Sci 2019;31:472–8. https://doi.org/10.1016/J.JKSUS.2017.07.012.

[132] Palma T, Munther M, Sharma M, Hackel L, Beheshti A, Davami K. Nanomechanical Characterization of Laser Peened Additively Manufactured Inconel 718 Superalloy. Adv Eng Mater 2019;21:1900499. https://doi.org/10.1002/ADEM.201900499.

[133] Zhou JZ, Huang S, Sheng J, Lu JZ, Wang CD, Chen KM, et al. Effect of repeated impacts on mechanical properties and fatigue fracture morphologies of 6061-T6 aluminum subject to laser peening. Mater Sci Eng A 2012;539:360–8. https://doi.org/10.1016/j.msea.2012.01.125.

[134] Vasilev AP, Struchkova TS, Nikiforov LA, Okhlopkova AA, Grakovich PN, Shim EL, Cho JH. Mechanical and tribological properties of polytetrafluoroethylene composites with carbon fiber and layered silicate fillers. Molecules 2019;24:224.

[135] Murty KL. Materials Ageing and Degradation in Light Water Reactors: Mechanisms and Management. Woodhead Publishing 2013.

[136] Lan P, Meyer JL, Economy J, Polycarpou AA. Unlubricated Tribological Performance of Aromatic Thermosetting Polyester (ATSP) Coatings under Different Temperature Conditions. Tribol Lett 2016;61:1–14. https://doi.org/10.1007/s11249-015-0621-3.

[137] Hua Y, Rong Z, Ye Y, Chen K, Chen R, Xue Q, et al. Laser shock processing effects on isothermal oxidation resistance of GH586 superalloy. Appl Surf Sci 2015;330:439–44. https://doi.org/10.1016/j.apsusc.2015.01.033.

[138] Yang H, Wu X, Cao G, Yang Z. Enhanced boronizing kinetics and high temperature wear resistance of H13 steel with boriding treatment assisted by air blast shot peening. Surf Coatings Technol 2016;307:506–16. https://doi.org/10.1016/j.surfcoat.2016.09.029.

[139] Pauschitz A, Roy M, Franek F. Mechanisms of sliding wear of metals and alloys at elevated temperatures. Tribol Int 2008;41:584–602. https://doi.org/10.1016/J.TRIBOINT.2007.10.003.

[140] Khun NW, Zhang H, Yue CY, Yang JL. Self-lubricating and wear resistant epoxy composites incorporated with microencapsulated wax. J Appl Mech Trans ASME 2014;81. https://doi.org/10.1115/1.4026941/370453.

[141] Lan P, Nunez EE, Polycarpou AA. Advanced Polymeric Coatings and Their Applications: Green Tribology. Encycl Renew Sustain Mater 2020:345–58. https://doi.org/10.1016/B978-0-12-803581-8.11466-3.

[142] Nunez EE, Bashandeh K, Polycarpou AA. Thermal and Mechanical Properties of Polymer Coatings. Polym Coatings 2020:157–75. https://doi.org/10.1201/9780429199226-9

[143] Pratt GC, Pratt, C. G. Bearing Materials: Plain Bearings. Emst 2001:488–96. https://doi.org/10.1016/B0-08-043152-6/00094-2.

[144] Nunez EE, Gheisari R, Polycarpou AA. Tribology review of blended bulk polymers and their coatings for high-load bearing applications. Tribol Int 2019;129:92–111. https://doi.org/10.1016/J.TRIBOINT.2018.08.002.

[145] Mohammed AS. UHMWPE Nanocomposite Coatings Reinforced with Alumina (Al2O3) Nanoparticles for Tribological Applications. Coatings 2018;8:280. https://doi.org/10.3390/COATINGS8080280.

[146] Zhu Y, Wang H, Yan L, Wang R, Zhu Y. Preparation and tribological properties of 3D network polymer-based nanocomposites reinforced by carbon nanofibers. Wear 2016;356–357:101–9. https://doi.org/10.1016/J.WEAR.2016.03.022.

[147] Bashandeh K, Lan P, Polycarpou AA. Tribology of self-lubricating high performance ATSP, PI, and PEEK-based polymer composites up to 300 °C. Friction 2023;11:141–53. https://doi.org/10.1007/S40544-021-0593-2/METRICS.

[148] Shi SC, Wu JY, Huang TF, Peng YQ. Improving the tribological performance of biopolymer coating with MoS2 additive. Surf Coatings Technol 2016;303:250–5. https://doi.org/10.1016/J.SURFCOAT.2016.03.055.

[149] Bashandeh K, Tsigkis V, Lan P, Polycarpou AA. Extreme environment tribological study of advanced bearing polymers for space applications. Tribol Int 2021;153:106634. https://doi.org/10.1016/J.TRIBOINT.2020.106634.

[150] Blanchet TA, Peng YL, Nablo S V. Tribology of selectively irradiated PTFE surfaces. Tribol Lett 1998;4:87–94. https://doi.org/10.1023/A:1019174331487/METRICS.

[151] Burris DL, Sawyer WG. Tribological behavior of PEEK components with compositionally graded PEEK/PTFE surfaces. Wear 2007;262:220–4. https://doi.org/10.1016/J.WEAR.2006.03.045.

[152] Lin Z, Yue H, Gao B. Enhancing tribological characteristics of PEEK by using PTFE composite as a sacrificial tribofilm-generating part in a novel dual-pins-on-disk tribometer. Wear 2020;460–461:203472. https://doi.org/10.1016/J.WEAR.2020.203472.

[153] Raviv U, Giasson S, Kampf N, Gohy JF, Jéröme R, Klein J. Lubrication by charged polymers. Nat 2003 4256954 2003;425:163–5. https://doi.org/10.1038/nature01970.

[154] Chen M, Kato K, Adachi K. Friction and wear of self-mated SiC and Si3N4 sliding in water. Wear 2001;250:246–55. https://doi.org/10.1016/S0043-1648(01)00648-2.

[155] Zhou F, Adachi K, Kato K. Friction and wear property of a-CNx coatings sliding against ceramic and steel balls in water. Diam Relat Mater 2005;14:1711–20. https://doi.org/10.1016/J.DIAMOND.2005.06.025.

[156] Matta C, Joly-Pottuz L, De Barros Bouchet MI, Martin JM, Kano M, Zhang Q, et al. Superlubricity and tribochemistry of polyhydric alcohols. Phys Rev B - Condens Matter Mater Phys 2008;78:085436. https://doi.org/10.1103/PHYSREVB.78.085436/FIGURES/8/MEDIUM.

[157] Fusaro RL, Fusako RL. Evaluation of Several Polymer Materials for Use as Solid Lubricants in Space. Tribol Trans 1988;31:174–81. https://doi.org/10.1080/10402008808981813.

[158] Hirano M, Shinjo K. Atomistic locking and friction. Phys Rev B 1990;41:11837. https://doi.org/10.1103/PhysRevB.41.11837.

[159] Erdemir A, Eryilmaz OL, Fenske G. Synthesis of diamondlike carbon films with superlow friction and wear properties. J Vac Sci Technol A 2000;18:1987–92. https://doi.org/10.1116/1.582459.

[160] Martin JM. Superlubricity of Molybdenum Disulfide. Superlubricity 2007:207–25. https://doi.org/10.1016/B978-044452772-1/50044-5.

[161] Bandeira P, Monteiro J, Baptista AM, Magalhães FD. Tribological performance of PTFE-based coating modified with microencapsulated [HMIM][NTf2] ionic liquid. Tribol Lett 2015;59:1–15. https://doi.org/10.1007/S11249-015-0545-Y/FIGURES/15.

[162] Gheisari R, Vazquez M, Tsigkis V, Erdemir A, Wooley KL, Polycarpou AA. Microencapsulated paraffin as a tribological additive for advanced polymeric coatings. Friction 2023:1–14. https://doi.org/10.1007/S40544-022-0733-3/METRICS.

[163] Economy J, Polycarpou AA, Meyer J. (2017). U.S. Patent No. 9,534,138. Washington, DC: U.S. Patent and Trademark Office.

[164] Khun NW, Liu E. Thermal, mechanical and tribological properties of polycarbonate/ acrylonitrile-butadiene-styrene blends. J Polym Eng 2013;33:535–43. https://doi.org/10.1515/polyeng-2013-0039.

APPENDIX

TRIBOMETERS

A1. High Temperature Tribometer (HTT)

The HTT shown in **Figure A1.1** is a versatile tribometer which allows in-situ tribological experiments in a wide range of temperatures, from -196 to 1000°C, under controlled atmospheres (e.g., N_2, CO_2). The furnace uses infrared radiation (IR) to heat up the sample by reflection on a quartz tube coated with gold. Yet, sufficient visible radiation is transmitted, thus the tube becomes transparent from the outside. The source of IR is a ferritic iron-chromium-aluminum (Fe-Cr-Al alloy) heating wire that is wrapped around the inside of gold-coated tube. The heating wires are separated with alumina tubes to avoid short circuits. The furnace sufficiently insulated via a muffle of clear quartz tubes, located between the outermost gold-coated tube and the heating wires, and the other one is located around the specimens. All electronics including the force transducer and the servo motor are cooled via a cooling fluid, that also passes from the upper and lower metallic stages around the furnace. For environment testing, the bell-shaped jar encloses the system, and the air is evacuated through a vacuum port and the desired gas is added though a different port. During the experiment a positive pressure should be maintained to prevent air from going into the system. The enclosure apparatus is not designed for high pressure testing, and a near AP should be maintained. Excessive pressure will burst through the rubber seal at the bottom.

Different pin-on-disk configurations, such as flat pin-on-disk, ball-on-disk, and curved pin-on-disk, enable plane, point, and line contacts, respectively. Also, the HTT offers both unidirectional (up to 1000 rpm) and oscillation motions (up to 5 Hz) for measurement of the kinetic and static friction, respectively. The electromagnetic force mechanism delivers a normal load up to 45 N and records both normal load and lateral frictional force, thus the in-situ COF can be calculated.

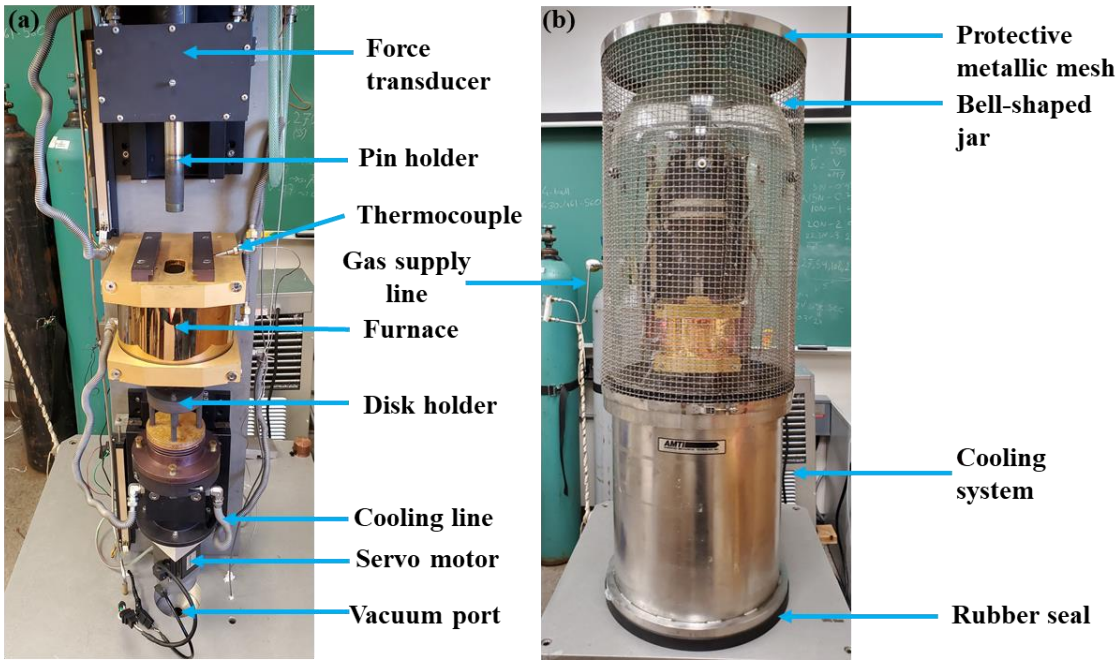

Figure A1.1 (a) Photograph of HTT and (b) bell-shaped jar enclosure for environment testing.

A2. Ultra-high Pressure Tribometer (UHPT)

UHPT is a unique tribometer with a pressurized chamber up to 13.8 MPa. The machine is equipped with a hydraulic system that actuates the transducer shaft to apply the desired normal force. The 6-axis force transducer records the forces and moments in

three directions, and the COF can be calculated either from the frictional forces or the moment in the direction normal to horizontal plane. Two different transducers are available, depending on the experiment and the desire maximum normal load. The low load transducer has an aluminum ring (wall thickness 0.2 mm) with a maximum capacity of 445 N (100 lbf), whereas the stainless-steel ring with a thickness of 1 mm has a maximum capacity of 4445 N (1000 lbf). Both rings are equipped with strain gauges for force and moments measurements. The spindle motor is located at the top and transfers rotational movement to the couples and subsequently to the upper specimen. The heating system has three temperature controllers: the main controller records the temperature on the stationary bottom sample (disk) and controls the main power output, and the other two temperature controllers get feedback from the ceramic heaters to avoid overheating (<600°C) and from the transducer for safe operation (<120°C). The following paragraph describes the modification of the apparatus with a heating chamber for HPHT testing.

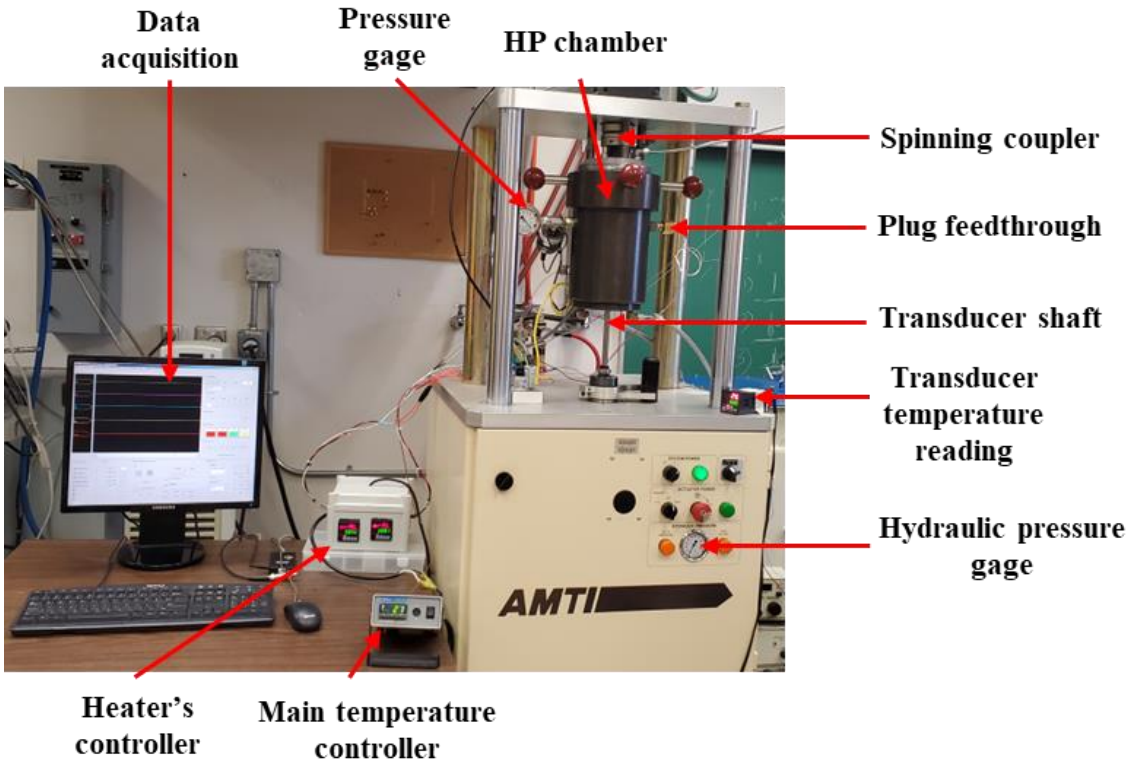

Figure A1.2 (a) Photograph of HTT and (b) bell-shaped jar enclosure for environment testing.

Two ceramic ring heaters (purchased from Watlow Electric Manufacturing Company) provided the heating source inside the testing chamber. The bottom ring is in indirect contact with the sample (disk), whereas the top ring is suspended around the top sample (**Figure A1.3(a)**). A ceramic flexible insulation is wrapped around the stage to minimize heat transfer to the surrounding environment (**Figure A1.3(b)**). The complete assembly with the pin holder is mounted onto the UHPT stage, as shown in **Figure A1.3(c)**. A mica insulation plate is placed beneath the heating assembly to enhance thermal insulation and reduce the heat being transferred to the transducer. Four lines are needed to provide enough power to the heaters and 4 lines are used to measure the

temperature of the top and bottom heaters. **Figure A1.3(d)** shows a proof-of-concept testing to ensure the heating capabilities of the setup.

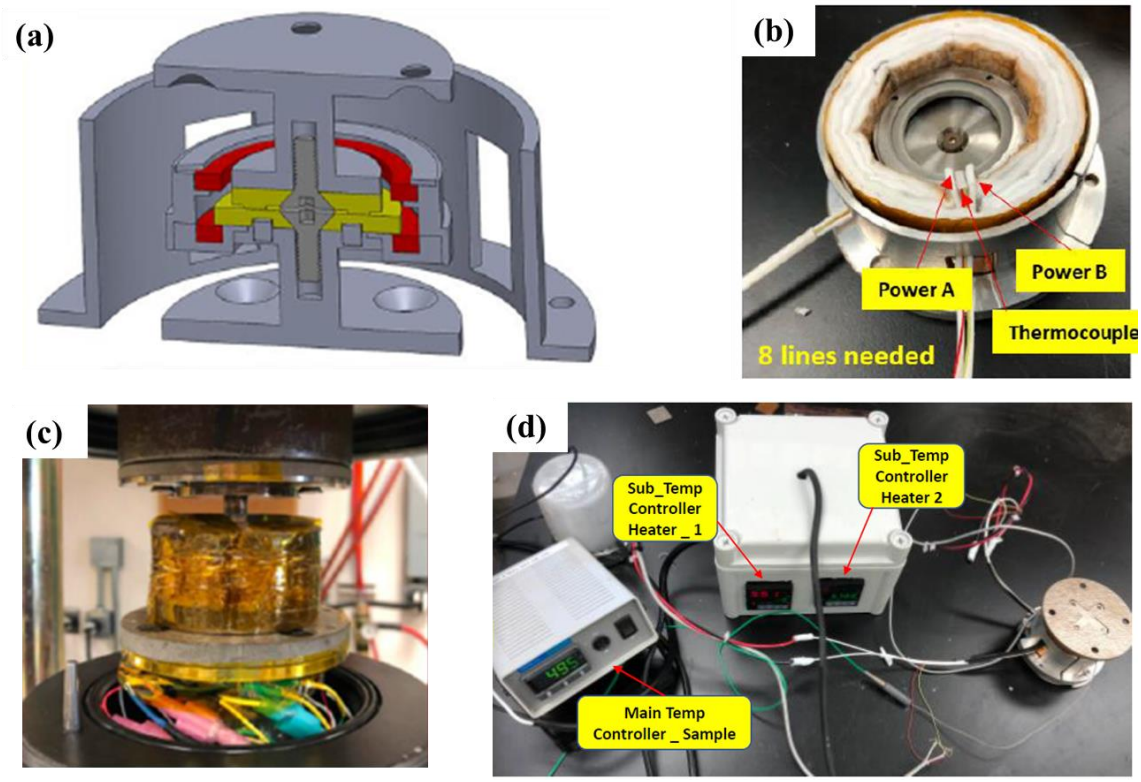

Figure A1.3 (a) Cross-section of heating chamber, (b) photograph of the apparatus showing the heating rings and ceramic insulation, (c) complete assembly mounted onto UHPT stage, and (b) proof-of-concept heat testing.